DISSERTATION

TROPICAL DEEP CONVECTION, ENTRAINMENT, AND DILUTION DURING THE DYNAMO FIELD CAMPAIGN

Submitted by

Walter Hannah

Department of Atmospheric Science

In partial fulfillment of the requirements

For the Degree of Doctor of Philosophy

Colorado State University

Fort Collins, Colorado

Summer 2014

Doctoral Committee:

Advisor: Eric Maloney

David Randall
Richard Johnson
Karan Venayagamoorthy

ABSTRACT

TROPICAL DEEP CONVECTION, ENTRAINMENT, AND DILUTION

DURING THE DYNAMO FIELD CAMPAIGN

This dissertation presents a study of outstanding questions in tropical meteorology relating to tropical deep convection, entrainment, and dilution. Much of the discussion in this study will focus on an important convectively-coupled phenomenon in the tropical atmosphere known as the Madden-Julian Oscillation (MJO), which is an eastward propagating atmospheric disturbance over the Indian and West Pacific Oceans that dominates the tropical variability on intraseasonal timescales (30-90 days). The MJO is most active during the Northern Hemisphere winter season and is characterized by alternating periods of enhanced and suppressed convective activity. A field campaign known as the "Dynamics of the MJO" (DYNAMO) was conducted in the boreal winter months from October 2011 through February 2012 to study the initialization of the MJO with in-situ observations.

The first part of this study examines hindcast simulations of the first two MJO events during DYNAMO in a general circulation model (GCM). The model used for this is the National Center for Atmospheric Research (NCAR) Community Atmosphere Model (CAM5) version 5, which uses parameterized convection. In these simulations, an entrainment rate parameter is varied to test its effects on the representation of the MJO, following previous studies. Hindcast simulations with CAM5 reveal that the entrainment parameter can improve the representation of the MJO. However, analysis of the column integrated moist

static energy (MSE) budget reveals that this improvement is the right answer for the wrong reason. CAM5 incorrectly enhances vertical MSE advection, which compensates for cloud radiative feedbacks that are too weak. A promising theory for the MJOs fundamental dynamics is that of a moisture mode. The gross moist stability (GMS) describes the ratio of advective MSE import to a measure of convective activity. Negative GMS, and specifically the vertical component of GMS (VGMS), is thought to be a necessary condition for the destabilization of a moisture mode. In CAM5, VGMS becomes negative when the entrainment parameter is increased, indicating that the model can more easily destabilize moisture modes. However, this is inconsistent with re-analysis data, which exhibits positive VGMS.

The second part of the study examines hindcasts using the super-parameterized version of CAM5 (SP-CAM) that uses embedded cloud-resolving models (CRM) to explicitly simulate convection on the sub-grid scale. SP-CAM was used for these hindcast simulations because previous studies have shown this type of model can reproduce the MJO much better than conventional GCMs. SP-CAM hindcasts yield a more robust MJO representation than CAM5, as expected. SP-CAM has an interesting systematic drift away from the initial conditions that projects well on the Real-time Multivariate MJO index (RMM), which negatively impacts the RMM skill scores. Analysis of the column MSE budget shows that SP-CAM has more realistic cloud-radiative feedbacks when compared to CAM5. SP-CAM also has a bias towards stronger import by vertical MSE advection that is similar CAM5 and inconsistent with re-analysis data. VGMS in SP-CAM is also found to be negative, which is similar to CAM5 and inconsistent with re-analysis data.

The results from the first part of this study highlight a paradox surrounding entrainment. Although, previous studies have shown that entrainment rates should be larger than typical values used in parameterizations, increasing the entrainment rate does not make global model simulations more realistic. This prompted a detailed investigation into entrainment processes in high-resolution CRM simulations. A series of simulations are conducted where deep convection is initiated with a warm humid bubble. The bubble simulations are compared to a more realistic field of deep convection driven by forcing derived from the DYNAMO northern sounding array data. Entrainment and detrainment are found to be associated with toroidal circulations, consistent with recent studies. Analysis of the directly measured fractional entrainment rates does support an inverse relationship between entrainment and cloud radius, as is often assumed in simple models of deep convection.

A method for quantifying the dilution by entrainment is developed and tested. Dilution and entrainment are generally not synonymous, but dilution is found to have a weak inverse relationship to cloud core radius. Sensitivity experiments show that entrainment and total water dilution are enhanced with environmental humidity is increased, contrary to the assumptions of some parameterizations. More vigorous convection in a more humid environment is better explained by a reduction of buoyancy dilution. An additional sensitivity experiment shows that entrainment and dilution are enhanced when convection is organized by the presence of vertical wind shear. The enhanced dilution is associated with entrainment of drier air on average.

ACKNOWLEDGEMENTS

I would like to thank my advisor, Dr. Eric D. Maloney, for his support and enthusiasm during this project. This dissertation would not have been possible without his insight, patience, and encyclopedic knowledge. I would also like to extend thanks to my committee members, Dr. David A. Randall, Dr. Richard H. Johnson, and Dr. Karan Venayagamoorthy for their time, comments, and suggestions that have helped to improve this work.

I would also like to thank several people that helped with make the technical aspects of this study possible. This includes Dr. Jerry Olson and Dr. Richard Neale at NCAR, Dr. Mike Pritchard at UC Irvine and Dr. Gabe Kooperman at UC San Diego for their help in setting up the hindcast experiments. The ECMWF, NCEP and NOAA, along with Dr. Matt Wheeler, provided high-quality datasets that were necessary for the model setup and analysis. Thanks also goes out to Dr. Marat Khairoutdinov who developed and maintains the System for Atmospheric Modeling (SAM), that was used to produce high-resolution cloud resolving simulations. I'd also like to Dr. Khairoutdinov for his help overcoming technical issues with the model. Dr. Jordan Dawe developed and kindly provided the direct entrainment measurement code that was implemented into SAM6.9.5, and for this I currently owe him a round of beers. Dr. Tak Yamaguchi provided the lagrangian parcel tracker (LPT) code, and was instrumental in helping to implement the code into SAM6.9.5. Matt Bishop, Ammon Redman, Dr. Mark Branson, Dr. Don Dazlich, and Kelley Wittmeyer deserve acknowledgement for technical support of numerous issues that arose during my time at Colorado State. A special thanks goes to my colleagues and research group members at

CSU, namely Robert Seigel, Gus Alaka, Brandon Wolding, Adam Rydbeck, Stephanie Henderson, Kate Thayer-Calder, Jim Benedict, Mark Branson and Charlotte Demott, for our valuable discussions.

I would also like to thank the agencies that funded this work. Specifically the Climate and Large-Scale Dynamics Program of the National Science Foundation under Grants AGS-1025584 and AGS- 1062161, and the Science and Technology Center for Multi-Scale Modeling of Atmospheric Processes (CMMAP), managed by Colorado State University under Cooperative Agreement No. ATM- 0425247. This work was also partially supported by Awards NA13OAR4310163 and NA12OAR4310077 from the National Oceanic and Atmospheric Administration, U.S. Department of Commerce.

Last but not least, I would like to thank my friends and family. To my parents, Bob and Linda, and my siblings, Brian and Megan, I appreciate the constant support you've given me that have shaped the person I am today. To all my friends, I thank you all for the wonderful distractions that brought joy and happiness to my life while pursuing my PhD.

TABLE OF CONTENTS

LIST OF FIGURES

CHAPTER 1 INTRODUCTION

1.1 Moist Convection in the Tropics

It has long been established that moist convection is of central importance in understanding the fundamental dynamics of the tropical atmosphere (Riehl and Malkus 1958; Emanuel et al. 1994). Perhaps the earliest work on this concept was published by Espy (1841), who correctly determined that latent heat release due to phase changes of water vapor was the primary driver of cumulus convection. Copious subsequent literature has verified the considerable impact of convection on the transport of water, heat, momentum and various atmospheric tracers. Even large-scale phenomena such as planetary Rossby waves that can be fundamentally understood by dry dynamics, are substantially affected by moist convection (Golding 1984). The Earth's radiative balance is also heavily influenced by the shortwave reflection and longwave emission associated with clouds, which provides a large source of uncertainty in estimates of the climate system response to a perturbation such as increased concentrations of greenhouse gases (Wetherald and Manabe 1980; Stephens 2005; Held and Soden 2000). Negative societal impacts of weather and climate also revolve around moist convective phenomena, such as hurricanes (Pielke et al. 2008) and monsoon systems (Mooley and Parthasarathy 1982). It is thus not difficult for one to grasp why we are motivated to understand the fundamental nature of moist convection due to the numerous pathways in which it is pivotal in atmospheric dynamics and the climate system.

The study of moist convection in the tropical atmosphere is particularly interesting due to the dynamical implications of a weak coriolis torque. At higher latitudes convection is more tightly controlled and organized by large-scale dynamics because pressure

gradients are more efficiently maintained when the background absolute vorticity is large (Bjerknes 1937; Rossby 1939; Charney 1947). The small background absolute vorticity in the Tropics allows for an efficient smoothing of pressure and temperature gradients by gravity waves (Charney 1948, 1963; Sobel et al. 2001; Romps 2012a). Consequently, tropical convection is generally sporadic and more difficult to forecast compared to convection at higher latitudes.

In spite of the weak tropical pressure and temperature gradients, it has long been recognized that tropical convection is organized on a range of spatial scales from mesoscale to synoptic to planetary (Chang 1970; Kiladis et al. 2009; Moncrieff et al. 2012). Several types of these organized convective systems are often observed to be equatorially trapped, and propagate nearly parallel to the equator, which can be explained on a fundamental level by the shallow water theory developed by Matsuno (1966) and Lindzen (1967). When a sufficiently long record of satellite measured outgoing longwave radiation (OLR) data became available, Wheeler and Kiladis (1999) were able to show that many aspects of observed convectively coupled equatorial waves are analogous to the dry linear wave theory (see also Wheeler et al. 2000). Although many studies have elucidated dynamical aspects of convectively coupled equatorial waves that make up much of the synoptic variability in the Tropics, simulated equatorial waves in global models exhibit many deficiencies associated with the treatment of moist convection (Lin et al. 2008b; Frierson and Kim 2011).

Tropical convection and convectively coupled disturbances have been shown to be important for understanding interactions with circulations outside of the tropical belt (Roundy 2012; Sardeshmukh and Hoskins 1988). Much of the research on this interaction

has focused on interannual variability associated with the El Niño/Southern Oscillation (ENSO) and revealed robust extratropical effects (Horel and Wallace 1981; Roundy et al. 2010; Moon and Ha 2003). Tropical synoptic waves have also been associated with variations in high latitude flow (Roundy and Gribble-Verhagen 2010). While tropical convection varies across a broad spectrum, interest in the intraseasonal band has been increasing due to the potential to extend predictive capabilities beyond the predictability limits associated with mid-latitude dynamics (Mo 2000; Waliser et al. 2003; Mo and Higgins 1998; Lin et al. 2010; Jones et al. 2004; Vecchi and Bond 2004; Jeong et al. 2005; Ding et al. 2010; Tung et al. 2011).

The leading mode of tropical intraseasonal variability is known as the Madden-Julian Oscillation (MJO; Madden and Julian 1971, 1994, 2005) and is characterized by a planetary scale envelope of enhanced convection that propagates slowly eastward over the equatorial Indian and West Pacific Oceans (Zhang 2005) associated with coherent wind anomalies in upper and lower tropospheric wind resembling a transient walker cell circulation (Madden and Julian 1972). Several difficulties have been encountered when attempting to explain MJO dynamics with theoretical models, as well as simulating it in numerical models. Obtaining a comprehensive understanding of what drives the MJO would have far-reaching societal benefits, due to its influence on numerous other atmospheric phenomena, such as tropical cyclogenesis (Camargo et al. 2009; Leroy and Wheeler 2008; Maloney and Hartmann 2000), African, Australian, Asian and Indian monsoon systems (Alaka and Maloney 2012; Kiladis et al. 2009; Lawrence and Webster 2002; Fu and Wang 2004), and extra-tropical circulation and precipitation (Cassou 2008; Flatau and Kim 2013; Donald et al. 2006; Lin et al. 2009). The MJO represents an important

gap in our understanding of convectively coupled phenomena and lies at the intersection of weather and climate (Zhang 2013), thus efforts to uncover more about how it works have justifiably moved to the forefront of research in tropical meteorology.

Many theories have been proposed to describe the governing dynamics of the MJO, but no current theory can explain all aspects of its initiation, maintenance and propagation. The theory of conditional instability of the second kind (CISK) was first described by Charney and Eliassen (1964) as a possible mechanism for hurricane intensification through a positive feedback, where surface friction induces low-level convergence into a vortex leading to enhanced deep convection and latent heating, which further amplifies the vortex. CISK was extended to "wave-CISK" by Yamasaki (1969), Hayashi (1970) and Lindzen (1974). Wave-CISK involves feedbacks between convection and tropical wave disturbances and has been implicated to play a role in the development of the MJO. Modified versions of wave-CISK that consider the affects of a frictional boundary layer have been examined and were found to be somewhat more realistic than the original formulation (Wang 1988; Liu and Wang 2012; Salby et al. 1994). However, wave-CISK theory is generally not favored as an explanation for the MJO on the basis that it is a difficult hypothesis to test and does not provide an explanation for scale selection of the observed MJO, among other issues (Bretherton 2002).

Another theory proposes that the convective envelope of the MJO arises from an instability driven by wind-induced surface latent heat flux (Emanuel 1987; Neelin et al. 1987a). This idea was referred to as the wind-evaporation feedback by Neelin et al. (1987), and wind-induced surface heat exchange (WISHE) by Yano and Emanuel (1991). In any case, convection is still important for redistributing moisture vertically, but the theory

centers around the evaporation anomalies induced by the anomalous wind. The phasing of wind anomalies and convection is an important aspect of the WISHE theory, which leads to a conceptual problem since the theory requires the mean state wind to be easterly in order to produce and eastward propagating disturbance. However, the mean state low-level wind in the Indian Ocean tends to be westerly on the equator. Furthermore, observations from the TOGA-COARE field campaign showed that the latent heat flux anomalies have the opposite sign of WISHE theory, with enhanced fluxes in the westerly phase occurring after the onset of enhanced convection (Weller and Anderson 1996; Lin and Johnson 1996; Zhang and Anderson 2003).

An alternative theory proposed originally by Mapes (2000) predicts that growth of a disturbance can occur due to fluctuations of convective inhibition (CIN). This theory is referred to as "stratiform instability" and results from a positive covariance between second baroclinic mode vertical profiles of temperature and diabatic heating. If stratiform instability was a principal mechanism for the MJO then top-heavy heating would lead enhanced convection, but instead, top-heavy heating occurs coincident with deep convection in observations (Straub and Kiladis 2003). In spite of this inconsistency Benedict and Randall (2007) suggested this mechanism may play a role in maintaining the convectively active phase of the MJO once it has initiated.

A forth theory put forth by Bladé and Hartmann (1993) and Hu and Randall (1995) hypothesized that the MJO is governed by a recharge-discharge cycle in which the timescale is set by the time required to thermodynamically condition the atmosphere, and the length of the ensuing period of deep convection that removes the instability. The processes that can contribute to the destabilization include extratropical synoptic eddies, shallow

convection, and radiative cooling (Hu and Randall 1995). Several studies have presented observational evidence for a recharge-discharge mechanism, although due to the localized scope of the theory it cannot fully explain all the characteristics of the MJO, such as the preference for eastward propagation and the specific timescale of approximately 50 days on average (Kemball-Cook and Weare 2001; Benedict and Randall 2007). The recharge-discharge paradigm stresses a fundamental role for the buildup of moisture anomalies in the atmosphere prior to an MJO convective outbreak. This has led to more recent discussion on the MJO to focus on the processes that are responsible for increasing column moisture (Powell and Houze 2013; Hohenegger and Stevens 2013).

Another idea that has become increasingly popular is that the MJO is fundamentally a moisture mode (Raymond and Fuchs 2009; Sobel and Maloney 2012, 2013; Pritchard and Bretherton 2014). A moisture mode is a disturbance destabilized and propagated by processes that regulate free tropospheric humidity under weak temperature gradient balance (WTG; Charney 1963; Sobel et al. 2001; Romps 2012). WTG assumes that diabatic heating is in balance with adiabatic cooling over a sufficiently large area such that horizontal temperature and pressure gradients remain small, as is observed in Tropics. A consequence of this balance is that, to first order, the large-scale dynamics do not provide a strong organizing mechanism, and so the location of convection is determined by column latent heat anomalies (i.e. moisture), which are nearly equivalent to moist static energy (MSE) anomalies under WTG (Maloney 2009). Moisture modes can become unstable when the net effect of convection and the associated divergent circulations allow for the growth of total column MSE anomalies over a sufficiently large area. A useful measure for quantifying this instability is the gross moist stability (GMS; Neelin and Held 1987;

Raymond et al. 2009), which we will define here generally as the net column divergent export of some conserved quantity, such as MSE, normalized by a measure of convective activity, similar to Raymond et al. (2009). Although moisture modes are theoretically unstable in the presence of negative GMS, previous studies have suggested that an "effective" GMS, that includes the effects of MSE sources such as radiation and surface fluxes, is more appropriate for characterizing the ability to destabilize the MJO (Raymond and Fuchs 2009; Sugiyama 2009; Sobel and Maloney 2013; Hannah and Maloney 2011; Chikira 2014).

1.2 Convection in Large-Scale Numerical Models

The MJO is an example of a large-scale atmospheric phenomenon where the horizontal scale of the disturbance is much larger than convective clouds, but its dynamics are critically dependent on the collective effects of convection (Zhang 2005). Hurricanes are perhaps the smallest phenomenon in this category, which are rotationally balanced circulations that heavily depend on moist convection to transport heat through the system (Emanuel 2003). The importance of this scale interaction becomes a problem when investigating these disturbances with numerical models because until recently, global models have never been able to adequately resolve individual convective clouds. A typical convective cloud has a horizontal footprint on the order of 1-10km and global numerical models used today for studying the climate system have horizontal grid spacing on the order of 100km. Although computing power has progressed to a point that allows for short integrations of "cloud permitting" simulations on a global scale (Miura 2005; Satoh et al.

2008; Sato et al. 2009), this method is limited when investigating climate and climate variability (Liu et al. 2009).

To remedy the issues encountered when modeling a convectively coupled phenomenon that is much larger in scale than cumulus convection, numerous methods have been developed to parameterize the collective effect of unresolved convection based on information from the large-scale environment (Arakawa 2004). This approach is based on the idea that convection exists in a statistical equilibrium with the generation of instability by the large-scale processes (Emanuel 1994). The earliest methods for parameterizing unresolved convection came from work on tropical cyclones (Charney and Eliassen 1964; Ooyama 1964) and the general circulation (Manabe and Strickler 1964). In either case, the main task of any convective parameterization is to provide a negative feedback on the lapse rate of temperature such that it is constrained to realistic values.

Some of the earliest generalized methods for parameterizing convection were based on the idea that precipitation should be balanced by the supply of moisture from large-scale convergence (Kuo 1965, 1974). This assumption was later realized to be fundamentally flawed and can lead to numerous problems such as artificial CISK modes, grid point storms and unrealistic water vapor biases (Numaguti and Hayashi 1991; Emanuel 1994). Another method for convective parameterization was based on the idea that convection acts to relax the atmosphere toward some equilibrium that is neutral to buoyant instability while conserving the total heat content of the column, commonly referred to as “moist convective adjustment”. Early prototype schemes for moist convective adjustment used in global models required that a grid point become completely saturated for sub-grid convection to become active (Manabe et al. 1965). These early schemes did not

require a conceptual cloud model to close the system of equations since the equilibrium state that dictated the adjustment was tightly constrained by the large-scale profiles of temperature and humidity. The lack of a cloud model resulted in some unrealistic characteristics such as convection that was confined to the unstable layer and was not allow it to penetrate to higher layers (Arakawa 2004). More sophisticated moist adjustment schemes have been developed, such as the scheme of Betts and Miller (1986), however these schemes still often take advantage of invariant reference states that can be tuned for use in weather prediction, but are unsuitable for climate modeling (Emanuel 1994).

It may seem obvious that the statistical properties of a population of convective clouds should be related to the properties of individual convective elements, but the way in which a cloud model should be incorporated into a convective parameterization is far from obvious. Numerous conceptual cloud models have been used for this purpose beginning with Ooyama (1969) and Arakawa (1969). These cloud models often make use of a similarity assumption such that clouds are horizontally homogeneous, which can be a issue when estimating radiative fluxes (Oreopoulos and Cahalan 2005; Hogan and Illingworth 2003). These models differ widely in how the cloud mass flux is determined from large-scale variables, as well as other aspects of convection such as downdrafts and microphysics (Arakawa 2004).

The mass budget of a cloud is of central importance when formulating a method for convective parameterization, and can be characterized by entrainment and detrainment, which represent the mass source and sink of cloud air, respectively. Entrainment and detrainment are often referred to as “mixing” parameters, since they determine the extent

of interaction between parameterized convection and the resolved environment of the model. These parameters also play an equally important role in controlling the overall cloud updraft mass flux. The upward mass flux in the cloud must be compensated by subsidence outside the cloud, which ultimately warms and dries the large-scale environment, and acts to reduces the convective available potential energy (Arakawa and Schubert 1974). This compensating subsidence is spread radially outward over a large area through gravity waves set off as the cumulus cloud penetrates upward through the troposphere (Bretherton 1987; Bretherton and Smolarkiewicz 1989).

The seminal work of Arakawa and Schubert (1974) outlined a theory based on an equilibrium between the rate of large-scale destabilization and the stabilizing effects of a spectrum of convective plumes with various heights and entrainment rates (see also Yanai et al. 1973). This concept relies on the assumption that convection induced large-scale tendencies are very fast compared to the observed tendency, which leads to a loose equilibrium, referred to as quasi-equilibrium, between large-scale and convective tendencies. Certain aspects of the approach used by Arakawa and Schubert (1974) have gained continued support over the years, such as the entraining plume spectrum approach (Lin and Arakawa 1997a) and the use of the quasi-equilibrium concept (Zhang 2003; Neelin et al. 2008). Many schemes have introduced simplifications or enhancements to the theory to account for overlooked processes or make the computations more economical (ex. Grell 1993). The success of these ideas have spawned numerous schemes that can trace their roots to the work of Arakawa and Schubert (1974) and are still in use today (Zhang and Mcfarlane 1995; Fritsch and Chappell 1980; Tiedtke 1989; Emanuel 1991; Moorthi and Suarez 1992; Pan and Randall 1998; Chikira 2010).

In spite of the successes and widespread use of convective parameterizations inspired from Arakawa and Schubert (1974), several deficiencies in our understanding of the interaction between convection and the large-scale environment remain. Specifically, microphysical processes and mesoscale organization are entirely neglected in many convective parameterizations. Accurately accounting for microphysical processes is essential for several problems in climate dynamics such as feedbacks between convection and radiation (Bony 2005) and indirect feedbacks resulting from varying aerosol concentrations (Albrecht 1989; Twomey 1977). The implications of neglecting mesoscale organization are not completely understood, however many studies have presented convincing evidence that mesoscale organization is crucial for certain large-scale flows (Moncrieff 2010; Lane and Moncrieff 2010; Mapes and Neale 2011). Other insufficiently treated processes in many cumulus parameterizations include downdrafts (Johnson 1976; Thayer-Calder 2012) and convective momentum transport (Romps 2012b; Moncrieff and Liu 2006).

The difficulties encountered when simulating the MJO discussed above are inherently tied to the treatment of subgrid-scale convection. To complicate matters further, a model's ability to simulate the MJO is not uniquely tied to its convective parameterization, but rather a complex of interaction of convection and other physical processes in the model (Kim et al. 2009; Slingo et al. 1996; Lin et al. 2006; Pritchard and Bretherton 2014; Maloney 2009; Sobel et al. 2010). A relatively new method, known as "super-parameterization", has been shown to be capable of reproducing a robust MJO signal by replacing certain physical parameterizations, including convection, with a higher resolution cloud-permitting model that is embedded into each grid cell of the host large-scale model (Randall et al. 2003).

Super-parameterization allows a more natural interaction between convection and the large-scale environment compared to traditional convective parameterization. However, it is far more costly to utilize and has been shown to introduce a few problems of its own, such as precipitation, moisture and temperature biases (Tao et al. 2009; DeMott et al. 2007). Despite these challenges super-parameterization and related model development efforts, these methods are likely to gain wider popularity in atmospheric modeling in the coming decades (Arakawa et al. 2011).

Aside from super-parameterized models, there are conventional global models that do indeed produce robust MJO variability, such as the European Center Hamburg (ECHAM) model (Kim et al. 2009). The ability to produce an MJO in parameterized models appears to be intimately related to the sensitivity of convection to environmental moisture, because models that cannot produce the MJO do exhibit a strong sensitivity (Tokioka et al. 1988; Neale et al. 2008; Bechtold et al. 2008; Sahany et al. 2012; Chikira 2010). A key factor that determines the sensitivity of convection to humidity is the entrainment rate, as this controls the degree to which convection can be affected by environmental conditions. The next section will discuss this issue in more detail.

1.3 The Entrainment Paradox

The way entrainment and detrainment rates are determined in a convective parameterization strongly influences the behavior of convection in a global model, especially that associated with the MJO (Rougier et al. 2009; Hannah and Maloney 2011; Chikira 2010). Typical convection schemes obtain the cloud mass flux from the continuity equation of a simple entraining plume:

$$\rho \frac{\partial a}{\partial t} + \frac{\partial M_c}{\partial z} = E - D \qquad (0.1)$$

Here a is the fractional area covered by the cloud updraft, M_c is the vertical cloud mass flux, and E and D are the total entrainment and detrainment rates respectively. This entraining plume represents either a single member of an ensemble of clouds, or an average over an ensemble of clouds. Once a method is specified for determining the cloud mass flux, several properties of the cloud can be determined, such as precipitation rate, vertical distribution of cloud water and cloud top height (de Rooy et al. 2013; Dawe and Austin 2011a). These properties can then be used in conjunction with certain "closure assumptions" to calculate how the convection will affect the large-scale environment (Arakawa and Schubert 1974; Pan and Randall 1998; Zhang 2003).

In practice, the tendency of the cloudy updraft area "*a"* is often neglected, based on the assumption that the combined area of all cloudy updrafts is very small compared to the size of the grid cell. The validity of this assumption becomes problematic in the presence of large organized convective systems that can span the area of a model grid box (Moncrieff 1992). This assumption is also a problem as model resolution becomes finer, because the convective response becomes increasingly non-deterministic (Jones and Randall 2011). Currently, Efforts are underway to create "scale aware" convective parameterizations that do not rely on this assumption (Arakawa 2004; Arakawa and Wu 2013; Randall 2013).

Determining the entrainment and detrainment rates in a parameterization requires the use of a conceptual cloud model as previously discussed. The cloud geometry of these models are often variations on a continuous *plume* (i.e. jet) or a discrete buoyant *thermal* as depicted in Figure 1.1 (Turner 1969). One of the earliest studies to estimate entrainment was that of Stommel (1947), who concluded that entrainment of air from outside a cloud

and above cloud base was required to explain the observed cloud volume. Investigations into the dynamics of simple convective flows were conducted in the 1950's and 60's and made use of tank experiments and dimensional analysis to develop a theoretical understanding of basic cloud dynamics (Morton et al. 1956; Turner 1962; Richards 1963). In the following decades aircraft-based thermodynamic measurements were used to directly probe the mixing processes of actual clouds (Telford 1975; Paluch 1979). When cloud model calculations were compared to these in-situ cloud observations (Warner 1955; Simpson et al. 1965), some interesting discrepancies became apparent (Warner 1970). A series of exchanges between Dr. Joanne Simpson and Dr. Jack Warner highlighted the unsatisfactory nature of the current entrainment theory, with the biggest disagreement surrounding the use of a prescribed precipitation "fallout" of decidedly non-precipitating clouds in order for the liquid water content of a one-dimensional cloud model to agree with observations (Simpson 1971; Warner 1972; Simpson 1972; Lin and Arakawa 1997b).

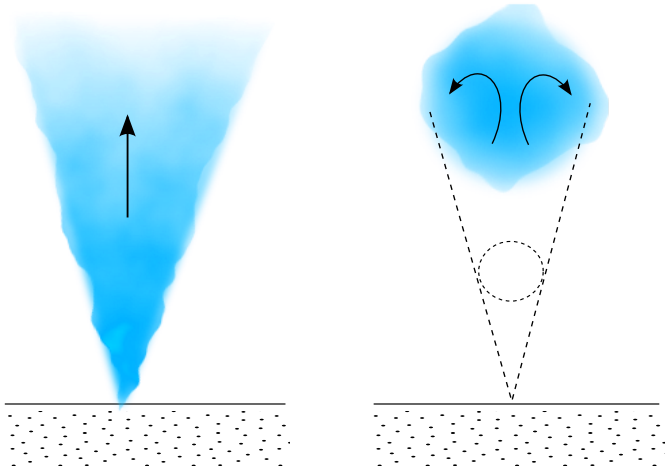

Fig. 1.1 Sketch of conceptual convective plume (left) and thermal (right).

Paluch (1979) introduced a thermodynamic method for diagnosing entrainment from glider observations in northeastern Colorado. This provided evidence that cloud air was a mixture of air from cloud base and levels above the observation level (see also Blyth et al. 1988). Several subsequent studies supported the notion that air is rarely entrained and carried appreciable distances within a cloud core, which painted a very different picture than theories based on simple entraining plumes. These studies paved the way for parameterizations based on episodic, rather than continuous, entrainment often referred to as "buoyancy sorting", in which parcels seek a new level of neutral buoyancy after mixing with environmental air (Telford 1975; Raymond and Blyth 1986; Emanuel 1991; Taylor and Baker 1991). More recent studies have challenged the conclusions of Paluch (1979), by suggesting alternative interpretations of the mixing diagram analysis (Lin and Arakawa 1997a). Another issue with these ideas is that it allows cloud parcels to experience substantial descent to reach the level of neutral buoyancy. This idea is consistent with the thinking of Squires (1958), who proposed that large entrainment may occur at cloud top through penetrative downdrafts driven by evaporative cooling. However, recent studies do not find evidence to support this hypothesis (Lin and Arakawa 1997a).

In addition to the complications of determining where entrained air comes from and how environmental air is mixed into a cloud, there is also the issue of knowing whether entrainment happens to all parcels within a cloud. A debate about the existence of undilute convective parcels that rise from the boundary layer to the upper tropopause was initiated by the results of Riehl and Malkus (1958). Based on observations of MSE in the upper tropical troposphere, they noted that MSE at the tropopause was roughly the same as that

near the surface. Due to the unimodal profile of MSE with a mid-tropospheric minimum, they hypothesized that any amount of entrainment in the middle troposphere would lower the cloud's MSE below that of the tropopause. Riehl and Malkus (1958) hypothesized that parcels in the inner core of deep convective clouds were able to remain protected from entrainment and therefore be undilute. If this were true it would have significant implications for parameterization development. However, several studies have shown that this reasoning neglects the latent heat released by the formation of ice through freezing and deposition, which can significantly alter a cloud's final height (Zipser 2003; Fierro et al. 2009). Evidence for undilute parcel ascent is also lacking from cloud-resolving simulations (Romps and Kuang 2010a), which stresses the need to explore other ways to explain the distribution of deep convective plumes at the tropopause.

1.4 Overview of this Study

Convective parameterization will continue to be a necessary technique for treating sub-grid scale convection in experiments designed to probe global scale problems, such as interannual, decadal and centennial variability and equilibrium responses to climate perturbations. Not all modeling studies can afford to take advantage of super-parameterization or cloud permitting resolution at a global scale to address these issues. In addition to a practical need for advancing the field of convective parameterization, the ability to build simple models that accurately represent the interaction between convection and large-scale processes enhances our general understanding of atmospheric dynamics. Newer methods of treating convection, such as prognostic cloud schemes (Pan and Randall 1998) and state-dependent entrainment parameterizations (Bechtold et al. 2008; Chikira

and Sugiyama 2010), are being explored, and provide a promising avenue for improvement. Focused investigations of convective processes through high resolution and modeling will greatly assist in further advancing these efforts.

The purpose of this study is two-fold. First, two treatments of deep convection that produce robust MJO-like variability are investigated to asses whether they can reproduce the dynamics of two observed MJO events in a realistic manner. Second, entrainment and detrainment processes of tropical deep maritime convection are explored in the context of the underlying assumptions used to formulate convective parameterizations in order to provide guidance for future convective parameterization development.

Chapter 2 investigates the effects of a typical approach to improving the MJO in a parameterized global model. This approach based on the idea that taller and more vigorous convection is characterized by small entrainment rates, and so deep convection can be suppressed by constraining entrainment parameters. Several simulations are conducted with the model to test its ability to hindcast two MJO events during a recent field campaign in the Indian Ocean. Modifying entrainment parameters to coerce convection to be more sensitive to free tropospheric humidity has been shown to improve the simulated MJO (Wang and Schlesinger 1999; Kim et al. 2009; Hannah and Maloney 2011). However, this study suggests that these methods produce the right answer for the wrong reasons. Analysis of the column MSE budget is used to show that cloud radiative feedbacks are too weak in the model, and that modifying an entrainment parameter allows this deficiency to be compensated by making vertical MSE advection overly efficient at importing MSE into the column. In order to account for differences in the strength of convection between the

datasets, the concept of GMS is invoked to interpret the change in vertical MSE advection in a normalized framework.

The results of Chapter 2 are compared with a super-parameterized version of the model in Chapter 3. The super-parameterized model has more realistic cloud-radiative feedbacks, but, surprisingly, the super-parameterized model has a vertical MSE advection bias similar to the parameterized model counterpart in Chapter 2. Chapter 3 also explores the impact of systematic model drift in the hindcast simulation of both models to show that it can significantly distort the interpretation of the predictive skill of the model. The impact of model drift on the column MSE budget is also studied, but is found to have a minimal influence on the quantities of consequence for moisture mode dynamics.

The results of Chapter 2 highlight a paradox surrounding convective entrainment, in that we know the entrainment should be sufficiently large, but coercing entrainment to be large often leads to undesired consequences. Chapter 4 attempts to reconcile this paradox by revisiting the type of experiment that provided the foundation for many assumptions used in current convective parameterizations. A cloud-resolving model is used to investigate entrainment and detrainment processes in clouds produced by the release of a warm and humid bubble in idealized tropical conditions. A large domain simulation forced with data from the DYNAMO northern sounding array to compare to convection that is triggered in a natural manner. Large entrainment and detrainment are found to result from coherent toroid-like circulations on the scale of the convecting thermal, which recirculate cloud air through the core of the thermal. Interestingly, the analysis suggests that the often-assumed inverse relationship between cloud radius and entrainment is invalid. A method for quantifying dilution is presented and used to illustrate that entrainment is not

synonymous with dilution. Sensitivity experiments are conducted to test the effect of enhanced humidity and mesoscale organization. Both enhanced humidity and organization are found to result in larger entrainment and dilution, which is counter-intuitive and reveals inconsistencies in assumptions of previous studies.

CHAPTER 2 DYNAMO HINDCASTS: THE MSE BUDGET IN CAM5

I always avoid prophesying beforehand, because it is much better to prophesy after the event has already taken place

-Winston Churchill

2.1 Introduction

The Madden-Julian Oscillation (MJO; Madden and Julian 1971) remains an important gap in our understanding of convectively coupled phenomena in the Tropics. The MJO occurs on subseasonal timescales at the interface of weather and climate (Zhang 2013), and the ability to accurately simulate it provides the potential to improve weather prediction at lead times up to 35-50 days (Ding et al. 2010; Tung et al. 2011). Ability to forecast MJO events has far-reaching societal benefits due to the MJO's influence on tropical cyclogenesis (Maloney and Hartmann 2000; Leroy and Wheeler 2008; Camargo et al. 2009), African, Australian, Asian and Indian monsoons (Alaka and Maloney 2012; Camargo et al. 2009; Lawrence and Webster 2002; Fu and Wang 2004), and extra-tropical circulation patterns (Cassou 2008; Flatau and Kim 2013).

Forecasts of the MJO have shown minimal improvement in recent years and their skill is still less than half of the potential predictability (Vitart et al. 2007; Seo et al. 2009; Waliser 2005; Gottschalck et al. 2010). Climate models notoriously struggle to produce a satisfactory MJO, with few exceptions (Slingo et al. 1996; Lin et al. 2006; Kim et al. 2009; Benedict and Randall 2009). Several methods have been shown to enhance tropical intraseasonal variability in models, such as higher vertical resolution (Inness et al. 2001), higher temporal SST resolution (Klingaman et al. 2008, 2011), ocean coupling (Zheng et al. 2004; Woolnough et al. 2007), inclusion of convective momentum transport (Zhou et al. 2012), and modified treatments of convection (Maloney and Hartmann 2001; Lin et al.

2008b; Hannah and Maloney 2011; Subramanian et al. 2011; Kim et al. 2012; Benedict et al. 2014). The most dramatic improvements have come from the use of a multi-scale modeling framework (MMF) in which a cloud resolving model is embedded in each grid cell of a host climate model (Randall et al. 2003; Benedict and Randall 2009; Zhu et al. 2009). Modifying the convection parameterization is the most common approach to enhance intraseasonal variability in conventional global models.

No consensus exists on a theory to explain the fundamental dynamics of the MJO. A leading hypothesis relevant to our results is that the MJO is fundamentally a moisture mode (Raymond and Fuchs 2009; Sobel and Maloney 2012, 2013; Pritchard and Bretherton 2014), which is a disturbance destabilized and propagated by the processes that regulate free tropospheric humidity under weak temperature gradient balance (WTG; Charney 1963; Sobel et al. 2001). WTG assumes that diabatic heating is in balance with adiabatic cooling over a large area average such that horizontal temperature gradients remain small. The location of convection is primarily determined by column latent heat anomalies, which are roughly equivalent to moist static energy (MSE) anomalies under WTG (Maloney 2009).

Moisture modes can be destabilized when the net effect of deep convection and associated divergent circulations allow for the growth of column MSE anomalies. A useful measure for quantifying this condition is the gross moist stability (GMS; Neelin and Held 1987), which we define here as the net column divergent export of some conserved quantity, such as MSE, normalized by a measure of convective activity. This definition is similar to that proposed by Raymond et al. (2009), although we concentrate primarily on exports due to vertical advection here (e.g. see also Hannah and Maloney 2011). In this

definition, negative GMS implies that convection and the associated divergent circulations are acting to moisten the column and promote further convection. Ling et al. (2013) found that the GMS was slightly smaller in ERAi data during MJO events when compared to non-MJO convective events, but generally concluded that the behavior of GMS was not fundamentally different and therefore not able to distinguish MJO and non-MJO events. Low GMS may be a necessary condition for MJO convective organization, but organization may not always occur for lack of an appropriate trigger or the presence of suppressing factors. Although moisture modes are theoretically unstable in the presence of negative GMS, previous studies have suggested that including the effects of radiation and surface fluxes to obtain a negative "effective" GMS may be most appropriate for characterizing the ability to destabilize the MJO (Raymond and Fuchs 2009; Sugiyama 2009; Sobel and Maloney 2013).

Hannah and Maloney (2011) compared how increasing either convective entrainment (Tokioka et al. 1988) or rain evaporation (Grabowski and Moncrieff 2004) in a deep convection scheme impacted the simulated MJO. Both parameters helped increase the sensitivity of convection to free tropospheric humidity and to enhance the MJO, but also had inconsistent effects on the mean state of the model, signifying no unique relationship between the quality of the MJO simulation and the mean state. While higher entrainment led to strongly reduced mean GMS, rain evaporation did not have any substantial affect on the mean GMS. Closer inspection of the temporal variability of GMS showed that both modifications caused a decrease in GMS 10 days prior to enhanced convection in a composite MJO event suggesting that intraseasonal GMS variations may be important to the fundamental dynamics of the MJO (see also Benedict et al. 2014).

A recent international field campaign (Yoneyama et al. 2013) was organized to help advance our understanding of the MJO, known primarily in the U.S. as DYNAMO (Dynamics of the MJO)/ AMIE (ARM MJO Investigation Experiment) and internationally as CINDY2011 (Cooperative Indian Ocean Experiment on Intraseasonal Variability in the year 2011) with further international contributions from LASP (Littoral Air-Sea Processes). The experiment was designed to capture the initiation of MJO events with field observations collected in the central Indian Ocean where the MJO convective signal is often observed to originate. Data was also collected from an extended sounding network stretching from East Africa to the West Pacific (Yoneyama et al. 2013). The early part of DYNAMO saw two coherent MJO events during 01 October - 15 December 2011. The first two events were somewhat atypical with a period around 30 days (Johnson and Ciesielski 2013). A less active period during 15 December – 31 January was followed by a strong, slowly-propagating MJO event in February and March (Gottschalck et al. 2013). DYNAMO provides a unique opportunity to conduct process-oriented model diagnosis in the context of the MJO using in situ data from a data sparse region.

This chapter extends the results of Hannah and Maloney (2011) to consider how the MSE budget responds to a moisture sensitivity parameter on short temporal scales when initialized from analyses during the DYNAMO period. Our results also complement those of Benedict et al. (2014), who showed that models with a lower GMS produce more realistic MJO behavior in long multiyear simulations. In this paper, a "hindcast" approach is employed for the first two MJO events of the DYNAMO period. Section 2 outlines the model and methods of analysis. Section 3 provides an overview of model performance, followed

by an inspection of the column MSE budget in section 4, and analysis of the GMS in section 5. Conclusions are found in section 6.

2.2 Methodology

2.2.1 Model Setup

Simulations are conducted with the Community Atmosphere Model version 5 (CAM5), which is the atmospheric component of the National Center for Atmospheric Research (NCAR) Community Earth System Model version 1 (CESM; Neale et al. 2010). For our simulations we use a finite volume dynamical core, 30 vertical levels and 0.9°x1.25° horizontal resolution. CESM contains a moist boundary layer scheme based on Bretherton and Park (2009), the prognostic two-moment bulk cloud microphysics scheme of Morrison and Gettelman (2008), and the shallow convection scheme of (Park and Bretherton 2009).

Deep convection is represented using the parameterization of Zhang and Mcfarlane (1994; ZM) modified to include a dilute calculation of convective available potential energy (CAPE; Neale et al. 2008). Convection in ZM is limited by a specified timescale at which CAPE can be consumed. Using undiluted CAPE has been shown to make ZM convection relatively insensitive to free tropospheric humidity (Donner and Phillips 2003). The dilute CAPE calculation assumes a fixed fractional entrainment rate of the reference parcel, which tends to result in a lower equilibrium level and less CAPE. In order to explore the model's sensitivity to free tropospheric humidity we use three model configurations with fractional entrainment rates of 0.2, 1.0 and 2.0 km^{-1} applied in the calculation of dilute CAPE, inspired by the experimentation of Klein et al. (2012) who showed that stronger CAPE dilution in CAM5 results in improved MJO hindcast skill, although Klein et al. (2012) did not analyze

the DYNAMO period. We distinguish the simulations as ZM_0.2, ZM_1.0 and ZM_2.0, where ZM_1.0 is referred to as the control, since this is the default configuration of CAM5. The low entrainment simulation (ZM_0.2) is meant to be similar, but not identical, to the older version of the model that assumed undilute CAPE (Lin et al. 2006). Deep convective momentum transport is also an addition to this version of the model relative to older versions (Neale et al. 2008; Richter and Rasch 2008).

Initial conditions for CESM were created from ECMWF operational analysis at 00z every 5 days from 01 October – 15 December 2011. Each simulation was integrated for 20 days with output every 6 hours. Hindcast skill is estimated using the Real-time Multivariate MJO index (RMM; Wheeler and Hendon 2004) following Rashid et al. (2010) and (Lin et al. 2008a) to estimate a bivariate correlation (COR) and root mean square error (RMSE) of the hindcast RMM given by,

$$COR(\tau) = \frac{\sum_{t=1}^{N}\left[a_1(t)b_1(t,\tau) + a_2(t)b_2(t,\tau)\right]}{\sqrt{\sum_{t=1}^{N}\left[a_1^2(t) + a_2^2(t)\right]}\sqrt{\sum_{t=1}^{N}\left[b_1^2(t,\tau) + b_2^2(t,\tau)\right]}}, \tag{2.2}$$

$$RMSE(\tau) = \sqrt{\frac{1}{N}\sum_{t=1}^{N}\left[a_1(t) - b_1(t,\tau)\right]^2 + \left[a_2(t) - b_2(t,\tau)\right]^2}, \tag{2.3}$$

where $a_{1,2}(t)$ is the verification RMM and $b_{1,2}(t,\tau)$ is the respective forecast for time t and lead time τ (see also Gottschalck et al. 2010). COR is insensitive to amplitude errors and so should be considered as a measure of RMM phase skill in the hindcast, whereas RMSE is sensitive to both phase and amplitude errors. Since both indices are normalized by their standard deviations, an RMSE of 2 indicates that the two indices are no longer correlated, and therefore the model has no skill beyond this threshold. Similarly, we use a

threshold of 0.5 for COR to indicate hindcast skill consistent with previous studies (Rashid et al. 2010). Note that we retain interannual variability in our RMM calculation.

Models are known to quickly drift when initialized from observations (Xie et al. 2012; Ma et al. 2013). This drift is often corrected at operational centers that can take advantage of a long record of forecasts (Gottschalck et al. 2010). Drift correction can significantly affect estimates of model skill, although we feel that applying such corrections to our simulations is not necessary to understand the fundamental role of convection in MJO dynamics, especially given that improvements in model performance engendered by increasing entrainment rate would be independent of any drift correction. Even if drift were of first order importance, the environmental changes associated with such drift provide an interesting opportunity to apply our diagnostics to characterize these environmental changes in the context of MJO hindcast performance. Chapter 3 will explore the influence of model drift in great detail, with respect to its influence on RMM skill and thermodynamic budgets. To facilitate the interpretation of our results, we present the hindcast data bundled together according to the time since initialization in 5-day segments. We will mainly focus on the 00-04 and 05-09 day datasets in our process-oriented diagnostics.

2.2.2 Validation Data

The European Centre for Medium-Range Weather Forecasts (ECMWF) interim reanalysis product (ERAi; Dee et al. 2011) is used throughout this study for model comparison and was obtained from the ECMWF data server. Reanalysis data provide comprehensive spatial coverage for the Indian Ocean where observations are sparse,

however ERAi fields may be highly model-dependent in this region. Mapes and Bacmeister (2012) noted that reanalysis models may produce substantial analysis increments due to physical deficiencies during an MJO lifecycle that make the reanalyzed fields consistent with observed constraints. Landu and Maloney (2011) showed a substantial residual in the column-integrated Indian Ocean ERAi MSE budget during an MJO lifecycle that might be partially associated with such analysis increments. Although ECMWF operational analysis data available to us were suitable for creating the initial model conditions, the radiative heating and surface flux fields necessary for evaluating the MSE budget were only available to us at 12 hour intervals instead of 6 hour intervals, as in ERAi data. Comparison of the MSE budget showed that this difference in sampling of the radiative heating and surface flux terms had a significant impact on the closure of the budget, which resulted in a larger budget residual in ECMWF data compared to ERAi (not shown). Therefore, we feel that the use of ERAi instead of ECMWF data is better justified in this study. The ERAi data used here are on a 1°x1° grid with 22 vertical levels from 975 to 70 hPa. For precipitation we make use of the Tropical Rainfall Measuring Mission (TRMM) 3B42 3-hourly high-resolution (0.25°x0.25°) merged satellite rainfall product (Huffman et al. 2007).

Hindcasts are validated using Eq. 1 and Eq. 2 against the Real-time Multivariate MJO index (RMM) produced using multivariate EOF analysis on National Centers for Environmental Prediction and National Center for Atmospheric Research (NCEP-NCAR) reanalysis (Kanamitsu et al. 2002) 200 hPa and 850 hPa equatorial averaged (15°N-15°S) zonal winds and National Oceanic and Atmospheric Administration (NOAA) interpolated outgoing longwave radiation (OLR; Liebmann and SMith 1996; Wheeler and Hendon 2004) following the method of Gottschalck et al. (2010). The long-term mean of wind and OLR

fields were removed from the hindcast data in an identical manner to Gottschalck et al. (2010) before projecting onto the RMM spatial patterns. Long-term means used for calculating RMM skill scores were calculated from NCEP reanalysis data and NOAA OLR. We use NCEP reanalysis winds here to be consistent with MJO skill assessment in recent literature (Gottschalck et al. 2010). Real-time Multivariate MJO index (RMM) values were acquired through a website maintained by Matt Wheeler (http://cawcr.gov.au/staff/mwheeler/maproom/RMM/).

2.3 Hindcast Results

Maps of precipitation averaged over the initial 5 days of the simulations (00-04 day leads) indicate similar patterns between TRMM and the case with small entrainment parameter (ZM_0.2). Precipitation is generally reduced in both cases with an increased entrainment parameter (ZM_1.0 and ZM_2.0) relative to ZM_0.2 (Fig. 2.1). One exception to this conclusion is that the precipitation increases over Papua New Guinea. This suggests that increasing the entrainment parameter does reduce the intensity of convection by reducing the amount of convective available potential energy. More dilute entrainment may also be effectively suppressing the intensity deep convection by lowering the altitude of equilibrium level, which determines the ultimate height of convective plumes (Zhang and Mcfarlane 1995).

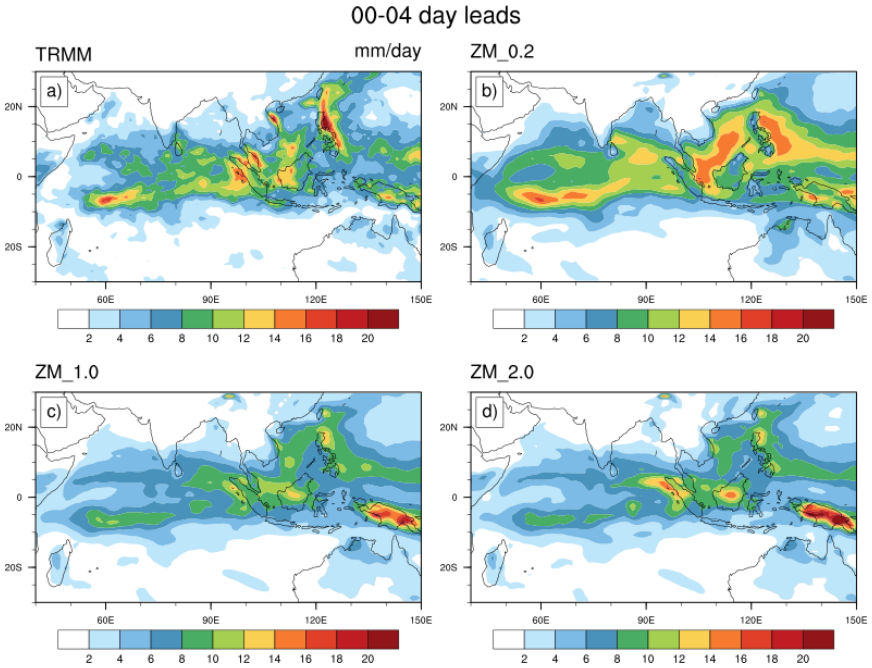

Fig. 2.1 Mean precipitation map for 00-04 day lead times.

At later lead times the amplitude of mean precipitation is reduced in ZM_0.2 and becomes comparable to ZM_1.0 and ZM_2.0 (Fig. 2.2b). ZM_1.0 or ZM_2.0 show a slight reduction in the intensity of mean precipitation, but do not show a notable change in the pattern at 05-09 day leads (Fig. 2.2c-d). The pattern of precipitation in ZM_1.0 and ZM_2.0 are grossly similar to TRMM (Fig. 2.1-2a), but the intensity in the southern hemisphere inter-tropical convergence zone (ITCZ) over the Indian Ocean is notably weak (0-10°S; 50-100°E).

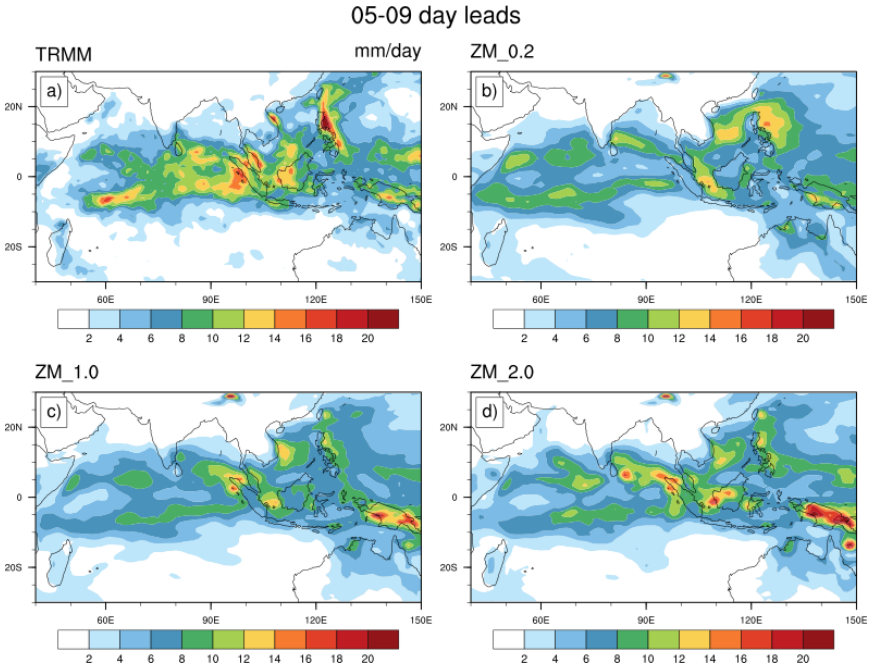

Fig. 2.2 Mean precipitation map for 05-09 day lead times.

Equatorial averaged 850 hPa zonal wind and precipitation for 00-04 day leads are shown in Figure 2.3 as a function of time and smoothed with three passes of a 1-2-1 filter. Alternating periods of easterly (cool colors) and westerly (warm colors) can be seen in ERAi across the Indian and West Pacific Ocean regions (Fig. 2.3a). These alternating wind patterns vary in quadrature with enhanced and suppressed precipitation periods in TRMM data (Fig. 2.3e) MJO wind and precipitation variations are better captured by ZM1.0 and ZM2.0, although the amplitude of precipitation variations is weaker than TRMM observations. ZM_0.2 exhibits a less coherent MJO precipitation signal at these short lead times (Fig. 2.3h).

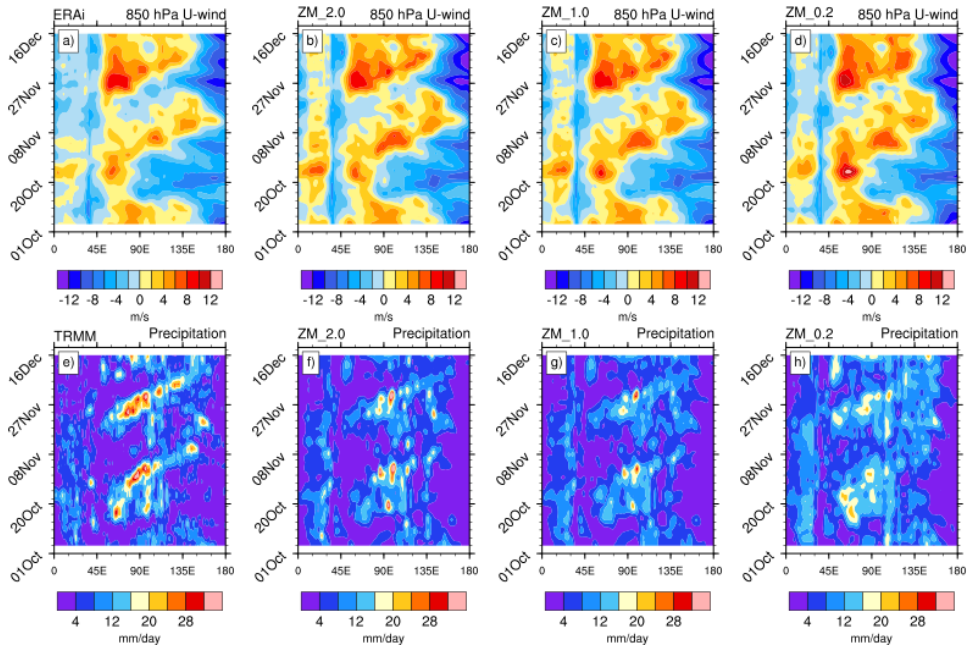

Fig. 2.3 Hovmöller diagram of equatorial 850 hPa wind (a-d) and precipitation (e-h) averaged from 5°S-5°N for 00-04 day lead times.

Figure 2.4 shows a similar hovmöller as Figure 2.3, except for hindcast lead days 05-09. The low-level wind and precipitation signals are less coherent in all simulations. This is especially true in ZM_0.2, which hardly shows any organization or propagation in low-level wind or precipitation (Fig. 2.4d,h). The MJO signal is only slightly degraded at 05-09 days in ZM_2.0 and ZM_1.0, and still qualitatively resembles ERAi and TRMM data with slow eastward propagation (Fig. 2.4b,c,f,g).

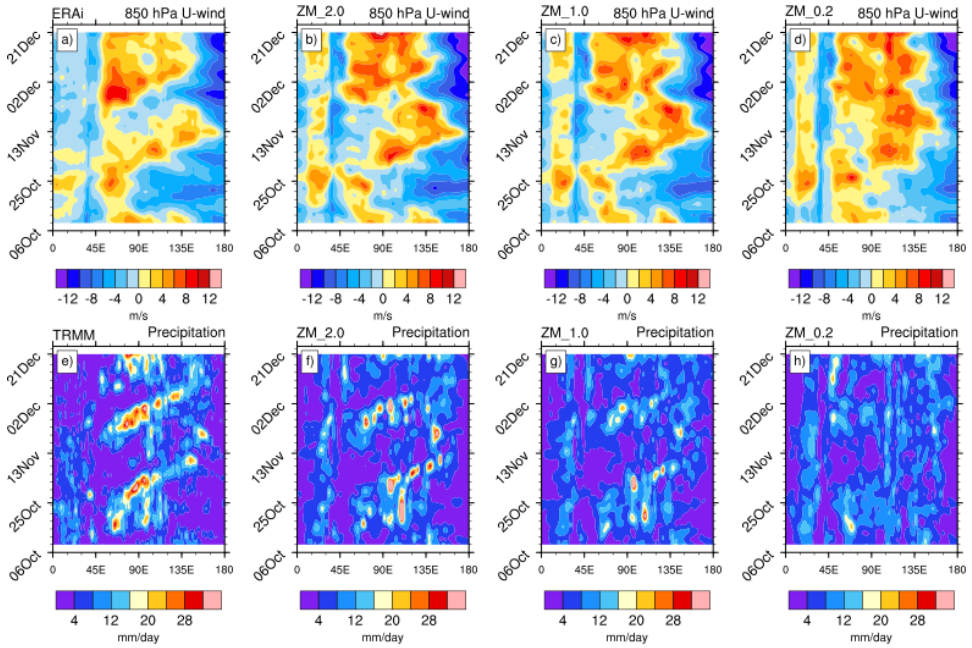

Fig. 2.4 Hovmöller diagram of equatorial 850 hPa wind (a-d) and precipitation (e-h) averaged from 5°S-5°N for 05-09 day lead times.

Figure 2.5 shows the COR and RMSE MJO skill metrics for each model configuration. Both metrics show no MJO hindcast skill past 12 days for the low entrainment case, whereas the runs with higher entrainment have skill out to 20 days. The RMM skill of the model saturates above the default entrainment of 1.0 km^{-1}, and so negligible skill would be gained from increasing the entrainment parameter above 2.0 km^{-1}. The RMSE and COR metrics exhibit a similar decrease in skill with lead time suggesting that the errors are not dominated by phase or amplitude errors alone. The RMM index is mostly influenced by circulation anomalies (Straub 2013) and so high RMM skill is relatively insensitive to agreement of the convective signal, although Figure 2.3 shows the convective signal is improved with higher entrainment. The skill metrics suggest slightly longer MJO hindcast skill than what has been presented by other studies (e.g. Gottschalck et al. 2010), although we note that there are some differences in the calculation shown here relative to other studies, which makes comparison to these studies difficult. The DYNAMO period is

relatively short when compared to hindcast skill generated using forecast systems having a large multi-year database of forecasts during all times of the year. Studies have shown that predictive skill tends to increase during boreal winter and especially during periods of strong MJO activity (Jiang et al. 2008; Ma et al. 2013), and so a high RMM skill score during DYNAMO is not necessarily indicative of superior model performance. Overall, Figures 2.2-2.4 confirm that the dilute plume entrainment rate has a substantial impact on the model's ability to produce a coherent MJO, consistent with behavior documented by Klein et al. (2012), which justifies further analysis to understand this behavior.

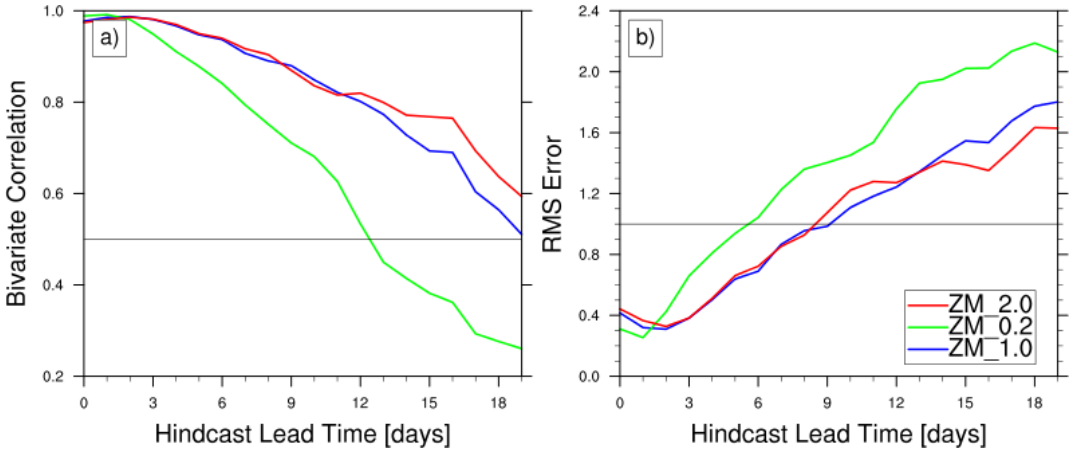

Fig. 2.5 Bivariate correlation (left) and RMSE error (right) RMM skill scores as a function of lead-time in days for ZM_2.0 (red), ZM_1.0 (blue) and ZM_0.2(green). Grey lines denote threshold of no MJO predictive skill (see text).

It is useful to consider the mean state thermodynamics and the drift of the simulations away from observations with lead-time. For a thermodynamic perspective consistent with our analysis of the MSE budget described below, we plot the mean profiles of moist static energy (MSE), which is the sum of dry static energy (DSE) and latent energy, in the left column of Figure 2.6 for 00-04, 05-09 and 10-14 day leads averaged over the equatorial Indian Ocean (60°-90°E; 10°S-10°N). Note that the slight shift in ERAi profiles for different lead times is simply due to the different averaging periods covered by the

dataset for different lead times. We also note that we compared ECMWF analysis MSE profiles to those from ERAi, and found the differences much smaller than those between ERAi and the models. In the lower troposphere where moisture has a large influence on MSE, the model indicates drier conditions than ERAi that become even drier at longer lead times (Fig. 2.6a,c,e). Upper tropospheric MSE is approximately equivalent to DSE and is lower than ERAi in ZM_1.0 and ZM_2.0, while ZM_0.2 is comparable to ERAi. The reduced upper tropospheric MSE is similar to that found in Kim et al. (2011) in which a convection scheme was modified to effectively reduce entrainment rate. The shape of the MSE profile in ZM_0.2 with dichotomous wet and dry biases straddling 600hPa is interesting. Hirons et al. (2013) similarly tested the effect of modifying entrainment on MJO hindcast simulations and concluded that a wet over dry signal was due to an increased detrainment by cumulus congestus. However, this explanation is not consistent with our results, because as the entrainment is increased, and deep convection more suppressed, we see a reduction of this wet bias.

The mean profile of omega in ZM_0.2 is most similar to ERAi at 00-04 day leads. Similar to the mean precipitation amplitude, omega exhibits a strong reduction in amplitude, and a less top-heavy structure at later lead times (Fig. 2.6b,d,f). ZM_1.0 and ZM_2.0 have mean omega profiles with weaker amplitude and do not show large amplitude changes with lead-time. As we will show in Section 2.5, differences in both the MSE and omega profiles play a role in explaining differences in GMS between the datasets, although this behavior is best examined in a context other than in the time mean.

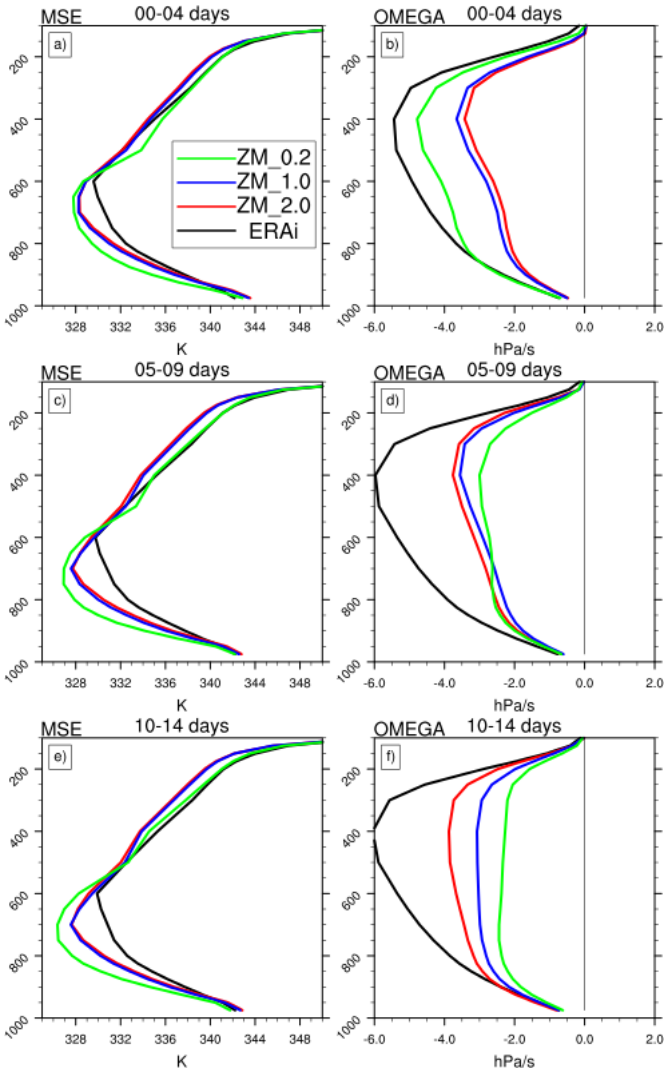

Fig. 2.6 Mean profiles of MSE (left column) and vertical pressure velocity (right column) for 00-04 (a-b), 05-09 (c-d) and 10-14 (e-f) day lead times averaged over the equatorial Indian Ocean (10°S-10°N; 60-90°E).

2.4 The MSE Budget in CAM

To understand the disparities in hindcast skill and maintenance of the MJO in the previous section, we would like to know how different processes influence the net column moisture in our simulations. MSE is a useful quantity for answering this question because it is approximately conserved in the presence of moist convection and MSE anomalies are nearly equivalent to latent heat anomalies in the deep tropics where horizontal temperature and pressure gradients are weak (see Fig. 2.7).

Here we make use of the column integrated MSE budget following Neelin and Held (1987) written as,

$$\langle \partial_t h \rangle = \langle -\mathbf{v} \cdot \nabla h \rangle + \langle -\omega \partial_p h \rangle + \langle Q_R \rangle + LHF + SHF \qquad (2.4)$$

where $h = s + L_v q$ is MSE, $s = c_p T + gz$ is dry static energy (DSE), L_v is the latent heat of vaporization, ω is the pressure velocity, $\mathbf{v}$ is the horizontal wind vector, q is the specific humidity, Q_R is net radiative heating, and *LHF* and *SHF* represent the surface latent and sensible heat flux, respectively. Angle brackets indicate a mass-weighted integral from 150 hPa to the surface. Benedict et al. (2014) presented a closely related analysis of the column moist entropy budget to diagnose variations in vertical and horizontal advective tendencies and the relationship to MJO simulation performance in long climate simulations.

Figure 2.7 shows a hovmöller diagram of column averaged MSE overlaid with contours of column $L_v q$ anomalies divided by c_p to convert to units of K for ERAi, and all model configurations for 00-04 day leads. The vertical dotted line denotes the approximate location of the DYNAMO sounding array and diagonal dashed lines provide a reference of the peak column MSE in ERAi for both events, corresponding to a propagation speed of 7m/s. These reference lines are identical to those identifying precipitation maxima in Figure 2.3, consistent with the structure of a moisture mode with strong coupling between convection and column water vapor (Raymond 2001). Column MSE and $L_v q$ anomalies provide a clear indicator of each event in ERAi, but the magnitudes are slightly smaller in the simulations at 00-04 day leads (Fig. 2.7a-d). At longer leads MSE anomalies in ZM_2.0 and ZM_1.0 are still comparable to ERAi, but ZM_0.2 has less coherent anomalies (not shown), consistent with Figures 2.1-2.2.

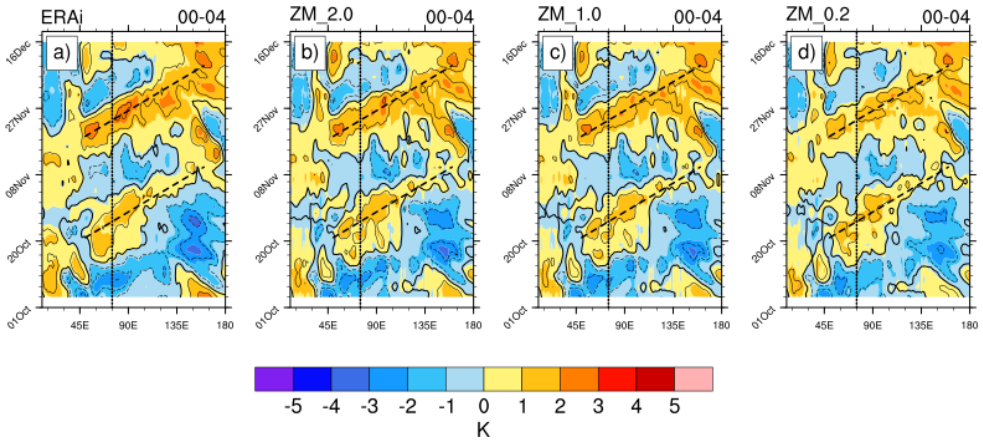

Fig. 2.7 Hovmöller plots of column MSE anomaly (colors) and column latent heat anomalies (contours) averaged from 5°S-5°N for 00-04 day leads. Vertical dotted line denotes the approximate location of the DYNAMO sounding array. Dashed lines mark the approximate location of each MJO event corresponding to a propagation speed of 7 m/s. Contour intervals are identical for each variable.

Hovmöller plots of individual MSE advective terms and the total MSE source are shown for 00-04 day leads in Figure 2.8. We have omitted ZM_1.0 in this analysis for brevity, since the results are qualitatively similar to ZM_2.0. All terms are plotted such that positive values signify a positive MSE tendency. Horizontal advection is generally negative in all datasets implying a drying tendency, but becomes anomalously positive prior to peak MSE anomalies and more strongly negative after MJO convection (Fig. 2.8a,d,g), consistent with previous studies that cite horizontal advection as a dominant propagation mechanism for the MJO (e.g. Benedict and Randall 2009; Maloney 2009; Pritchard and Bretherton 2014; Kim et al. 2013). The sum of MSE sources is anomalously negative prior to each MJO event, and positive near and to the west of enhanced convection, suggesting a maintenance role for these terms (Maloney 2009).

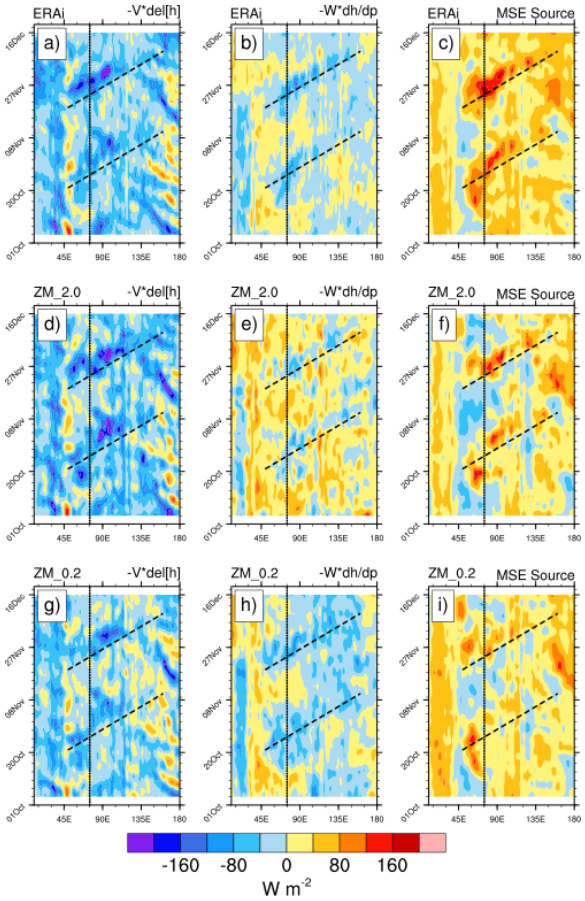

Fig. 2.8 Hovmöller plots similar to Fig. 2.7 except for horizontal advection (left column), vertical advection (center column) and all MSE sources (right column) averaged from 5°S-5°N for 00-04 day leads.

The vertical advection term in Figure 2.8b,e,h exhibits the largest impact from increased entrainment. Large MSE import leads and weak MSE export lags each MJO event in ZM_2.0. The mean vertical advection is negative for ERAi and ZM_0.2, but positive in ZM_2.0 (not shown). The general tendency for import by vertical MSE advection in ZM_2.0 would make it easier to support strong MSE anomalies in the model, since convection and associated divergent circulations are less able to discharge a column MSE anomaly. Vertical MSE advection looks surprisingly similar between ZM_0.2 and ERAi in Figure 2.8, suggesting that the change to vertical MSE advection in ZM_2.0 is enhancing the MJO for the wrong reason by counteracting the weak MSE sources. Longer lead times yield a less

coherent signal and weaker anomalies in all MSE budget terms for ZM_0.2, but the qualitative interpretation is the same as in Figure 2.8 (not shown). Analysis of the MSE budget from in-situ data collected at the northern DYNAMO sounding array is broadly consistent with ERAi data averaged over a comparable area (not shown), although these results are very noisy given the relatively small area. Thus, we have chosen not to discuss the MSE budget of the DYNAMO sounding array in detail.

Figure 2.9 provides a complementary view of the MSE budget by characterizing feedbacks between the various MSE budget terms and the column MSE anomaly. This is done by binning the budget terms by the anomalous column MSE for 00-04 day leads over the equatorial Indian Ocean (10S-10N and 60-90E), with 95% error bounds for the binned estimate calculated using a Student's *t*-statistic as indicated with triangular markers. Degrees of freedom are calculated by assuring that each 5^o x 5^o region is not represented more than once a day in each bin. As the entrainment parameter is increased horizontal advection contributes a stronger drying tendency from both zonal and meridional advection, especially at positive MSE anomalies (Fig. 2.9a-b). Surface fluxes however contribute slightly weaker moistening at all bins (Fig. 2.9c). It seems that these changes in horizontal advection and surface fluxes would make column MSE anomalies harder to maintain, and thus cannot help us explain why increasing the entrainment parameter promotes a more robust MJO. The difference in slopes of the horizontal advection and surface fluxes terms relative to ERAi do not indicate a large change in the nature of the feedbacks from these terms. Interestingly, net column radiative heating is relatively unaffected by the entrainment parameter. However, the slope of radiative heating per unit MSE change is much weaker than ERAi, implying weaker cloud-radiative feedbacks in all

model versions (Fig. 2.9d). Cloud-radiative feedbacks have been suggested by several studies to be important in regulating the growth and phase speed of tropical disturbances (Bony and Emanuel 2005; Andersen and Kuang 2012). If they are too weak in the models, as suggested by Figure 2.9d, it becomes more difficult to destabilize the MJO. Some other factor must therefore be compensating in the high entrainment runs to maintain a strong MJO, which we find to be the vertical MSE advection.

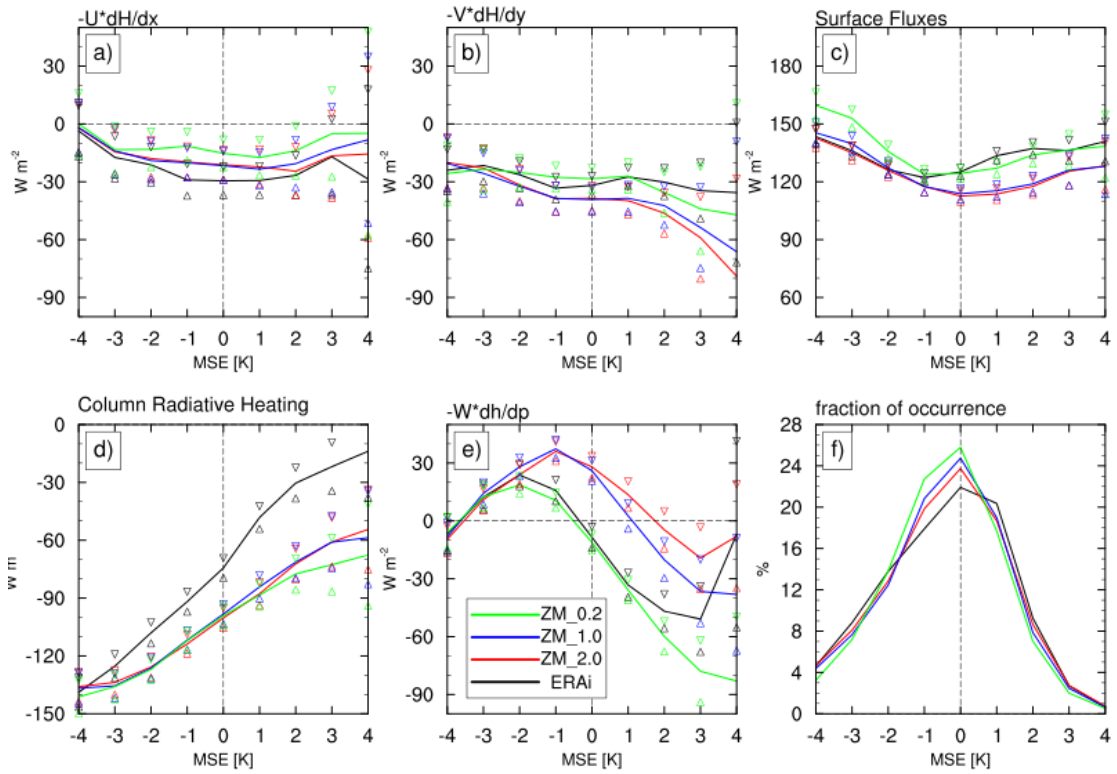

Fig. 2.9 Average MSE budget terms (a-e) and fraction of occurrence of each MSE anomaly bin (f) binned by the MSE anomaly for 00-04 day lead times over the equatorial Indian Ocean (10°S-10°N; 60-90°E). Error bound estimates are indicated by triangle markers and were calculated using a Student's *t*-statistic.

The vertical MSE advection shown in Figure 2.9e exhibits an interesting difference as the entrainment parameter is increased. For small MSE anomalies (-2 to 2 K) that comprise the majority of conditions (Fig. 2.9f), the vertical MSE advection in ZM_0.2 closely

tracks ERAi, whereas ZM_1.0 and ZM_2.0 are unrealistically positive. This demonstrates that increasing the entrainment parameter increases the efficiency with which convection and associated divergent circulations import column MSE. Given the non-linearity of the curves, the slope of the vertical advection-MSE relationship cannot be used as successfully as for radiative feedbacks to characterize changes in MSE advection as a function of MSE anomaly. Comparison with ERAi suggests that the simulations with a more robust MJO are getting the right answer for the wrong reason, as the change in divergent MSE export compensates for a weaker radiative feedback (Fig. 2.9d). This appears to be the main factor in destabilizing the MJO in the model by enhancing the ability to maintain strong MSE anomalies. This conclusion is supported further in the next section.

2.5 Gross Moist Stability in CAM

In order to put our results in the context of moisture mode theory, we use the concept of GMS (Neelin and Held 1987). GMS allows for comparison across models and ERAi analyses through normalization of the advective import of column MSE by the strength of convective activity. For our purposes we define the total GMS similar to (Raymond et al. 2009) as,

$$\Gamma = \frac{\left\langle -\nabla \cdot (\mathbf{v}h) \right\rangle}{\left\langle -\omega \partial_p s \right\rangle}, \tag{2.5}$$

where h is MSE and s is DSE. We use the vertical advection of DSE as a measure of convective activity in the denominator of (2.4), as it is well correlated with precipitation (not shown). Following convention, we define GMS such that negative values indicate a net import of column MSE (Raymond et al. 2009; Hannah and Maloney 2011; Frierson and Kim

2011; Benedict et al. 2014). We further decompose GMS into horizontal (HGMS) and vertical (VGMS) components,

$$\Gamma_H = \frac{\langle -\mathbf{v}\cdot\nabla h \rangle}{\langle -\omega \partial_p s \rangle}, \tag{2.6}$$

$$\Gamma_V = \frac{\langle -\omega \partial_p h \rangle}{\langle -\omega \partial_p s \rangle}. \tag{2.7}$$

To obtain (2.5) and (2.6) we have made use of the continuity equation, integration by parts, and assumed that vertical velocity is zero at the limits of integration following Back and Bretherton (2006) and Raymond et al. (2009). We can also include the MSE sources in our definition of VGMS to obtain an "effective VGMS",

$$\Gamma_{eff} = \frac{\langle -\omega \partial_p h \rangle + \langle Q_R \rangle + LHF + SHF}{\langle -\omega \partial_p s \rangle}. \tag{2.8}$$

Our definition of effective VGMS differs slightly from previous literature in that most previous version do not include surface fluxes (e.g. Frierson et al. 2011). We include surface fluxes here as previous studies have suggested they are important for MJO destabilization (Maloney et al. 2010). GMS is a very sensitive calculation due to the volatility of the quantity used for normalization (Benedict et al. 2014), and substantial spatial and/or temporal smoothing is often used to calculate a stable value of GMS (Raymond et al. 2009). Even with smoothed data, the denominator can be equal or close to zero, which necessitates the use of a subjective threshold for omitting data.

Here we present a novel method of calculating GMS that avoids the pitfalls of other methods. To do this, we first sort the numerator (i.e. advective MSE tendency) into 100 W m^{-2} wide bins determined by the denominator (i.e. vertical DSE advective tendency). We then take the bin mean of the numerator values, and divide by the corresponding

denominator value defined as the midpoint of the bin. Finally, the GMS is obtained by calculating an average of this ratio across all bins weighted by the frequency of occurrence.

This new method has several advantageous attributes. First, no subjective choices are necessary after the bins are chosen. This eliminates the need of arbitrary thresholds for omitting denominator values that are too small, and so all data points can be considered. Second, our method allows for the linear decomposition of the numerator for each bin, independent of the denominator, since the denominator value is constant for a given bin by construction. This is useful for probing how specific processes or specific space and/or time scales affect GMS. Third, the denominator bins represent various convective regimes. Positive DSE import is indicative of subsidence and suppressed convection, whereas strong negative DSE import is characteristic of regimes with strong upward motion and enhanced convective activity. This can be used to assess how different convective regimes influence the net GMS and its changes among models. Finally, our method allows for straightforward estimate of the statistical significance and error bounds of GMS.

The calculation of VGMS and effective VGMS using this new method is illustrated in Figure 2.10, with the center of dry static energy export bins spaced 100 W m^{-2} apart from -950 to 150 W m^{-2}. For the following analysis we use data with forecast leads of 00-04 days over the equatorial Indian Ocean (10°S-10°N; 60°-90°E). Here we have used a 4°x4° running spatial average to smooth out small-scale noise, an appropriate method of pre-filtering data before calculating GMS as discussed by Raymond et al. (2009). The use of spatially smoothed data does not affect our general results. The top panels show binned numerator values for the calculation of VGMS (Fig. 2.10a) and effective VGMS (Fig. 2.10b). Differences in the frequency of denominator values between the datasets are manifested in

the distributions of data points in each bin (Fig. 2.10c). The resulting estimates of VGMS and effective VGMS are plotted in Figure 2.10d, with error bars representing 95% confidence limits. The confidence limits are calculated by first using the *t*-statistic to calculate 95% confidence limits for each bin, with the degrees of freedom calculated by assuring that each 5º x 5º region is not represented more than once a day in each bin. Then, a weighted average of the upper and lower confidence limits across all bins using the frequency distribution in Figure 2.10c is used to calculate the upper and lower confidence bounds on the VGMS and effective VGMS in Figure 2.10d. Note that confidence bounds on individual bins in Figures 2.10a-b are not shown here to maintain clarity of display.

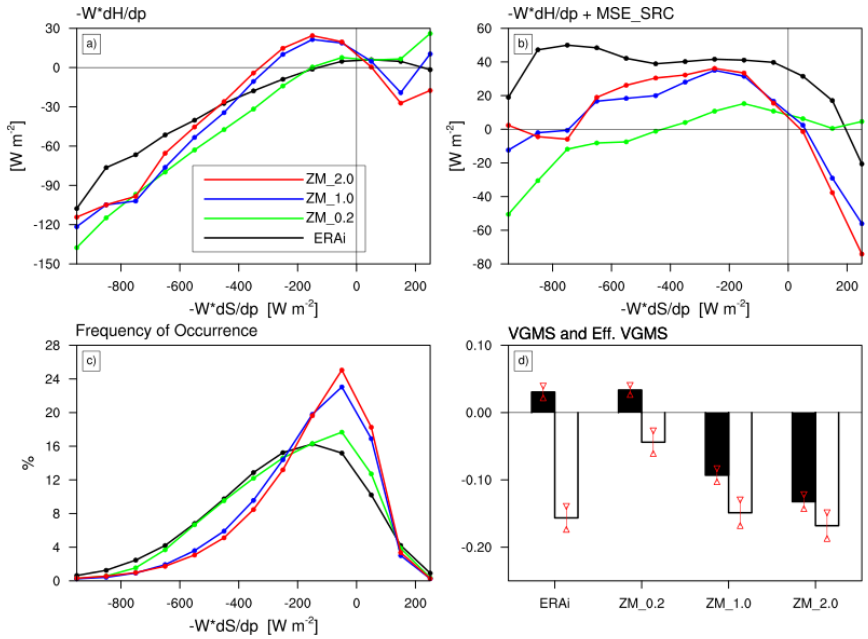

Fig. 2.10 Top row shows the vertical MSE advection (top left) and vertical MSE advection plus the total MSE source (top right) binned by the vertical DSE advection. Bottom row shows the frequency of occurrence associated with the top panels (bottom left) and resulting VGMS (black bars) and effective VGMS (white bars; see text). 95% confidence limits on the VGMS and effective VGMS are calculated as described in the text.

For ERAi we find that VGMS is slightly positive, consistent with previous studies (Yu et al. 1998; Raymond and Fuchs 2009; Landu and Maloney 2011; Benedict et al. 2014). On the other hand, effective VGMS in ERAi is significantly negative. As the model entrainment parameter is increased a significant reduction of VGMS occurs, such that VGMS and effective VGMS have similar magnitudes. Effective VGMS in the high entrainment models is consistent with that of ERAi, although VGMS is too low.

Figure 2.11 uses our new method to summarize and compare HGMS, VGMS and effective VGMS across all datasets for 00-04 and 05-09 day leads over the equatorial Indian Ocean (10°S-10°N and 60°-90°E). Each value is plotted against a metric for the strength of the MJO variability, calculated as the standard deviation of daily mean column integrated MSE (σMSE) smoothed with three passes of a 1-2-1 filter. Note that the slight changes of ERAi with lead-time simply reflect different averaging periods used to isolate the lead times of the hindcast data. HGMS is positive (Fig. 2.11a), consistent with Figure 2.8-2.9 showing that horizontal advection exports column MSE. HGMS in ZM_0.2 is lower than ERAi and becomes larger than ERAi as the entrainment parameter is increased. This differs from the finding of Benedict et al. (2014) who found that HGMS was not systematically different between models with varying degrees of MJO variability. Comparison of Figures 10a-b indicates a tradeoff between HGMS and VGMS among simulations, in that as VGMS goes down, HGMS goes up. This trade-off relationship is also noticeable for 05-09 day leads. Our interpretation of this trade-off is that as intraseasonal variability increases associated with decreased VGMS, horizontal flows generally become more organized (e.g. Rossby gyres; synoptic eddies; Benedict and Randall 2007; Maloney 2009), leading to more efficient column MSE export by horizontal advection.

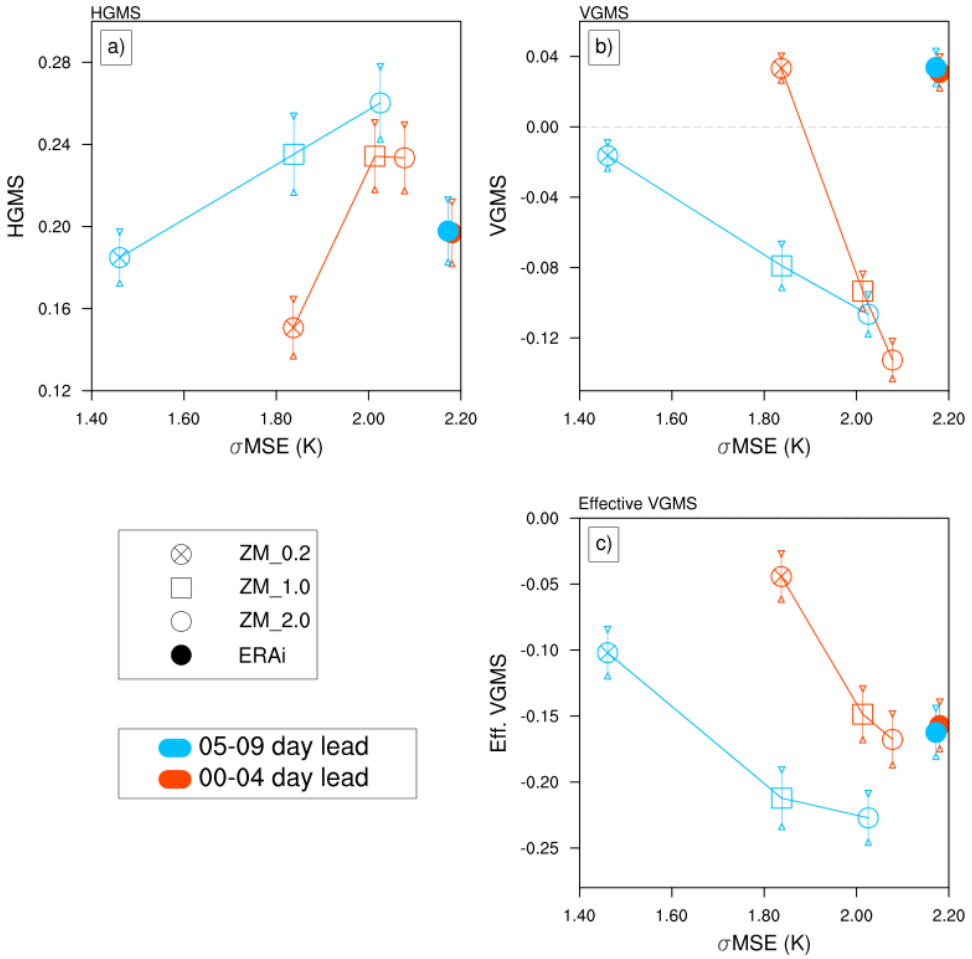

Fig. 2.11 HGMS (a), VGMS (b) and effective VGMS (c) plotted against the standard deviation of column MSE, which gives a crude estimate of the MJO variability. Datasets are indicated by marker style and lead times are indicated by color. 95% confidence limits are calculated as described in the text.

As we saw in Figure 2.10, VGMS is slightly positive in ERAi (Fig. 2.11b). VGMS in ZM_0.2 is also slightly positive, while the simulations with higher entrainment are decidedly negative. VGMS changes slightly with lead time, but does not affect the qualitative differences between cases. Effective VGMS is strongly negative in ERAi. ZM_1.0 and ZM_2.0 have similar strong negative values of effective VGMS, which are close to ERAi for forecast lags of 0-4 days. However, effective GMS in ZM_0.2 is only weakly negative (Fig. 2.11c).

Negative VGMS indicates that vertical MSE advection helps to grow and sustain column MSE anomalies. Therefore the similarity in magnitudes of VGMS and effective VGMS in the models with higher entrainment suggests that they can more easily support moisture modes regardless of whether MSE source terms are providing strong positive feedbacks on column MSE anomalies. Conversely, the large difference between VGMS and effective VGMS in ERAi shows that it cannot support a moisture mode unless the combined effect of vertical advection and MSE sources contribute a net positive feedback on the column MSE anomaly. This further confirms the results of Figure 2.9, and provides a plausible explanation for why the entrainment parameter erroneously improves the MJO in the model. Specifically, increasing the entrainment parameter fundamentally changes the nature of column MSE import by vertical advection such that it compensates for overly weak cloud-radiative feedbacks, and therefore gets the right answer for the wrong reason.

We can take advantage of our new method to obtain a physical understanding of this difference by isolating contributions from ω and $\partial_p h$ through the following decomposition of the difference in the mean component of VGMS between two datasets for a given bin,

$$\begin{aligned}
\Delta\Gamma_V &= \Gamma_2 - \Gamma_1 \\
&= \frac{\left\langle -\overline{\omega}_2 \partial_p \overline{h}_2 \right\rangle - \left\langle -\overline{\omega}_1 \partial_p \overline{h}_1 \right\rangle}{\left\langle -\omega \partial_p s \right\rangle} \\
&= \frac{\left\langle -(\overline{\omega}_1 + \Delta\omega)\left(\partial_p \overline{h}_1 - \Delta \partial_p h\right) + \overline{\omega}_1 \partial_p \overline{h}_1 \right\rangle}{\left\langle -\omega \partial_p s \right\rangle} \\
&= \frac{\left\langle -\overline{\omega}_1 \partial_p \overline{h}_1 - \Delta\omega \partial_p \overline{h}_1 - \overline{\omega}_1 \Delta \partial_p h - \Delta\omega \Delta \partial_p h + \overline{\omega}_1 \partial_p \overline{h}_1 \right\rangle}{\left\langle -\omega \partial_p s \right\rangle} \\
&= \frac{\left\langle -\Delta\omega \partial_p \overline{h}_1 \right\rangle + \left\langle -\overline{\omega}_1 \Delta \partial_p h \right\rangle + \left\langle -\Delta\omega \Delta \partial_p h \right\rangle}{\left\langle -\omega \partial_p s \right\rangle}
\end{aligned} \quad . \qquad (2.9)$$

Here, the overbar represents a mean for the given bin. The delta operator signifies a difference between the bin mean of the second dataset from the bin mean of the first. The right side of the bottom line of (2.9) provides three terms that describe the difference in the mean component of VGMS ($\Delta\Gamma_v$) due to the difference in ω ($\Delta\omega$), the difference in $\partial_p h$ (Δh), and the product of differences of ω and $\partial_p h$ ($\Delta\omega\Delta h$), respectively. We have verified that the method described by (2.9) explains nearly the entire difference between any two simulations (not shown), and the covariance within individual bins is not needed to understand the effect of increasing the entrainment parameter.

Figure 2.12a shows the binned values of $\Delta\Gamma_v$, $\Delta\omega$, Δh and $\Delta\omega\Delta h$ from (2.9), using ZM_2.0 and ERAi data. Note that the values being plotted are normalized by the denominator value of each bin, so the curves in Figure 2.12a effectively show the VGMS difference as a function of DSE import. Figure 2.12c-d shows averages of $\Delta\Gamma_v$, $\Delta\omega$, Δh and $\Delta\omega\Delta h$, weighted by the frequency of occurrence. From Figure 2.12c we can see that the difference in VGMS between ZM_2.0 and ERAi is largely explained by the difference in the omega profile, with smaller contributions from the change in the MSE profile. This difference mainly occurs in the upper range of vertical DSE import, which corresponds to subsidence and suppressed convection (Fig. 2.12a). Conversely, in regimes with large negative DSE import and active deep convection, the difference in the omega profile acts to increase the VGMS. Comparing ZM_2.0 and ZM_0.2, we find that increased entrainment leads to decreased VGMS through a combination of $\Delta\omega$ and Δh (Fig. 2.12d). Suppressed precipitation regimes with positive vertical DSE advection appear to mainly be influenced by $\Delta\omega$, whereas for moderate precipitation regimes (-350 to -150 W m^{-2}) $\Delta\Gamma_v$ is better explained by Δh.

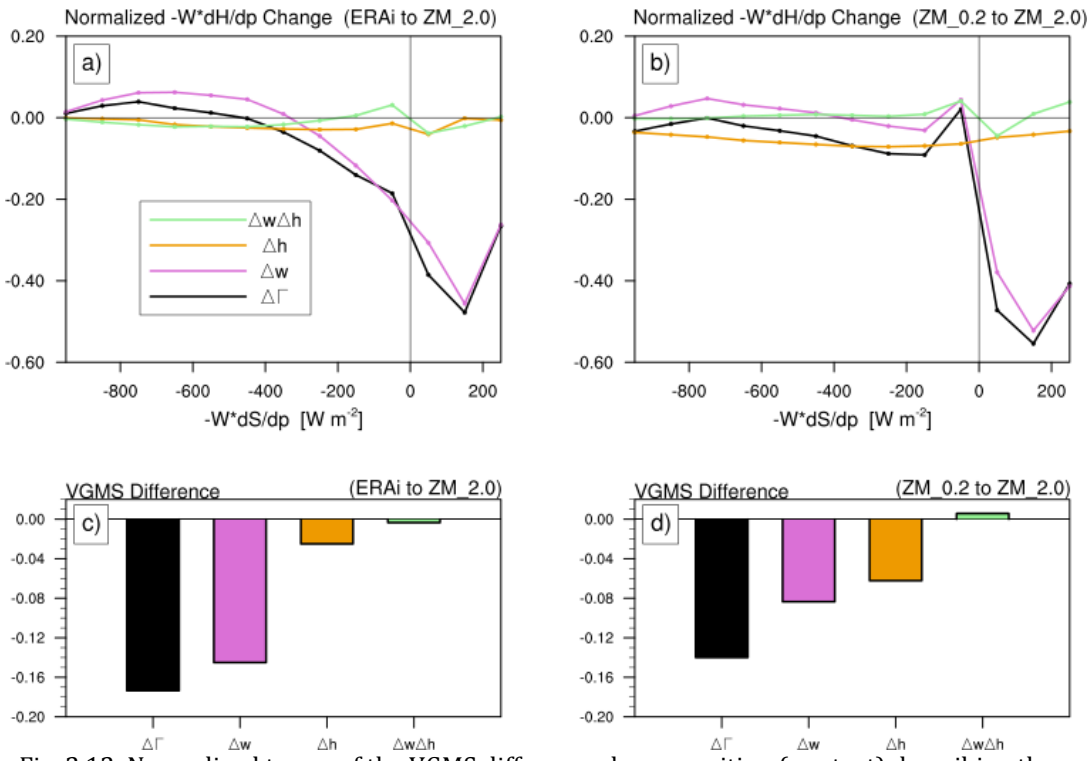

Fig. 2.12 Normalized terms of the VGMS difference decomposition (see text) describing the difference between ZM_2.0 and ERAi (a,c), and ZM_2.0 and ZM_0.2 (b,d). Bottom row shows weighted averages of each term across all bins based on the frequency of occurrence (see Fig. 2.10).

To better understand these differences, we now consider the average profiles of omega and MSE for weakly negative (-250 to -50 W m^{-2}) and weakly positive (50 to 250 W m^{-2}) DSE import bins (Fig. 2.13), the regimes in Figure 2.12 that are most responsible for differences in GMS among models and ERAi. Specifically, isolating the comparisons made in Figure 2.12, ZM_2.0 has a more bottom-heavy vertical velocity profile than ERAi for both weakly positive and weakly negative export bins that would act to lower GMS (e.g. Peters and Bretherton 2006), consistent with Figure 2.12. In weak import bins, ZM_2.0 has a more bottom-heavy vertical velocity profile than ZM_0.2, and also reduced upper tropospheric MSE and a reduced deep-layer averaged upper tropospheric MSE gradient compared to

ZM_0.2. These changes to the MSE and omega profiles would both reduce GMS in ZM_2.0 consistent with that shown in Figure 2.12 (Peters and Bretherton 2006; Frierson and Kim 2011). We also note that high entrainment models spend more time in suppressed precipitation regimes (Figure 2.10c), consistent with a general stronger suppression of deep convection. Further physical insight into how changing entrainment produces these variations in vertical velocity and MSE profiles will be left to future work. However, these results support the conclusion of the previous section that the improvement of the MJO signal from an increased entrainment parameter is the right answer for the wrong reason.

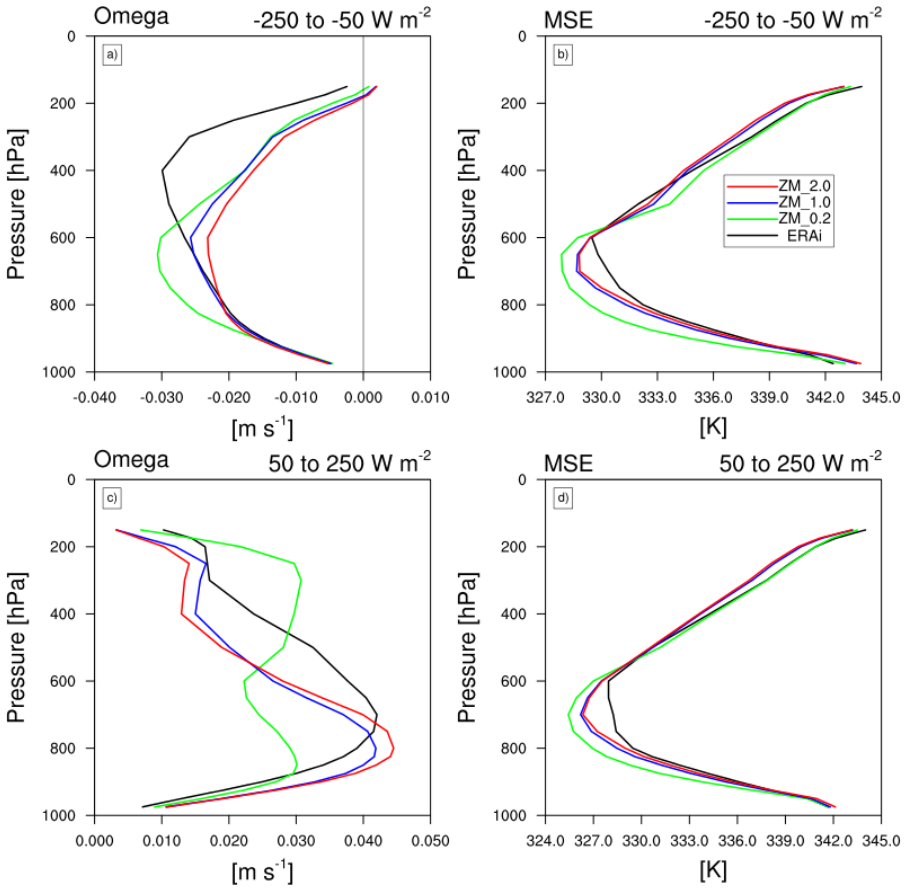

Fig. 2.13 Mean profiles over bins of vertical DSE advection from -250 to -50 W m^{-2} (a-c) and 50 to 250 W m^{-2} (d-f). Positive (negative) vertical DSE advection generally corresponds to suppressed (enhanced) convection.

2.6 Conclusions and Discussion

In this chapter we have explored the MSE budget in hindcast simulations during the first two MJO events of the DYNAMO field campaign. Varying the dilute CAPE entrainment rate parameter of the Zhang-McFarlane deep convection parameterization was shown to have a large impact on MJO prediction skill. At 00-04 days after initialization, all model configurations have comparable skill. By 05-09 days simulations with a lower entrainment rate show a substantial reduction in RMM skill and have no coherent convective signal. Simulations with a higher entrainment rate exhibit significant RMM skill out to 20 days (Fig. 2.3). These results are similar to those of Klingaman and Woolnough (2014), who also explored how an entrainment parameter affected MJO hindcast simulations during the Year of Tropical Convection (YOTC) and found a similar improvement in RMM skill by increasing entrainment.

Analysis of the column MSE budget of the equatorial Indian Ocean reveals that simulations with a higher dilute CAPE entrainment rate have an unrealistically large positive tendency from vertical MSE advection (Fig. 2.8e, 2.9e). The total column MSE source was found to be weaker than observations in all simulations (Fig. 2.8f,i). Characterization of feedbacks among terms of the MSE budget and column MSE anomalies revealed overly weak cloud radiative feedbacks that appear to be compensated by overly efficient vertical MSE advection in the high entrainment simulations to produce a strong MJO (Fig. 2.9d-e).

The problem of weak cloud-radiative feedbacks involves some subtle aspects, and deserves further discussion. The feedback between column MSE and column radiative heating can be summarized by Figure 2.14. The upper arrow represents how a change in

MSE affects the column radiative heating. Given that column MSE anomalies are nearly equivalent to column moisture anomalies in regions of weak horizontal temperature gradients, an increase in column MSE is generally associated with an increase in convective activity that reduces the longwave radiation emitted to space at the top of the atmosphere and consequently increases the total column radiative heating. This relationship is treated in CAM5 in a somewhat unphysical manner, since it involves multiple physical parameterizations that are basically stapled together, but the fundamental relationship is captured.

The lower arrow in Figure 2.14 represents how a change in column radiative heating affects the column MSE, but it is not as straightforward to understand. Suppose a reduction in column radiative cooling occurs by advection of cirrus clouds into a region (i.e. anomalous radiative heating). The immediate increase in temperature from this heating would increase the MSE, but this understanding is only valid on short timescales. On longer timescales we need to consider the consequences of weak temperature gradient balance (WTG). In the case of strict WTG, an increase in radiative heating would be balanced by anomalous upward motion, which would drive moistening and cooling. The actually response of MSE to an increase in column radiative heating involves both fast and slow responses. In light of the complexity of these interactions, it is challenging to understand the model's weak cloud-radiative feedback problem in Figure 2.9, because it is difficult to diagnose how accurately the model represents each side of this feedback relationship.

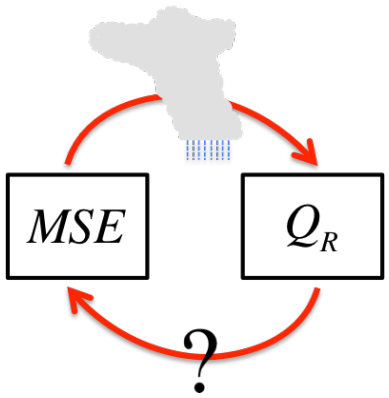

Fig. 2.14 Schematic cartoon for understanding the feedback relationship between column MSE and column radiative heating. The upper arrow represents how a change in column MSE affects the column radiative heating, and the lower arrow represents how a change in the column radiative heating affects the column MSE (see text).

A novel method of calculating GMS was introduced and shown to have several advantages over conventional methods. The new method first calculates bin averages of MSE advection (numerator) sorted by intervals of vertical DSE advection (denominator). The GMS is obtained by calculating a weighted average across all bins of the ratio of the bin average numerator and bin midpoint denominator. MSE sources are entrained into the numerator for the calculation of effective VGMS.

The vertical component of GMS (VGMS) and effective VGMS, which considers the influence of MSE sources, were used to compare the ability to grow and maintain large-scale MSE anomalies. ERAi was found to have positive VGMS and negative effective VGMS, suggesting that large-scale MSE anomalies can be maintained only through the combined feedbacks of vertical advection and MSE sources. The simulations with low entrainment were shown to also have positive VGMS and weak negative effective VGMS. VGMS in the high entrainment runs is far too low compared to ERAi, indicating that it cannot be used in isolation as a measure of model success in producing a realistic MJO hindcast. With a higher entrainment parameter VGMS is significantly negative, and similar in magnitude to the effective VGMS. This suggests that the entrainment parameter is erroneously improving the

MJO by allowing large vertical advection to grow and maintain column MSE anomalies in the presence of weak MSE source feedbacks. These results also suggest that caution should be used in interpreting the results of studies such as Hannah and Maloney (2011) and Benedict et al. (2014), where VGMS is related to changes in MJO activity among models, since effective VGMS is a better predictor than VGMS of a model's ability to sustain a robust MJO. The resulting estimate of GMS shows that increasing the entrainment parameter is reflected in a trade-off between horizontal components of GMS (HGMS) and VGMS, in that HGMS is increased as VGMS is reduced. We interpret the increase in HGMS to reflect more organized circulations resulting from the stronger MJO, which can more efficiently export column MSE.

The new method of calculating GMS allows a unique decomposition, in which differences in VGMS between datasets can be quantifiably attributed to specific processes. Changes in the profile of omega were found to play an important role in reducing VGMS from ERAi to the high entrainment runs. Reduced VGMS in high entrainment models versus ERAi is associated with a more bottom-heavy omega profile during subsidence periods. A combination of differences in the vertical profiles of MSE and omega are needed to explain the reduction in VGMS from the low entrainment to high entrainment runs (Fig. 2.12d).

These results suggest that modifying a parameterization of convection in order to enhance the schemes sensitivity to tropospheric moisture and stifle the deepest convection does not necessarily produce a realistic simulation of the MJO for the correct reasons. This technique allows divergent circulations to become unrealistically efficient at importing column MSE to compensate for cloud-radiative feedbacks that are too weak. The

importance of cloud-radiative feedbacks has been highlighted by several studies, such as Bony and Emanuel (2005), who show that these feedbacks have a large role in slowing the phase speed of tropical disturbances in a simplified model. Andersen and Kuang (2012) also found that longwave heating was a significant source in the maintenance of column MSE anomalies in a multi-scale modeling framework (MMF) that simulates cloud-radiative interactions in a more realistic way than a conventional global model (see also Benedict and Randall 2009; Pritchard and Bretherton 2014).

Other model studies have found that tweaking entrainment parameters, similar to the one used here, results in a lower GMS and stronger MJO, coincident with a degraded mean state (e.g. Kim et al. 2009; Hannah and Maloney 2011). Our results imply that these methods allow moisture mode type disturbances to be more easily destabilized by enhancing the efficiency of divergent MSE import, but also modify the fundamental nature of how convection interacts with the large-scale fields through associated divergent circulations. This may explain why detrimental mean state biases tend to accompany an improved MJO (Kim et al. 2011). However, mean state bias trade-offs do not appear to manifest in models with super-parameterization (Pritchard and Bretherton 2014). As Figure 8 indicates, increased export by the horizontal flow may compensate for excessive import by vertical advection, possibly contributing to mean state precipitation and wind biases in the Tropics, such as excessive off-equatorial precipitation in the western north Pacific in models that produce a strong MJO through enhanced moisture sensitivity (e.g. Kim et al. 2009).

Our results also highlight a paradox in how entrainment is treated in parameterizations, because while some have shown evidence that entrainment rates

should be larger than what is typically used in convective parameterizations (Romps 2010; Dawe and Austin 2011b), coercing a scheme to use larger entrainment rates can yield undesirable side effects. Addressing the entrainment paradox in convection parameterizations will likely involve adding complexity and computational cost. Alternatively, moving towards widespread use of MMF that use embedded cloud resolving models in place of convective parameterizations may be a better option for exploring the interaction of convection and the large-scale circulations, which is at the core of understanding the MJO. Our work is currently being extended to evaluate the MSE budget of MMF DYNAMO hindcast experiments.

CHAPTER 3 DYNAMO HINDCASTS: COMPARISON WITH SP-CAM

Forecasts may tell you a great deal about the forecaster;
they tell you nothing about the future.

-Warren Buffet

3.1 Introduction

In Chapter 2 it was shown that increasing the entrainment rate of the dilute CAPE calculation of a convective parameterization resulted in an improvement in hindcast simulations of Madden-Julian Oscillation (MJO), but also that changes in physical processes that engendered this improvement were erroneous. It is reasonable to expect that the physical realism of the simulation would improve in a global model with an explicit representation of convection. The technique of super-parameterization allows us to test this hypothesis. Super-parameterization is based on the idea of a multi-scale modeling framework (MMF; Khairoutdinov and Randall 2001; Jung and Arakawa 2005), in which a model's unresolved processes are estimated using a second model that is specialized for these unresolved scales. In the case of global atmospheric models this second model is a cloud-resolving model (CRM). A CRM explicitly represents convective entrainment processes, and therefore super-parameterization provides an interesting comparison with the parameterized model hindcast experiments in the previous chapter.

The methods used to represent unresolved convection in a conventional climate model are some of the most uncertain and problematic components (Arakawa 2004). The unresolved convective phenomena that need to be represented include deep and shallow cumulus convection, negatively buoyant downdrafts, neutrally buoyant stratiform cloud layers, and mesoscale convective systems; some of which are neglected completely for the sake of simplicity (Randall et al. 2003). Ideally, all these processes need to interact with one

another, as well as radiation and microphysical processes. In order to address this overwhelming complexity in a practical manner, the MMF approach adopts the spirit of conventional parameterizations by assuming a scale separation between convective and large-scale processes (Grabowski 2001; Khairoutdinov and Randall 2001; Khairoutdinov et al. 2005), and is therefore often referred to as a "convection resolving cloud parameterization" (CRCP).

Many studies over the last decade have documented the superior utility of the MMF approach to simulating various atmospheric processes when compared to conventionally parameterized models. These benefits include improved representations of the diurnal cycle (Pritchard and Somerville 2009), the relationship between convection and environmental humidity (Thayer-Calder and Randall 2009), heavy rainfall events (Li et al. 2012), and tropical transient disturbances, such as convectively coupled Kelvin waves (DeMott et al. 2011). Furthermore, several studies have shown that super-parameterization produces robust MJO variability (Khairoutdinov et al. 2005; Benedict and Randall 2009; Thayer-Calder and Randall 2009; Zhu et al. 2009; Andersen and Kuang 2012; Pritchard and Bretherton 2014). Another benefit of the MMF approach is that radiation calculations are done on the embedded cloud-resolving model, instead of on the GCM grid, and thus cloud-radiative feedbacks can be more accurately represented when compared to conventional models.

The disadvantage of the MMF approach is that it increases the computational expense of the model by roughly a factor of 200 (Randall et al. 2003). However, this difference in cost is paltry when compared with a global cloud-resolving model. Two-dimensional (2D) cloud-resolving models are typically used to limit the computational

expense of super-parameterization. Some three-dimensional (3D) CRMs have been used in experiments (e.g. Khairoutdinov et al. 2005), so that convective momentum transport can be represented. However, using a 3D CRM comes at even larger expense that is hard to justify with current computational resources.

The study of Kim et al. (2009) showed SP-CAM to have the most realistic MJO simulation out of eight state-of-the-art, un-coupled GCMs, but an explanation for this success is not clear. Some have suggested that SP-CAM's success is due to the ability to delay the large-scale organization of the convection until the troposphere can be sufficiently moistened by processes, such as detrainment by shallow convection (Thayer-Calder and Randall 2009; Zhu et al. 2009). A delay in deep convection should allow more vigorous deep convection and higher precipitation rates after the environment has been sufficiently primed, unlike models that allow deep convection to form in relatively dry environments (Grabowski and Moncrieff 2004; Bechtold et al. 2008; Thayer-Calder and Randall 2009). Andersen and Kuang (2012) showed that radiative processes are important for maintaining MSE anomalies associated with the convectively active phase of the MJO in SP-CAM. Radiative processes were also shown to help slow the propagation, which is mainly driven by horizontal and vertical advection associated with synoptic scale eddies (see also Landu and Maloney 2011; Maloney 2009). If the real MJO is also critically dependent on radiative processes, then it makes sense that a model with more realistic cloud-radiative feedbacks should produce a more realistic MJO.

The representation of the MJO in SP-CAM is not without some notable deficiencies. Generally, the convective intensity of the MJO has been found to be too strong, which Benedict and Randall (2009) attribute to differences in the model's mean state and

unrealistic interactions between deep convection and the boundary layer. Luo and Stephens (2006) also suggest that the SP-CAM may also have an unrealistically intense wind-evaporation feedback stemming from the use of periodic boundary conditions in the embedded CRM. A persistent near-surface temperature bias has also been found in many SP-CAM experiments (DeMott et al. 2007).

A lack of published work exists on hindcast studies with SP-CAM, and so the impacts of model drift have yet to be investigated in this context. Systematic errors in hindcast simulations with the conventionally parameterized CAM tend to resemble model biases in long-term simulations (Ma et al. 2013). Most errors from systematic model drift are evident by day 2 of a hindcast simulation and become saturated by day 5 (Xie et al. 2012). These systematic errors are most strongly associated with moist processes but can also be associated with processes dominated by dry dynamics (Jung 2005). Systematic drift also tends to be very different depending on the region of interest (Kang et al. 2004; Huang et al. 2007). Many methods can be utilized to reduce such errors, such as multi-model ensembles that cancel out systematic errors (Pavan and Doblas-Reyes 2000), or statistical methods (Feddersen et al. 1999). However tempting it may be to correct systematic errors, their existence may be able to shed light on model deficiencies that can be corrected to produce a more physically consistent solution.

In light of the advantages of SP-CAM, the current chapter extends the previous chapter to compare hindcast simulations of DYNAMO MJO events with a parameterized global model (i.e. CAM5) and its SP counterpart (SP-CAM). Additionally, analysis is conducted to investigate and quantify the impacts of systematic model drift on RMM skill scores and MSE budget calculations in SP-CAM and CAM5. Section 3.2 outlines the methods

and model configurations. Section 3.3 details differences between the two models and characterizes the effect of systematic model errors on RMM skill scores. This is followed by a discussion of the MSE budget and gross moist stability in Section 3.4. Conclusions and discussion are presented in Section 3.5.

3.2 Methodology

3.2.1 Model Setup

SP-CAM hindcast simulations were configured in an identical manner to those of the CAM5 simulations in Chapter 2, using the same finite volume dynamical core, 30 vertical levels and 0.9°x1.25° horizontal resolution. The version of SP-CAM is the atmospheric component of the currently available SP- Community Earth System Model (SP-CESM) available from the National Center for Atmospheric Research (NCAR). Initial conditions were similarly created from ECMWF operational analysis at 00z every 5 days from 01 October – 15 December 2011. Instead of 20-day hindcasts that were performed with CAM5, SP-CAM hindcasts are integrated for 10 days with output every 6 hours to minimize the computational expense.

The cloud-resolving model in the SP-CAM hindcasts is based on the System for Atmospheric Modeling (SAM; Khairoutdinov and Randall 2003). The domain of the embedded CRM is a two-dimensional "curtain", with 32 columns and 28 vertical levels corresponding to the lowest 28 levels in CAM. A Newtonian damping layer is included in the top 3 layers of the CRM to reduce gravity wave reflection and buildup. Model equations are discretized with Arakawa C staggering, and a third-order Adams-Bashforth time-stepping scheme with variable time stepping to maintain linear stability. A single-moment

bulk microphysics scheme is used in the CRM, with five species of hydrometeors, including cloud water, rain, cloud ice, snow, graupel and hail. Similar to Chapter 2, much of the following analysis will present the hindcast data organized into 5-day segments based on the time since initialization. This will only include 00-04 and 05-09 day lead-times, since the SP-CAM hindcasts are only ten days long.

The initialization of hindcasts with SP-CAM raises the question of whether it is necessary for the embedded CRM to be "spun up" prior to the initialization time. There is currently no published study that addresses the effects of the CRM state on SP-CAM hindcasts. Several personal communications with SP-CAM users suggests that a "cold start" initialization, without spinning up the CRMs, does not affect hindcast simulations of the MJO. In particular, Dr. Mike Pritchard (personal communication) has tested a method of nudging the large-scale state of the model to allow convection in the embedded CRMs to develop. Comparing this nudging method with a cold start method resulted in no noticeable difference in short-term simulations. This nudging method is also unappealing because of the complexity and added computational cost, and so for the current study, hindcasts are initialized with a cold-start of both the embedded CRM and parent GCM. This question ultimately gets at the issue of the importance of memory in the sub-grid convection of a GCM. Super-parameterization is a great tool for addressing this question, however, this issue is outside the scope of the present study.

3.2.1 Validation Data

A central motivation of this study is to compare DYNAMO hindcasts from SP-CAM and the conventional CAM5 that employs the deep convection scheme of Zhang and

Mcfarlane (1995). Thus, the following analysis will include results from the control simulation in Section 2.2, which uses the default dilute CAPE entrainment rate of 1 km^{-1}, which will be referred to as ZM_1.0. This chapter also uses the same validation data for consistency, namely the European Centre for Medium-Range Weather Forecasts (ECMWF) interim reanalysis product (ERAi) and the Tropical Rainfall Measuring Mission (TRMM) 3B42 3-hourly high-resolution (0.25°x0.25°) merged satellite rainfall product.

For analysis of the Real-time Multivariate MJO index (RMM; Wheeler and Hendon 2004), hindcast RMM projections are obtained with the same method described in Chapter 2 (Gottschalck et al. 2010). Calculations of a modified RMM index and projections of hindcast data utilize the National Centers for Environmental Prediction and National Center for Atmospheric Research (NCEP-NCAR) reanalysis (Kanamitsu et al. 2002) zonal winds at 200 hPa and 850 hPa, and National Oceanic and Atmospheric Administration (NOAA) interpolated outgoing longwave radiation (Liebmann and Smith 1996). All data for RMM calculations are averaged about the equator from 15°S to 15°N. These datasets are intentionally used, instead of ERAi data, to be consistent with previous studies (e.g. Gottschalck et al. 2010).

3.3 Model Drift and RMM Skill Scores

3.3.1 Hindcast results

Maps of mean precipitation for 00-04 and 05-09 day leads are shown in Figures 3.1 and 3.2 for TRMM, ZM_1.0 and SP-CAM. In Chapter 2 it was shown that CAM hindcasts exhibit a reduction of precipitation intensity with lead-time. In contrast, SP-CAM shows a slight intensification of precipitation with lead-time (Fig. 3.1-3.2c). The pattern of

precipitation in SP-CAM is slightly more realistic than CAM, especially at 00-04 day leads, with more intense precipitation in the Indian Ocean inter-tropical convergence zone (ITCZ; 0-10°S; 50-100°E). SP-CAM does share some precipitation biases with ZM_1.0, such as too much precipitation over Papua New Guinea and too little precipitation near the Philippines (Fig. 3.1b-c).

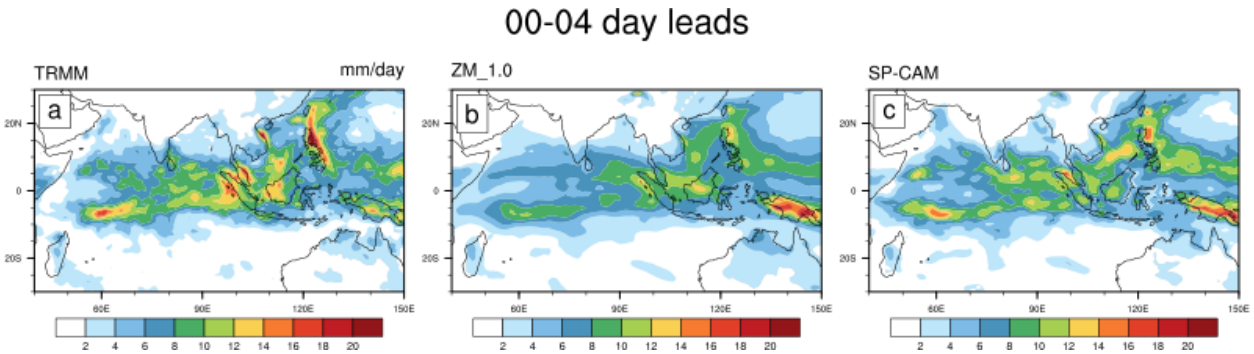

Fig. 3.1 Mean precipitation for 00-04 day lead times.

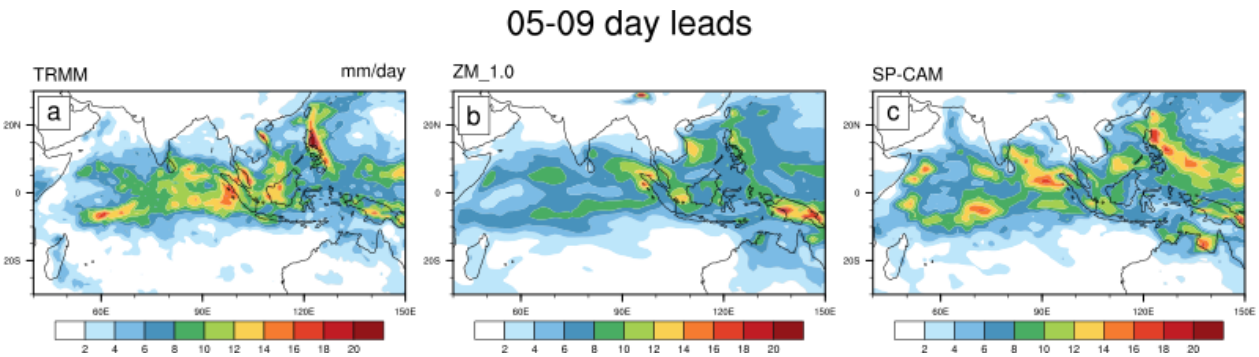

Fig. 3.2 Mean precipitation for 05-09 day lead times.

Figure 3.3 shows mean profiles of moist static energy (MSE) and vertical pressure velocity (omega), for ERAi, SP-CAM, and ZM_1.0 at 00-04 and 05-09 day leads (see also Fig. 2.6). The MSE profile in SP-CAM shows better agreement with ERAi, and less change with lead-time than ZM_1.0. The profile of omega in SP-CAM is weaker in amplitude than ERAi, but is generally in better agreement and larger in magnitude when compared with ZM_1.0. The omega profile in SP-CAM is consistent with more intense precipitation over the Indian

Ocean as shown in Figure 3.1. The omega profile also shows less change between the 00-04 and 05-09 day leads in SP-CAM when compared to ZM_1.0.

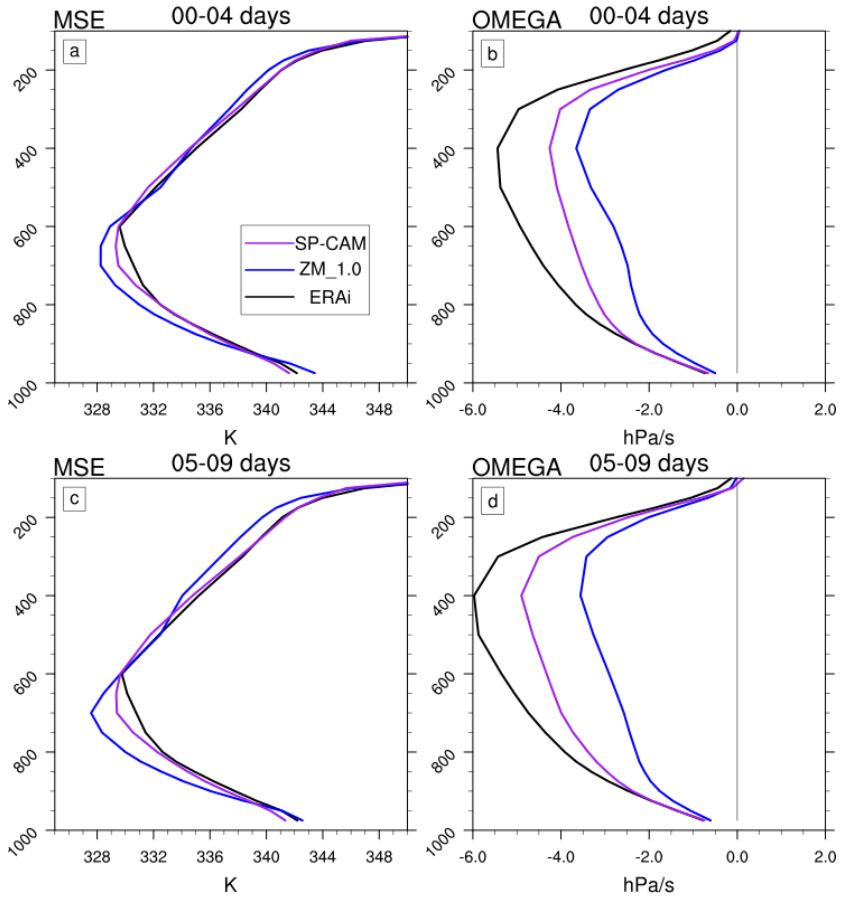

Fig. 3.3 Mean profiles of MSE (left column) and vertical pressure velocity (right column) for 00-04 (a-b) and 05-09 (c-d) day lead times averaged over the equatorial Indian Ocean (10°S-10°N; 60-90°E).

To get a sense of how well the hindcasts capture the DYNAMO MJO events, Figure 3.4 shows hovmöller plots of equatorial averaged precipitation for 00-04 day leads. The data in Figure 3.4 has been temporally smoothed with three passes of a 1-2-1 filter to bring out MJO scale variability. TRMM shows clearly defined periods of enhanced precipitation that make up the October and November DYNAMO events (Fig. 3.4a). SP-CAM also shows periods of enhanced and suppressed precipitation that agree well with TRMM data, but are slightly less coherent (Fig. 3.4b). The DYNAMO MJO events are less prominent in ZM_1.0

data (Fig. 3.4c), but the periods of enhanced and suppressed precipitation still occur at the right place, and at the right time. Precipitation in ZM_1.0 is generally weaker than SP-CAM or TRMM, consistent with the mean precipitation pattern in Figure 3.1c.

The precipitation hovmöller at 05-09 day leads shows a degradation of the MJO signal in both models (Fig. 3.5; see also Fig.2.4). SP-CAM still maintains clear periods of enhanced and suppressed precipitation, although the envelope of enhanced convection is less coherent than that of TRMM (Fig. 3.5b). Degradation of the convective signal is even more dramatic in ZM_1.0 at 05-09 day leads (Fig. 3.5c). Overall, we can conclude from these hovmöller plots that SP-CAM hindcasts have a superior representation of the convective signal of the DYNAMO MJO events compared to the conventional CAM5.

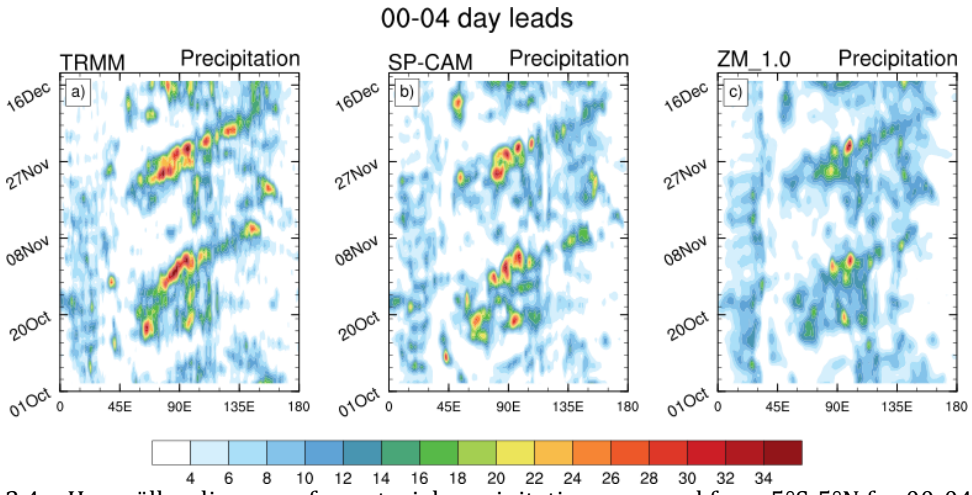

Fig. 3.4 Hovmöller diagram of equatorial precipitation averaged from 5°S-5°N for 00-04 day lead times.

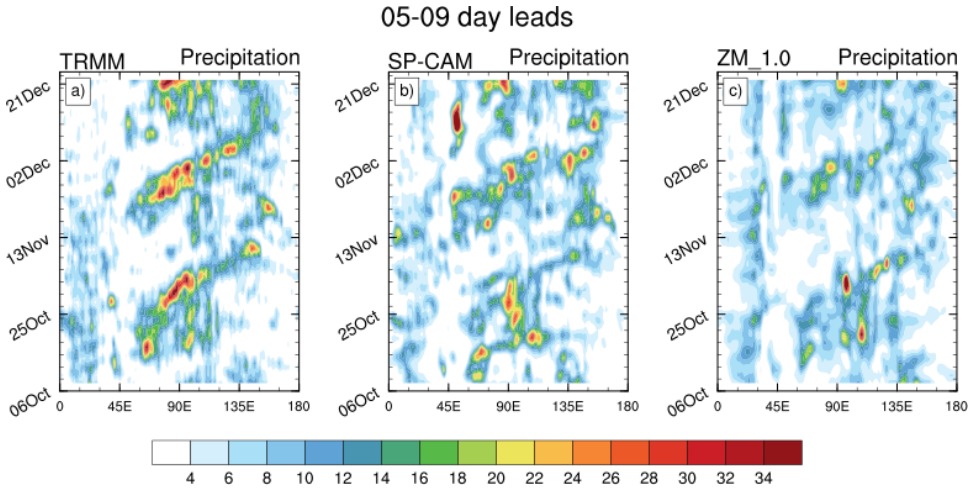

Fig. 3.5 Hovmöller diagram of equatorial precipitation averaged from 5°S-5°N for 05-09 day lead times.

Figure 3.6 shows Hovmoller plots of 850 hPa zonal wind for all datasets at 00-04 day leads. SP-CAM overestimates the strength of the westerly phase of the low-level wind associated with the MJO. Similar analysis of upper-level wind reveals a similar overestimation (not shown). ZM_1.0 also shows a slight overestimation of low-level wind. At 05-09 day leads, the strength of the low-level wind in SP-CAM becomes even stronger, while ZM_1.0 exhibits less coherent wind structure with no obvious change in wind amplitude (Fig. 3.7). We will see in the next section that the overly strong winds in SP-CAM have significant consequences for the RMM skill scores.

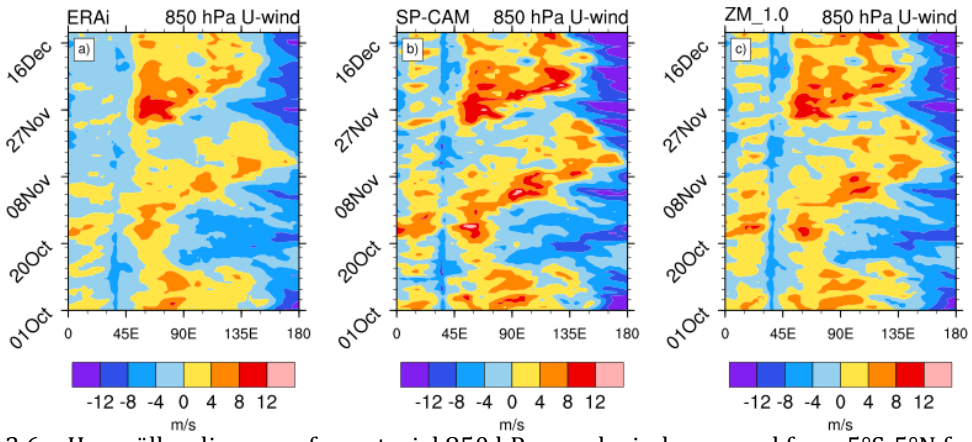

Fig. 3.6 Hovmöller diagram of equatorial 850 hPa zonal wind averaged from 5°S-5°N for 00-04 day lead times.

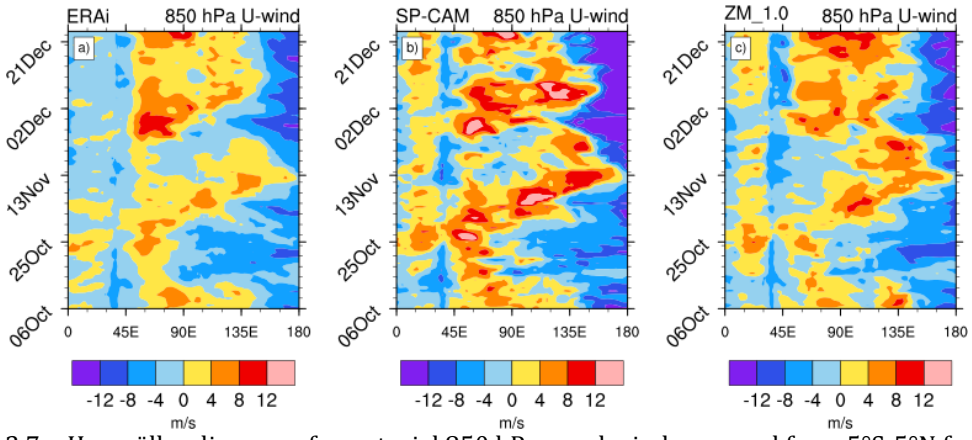

Fig. 3.7 Hovmöller diagram of equatorial 850 hPa zonal wind averaged from 5°S-5°N for 05-09 day lead times.

3.3.1 RMM Skill Metrics

The COR and RMSE skill scores are shown in Figure 3.8 (see (2.2) and (2.3)). The COR metric, in which a higher value is better, indicates a better skill in SP-CAM than ZM_1.0. On the other hand, the RMSE metric, in which a lower value is better, shows that SP-CAM is worse than ZM_1.0, which is seemingly inconsistent with the precipitation Hovmöller plots in Figures 3.4-3.5. The RMM index is dominated by wind variability (Straub 2013), and so the high RMSE is more likely related to the overestimation of the wind signal (Fig. 3.6). The COR metric is normalized by the amplitude of the RMM

projection, and can only tell us how well the model is predicting the phase of the RMM index, which is defined mathematically in (3.11). Therefore, based on Figure 3.8a we can conclude that SP-CAM is reproducing the observed RMM phase slightly better than ZM_1.0. The RMSE metric contains information about both phase and amplitude, and so the large RMSE error score indicates that SP-CAM hindcasts have a significant RMM amplitude bias.

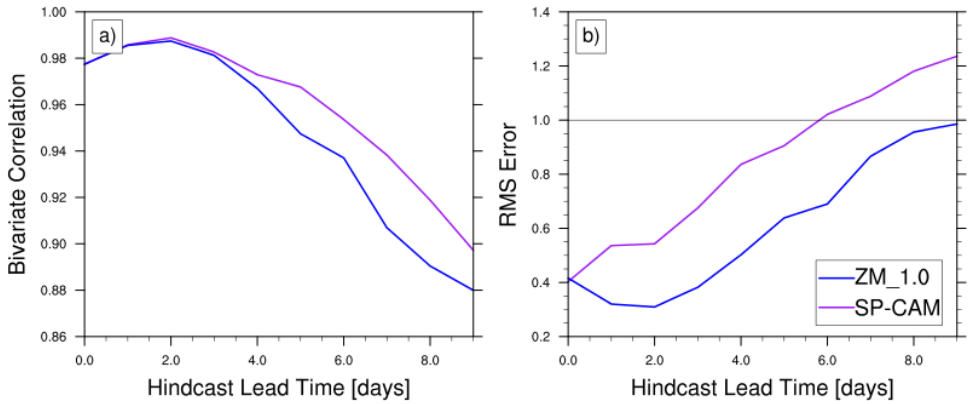

Fig. 3.8 Bivariate correlation (left) and RMSE error (right) RMM skill scores as a function of lead-time in days for SP-CAM (purple), ZM_1.0 (blue) and ZM_0.2(green). Grey lines denote threshold of no MJO predictive skill (see text).

To better understand the RMM amplitude bias in SP-CAM we will start by looking directly at the hindcast RMM projections. Figure 3.9 shows the evolution of the RMM projections for the October and November DYNAMO MJO events for data at 00-04 day leads. The projections are plotted in the RMM "phase space", with RMM1 on the abscissa and RMM2 on the ordinate. In this phase space an eastward propagating event will manifest as a line that traces out a counter-clockwise path. The unit circle denotes an amplitude of one standard deviation of the RMM index, and is often used to distinguish high and low amplitude MJO events (Wheeler and Hendon 2004; Straub 2013). Both SP-CAM and ZM_1.0 capture the evolution of the October event at 00-04 day leads, but both models overestimate the RMM amplitude at certain points during the event. For the November

event, the amplitude in the mature phase of the event in late November and early December is overestimated in SP-CAM, and underestimated in ZM_1.0 (Fig. 3.9b).

At later lead times, the RMM amplitude biases are more dramatic (Fig. 3.10). At these lead times ZM_1.0 tends to overestimate the RMM amplitude in the October event (Fig. 3.10a), but underestimates the November event (Fig. 3.10b). SP-CAM more strongly overestimates the RMM amplitude for both events, although the RMM phase is reasonably captured (see also Fig. 3.13), consistent with the RMM skill scores (Fig. 3.8).

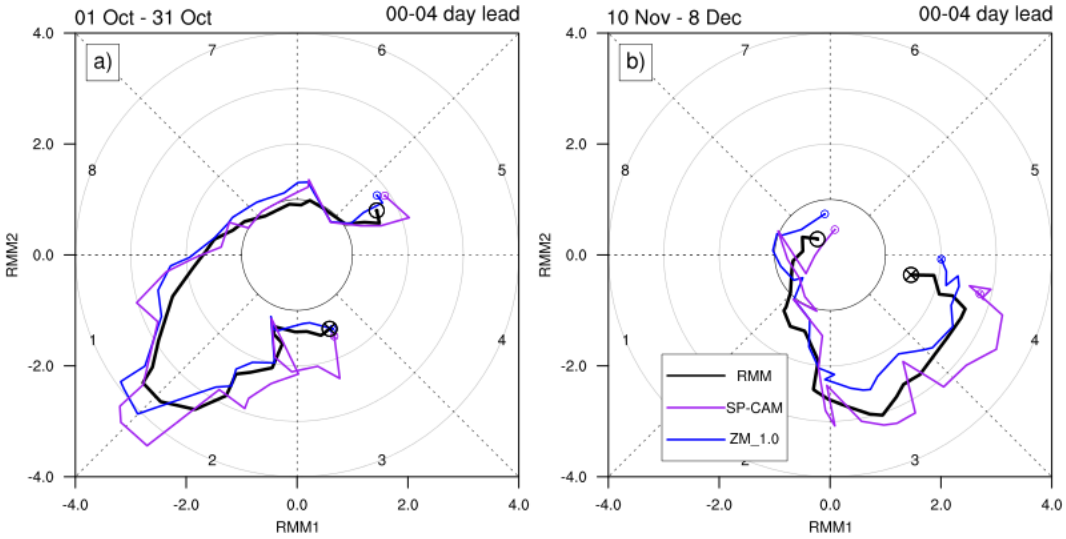

Fig. 3.9 RMM phase space plots of the October (left) and November (right) MJO events in 2011 from DYNAMO. Only data from 00-04 day lead times is used.

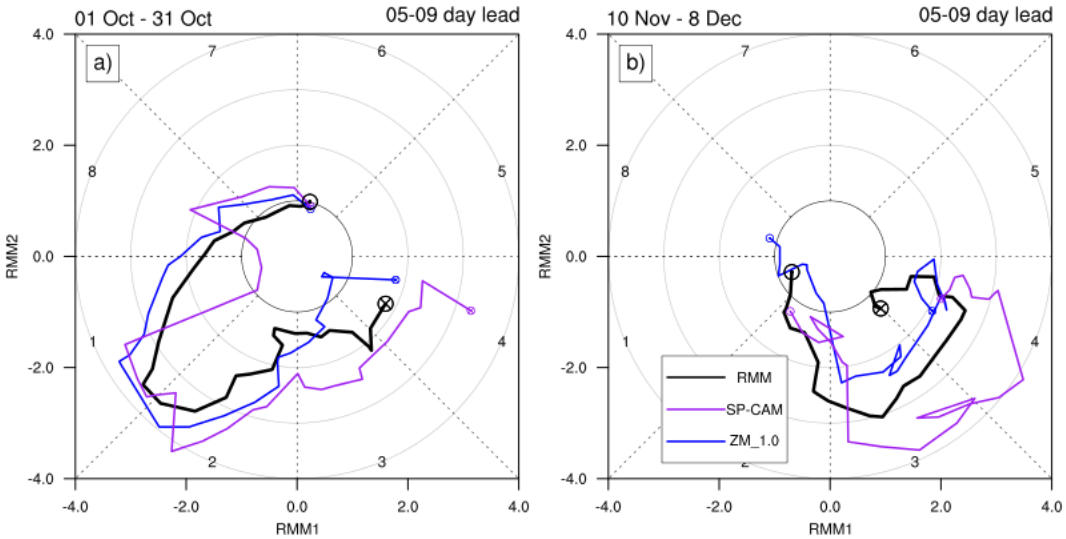

Fig. 3.10 Similar to Figure 3.9, except that only data from 05-09 day lead times is used.

The RMM index has been shown to be dominated by the upper and lower level wind components, and having only minimal influence from the convective signal of the MJO (Straub 2013). The October event during DYNAMO is a prime example of this problem. This event was a very large amplitude event in the RMM index, but observations of moisture and convection suggest that this large amplitude is not representative of exceptionally strong convection in the Indian Ocean (Fig. 3.9; Johnson and Ciesielski 2013; Yoneyama et al. 2013). By re-calculating the RMM projection without OLR data we can see that the gross features and amplitude biases are still present for both events (Fig. 3.11). The November event appears to have a larger influence from the projection of a convective signal, but the large amplitude bias in SP-CAM is noticeable nonetheless. This conclusion holds for data at 05-09 day lead times as well (Fig. 3.12)

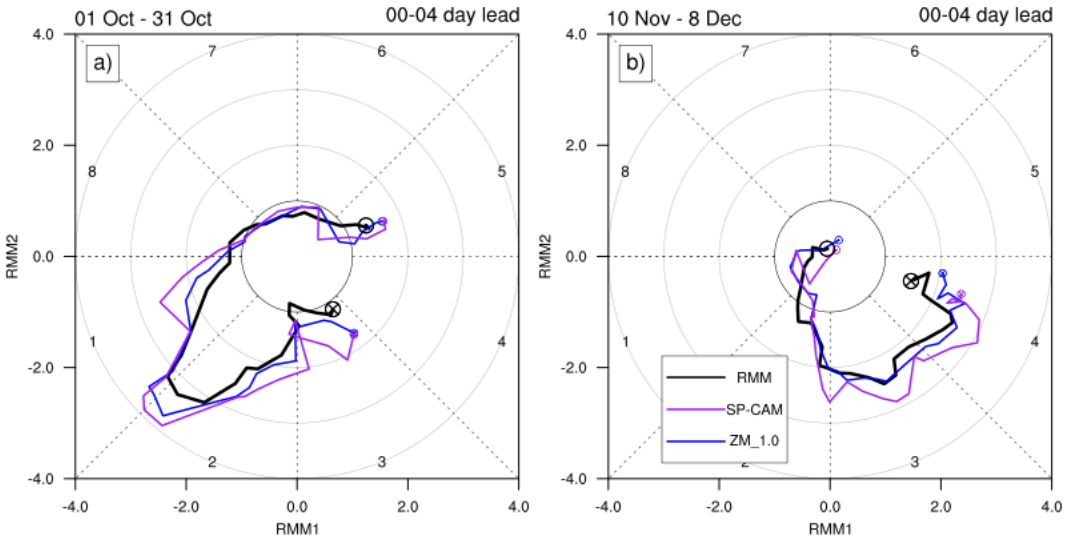

Fig. 3.11 Similar to Figure 3.9, with data from 00-04 day lead times, but only the wind components of the RMM projection are considered.

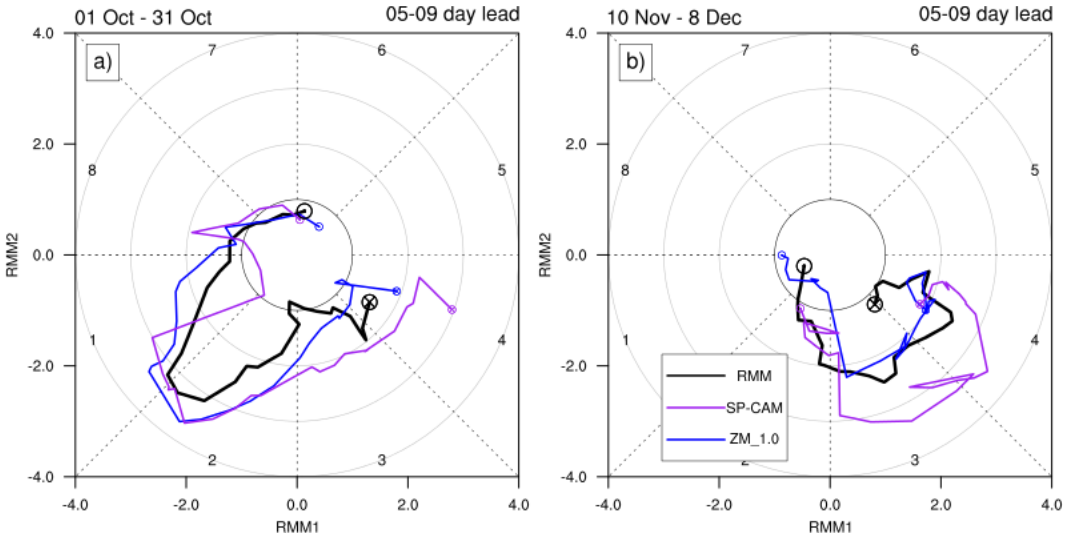

Fig. 3.12 Similar to Figure 3.9, with data from 05-09 day lead times, but only the wind components of the RMM projection are considered.

The large amplitude bias in SP-CAM is further confirmed by the time series of RMM amplitude, phase, and individual components in Figure 3.13. The amplitude and phase of the RMM index are calculated as follows:

$$AMP = \sqrt{RMM_1^2 + RMM_2^2} \tag{3.10}$$

$$PHS = \arctan\left(\frac{RMM_2}{RMM_1}\right) \tag{3.11}$$

The systematic over-amplification of the RMM projection in SP-CAM is evident in Figure 3.13a. Time series of individual RMM components (Fig. 3.13b,d) show an interesting tendency of SP-CAM to amplify situations of positive RMM1 and negative RMM2. This is not to say that errors are not evident at other phases, however the selective amplification of positive RMM1 and negative RMM2 appears to be robust. Time series of RMM amplitude, phase, and individual components for ZM_1.0 do not show any systematic errors (Fig. 3.14). This result is indicative of a systematic drift of the SP-CAM hindcast simulations. If this is the case, then the amplitude problem identified in the RMM skill metrics may have nothing to with the model's intrinsic ability to produce a realistic representation of the DYNAMO MJO events.

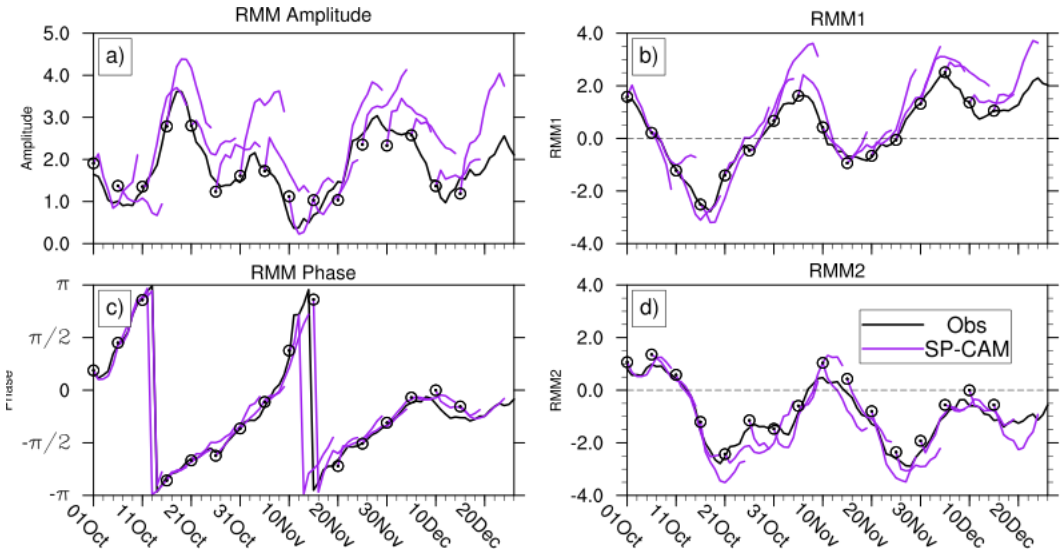

Fig. 3.13 Time series of RMM amplitude (a), RMM phase (c), RMM1 (b), and RMM2 (d) from observations (black) and individual SP-CAM hindcast projections (purple).

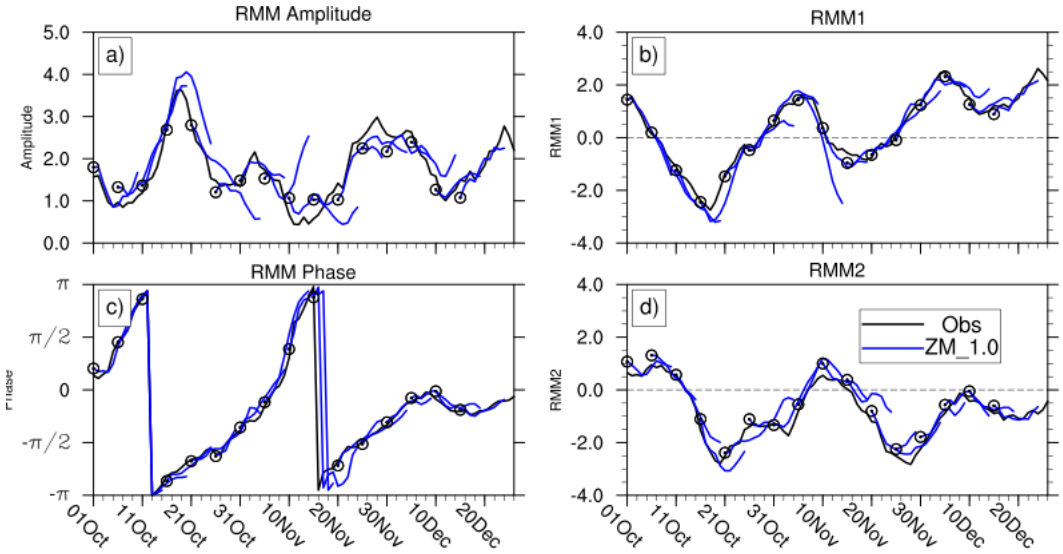

Fig. 3.14 Similar to Fig. 3.13. Time series of RMM amplitude (a), RMM phase (c), RMM1 (b), and RMM2 (d) from observations (black) and the first 10 days of individual CAM hindcast projections (blue).

In order to know if model drift is impacting the RMM index, we need to first isolate the signal of this drift. Model drift is a systematic evolution of the model state that is independent of perturbations in the initial conditions. To isolate this drift signal for a given variable, we first locate all data points at a given spatial location that fall on a given lead-time. We then compute the average of these data, and repeat this for all spatial locations and lead-times. The resulting dataset is a four-dimensional array that is a function of lead-time and the three spatial dimensions. The purpose of this averaging method is to remove the "weather" and bring out the signal of the intrinsic model drift that occurs systematically in every hindcast simulation.

At this point, we could subtract the value at the time of initialization for every spatial point to obtain a drift signal relative to the initial state, but this approach is problematic. To illustrate the problem, consider the case in which a variable has a large error at the time of initialization, but becomes closer to the observed value at later times of the hindcast. This is the case for the average precipitation over the equatorial Indian Ocean

as shown in Figure 3.15. If we subtract out the initial value that has a large error, we might incorrectly interpret that SP-CAM is drifting *away* from the observed state by ~4 mm day^{-1}, instead of toward it with a small overestimation on the order of ~1 mm day^{-1}. Initial calculations to isolate model drift encountered this exact problem, which motivated an alternate method. We are interested in how the model drifts relative to the observations. Therefore, after we have averaged the hindcast data at every lead-time, we average ERAi data in a comparable manner and subtract the temporal mean of this data from the hindcast drift signal at all spatial points.

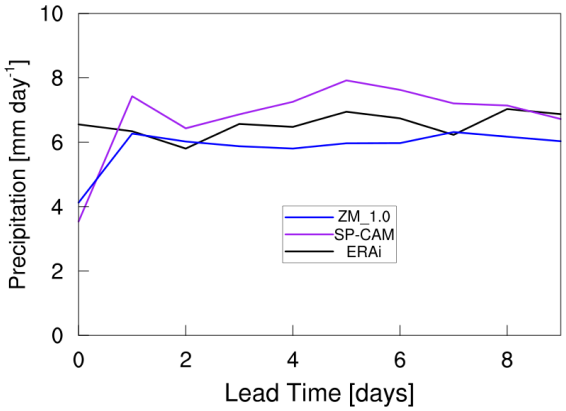

Fig. 3.15 Average precipitation in the equatorial Indian Ocean (15°S-15°N; 60°-90°E) organized by the day since hindcast initialization (i.e. lead-time).

Note that the drift obtained from the hindcasts is limited in scope, and may not fully describe the intrinsic model drift. A more thorough method of characterizing the drift tendencies of a model would be to create hindcasts for each day of the year over several decades so that any seasonal evolution of the systematic model drift could be accounted for. However, this alternate method is extremely expensive and is not feasible in the present study.

To characterize the evolution of the drift in the equatorial region, hovmöller plots are shown in Figure 3.16 for each variable used in the RMM index, namely 850 hPa and 200

hPa zonal wind (U850; U200), and outgoing longwave radiation (OLR). Results from ERAi are included to show that the method does not reveal any drift in the observations, with the exception of a slight shift towards more westerly upper level wind over the East Pacific, which is likely a signature of the seasonal cycle. In the hindcast simulations, upper and lower level wind display a drift pattern with a rich longitudinal structure. The circulation patterns do not show any structure that resemble observed large-scale circulation features, such as a Walker cell circulation. SP-CAM shows the development of a strong low-level easterly bias around 180˚-120˚E. There is a slight hint of a similar low-level easterly bias in ZM_1.0. Drift of the upper level wind in SP-CAM shows a mostly weak easterly bias, with a patch of strong easterlies over the western Indian Ocean. ZM_1.0 also shows more a more easterly upper-level zonal wind bias, but also a strong westerly bias in the central Indian Ocean. Plots of zonally averaged meridional wind show a similar rich spatial structure, and do not indicate a coherent shift or intensity change of the ITCZ (not shown).

The drift of the OLR field of SP-CAM is reminiscent of a zonal wavenumber one pattern, with a stronger reduction of OLR (i.e. enhanced cloudiness) in the Indian Ocean and West Pacific Oceans (60-180°E). This pattern appears likely to project well onto the RMM spatial patterns, which also have a wavenumber 1 pattern. The OLR drift in ZM_1.0 also shows a reduction in OLR with lead-time, but in this case the drift is more gradual. Both models show higher OLR (i.e. suppressed convection) at day 0, consistent with the average precipitation drift over the whole Tropics (Fig. 3.15). This could be related to the spin-up of the embedded CRM in SP-CAM. Parameterized convection in ZM_1.0 does not develop in the same sense as in SP-CAM, but the ambient cloud water and ice used in radiative calculations is initially absent, and therefore some “spin-up” time is required to

adjust these fields. This explains the slow adjustment of OLR in both models, although it is still somewhat surprising that OLR in ZM_1.0 exhibits a slower drift than SP-CAM.

So far, we have shown the drift signal of the two models relative to ERAi, but the RMM projections are done using NCEP reanalysis and NOAA OLR. The wind fields are well constrained, and therefore the results are not any different when comparing to NCEP winds. However, NOAA OLR is satellite derived, whereas ERAi OLR is produced by the model physics. In light of this difference we have plotted the OLR drift signal of ERAi, SP-CAM and ZM_1.0 relative to NOAA OLR in Figure 3.17. The results are similar to Figure 3.16, however ERAi OLR is biased positive relative to NOAA OLR. With respect to NOAA, SP-CAM has a negative bias in the Indian and West Pacific Oceans and a positive bias over the Western Hemisphere that doesn't appear to show much sensitivity to lead time, whereas ZM_1.0 has a strong positive bias that decreases with lead time.

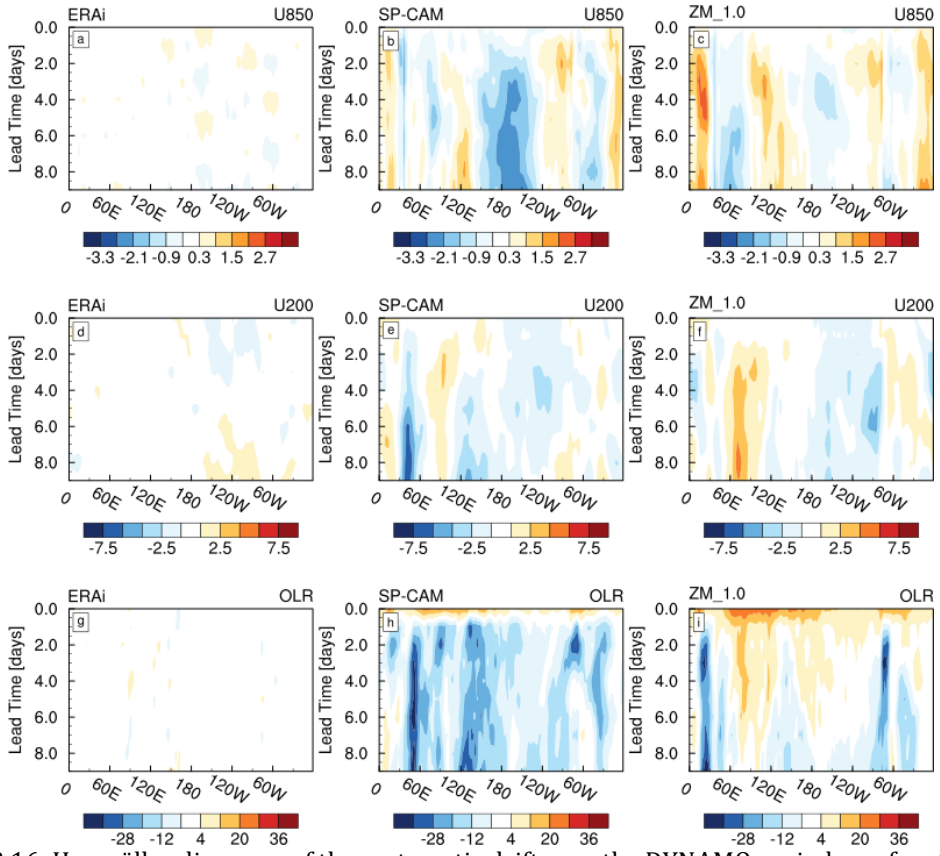

Fig. 3.16 Hovmöller diagrams of the systematic drift over the DYNAMO period as a function of time since hindcast initialization (see text) in the three variables that make up the RMM index in ERAi, SP-CAM, and ZM_1.0. Data was equatorial averaged from 15°S-15°N, consistent with the RMM index.

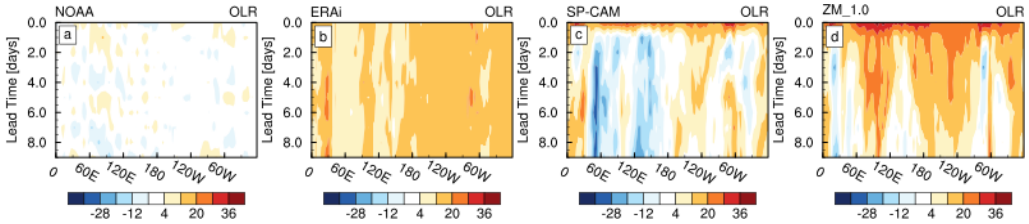

Fig. 3.17 Similar to Figure 3.16, except only for OLR and NOAA OLR is used as the baseline to isolate the drift.

Now that we have verified our method for isolating the signal of model drift in the hindcast simulations, we can further quantify its impact on the RMM index by projecting the longitudinally averaged data at each lead-time onto the RMM spatial structures defined by Wheeler and Hendon (2004). Figure 3.18 shows this calculation using SP-CAM data for

the full RMM index as well as separately for each of the RMM component projections of U200, U850 and OLR. The projections of the drift confirm the selective amplification of positive RMM1 and negative RMM2 revealed in Figure 3.13. During days 0-6 the 200 hPa wind compensates the general positive RMM1 bias, but becomes positive at later lead times (Fig. 3.18a). While it was confirmed that the wind components dominated the RMM index (Fig. 3.11-3.12), Figure 3.18 suggests that OLR also contributes substantially to the RMM amplification problem. Overall, 850 hPa wind is the biggest offender to both components in SP-CAM, contributing the strongest drift signal to the RMM bias. Similar plots for ZM_1.0 show the model drift weakly contributing a negative RMM1 and positive RMM2 (Fig. 3.19). Therefore, we can conclude that model drift in the conventional CAM is not problematic, and less of a concern for interpreting the RMM skill scores. On the other hand, the SP-CAM better reproduces the DYNAMO MJO events, but the inherent drift of the model induces a large bias in the RMM projections, that obscures the interpretation of RMM skill scores, especially for the RMSE metric.

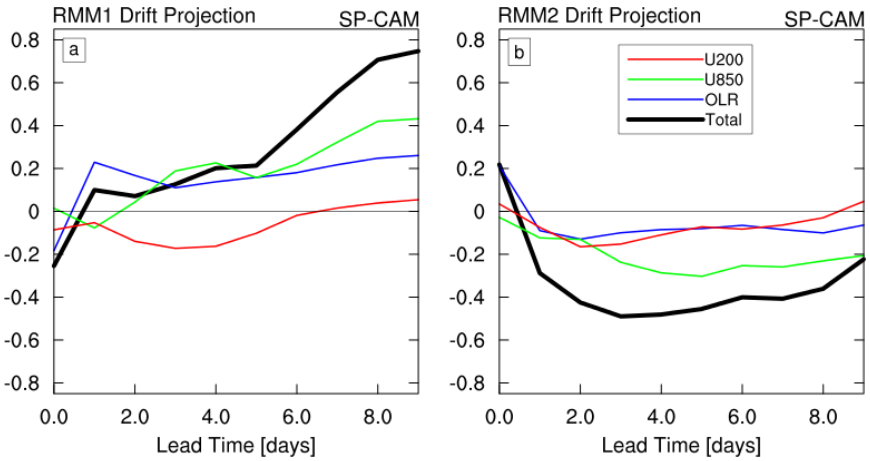

Fig. 3.18 Projection of the isolated drift pattern in Figure 3.8 onto the RMM spatial structures (see text) as a function of lead-time for SP-CAM. The total projection (thick black) is broken into three components of the projection from OLR (blue), U850 (green), and U200 (red).

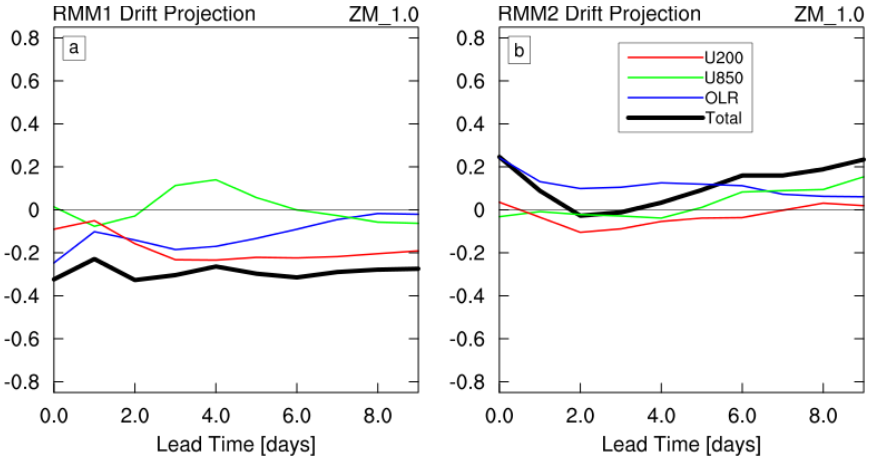

Fig. 3.19 Similar to Figure 3.18, except for ZM_1.0.

3.4 The MSE budget and Model Drift in SP-CAM

In spite of the large SP-CAM RMM RMSE score in (Fig. 3.8b), hovmöller plots of precipitation reveal that SP-CAM can better reproduce the convective signal of the DYNAMO MJO events (Fig. 3.4). In Chapter 2, CAM hindcasts were shown to produce a better MJO signal through an inaccurate compensation of weak cloud-radiative feedbacks by enhanced import from vertical moist static energy (MSE) advection. This change in vertical MSE advection was found to be associated with a strongly negative gross moist

stability (GMS) that can destabilize a moisture mode in spite of weak MSE source feedbacks, inconsistent with observations. Given that SP-CAM can produce a natural interaction between sub-grid scale convection and large-scale dynamics, we expect SP-CAM to produce a more realistic MJO due to an improved representation of the salient processes. To test this hypothesis we now explore the column integrated MSE budget and GMS, and how these are affected by model drift in SP-CAM and CAM. Defintions of the column integrated MSE budget and GMS are discussed in detail in Sections 2.4 and 2.5.

Column integrated MSE budget terms for 00-04 day lead-times are shown in Figure 3.20, binned by the column MSE anomaly (see also Fig. 2.9). All terms are plotted such that positive values correspond with a positive column MSE tendency. Error bounds were calculated using Student's t-statistic at the *95%* confidence level and are denoted with triangles. Zonal and meridional advection are not significantly different from ERAi in both models (Fig. 3.20a-b). Surface fluxes, which include latent and sensible heat flux, are slightly underestimated in CAM for positive MSE anomalies. SP-CAM surface fluxes show better agreement with ERAi (Fig. 3.20c). The slope of column radiative heating per change in column MSE provides a gross characterization of the cloud-radiative feedback strength. SP-CAM shows much better agreement with ERAi in the slope and magnitude of column radiative heating, whereas cloud-radiative feedbacks in CAM are too weak (Fig. 3.20d).

In Section 2.4, ZM_1.0 was shown to have an unrealistic relationship of vertical MSE advection to column MSE anomaly. Surprisingly, this is also evident in SP-CAM (Fig. 3.20e), which has a positive bias in the tendency from vertical advection for -2 to +2 column MSE anomaly bins. This is a somewhat surprising result, and suggests that the processes underlying the MJO in SP-CAM may not be entirely realistic in spite of the strength and

robustness of the MJO signal (see caveat below). Overall, SP-CAM is demonstrating a bias in the efficiency of vertical MSE advection, similar to CAM, that is likely influencing it's representation of the MJO.

Due to the non-montonic nature of the curve in Figure 3.20e, it is difficult to assess the feedback relationship between vertical advection and coluimn MSE, as was done for column radiative heating. Although we can still interpret this figure in terms of a feedback relationship by recognizing that a positive MSE tendency in a column with a positive MSE anomaly exerts an amplifying effect on the column MSE (i.e. positive feedback). This is the case for any point of the curve in Figure 3.20e that falls in the upper-right quadrant. Likewise, any points in the lower-left quadrant represent a negative MSE tendency for a negative MSE anomaly and act to amplify the negative anomaly, indicating a positive feedback. Similar reasons shows that points in the upper-left and lower-right quandrants indicate a negative feedback, or a damping effect on the column MSE anomaly. With this line of thinking we can see that for small positive column MSE anomalies, ERAi indicates that vertical advection should contribute a damping effect while both model indicate a weak amplifying effect. This would help to amplify a column MSE anomaly and perhaps make moisture modes unrealistically unstable, which is discussed further in the next section. Similarly, for small negative column MSE anomalies, ERAi shows that vertical advection provides a weak positive tendency, whereas both models show a strong positive tendency. This will act to supress the dry phase of the MJO, which was shown to be important for distinguishing propagating and non-propagating MJO events by Kim et al. (2013).

A noteworthy caveat of this conclusion is that we are comparing a model to a reanalysis product, which is largely influenced by model physics in data-sparse regions, like the Indian Ocean. Mapes and Bacmeister (2012) provided a detailed description of the analysis tendencies of the model used for the Modern Era Reanalysis (MERRA) product, as this indicates when and where assimilation corrections are needed to compensate for model errors. The model in their analysis does not produce a robust MJO on it's own. Analysis tendencies of MJO events in the reanalysis product showed a moistening correction during the period of moistening that precedes the convectively active phase, indicating that the model was far too dry. If the model used in the ERAi product has a similar issue, then our conclusions regarding Figure 3.20e require a caveat. There is evidence that this is the case, as Landu and Maloney (2011) found a similar budget residual during the MJO moistening period in ERAi as Mapes and Bacmeister (2012) found for MERRA. Data from the DYNAMO sounding array only covered a limited area and was found to be insufficient for producing a comparable analysis. Nonetheless, ERAi is currently one of the best resources for investigating the dynamics of the MJO at the larger-scales.

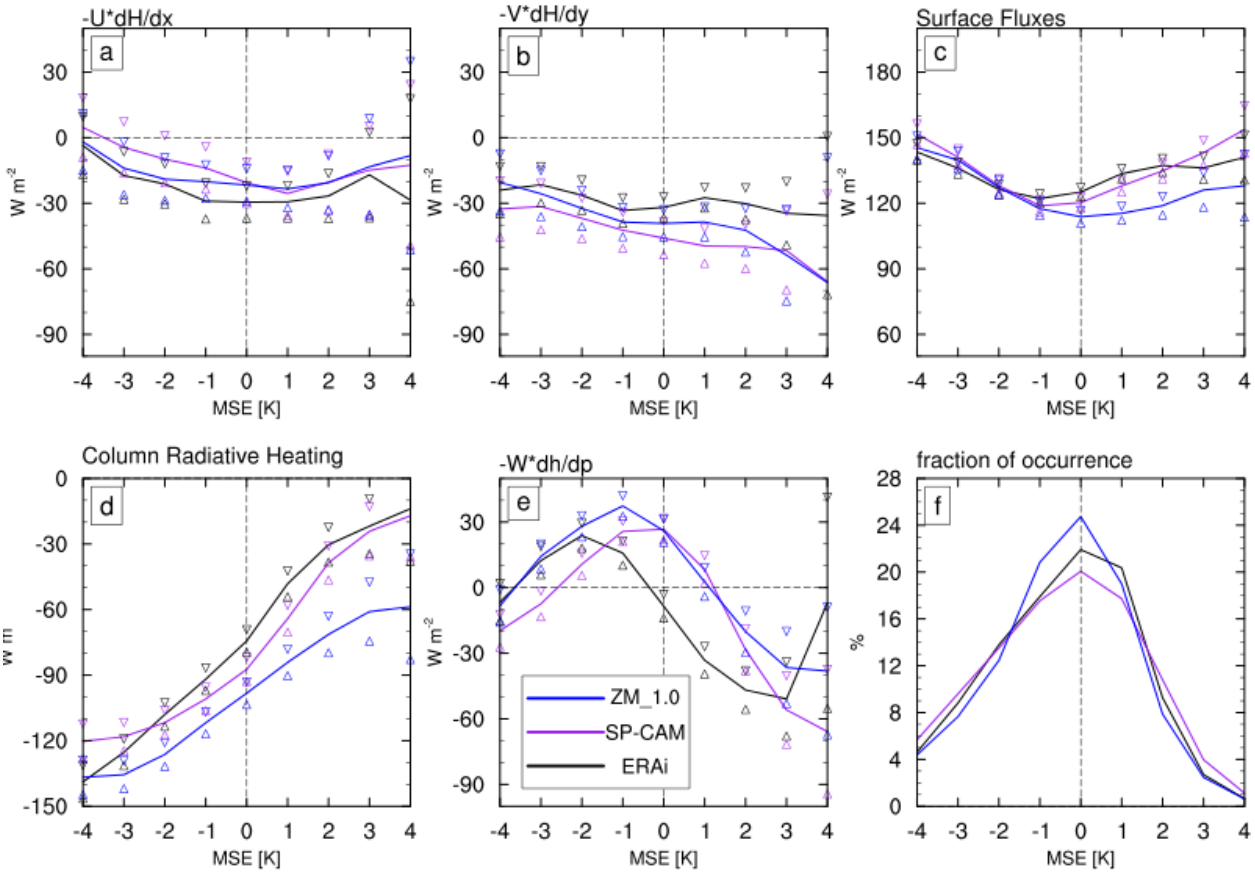

Fig. 3.20 Average MSE budget terms (a-e) and fraction of occurrence of each MSE anomaly bin (f) binned by the MSE anomaly for 00-04 day lead times over the equatorial Indian Ocean (10°S-10°N; 60-90°E). Error bound estimates are indicated by triangle markers and were calculated using a Student's t-statistic.

The behavior of column MSE budget terms does not change substantially at 05-09 day leads, although there are some notable small changes (Fig. 3.21). Export of column MSE by meridional advection appears to become slightly stronger in SP-CAM, although this is only significant for very small MSE anomalies (Fig. 3.21b). Interestingly, the relationship between column radiative heating and column MSE shows modestly improved agreement between ZM_1.0 and ERAi (Fig. 3.21d). This change may reflect the spin-up of the convection for both models evidenced in Figures 3.15-3.16. If this is true, then we might be able to improve the hindcast skill of the model by developing a method to effectively spin-up the cloud-radiative feedbacks using more sophisticated methods of assimilation and

initialization. The bias in vertical MSE advection noted in the previous figure does not change significantly.

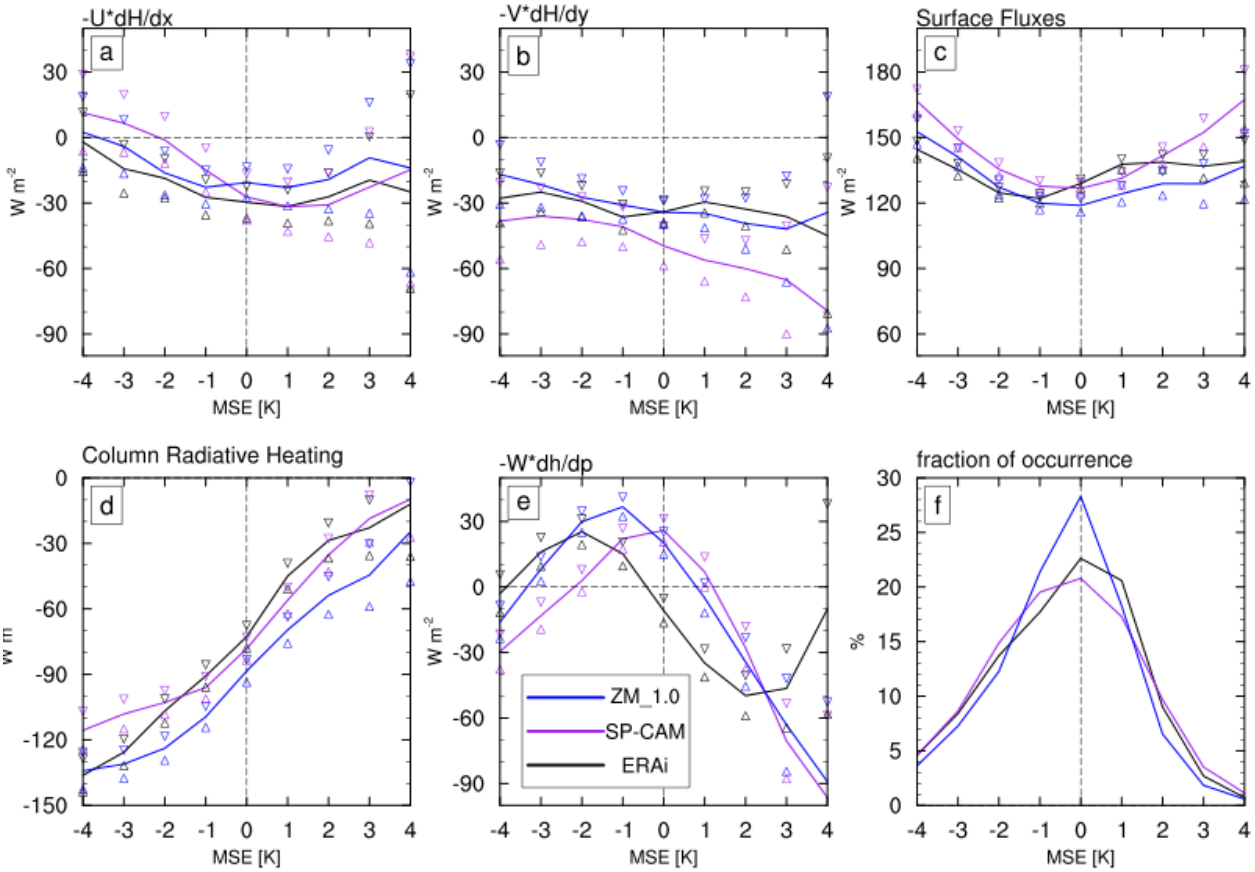

Fig. 3.21 Similar to Figure 3.20, except for 05-09 day lead times.

The binned analysis in Figures 3.20-3.21 does not distinguish between periods of increasing or decreasing column MSE, which may obscure the interpretation since the MJO has distinct periods where the column MSE tendency is either increasing or decreasing over a large area for the same MSE anomaly. For example, prior to the enhanced convective phase of the MJO there is a positive advective tendency from low level easterly flow, whereas in the suppressed phase there is a strong negative advective tendency from westerly zonal wind in addition to MSE export by merdional wind. Both of these scenarios can occur in the bins with a weak MSE anomaly (-2 to 2 K; Fig. 3.20). In order to clarfy this

point we plot the advective terms of the column MSE budget averaged over the equatorial Indian Ocean (10°S-10°N; 60°-90°E) as a function of lead-time and also segregated the based on the total MSE tendency (Fig. 3.22). In order to make the total MSE tendency representative of MJO scales we employ a 4°x4° running spatial smoother to damp any small-scale noise. Zonal advection generally contributes a positive tendency when the total tendency is positive and a negative tendency when the total tendency in negative, consistent with previous studies that highlight the importance of zonal advection over the MJO lifecycle (Maloney 2009; Landu and Maloney 2011). Zonal MSE advection in SP-CAM is biased towards stronger import during periods of increasing column MSE (Fig. 3.22a), but does not suggest any large sesntivity to lead-time. On the other hand, meridional MSE advection in SP-CAM is biased toward stronger export when the total tendency is negative (Fig. 3.22b), and has a stronger export bias at longer lead times. ZM_1.0 shows better agreement with ERAi in both zonal and meridional advection terms. The positive vertical MSE advection bias identified in Figure 3.20 is also evident in Figure 3.22c in both situations of positive and negative total tendency, with the ZM_1.0 having a noticeably stronger bias than SP-CAM. This shows that vertical MSE advection in both models is almost always either importing too strongly or not exporting strongly enough, with a stronger bias in ZM_1.0 for periods of increasing column MSE (Fig. 3.22c).

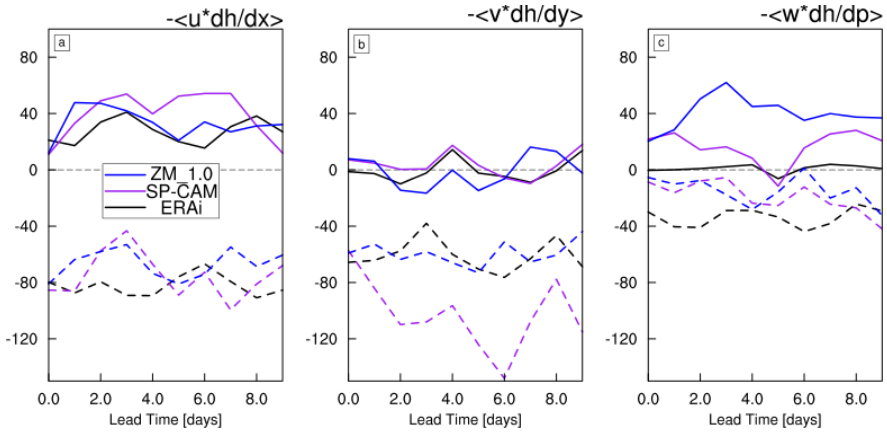

Fig. 3.22 Advective terms of the MSE budget averaged over the equatorial Indian Ocean (10°S-10°N; 60°-90°E) and plotted as a function of lead time. Data is categorized based on whether the total column MSE tendency is positive (solid) or negative (dashed).

The meridional advection bias in SP-CAM is an interesting feature that deserves closer attention. Pritchard and Bretherton (2014) found that the strength and propagation of the MJO in SP-CAM is strongly related to moisture advection by vorticity anomalies. The meridional component of this advection is related to synoptic eddies that mix across the meridional MSE gradient (Maloney 2009; Landu and Maloney 2011; Andersen and Kuang 2012). Therefore, the enhanced MSE export by meridional advection in Figure 3.22b is likely associated with enhanced synoptic eddy activity in SP-CAM. To test this hypothesis we can characterize the synoptic eddy activity with the eddy vorticity variance, which we define here as

$$\overline{\zeta'^2} = \overline{\left(\frac{\partial v'}{\partial x} - \frac{\partial u'}{\partial y} \right)^2} \quad . \tag{3.12}$$

The bar in (3.12) represents a 5-day running mean and primes denote deviations from that mean. Figure 3.23 shows the temporal and zonal mean eddy vorticity variance over the equatorial Indian Ocean from 60°-90°E for 00-04 day leads. The meridional profile of column MSE (solid line) and *850 hPa* zonal wind (dashed line) are also plotted for

reference. At low-levels, where moisture anomalies dominate MSE anomalies, SP-CAM has a substantial eddy activity bias relative to ERAi, with stronger eddy vorticity around 5-15°N. This implies stronger mixing across the meridional MSE gradient by synoptic eddies consistent with the MSE export in Figure 3.22. At 05-09 day leads the eddy vorticity variance bias in SP-CAM becomes even larger (Fig. 3.24). A bias of somewhat smaller latitudinal extent can also be seen south of the equator at low levels around 10°S. To put the synoptic eddy activity in context with the previous analysis, we can directly calculate the eddy component of meridional MSE advection and compare to the total meridional advection (Fig. 3.25). From this calculation we can see that the meridional eddy advection of MSE has a large export bias for situations where the total MSE tendency is negative, and we also note that this bias increases slightly with lead time (Fig. 3.25). This does not explain all of the meridional MSE advection bias, but it does show that synoptic eddies explain roughly *0.3-0.5* of the bias in Figure 3.22b. The physical reason for the enhanced synoptic eddy activity is not clear from this analysis. We conclude that the impact of horizontal advection on column MSE in SP-CAM is somewhat unrealistic, but in the opposite sense of the vertical MSE advection bias, and that this likely has consequences for the dynamics of the simulated MJO.

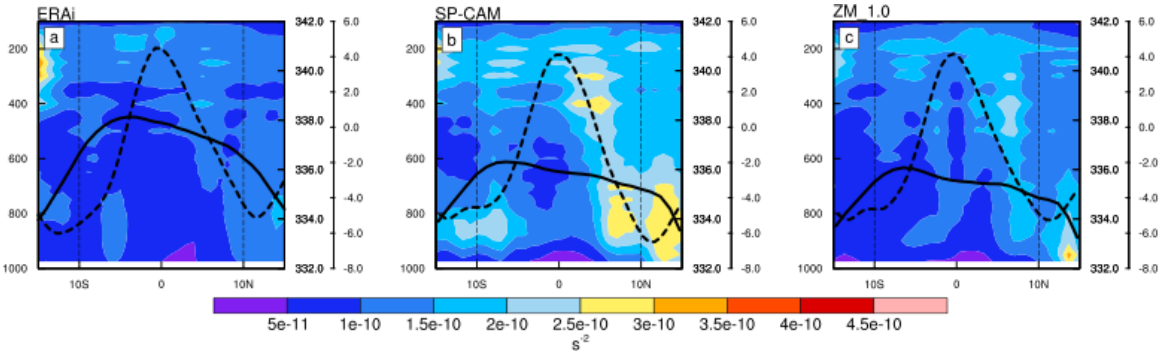

Fig. 3.23 Temporal and zonal mean eddy vorticity variance (shaded), column MSE (solid black line), and 850 hPa zonal wind (dashed) over the equatorial Indian Ocean (10°S-10°N; 60°-90°E) for 00-04 day leads. Vertical dashed lines indicate the region considered in previous MSE budget analysis.

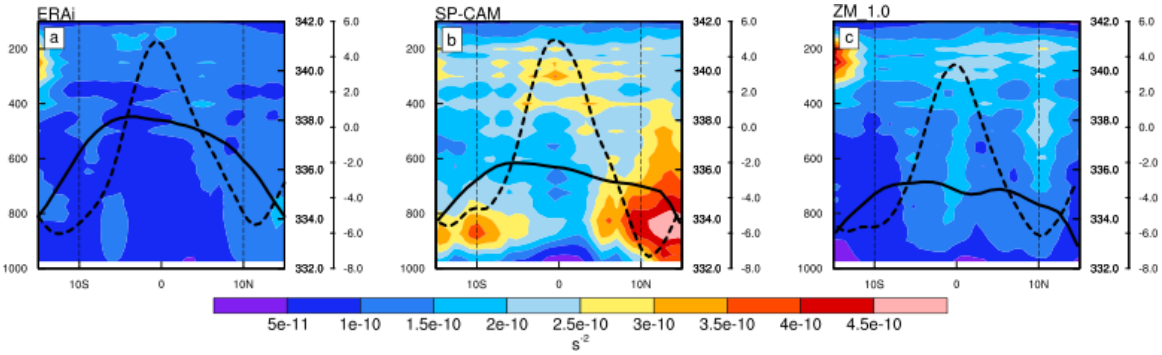

Fig. 3.24 Similar to Figure 3.23, except for 05-09 day leads.

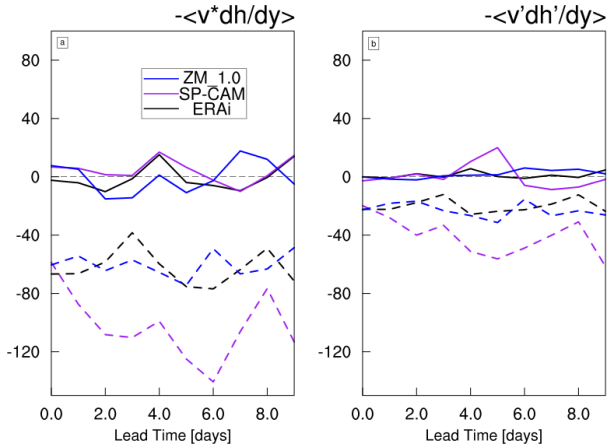

Fig. 3.25 Similar to Figure 3. 22, except for 05-09 day leads.

3.5 Gross Moist Stability and Model Drift in SP-CAM

In Section 2.5 the overly efficient moist static energy (MSE) import by vertical advection in CAM was associated with a negative vertical component of gross moist stability (GMS). In order to compare this result with SP-CAM, we will now examine the horizontal GMS (HGMS), vertical GMS (VGMS) and effective VGMS. For reference, the definitions of GMS, HGMS, VGMS, and effective VGMS are,

$$\Gamma = \frac{\left\langle -\nabla \cdot (\mathbf{v}h) \right\rangle}{\left\langle -\omega \partial_p s \right\rangle}, \tag{3.13}$$

$$\Gamma_H = \frac{\left\langle -\mathbf{v} \cdot \nabla h \right\rangle}{\left\langle -\omega \partial_p s \right\rangle}, \tag{3.14}$$

$$\Gamma_V = \frac{\left\langle -\omega \partial_p h \right\rangle}{\left\langle -\omega \partial_p s \right\rangle}, \tag{3.15}$$

$$\Gamma_{eff} = \frac{\left\langle -\omega \partial_p h \right\rangle + \langle Q_R \rangle + LHF + SHF}{\left\langle -\omega \partial_p s \right\rangle}, \tag{3.16}$$

where h is MSE and s is dry static energy (DSE), ω is the pressure velocity, $\mathbf{v}$ is the horizontal wind vector, Q_R is net radiative heating, and *LHF* and *SHF* are the surface latent and sensible heat flux, respectively.

The method for calculating GMS and its components is identical to the method described in Section 2.5, in which the numerator is first binned by the denominator. GMS is then calculated at every bin from the bin average numerator normalized by the denominator bin center value. This methods avoids any problems from normalizing by values close to zero, and also ensures no data is omitted from the calculation. The final GMS estimate is obtained by performing a weighted average of this ratio across all bins, using the frequency of occurrence as the weighting.

The distribution of denominator values used in the GMS calculation are shown in Figure 3.26 for reference. The abscissa of Figure 3.26 is inversely related to the convective activity, such that positive values represent environments with subsidence and suppressed convection, and strong negative values are associated with vigorous deep convection. The frequency of occurrence in ERAi peaks at small negative values, indicative of modest convective activity. Both SP-CAM and ZM_1.0 also peak at small negative values, but the distributions have less occurrence of modest deep convection (-700 to -200 W m^{-2}). The distribution in SP-CAM is shifted towards more suppressed conditions compared to ZM_1.0. These distributions do not seem to show any relevant sensitivity to hindcast lead time (Fig. 3.26b).

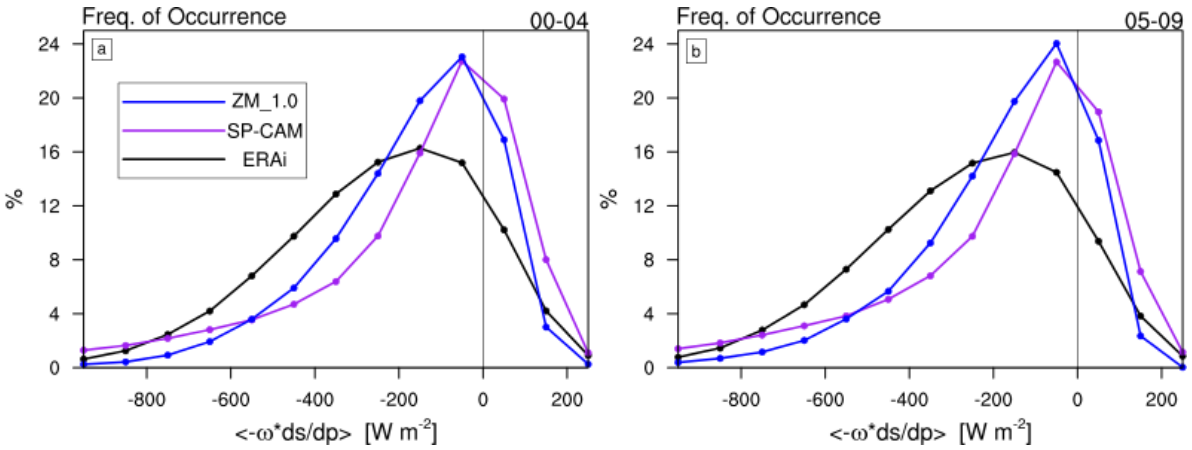

Fig. 3.26 Frequency of occurrence of column integrated vertical dry static energy advection, which is used here in the denominator of the gross moist stability to serve as a proxy of convective activity. Distributions are shown for 00-04 (a) and 05-09 (b) day lead times.

Figure 3.27 shows GMS component estimates plotted against the standard deviation of column MSE, which serves as a proxy for MJO activity. Note that the use of color is meant to distiguish the 00-04 and 05-09 day lead-time datasets. HGMS is positive in all datasets, indicating that horizontal advection tends to damp column MSE anomalies. HGMS is significantly less than ERAi in SP-CAM and significantly more than ERAi in ZM_1.0 (Fig.

3.27a). At 05-09 day leads, HGMS becomes slightly larger in SP-CAM, consistent with enhanced meridional MSE export by synoptic eddies (Fig. 3.24-3.25). The fact that HGMS is similar in SP-CAM and ERAi shows that the bias in column MSE export by meridional advection in Figure 3.20 is not of any significant consequence with respect to the models ability to support a moisture mode.

VGMS in both SP-CAM and ZM_1.0 is significantly negative at both 00-04 and 05-09 day leads, which is not consistent with the positive VGMS in ERAi (Fig. 3.27b). At 05-09 day leads, neither model shows any significant change in VGMS, consistent with Figure 3.21e. This disparity in VGMS suggests that both models are inaccurately representing the dynamics of the MJO to some degree, subject to the caveat that ERAi advection has a strong model dependence. This has serious implications for the "recharge" phase of the MJO that modelling studies of the MJO need to be aware of. Neglecting this fact could lead some to erroneously place too much emphasis on the moistening by vertical advection prior to the enhanced convective phase of the MJO in a model.

Effective VGMS at 00-04 day leads is negative in SP-CAM, and significantly more negative than ERAi (Fig. 3.27c). This indicates a strong tendency for SP-CAM to amplify a column MSE anomaly, implying that a moisture mode would be more easily destabilized than in either ZM_1.0 or ERAi. At 05-09 day leads the effective VGMS in SP-CAM becomes less negative and more in line with ERAi, whereas ZM_1.0 becomes more strongly negative and less in line with ERAi. This contrasting change with lead time cannot be explained by any drift in the vertical MSE advection, because otherwise the VGMS would change with lead time. This might also happen if the distribution of column $\left\langle -\omega \partial_p s \right\rangle$ changed, but this is not the case (see Fig. 3.26). Instead, this behavior must result from drift in the column

radiative heating and surface flux fields, but it is difficult to discern obvious systematic changes in these quantities from Figures 3.20c-d and 3.21c-d. We can better understand this behavior by examination of the column radiative heating and surface fluxes binned and normalized by $\langle -\omega \partial_p s \rangle$, similar to the method used to calculate GMS. Figure 3.28 shows the difference in these normalized quatities between 05-09 and 00-04 day lead-times, and also applies a weighting based on the frequency of occurrence (Fig. 3.26). Note that the values on the ordinate represent units of change (with lead time) in the effective VGMS. The increase in effective VGMS with lead time in SP-CAM occurs mostly from a change in radiative heating, in regimes of positive $\langle -\omega \partial_p s \rangle$ (i.e. suppressed convection and subsidence). Surface fluxes produce a similar change, but this is largely opposed by a negative contribution in the regimes of weakly negative $\langle -\omega \partial_p s \rangle$, which shows that the radiative heating change is dominant. The decrease of effective VGMS with lead time in ZM_1.0 can also be largely explained by changes in radiative heating in regimes with weak negative $\langle -\omega \partial_p s \rangle$ (i.e. weak convective activity; Fig. 3.28a). The physical interpretation of this result is simply that the systematic model drift in SP-CAM leads to enhanced convection at later lags (Fig. 3.15). This decreases the outgoing longwave radiation (Fig. 3.16), which has the biggest impact for regimes with weakly negative $\langle -\omega \partial_p s \rangle$. The result is increased net radiative heating of the column, which consequently makes the effective VGMS more strongly negative. This interpretation is also confirmed by a positive diabatic heating bias at upper levels during periods of supressed convection that increases with increasing lead time, relative to ERAi in Figure 3.31.

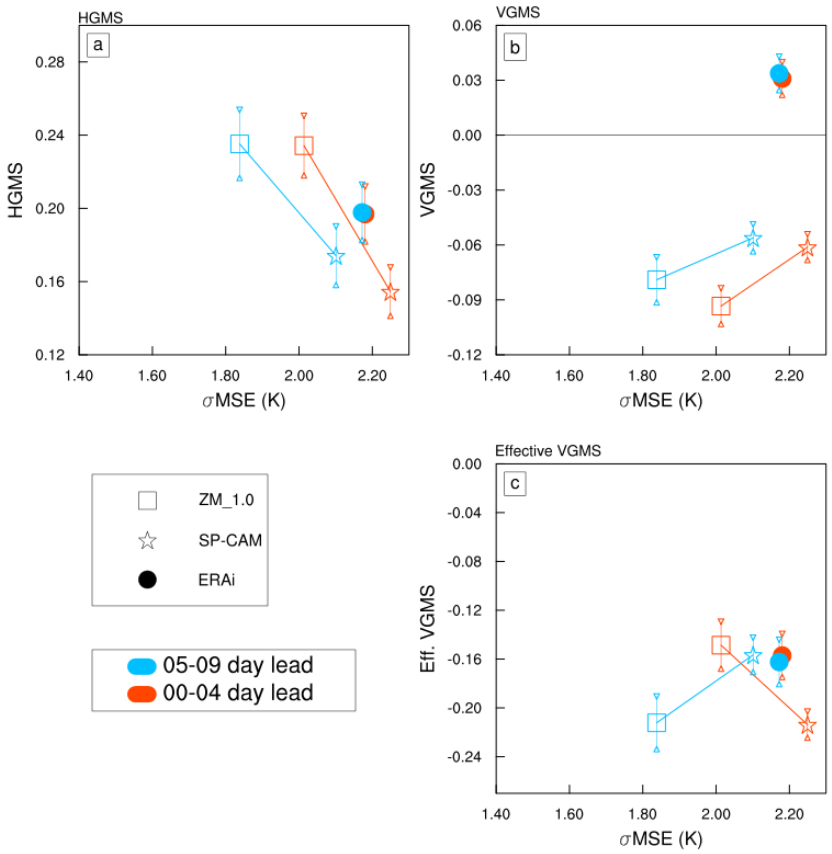

Fig. 3.27 Similar to Fig. 2.11, HGMS (a), VGMS (b) and effective VGMS (c) plotted against the standard deviation of column MSE, which gives a crude estimate of the MJO variability. Datasets are indicated by marker style and lead times are indicated by color. 95% confidence limits are calculated as described in the text.

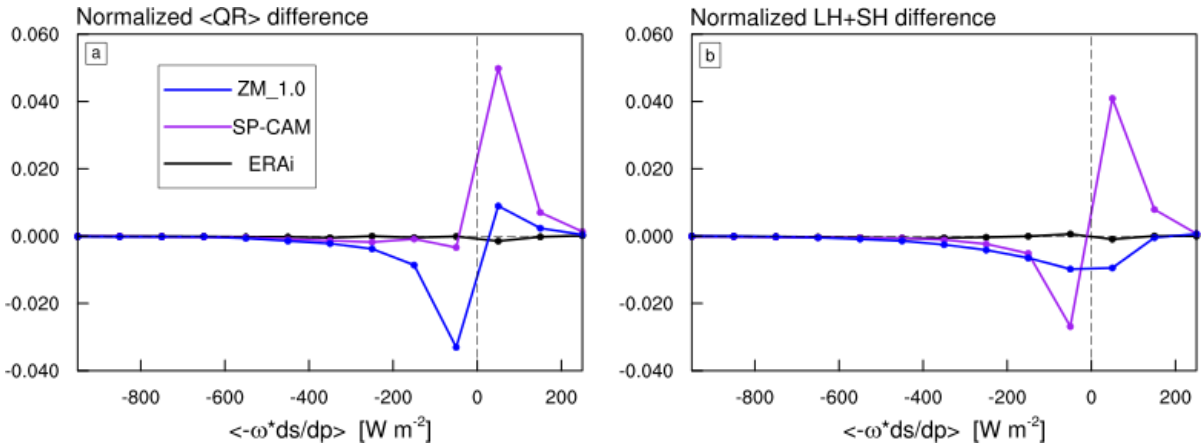

Fig. 3.28 Difference between 05-09 and 00-04 day lead times of bin-averaged contributions to effective VGMS from column radiative heating (a) and latent and sensible surface fluxes (b). To obtain units of GMS, values were normalized by the bin center values of the corresponding vertical DSE advection bins, and also weighted by the distributions in Fig. 3.26.

In Section 2.5, the derivation in (2.9) showed a way for decomposing the difference of VGMS between two datasets. The difference components are calculated at each denominator bin with the following formula,

$$\begin{aligned}\Delta\Gamma_V &= \Gamma_2 - \Gamma_1 \\ &= \frac{\left\langle -\Delta\omega\,\partial_p \overline{h_1} \right\rangle + \left\langle -\overline{\omega_1}\Delta\,\partial_p h \right\rangle + \left\langle -\Delta\omega\Delta\,\partial_p h \right\rangle}{\left\langle -\omega\,\partial_p s \right\rangle} \ . \end{aligned} \tag{3.17}$$

This tool allows us to attribute the total difference to the difference in the profiles of omega, MSE or a combination of both. This also helps to gain some physical insight into why SP-CAM has a negative VGMS that is inconsistent with ERAi. Figure 3.29 shows the difference between SP-CAM and ERAi and the three difference components of (3.17) as a function of $\left\langle -\omega\,\partial_p s \right\rangle$ for 00-04 and 05-09 day leads. All terms are normalized and weighted to show the difference in GMS contributed by each bin, similar to Figure 3.28. The analysis clearly shows that the difference in the vertical pressure velocity (i.e. omega) profile is responsible for the difference in VGMS between SP-CAM and ERAi at both 00-04 and 05-09 day leads. Interestingly, at 05-09 day leads the omega profile difference changes such that suppressed convective regimes play a more important role in the reduction of VGMS.

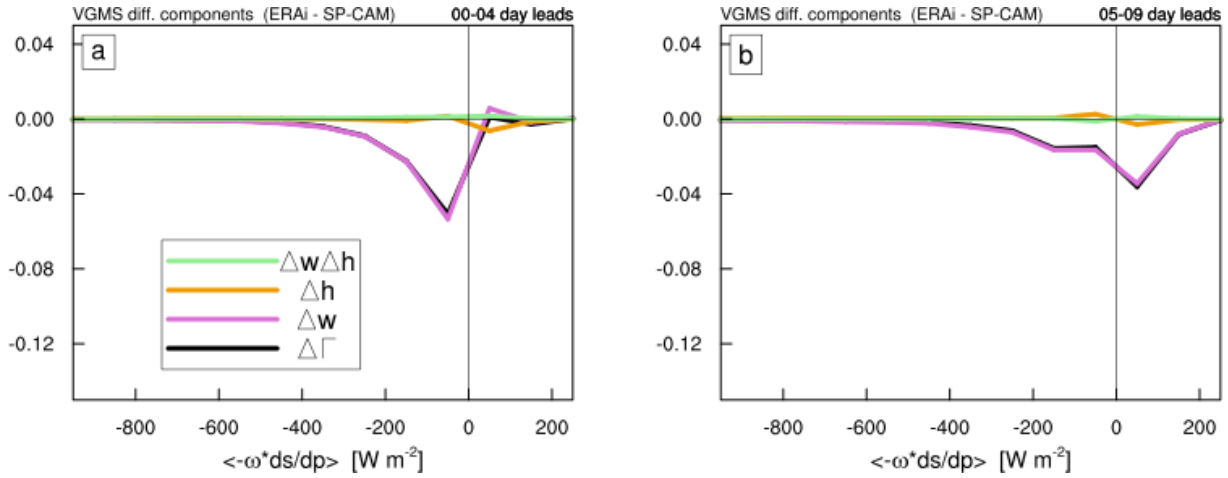

Fig. 3.29 Normalized terms of the VGMS difference decomposition (see text) describing the difference between ZM_2.0 and ERAi (a,c), and ZM_2.0 and ZM_0.2 (b,d) (see also Fig. 2.10).

To more clearly see the disparity in the omega profile that is causing the unrealistic reduction in SP-CAM VGMS, Figure 3.30 shows the difference in the binned omega profiles of SP-CAM and ERAi for 00-04 and 05-09 day leads. At all bins with negative $\langle -\omega \partial_p s \rangle$, where the difference in VGMS is the largest at 00-04 day leads (see Fig. 3.29), the omega profile in SP-CAM is more bottom-heavy than ERAi. Similar analysis of the difference in the apparent diabatic heat source (Q1; Yanai et al. 1973) shows that SP-CAM has a more shallow convective heating profile (Fig. 3.31). At 05-09 day lead times the difference patterns of omega and Q1 are similar to that of 00-04 day leads, but slightly amplified (Fig. 3.30b). This suggests enhanced high cloudiness in suppressed periods, consistent with the reduction in radiative cooling that is responsible for the increases in effective VGMS at longer leads (Fig. 3.27-3.28).

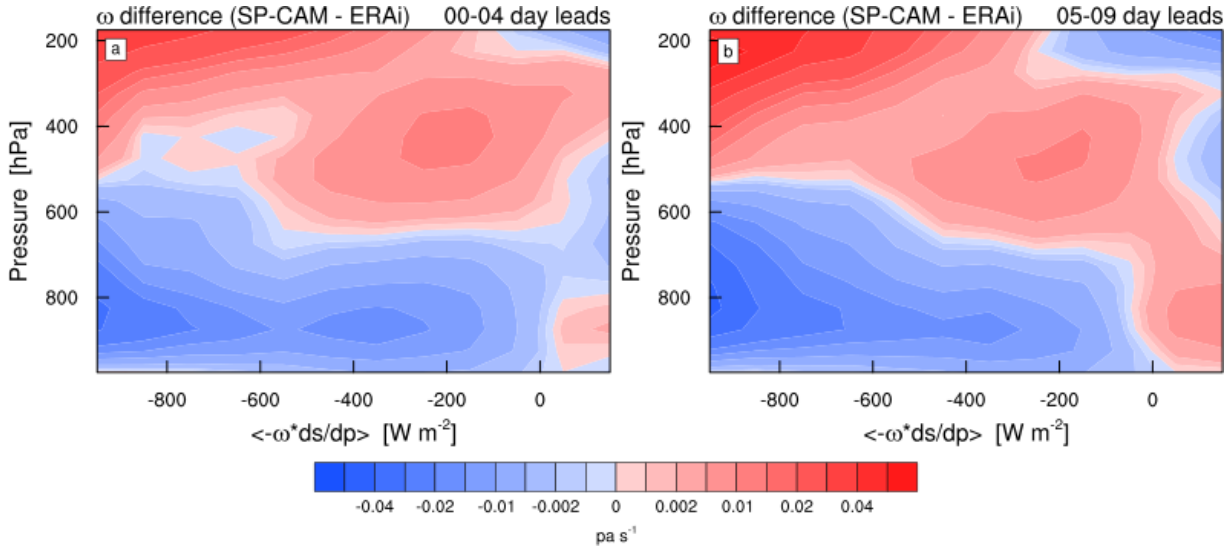

Fig. 3.30 Bin averaged profile of vertical pressure velocity as a function of vertical DSE advection. Negative (positive) vertical DSE advection generally corresponds to enhanced (suppressed) convection.

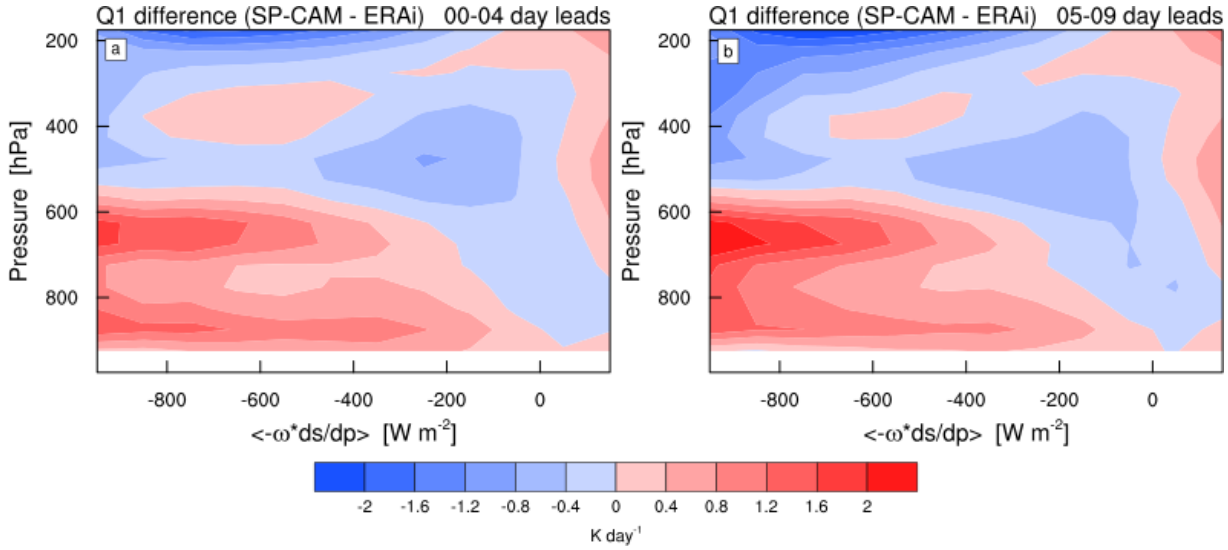

Fig. 3.31 Similar to Figure 3.30, except for the apparent diabatic heat source (Q1).

Bottom-heavy convective heating is generally understood to provide an overall moistening effect on an atmospheric column that is consistent with negative GMS (Peters and Bretherton 2006; Khouider and Majda 2006; Raymond and Fuchs 2009; Fuchs et al. 2012). Shallow convection dominates the cloud population in relatively dry environments and consequently has a low precipitation efficiency such that cloud water is evaporated

into the ambient environment and acts to moisten the column (Raymond and Torres 1998; Johnson et al. 1999; Hohenegger and Stevens 2013). These environments often have subsidence aloft, which acts to warm the upper levels. Both of these traits lead to a positive column MSE tendency by vertical circulations in shallow convective environments, consistent with negative GMS. Alternatively, an environment with stratiform convection has a bimodal vertical velocity profile of the opposite sign, and is therefore highly efficient at discharging column MSE and damping the growth of column MSE anomalies, consistent with positive GMS (Peters and Bretherton 2006). This helps to reinforce our conclusion that SP-CAM's bottom-heavy bias in the vertical profiles of omega are directly related to the strong negative bias in VGMS.

3.6 Conclusions and Discussion

In this chapter, SP-CAM hindcast simulations of the first two MJO events during the DYNAMO field campaign are characterized and compared to hindcasts with the conventional CAM5 (ZM_1.0) and ERAi reanalysis data. SP-CAM produces a better mean precipitation pattern and a more robust MJO convective signal than ZM_1.0 at both 00-04 and 05-09 day lead times. In spite of these results, RMM skill scores suggest that SP-CAM has less skill than ZM_1.0 at reproducing the observed RMM amplitude. Closer inspection shows that a systematic model drift in SP-CAM wind and outgoing longwave radiation heavily influence RMM skill scores. This RMM bias in SP-CAM is most heavily influenced by the drift of 850 hPa zonal wind, but the drift of 200 hPa zonal wind and outgoing longwave radiation fields also have an impact on RMM skill scores.

Analysis of the column MSE budget of the equatorial Indian Ocean shows that SP-CAM has stronger and more realistic cloud-radiative feedbacks than ZM_1.0 at 00-04 day leads, but shares the bias of overly efficient MSE import by vertical advection when compared to ERAi that was discussed in Chapter 2. MSE export by meridional advection in SP-CAM is larger than ERAi and becomes even larger at later lead times, associated with enhanced off-equatorial synoptic eddy activity. Inspection of the cloud-radiative feedbacks reveals a tendency for SP-CAM to have too little radiative cooling in periods of negative anomalous column MSE, associated with too much diabatic heating at upper levels in suppressed convective regimes (Fig. 3.31).

The gross moist stability is examined by separating the horizontal and vertical components, following Back and Bretherton (2006) and Raymond et al. (2009). The horizontal component of gross moist stability (HGMS) describes the export of MSE by horizontal advection per unit convective activity and is generally comparable between datasets, but slightly less positive in SP-CAM. HGMS increases with lead-time in SP-CAM to be more in line with ERAi, consistent with increased export by meridional advection (Fig 3.21). Generally, the difference in HGMS between datasets is small, and thus is not important in the context of moisture mode dynamics. The vertical component of gross moist stability (VGMS) describes the export of column MSE due to convection and divergent circulations per unit convective activity. VGMS in SP-CAM is significantly negative, similar to ZM_1.0. Both models disagree with ERAi in this respect, which has a weak positive VGMS. This difference is quantifiably attributed to more bottom-heavy omega and diabatic heating profiles in SP-CAM.

VGMS can be modified to obtain an effective VGMS, which is thought to be more relevant to the observed MJO, by including the influence of column MSE source terms. Negative effective VGMS implies a positive feedback between the column MSE anomaly and the combined effects of convection, divergent circulations and MSE sources. This positive feedback is necessary for building up column moisture on a large scale, which can destabilize a moisture mode. Effective VGMS is significantly negative in both models and ERAi, but slightly more negative in SP-CAM. Effective VGMS exhibits an interesting sensitivity to hindcast lead-time by becoming less negative in SP-CAM and more negative in ZM_1.0, mostly due to a change in the column radiative heating in subsidence regimes, likely associated with the presence of high clouds (Fig. 3.28). Overall, we conclude from the strong negative effective VGMS that moisture modes can be destabilized in all three cases, but the differences in model physics with respect to ERAi in the context of the MJO are better understood from the analysis of the VGMS.

The underlying motivation for this work is to address the long-standing question of "what is the MJO?" The current and previous chapters addressed a slightly different version of the same question, by trying to identify what factors are responsible for a successful or unsuccessful reproduction of observed MJO events in a global atmospheric model. This study is limited in answering these questions because the intensive observation period of DYNAMO only witnessed two distinct events. There is the additional caveat that we are comparing models to a reanalysis product that is heavily influenced by a model. This leaves us to speculate on how well our results relate to other events in the real atmosphere that do not have in-situ observations. Therefore, in order to work within the confines of lacking data, the analysis here was designed to diagnose aspects of large-scale moist dynamics that

previous theoretical work has suggested to be relevant to the basic nature of the MJO. The conclusions gained through this approach support the hypothesis that the MJO is fundamentally a moisture mode.

The findings here are useful for understanding model shortcomings, and can be abridged into two main conclusions. The first being that systematic drift of MJO hindcast experiments can greatly obscure the interpretation of results, through the distortion of RMM skill scores. This highlights one of several weaknesses of the RMM index that have been discussed by recent studies (Straub 2013; Kiladis et al. 2014). The second conclusion is that SP-CAM and CAM5 represent the interaction between convection and large-scale dynamics in a somewhat different way than suggested by ERAi.

A natural follow-up questions is "Where do we go from here?" This study did not reveal any clear way that the either model should be modified so that the VGMS is reconciled with ERAi. However, our results suggest that the treatment of convection in both models is a candidate. This is not a new conclusion for a parameterized model, as convective parameterizations are often blamed for inadequate model performance. It is somewhat more novel to think about why the MSE budget may differ between ERAi and SP-CAM, which is known to have one of the best representations of the MJO when compared to state-of-the-art parameterized global models.

SP-CAM offers endless possibilities for modifying the embedded CRM to test how factors of the convective-scale physics affect large-scale phenomena, but what factors should be tested? One possibility motivated from the bottom-heavy bias in diabatic heating is that the geometry of the CRM may affect the diabatic heating profiles. Repeating the analysis on SP-CAM hindcasts using a 3D CRM would be one interesting avenue of research,

since modeling clouds in two dimensions has been shown to be less realistic in previous studies (Grabowski et al. 1998; Tompkins 2000; Khairoutdinov and Randall 2003). Another possibility is that the aspect ratio of the CRM could be changed. The CRM grid of the current study used 28 vertical levels and 4km horizontal grid spacing. This would be inadequate for studying tropical maritime convection in a standalone CRM model, because this type of convection has been observed to be on the order of 1km wide (LeMone and Zipser 1980; Williams et al. 1992; Rickenbach and Rutledge 1998; Igel and van den Heever 2014). Repeating our analysis with a CRM of higher resolution would likely provide interesting results, and might improve the bottom heavy omega bias and address the negative VGMS bias relative to ERAi.

CHAPTER 4 ENTRAINMENT AND DILUTION IN TROPICAL DEEP CONVECTION

Besides learning to see,
there is another art to be learned
-- not to see what is not.

- Maria Mitchell

4.1 Introduction

In Chapter 2 it was shown that increasing an entrainment rate parameter in the Community Atmosphere Model version 5 (CAM5) effectively suppressed convection by making it more sensitive to environmental humidity and improved the simulation of the Madden-Julian Oscillation (MJO) events during the DYNAMO field campaign. However, the improved simulation was achieved through an inaccurate partitioning of moist static energy (MSE) budget terms. The model with a low entrainment rate exhibited convection that was too easily triggered and was not able to reproduce the relatively dry periods of the MJO, which are characterized by suppressed precipitation. Simply increasing the entrainment rate fundamentally changed how divergent circulations influenced the column MSE in a way that is inconsistent with observations. This highlights a paradox in our understanding of processes that control entrainment in deep convection that was recognized in early modeling studies of convection (Warner 1972), and also has been discussed by several more recent studies (Romps 2010; Dawe and Austin 2011b; Sherwood et al. 2013). The entrainment paradox can be summarized by two mutually exclusive ideas:

1. There is strong evidence that cumulus convection does not form without dilution. Therefore, entrainment has a lower limit that conceptual models should reproduce.
2. Coercing entrainment to be larger in parameterized convection often results in undesirable effects, most notably a degradation of the model's mean state.

The issues and uncertainty surrounding simple cloud models is not a new problem. Entrainment is thought to be a central limiting factor on the height and intensity of deep convection, since this allows the cloud to be affected by the conditions of the relatively dry ambient environment (Derbyshire et al. 2004; Del Genio 2012). Attempts to constrain bulk entrainment relationships have often concluded that no single bulk entrainment rate in a parcel model could simultaneously predict cloud height, water content and tracer concentrations (Warner 1970; Betts 1982; Romps 2010). Several studies have identified similar problems in global models that appear to stem from the parameterization of deep convection. One such problem is that too many clouds penetrate into the upper troposphere, while too few clouds are found at lower levels (Chepfer et al. 2008; Del Genio 2012). Zhang et al. (2010) showed that increasing the entrainment rate of deep convection affected the cloud height distribution in a global model, by reducing the frequency of the highest clouds. However, this did not affect the overall frequency of precipitating convection, which remained higher than observations.

The cloud height is not the only important cloud property affected by increasing the entrainment. An equally important aspect of deep convection is the vertical mass-flux, because it is important for determining how cloud populations feedback onto the large-scale thermodynamics (Arakawa and Schubert 1974). The cloud mass flux in simple plume models of moist convection is directly tied to mixing process, such that entrainment increases it and detrainment decreases it. Thus, forcing entrainment to be larger in an entraining plume model may also inadvertently change the profile of convective heating in unrealistic ways.

Before going further, it is useful to provide a specific definition of entrainment and detrainment. Romps (2010) gives a general definition that centers around the transition of a volume of air from "non-cloud" to "cloud". Since the use of "cloud" air is somewhat ambiguous, we can refer to "non-active" and "active" air instead, to maintain generality. Following Romps (2010), entrainment is defined as the transition of a volume of non-active air to active air. Similarly, detrainment is defined when a volume of active air becomes non-active. This definition of entrainment hinges on what we define as "active", which depends on what we are interested in studying. In this way entrainment is a flexible concept in the study of general fluid dynamics, and can be applied to a wide range of problems. For moist convection, we may want active air to represent the whole cloud, which is a volume of saturated air, or we may be specifically interested in the cloud updraft, which is the part of the cloud that is moving upward due to buoyancy acceleration. This choice can have large consequences for the resulting spatial distribution of entrainment and detrainment. If we define active air based on the updraft, then the formation of an anvil cloud at the top of a deep thunderstorm would be considered detrainment, whereas if we only define active air based on a saturation criterion, the anvil would not be associated with detrainment. We could similarly study the entrainment of a dry thermal, but we need to know what property of the thermal should be used to define it. In this case, properties that relate to buoyancy or momentum would be appropriate choices for defining the "active" air.

A stricter definition of entrainment that is possibly more relevant to the study of deep moist convection would be the incorporation of non-turbulent environmental fluid into a current of turbulent fluid (e.g. Morton et al. 1956; Bretherton 1997). Using such a definition for cumulus clouds, a boundary might be defined between the turbulent flow in

the updraft and the non-turbulent environment (Bretherton 1997). Later in this chapter, a cloud "core" consisting of saturated and positively buoyant air is used to define a volume for which air can be entrained or detrained. Defining such a boundary might be considered generally compatible with the stricter definition of entrainment stated above, with some exceptions. Less compatibility between these definitions occurs near cloud base where a cloud forms from turbulent air that becomes saturated, and also near cloud top where overshooting clouds have negative buoyancy.

Laboratory studies of buoyant thermals have been the cornerstone for developing conceptual models of moist convection. These studies have shown that mixing occurs at the leading edge and wake of a buoyant thermal due to a vortical ring or toroidal circulation (Woodward 1959; Scorer 1957; Johari 1992). These studies also show that thermals often shed mass in the wake (Scorer and Ronne 1956), leading to the development of the "shedding thermal" model (Blyth et al. 1988). The presence of this toroidal circulation that accompanies the ascending thermal is somewhat supported by observational studies of isolated clouds (Jonas 1990; Stith 1992; Damiani et al. 2006).

A concept garnered from laboratory studies still used in many cloud models today is that entrainment is inversely related to cloud radius. The thinking is that a wider cloud effectively produces a larger buffer between the cloud core and the ambient environment. One problem with this idea is that it appears to be more about "dilution" of a cloud, rather than the amount of mass being entrained into the cloud, which may dilute the cloud at various rates depending on the properties of the entrained air. Laboratory experiments provide a valuable tool, but they are limited in how well they can reproduce thermals that are analogous to deep moist convection in the real atmosphere. This is because

atmospheric convection differs from laboratory thermals in several ways. The important differences can be characterized by (1) phase changes of water that can increase or decrease buoyancy (Narasimha et al. 2011), (2) sub-cloud layer turbulence that can influence initial thermal kinematics (Romps and Kuang 2010b), (3) vertically varying stratification, and (4) large Reynolds numbers characteristic of very turbulent flow that can not be reproduced in a laboratory.

Very few studies have tried to estimate entrainment from observations (Sloss 1967a; McCarthy 1974a; Lu et al. 2012b), but a frequent problem with these approaches is that detrainment is ignored. An accurate expression of the mass budget of a cloud or population of clouds, ignoring changes in cloud area, would be

$$\frac{\partial M}{\partial z} = E - D, \tag{4.18}$$

where M is the cloud mass flux, E and D are the total entrainment and detrainment rates, respectively. Many studies assume that detrainment is zero except at cloud top, so that entrainment can be easily estimated from measuring changes in cloud mass with height (Lu et al. 2012c),

$$\frac{\partial M}{\partial z} = E. \tag{4.19}$$

Similar assumptions have been used with thermodynamic measurements (McCarthy 1974a). As we will see, this assumption of negligible detrainment is a very poor assumption, and would lead to an underestimation of the actual entrainment. However, it is easy to see why this is an attractive simplification, as it makes estimating the entrainment from observations straightforward and simplifies convective parameterizations.

Recent advances in computing power have allowed detailed investigations of turbulent circulations within individual clouds, which have changed how entrainment

processes can be studied. These so-called cloud resolving models (CRM) can be run with very fine resolution, allowing detailed examinations of small-scale interfacial mixing that are difficult to measure in observations or laboratory studies (Klaassen and Clark 1985; Grabowski and Clark 1993). These studies generally find that entrainment is dominated by toroidal circulations (Zhao and Austin 1998; Sherwood et al. 2013), which is consistent with laboratory studies. The majority of these studies are limited to simulating shallow cumulus convection, so more detailed investigations of entrainment processes in deep convection are needed.

CRMs have also been used as a tool to look at entrainment processes from a bulk statistical perspective. Del Genio and Wu (2010) simulated the diurnal cycle of convection over a large area and compared the entrainment rates to various theoretical formulations of entrainment. They found that the necessary parameter values needed to predict the entrainment of the cloud ensemble were highly variable in height and time as convection developed. This and other studies have concluded that entrainment in deep convection might be more accurately parameterized as dependent on the time varying kinematic and thermodynamic properties of the parcel and the surrounding environment (Cohen 2000; Lin 1999). Recent parameterization development efforts have worked to build in these relationships into new schemes with some success (Bechtold et al. 2008; Chikira and Sugiyama 2010). The recent study of Sherwood et al. (2013) presented a novel approach to developing a simple cloud model that includes the effects of a toroidal circulation pattern around the thermal that has been identified in past studies. The new model uses the concept of a Hill vortex (Hill 1894), which is an exact solution of the Navier-Stokes equations that resembles a buoyant spherical bubble with a toroidal circulation. The Hill

vortex circulation is unique because it allows a thermal to move through an ambient fluid with no friction. This new approach led to a much better prediction of cloud properties using much higher entrainment rates than conventional models (Sherwood et al. 2013).

Convective parameterizations used in global models often ignore the mesoscale organization of convection (Moncrieff 1992; Moncrieff and Liu 2006; Moncrieff 2010). In essence, traditional convective parameterizations aim to represent a group of random, unorganized, and non-interacting clouds (Arakawa 2004). This population of unorganized convective elements evolves in a homogeneous grid-cell average environment in order to fulfill the functional need of heating and drying the column (Lord 1982). Organized convection is unique in that it provides a positive feedback on the cloud population to promote further convection (Mapes 1993; Mapes and Neale 2011). This property of organized systems allows them to persist longer than isolated cumulus clouds. It has been hypothesized that convection within a mesoscale convective system is less dilute due to enhanced buffering of the cloud updrafts from the detrimental effects of dry air entrainment (Mapes and Neale 2011). However, this is a difficult hypothesis to test, partly because organized convective systems cannot be modeled using the simple theories used in plume and thermal models of isolated deep convection. This has also not been thoroughly investigated due to the difficulty of estimating the entrainment rate, and the lack of suitable experiment control.

Some studies suggest that the root of the entrainment paradox lies in the degree of heterogeneity within deep convection. More heterogeneity would imply that various quantities are not affected equally by a given amount of mixing between a cloud and the ambient environment due to the horizontal gradients across the cloud "shell" (Dawe and

Austin 2011a; Sherwood et al. 2013). To illustrate this problem, consider a scenario where a cloud is entraining air laterally, but the total water of the entrained air is similar to that in the core of the cloud, due to the evaporated cloud droplets at the periphery. If we infer the entrained mass of air from the effective dilution of the total water in the core of the cloud, we would be substantially underestimating the actual mass entrainment. Thus, our understanding of entrainment processes can be grossly obscured depending on what fields we chose to focus our analysis and how well we understand the path that the entrained air takes to become part of the cloud. This presents a problem for convective parameterization, because it relies on our conceptual understanding of bulk entrainment processes. This problem is circumvented by super-parameterization, but as was shown in Chapter 3, this does not necessarily produce the most accurate representation of the interaction between convective and large-scale processes in MJO hindcasts.

Entrainment is often discussed in a way that implies it is synonymous with dilution. Most convective parameterizations are formulated such that this is always the case. In reality, this notion reflects an inconsistency in how entrainment is defined. A rigorous and quantifiable definition of dilution in the context of convection is lacking in the current atmospheric science literature. The word "dilution" is often invoked in a qualitative way, and loosely associated with mixing and entrainment. A formal definition of dilution that would allow it to be quantified would need to be specific to a certain variable. "Dilution of a cloud" does not provide any measurable quantity or scientific value. However, "dilution of buoyancy" provides something that can be quantified. Almost any quantity that we use for this definition will not be conserved, especially on the scale of a single convective thermal. So, it is also necessary to associate the dilution of a quantity with a process that is

responsible for the dilution. For example, “dilution of buoyancy by entrainment” would be a useful quantity to compare among cloud types or environmental conditions in order to gain better physical understanding of entrainment processes.

Two methods of directly measuring entrainment in cloud resolving models were recently developed to address this issues surrounding the estimation of entrainment rates in numerical models (Romps 2010; Dawe and Austin 2011b). These methods differ in how they employ interpolation to determine entrainment, but the underlying concept is the same in that they both determine when a volume of air transitions from being defined as non-cloudy to cloudy, or non-active to active. The method of Romps (2010) uses temporal interpolation to determine when the entire volume of a model grid cell becomes active. Alternatively, the method of Dawe and Austin (2011b) uses spatial interpolation to quantify how much air has become active at any given time. This is an advantage over the Romps method, in which a grid cell must be completely entrained before the entrainment amount is estimated, which can take several time steps. Both methods take special care to ensure that if the interface of an existing cloud is simply advected through a grid cell, then it will not be considered entrainment.

The purpose of this chapter is to investigate entrainment processes in deep tropical maritime convection in order to present a refined conceptual model that can be used to improve parameterizations in large-scale models. This will be accomplished by comparing idealized simulations of individual deep convective clouds that form from the release of a warm, humid bubble. This approach allows convection to be investigated in a systematic way, which is difficult to achieve in more realistic simulations of a cloud population. However, we would also like to put our results in the context of realistic convection, and so

we also perform a more realistic simulation forced with data from the enhanced convective period of the October MJO event during the DYNAMO field campaign. All simulations will take advantage of the Dawe and Austin (2011b) method for estimating entrainment and detrainment rates. Section 2 outlines the methods and data used for this study. Section 3 presents a comparison of the simulated clouds, which is followed by a detailed analysis of entrainment and detrainment rates in Section 4. Section 5 provides a quantifiable definition of dilution, and explores the relationship between dilution and entrainment. Sensitivity experiments are explored in Section 6 to test specific ideas about entrainment and dilution in the presence of enhanced humidity and convective organization. Conclusions and discussions are presented in Section 7, which outline a conceptual picture of entrainment processes in deep tropical convection based on the results.

4.2 Methodology

4.2.1 The Cloud Resolving Model

The model used for these experiments is the System for Atmospheric Modeling (SAM; Khairoutdinov and Randall 2003) version 6.9.5, which solves the anelastic system of momentum equations. Thermodynamic energy is prognosed with the liquid/ice water static energy,

$$\theta_l = c_p T + gz - L_v q_v - L_f q_i, \tag{4.1}$$

which is conserved for all adiabatic processes and water phase transitions, but not gravitational sedimentation. The distribution of water is described by two prognostic variables for precipitating (rain, snow and graupel) and non-precipitating (vapor, cloud water and cloud ice) water mixing ratios. The use of these composite prognostic water

variables was justified on the basis of computational efficiency (Khairoutdinov and Randall 2006). Sub-grid scale turbulent fluxes are parameterized with a Smagorinsky-type closure. All simulations presented here are configured with periodic lateral boundary conditions and Newtonian damping in the top 3 layers to reduce gravity wave reflection. To be sure that the upper boundary condition does not influence our results, the model top is set near *25 km*, well above the terminating level of deep convection. The grid spacing is set to *200 m* in all directions.

4.2.2 Experiment Setup

In order to analyze the entrainment in deep convection in the Tropical atmosphere we would like to simulate clouds in a generic Tropical environment. To do this, European Center for Medium Range Forecasting (ECMWF) interim reanalysis (ERAi) data is averaged over all longitudes of the tropical belt covering 10°S to 10°N for the ten year period from 2000-2009. Simulations are initialized with this sounding of temperature and humidity (see Fig 4.1) and no horizontal wind or other large-scale forcing. The initial sounding has a moderate amount of convective available potential energy (*785 J*). The surface temperature is set at *300.5 K* and surface sensible and latent heat fluxes are specified as *10 W* m^{-2} and *90 W* m^{-2} respectively. This approach has a slight disadvantage in that these conditions do not reflect any certain tropical region that one may be specifically interested in. However, we do not feel that this problem alters the general results regarding entrainment and dilution in tropical convection.

To initiate deep convection, a Gaussian bubble is added to the initial condition at the center of the domain with a temperature perturbation of 1K and specific humidity perturbation of *3 g* kg^{-1}. These full perturbation values are realized at the center of the

bubble and then decrease toward the edge of the bubble, according to a Gaussian distribution. This feathering helps to reduce the dispersive effect of gravity waves on the initial temperature perturbation. The center of the bubble is set at an altitude of *500 m*, and the vertical radius is *1500 m*, so that the top of the bubble reaches to *2 km* and a portion of the bubble is underground. Given this geometry of the bubble, it be more accurate to refer to it as a "pancake", rather than a spherical bubble. A small white noise perturbation is also added to the initial temperature field so the resulting clouds have some initial turbulence. For each case the model is integrated for 60 minutes to capture the lifecycle of the resulting convection.

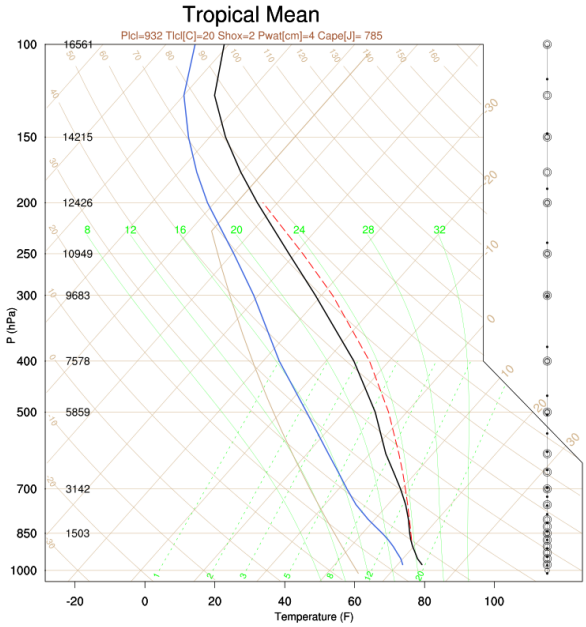

Fig. 4.1 Skew-T diagram of the initial sounding used for the control simulations, calculated from ten years of ERAi data (2000-2009).

For the results of these idealized experiments to be useful they need to be contextualized against more realistic convection that is not artificially triggered. To this end we also will present results from a large-domain simulations of the enhanced convective phase of the October 2011 MJO during the DYNAMO field campaign. The specific

period of 28 October through 02 November, 2011 was used to calculate average initial conditions and forcing, which is during the convectively active phase of the MJO event (Johnson and Ciesielski 2013). Figure 4.2 shows the initial sounding used for the idealized DYNAMO simulations. The saturated values at the top of the troposphere reflect widespread cirrus clouds from detrainment of large convective systems. This is a consequence of choosing a period from the peak active phase of the October MJO event. We will only present results from 24-32 hours of the DYNAMO simulation, for which there is not cirrus layer in the upper troposphere, and so we do not feel that the saturated part of the initial sounding is of much consequence for the simulation of deep convection. The DYNAMO simulation is forced with horizontal advective tendencies and sea surface temperature derived from the northern sounding array (Johnson and Ciesielski 2013). Large-scale vertical velocity from the sounding array is also used, which vertically advects the domain mean quantities of the model. Interactive surface fluxes and radiation (both shortwave and longwave) are computed by the model, with a diurnal cycle of shortwave radiation. The large-scale horizontal wind was prescribed to be $5\ m\ s^{-1}$ throughout the column. This was done to avoid the affects of vertical wind shear when comparing to the bubble simulations. Section 4.6 investigates some sensitivity experiments, which include a separate DYNAMO simulation with realistic vertical wind shear.

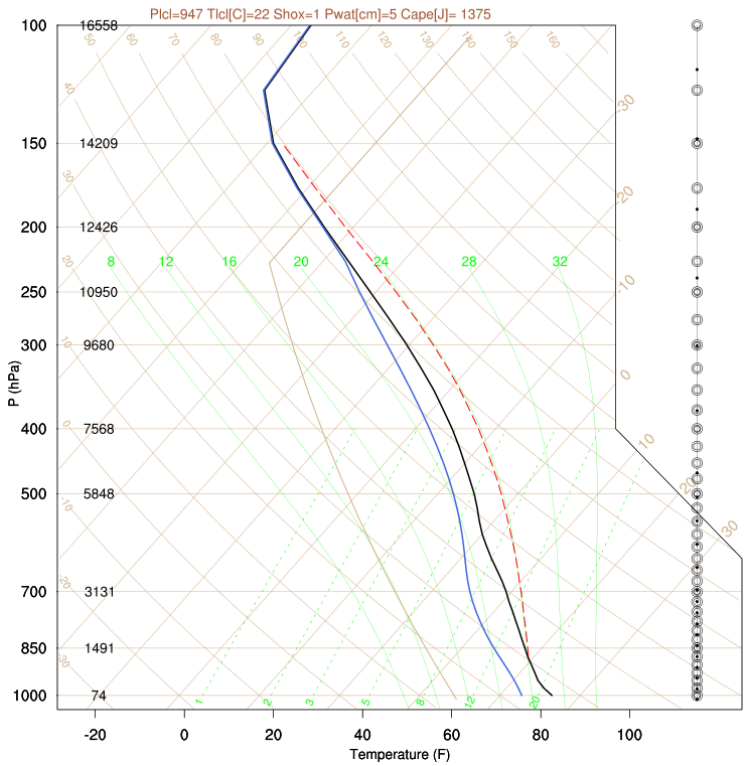

Fig. 4.2 Skew-T diagram of the idealized sounding used for the DYNAMO simulation, calculated from data for the northern DYNAMO sounding array (~0°-7°N; 70°-80°E) during 28 October through 02 November, 2011.

Many studies have shown that a very fine grid spacing of *100 m* or smaller is needed to fully resolve the inertial sub-range where turbulent entrainment processes occur (Bryan 2003). However, the necessary simulations for exploring entrainment processes need to be balanced with the capabilities of available computational resources. Various sensitivity experiments were performed that suggested a grid spacing of *200 m* was a satisfactory compromise. This resolution allows reasonable simulations of large domains of *~100 km* that can support a diverse population of deep convection, as well as organized convective systems, and also resolves much of the fine-scale turbulent entrainment in deep convection. The sensitivity of direct entrainment calculations to horizontal grid spacing was investigated, and it was found that entrainment showed no qualitative sensitivity for grid spacing between *100-500 m* for the same domain size and forcing (not shown).

Quantitative values of entrainment are somewhat sensitive to horizontal resolution, however for the purpose of this study the compromise of a *200 m* grid mesh is adequate.

4.2.3 Lagrangian Parcel Tracking

Many of the outstanding questions surrounding entrainment processes are about the origin of entrained air and the evolution of such air before and after entrainment. In order to make a detailed characterization of the flow structure and address these questions, a Lagrangian parcel tracker (LPT) module was implemented into the model (Yamaguchi and Randall 2012). A fifth-order Lagrangian polynomial interpolation scheme (Leonard 1991) is used to determine the values of scalar variables at the parcel positions. This will allow us to determine when air is entrained multiple times. Due to computational limitations, we are not able to use the number of particles necessary to determine entrainment rates, as was done by Yeo and Romps (2013).

4.2.4 Effective Radius Estimation

Previous studies have often relied on an the assumption that entrainment processes are strongly related to the horizontal size of a cloud. Revisiting this assumption will be a central element of this study, and so the method of estimating the horizontal footprint of a cloud or cloud core is important to document. The method of Khairoutdinov and Randall (2006) is adapted and used here for the purposes of this study. The basic algorithm is illustrated in Figure 4.3.

The first step of the cloud size algorithm is to determine the feature of interest. This is a trivial task for bubble simulations, in which a single cloud is initialized in the center of the domain. For a large domain with many clouds, determining the features of interest can be quite difficult and computationally expensive, and also require many subjective choices.

For the DYNAMO simulation this is done by identifying all local maxima of the cloud or cloud core field at a given time and altitude, and randomly selecting *50* of them to analyze. By providing a cutoff is this manner we can gain sufficient sampling of the cloud population, while minimizing the time it would take to loop through all cloud objects, which can include thousands of small elements at any given time.

After the feature is located at a given vertical level, a rough estimate of the center of the grid points that define the feature is located. From that center pixel we measure the outward radial distance r_i to the edge of the feature along a number of vectors, spaced at equal angles around the centroid. In practice, eight radial measurements is found to be sufficient. The effective cloud radius R is then calculated as the geometric mean of these measurements,

$$R = \sqrt{\frac{1}{8}\sum_{i=1}^{i=8} r_i^2} \,. \qquad (4.2)$$

Khairoutdinov and Randall (2006) note that for the case of a circular cloud feature, finding the centroid is not necessary because the calculation is insensitive to the starting point. They also mention that this algorithm may misrepresent the size of very elongated clouds, but this caveat should not influence the results presented here.

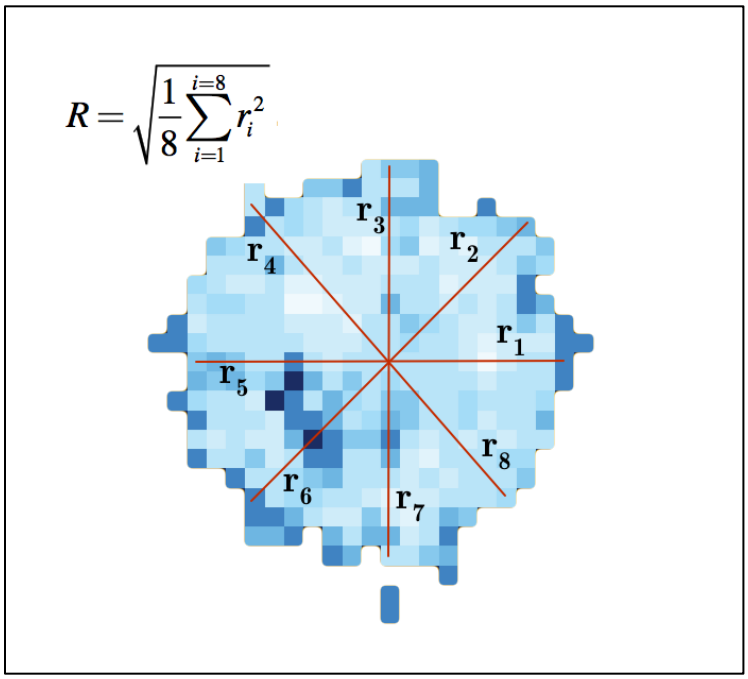

Fig. 4.3 Schematic illustration of the algorithm used to determine the effective cloud radius of a cloud cross section in a bubble release simulation.

4.3 Simulation Results

4.3.1 Cloud Comparison

Before we examine the entrainment and detrainment, it is useful to characterize the basic nature of the simulated clouds that result from the release of a warm, humid bubble in average tropical conditions. Figure 4.4 shows the time vs. height evolution of horizontally averaged mixing ratio of cloud condensate and precipitating condensate for the five control simulations. Clouds with initial bubble radii of *2 km* or greater produce a deep cumulus cloud that tops out above the mid troposphere and produces modest precipitation rates equivalent to *4-8 mm day*$^{-1}$.

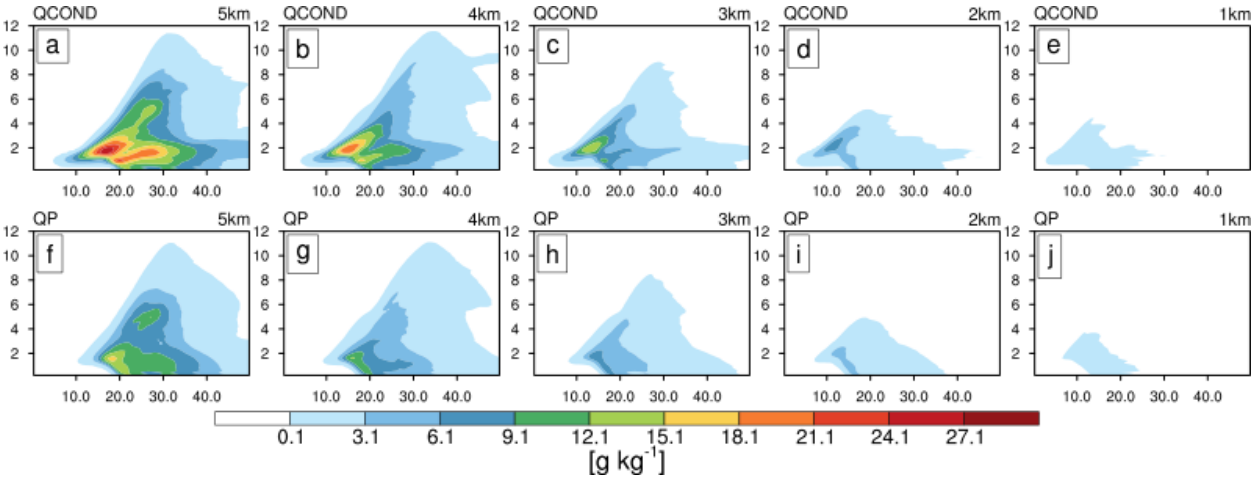

Fig. 4.4 Time vs. height evolution of cloud condensate (top) and precipitating condensate (bottom) for the control bubble simulations. The abscissa is time in units of minutes.

It is useful to distinguish between the regions of saturated air (i.e. the cloud) and regions within the cloud that constitute a positively buoyant updraft (i.e. the core). Note these regions overlap by definition, so that a data point that is in a core, is also in a cloud. When we wish to distinguish regions that are in a cloud and not in a core, these will be referred to as a the "shell". Figure 4.5 shows the dimensionless area fraction for the core and cloud regions of the control simulations. The area of the core is smaller than the cloud in all simulations, as expected. The cloud fraction also shows that cloud points extend to higher altitudes than the core. This indicates that the clouds overshoot their level of neutral buoyancy, which makes the core area go to zero since the core is defined as being positively buoyant. If we had alternatively defined the core based only on criteria of saturation and vertical velocity, the final height of the core would most likely be the same as the cloud.

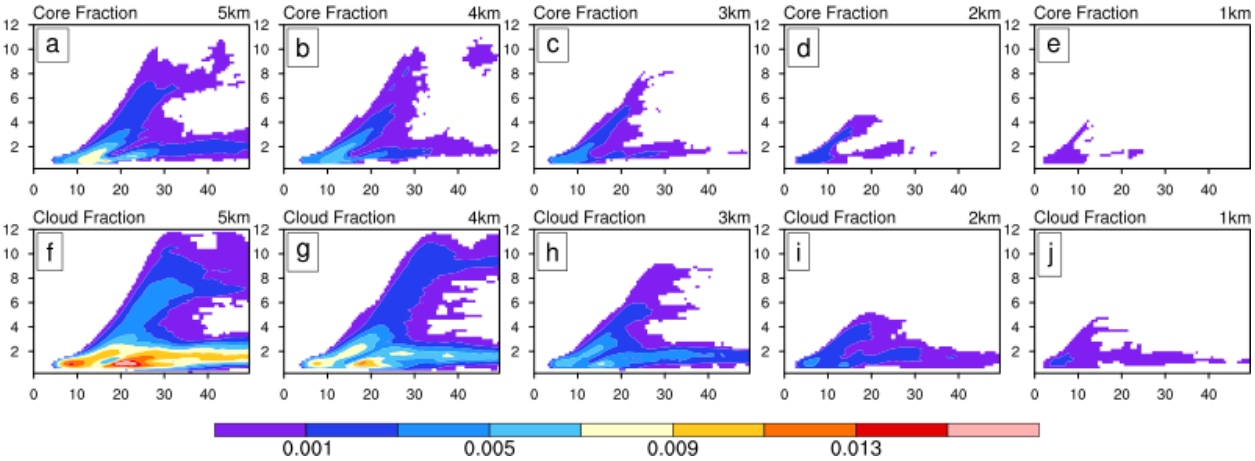

Fig. 4.5 Time vs. height evolution of the domain area fraction for the cloud core (top) and cloud (bottom) for the control bubble simulations. The abscissa is time in units of minutes.

Buoyancy is an important variable for convective parameterization, and plays a large role in determining the terminal height of a cloud. For our purposes we define buoyancy simply as,

$$B = \frac{T_v - \overline{T_v}}{\overline{T_v}}, \tag{4.3}$$

where $T_v = T\left(1 + 0.61 r_v\right)$ is the virtual temperature, T is temperature, and r_v is the water vapor mixing ratio. Horizontally averaged core and cloud buoyancy are plotted in Figure 4.6 for the control simulations. Core buoyancy is always positive by definition, and does not exhibit much change in peak amplitude for bubble radii greater than *2 km* (Fig. 4.6a-e). This is somewhat expected because all bubbles in the control simulations have the same temperature and moisture perturbation. However, we might expect the peak buoyancy to be greater for a wider cloud, due to less dilution of buoyancy by entrainment.

Cloud buoyancy exhibits regions of strong negative buoyancy, mostly in the wake of the cloud (Fig. 4.6f-j). A thin layer of negative buoyancy can be seen at the leading edge of the cloud, slightly above the leading edge of the cloud core. This suggests that evaporative cooling at cloud top is playing a role in the turbulent circulations of the thermal, which

some have suggested may lead to cloud top entrainment (Deardorff 1980; Stith 1992; Salzen and McFarlane 2002). Cloud buoyancy is negative at the maximum height of the cloud, indicating that the cloud has overshot it's level of neutral buoyancy. The cloud are shown to overshoot the neutral buoyancy level by a substantial amount of roughly *~2 km*, which is generally not captured by convective parameterizations.

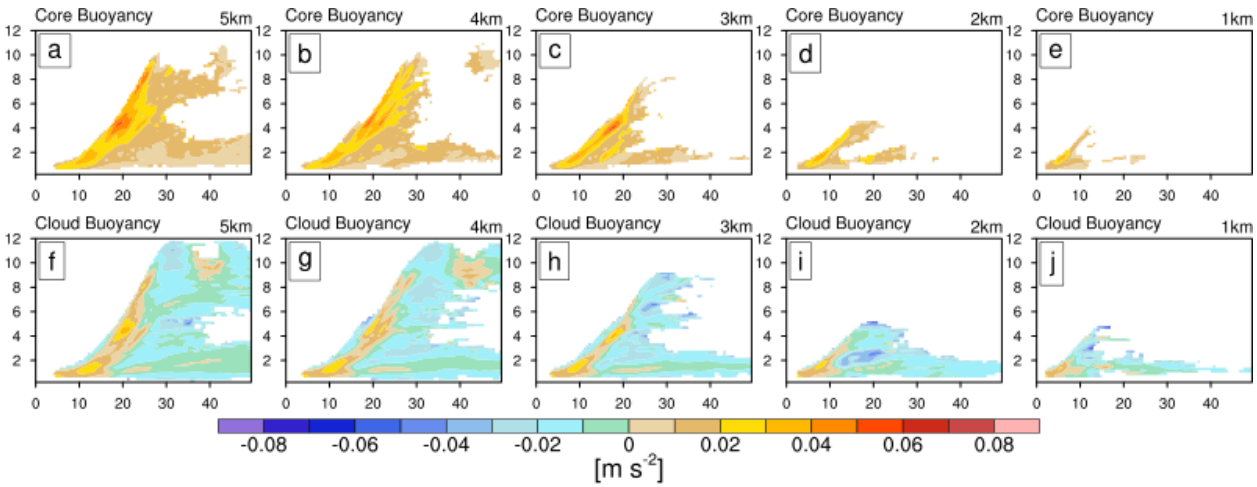

Fig. 4.6 Time vs. height evolution of buoyancy for the cloud core (top) and cloud (bottom) for the control bubble simulations. The abscissa is time in units of minutes.

The vertical mass flux of clouds and cores is also an important quantity for a convective parameterization, because it is used to determine the net heating and drying of the large-scale environment due to convection (Yanai et al. 1973; Arakawa and Schubert 1974). Horizontally averaged core and cloud vertical velocity is closely related to the vertical mass flux and is plotted in Figure 4.7 for the control simulations. The peak amplitude of core and cloud vertical velocity increases systematically with the initial bubble width. This makes phsyical sense because a larger bubble has more mass that is gravitationally unstable.

Downdrafts are known to play a significant role in observed convection, but cloud mass flux does not indicate strong downdrafts, except for the region where the cloud has

overshot its level of neutral buoyancy (Fig. 4.7f-j). More direct metrics of downdraft mass fluxes confirm that strong downdrafts are not prevelant in the bubble simulations discussed here (not shown). Forthcoming analysis of Lagrangian parcel data shows that parcels experience downward motion during detrainment, but the motion is weak on average. The lack of downdrafts is likely a consequence of the idealized nature of the simulated convection.

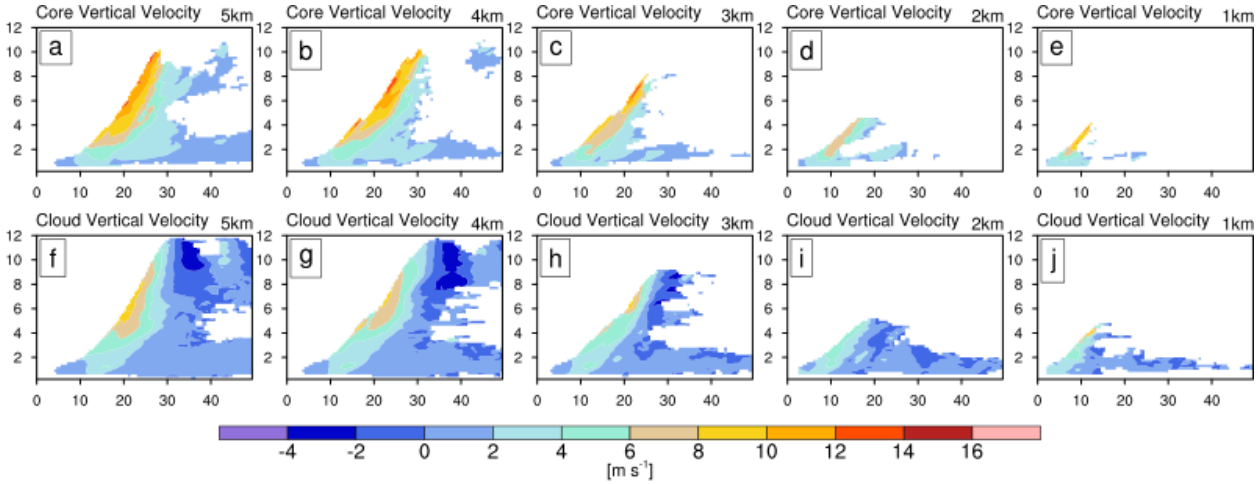

Fig. 4.7 Time vs. height evolution of vertical velocity for the cloud core (top) and cloud (bottom) for the control bubble simulations. The abscissa is time in units of minutes.

Figure 4.8 shows a comparison of mean profiles of potential temperature, vertical velocity and total water in the core between the idealized bubble release simulations and the large domain DYNAMO simulation. This analysis is meant to show that the convection produced from the bubble release simulations are comparable to a field of convection simulated in a more realistic manner. The mean profile of virtual potential temperature is related to buoyancy, and is slightly larger in the *3-5 km* bubbles, but generally of a similar magnitude to the DYNAMO simulation (Fig. 4.8a). Vertical velocity is also of a similar magnitude between the simulations, except for the smallest clouds with *1-2 km* bubbles (Fig. 4.8b). The mean profile of total water shows that the bubble simulation clouds are too

wet at lower levels for the *3-5 km* bubbles (Fig. 4.8c). Overall, these results confirm that deep convection initialized from a warm, humid bubble is generally realistic and is suitable for a systematic investigation of entrainment processes.

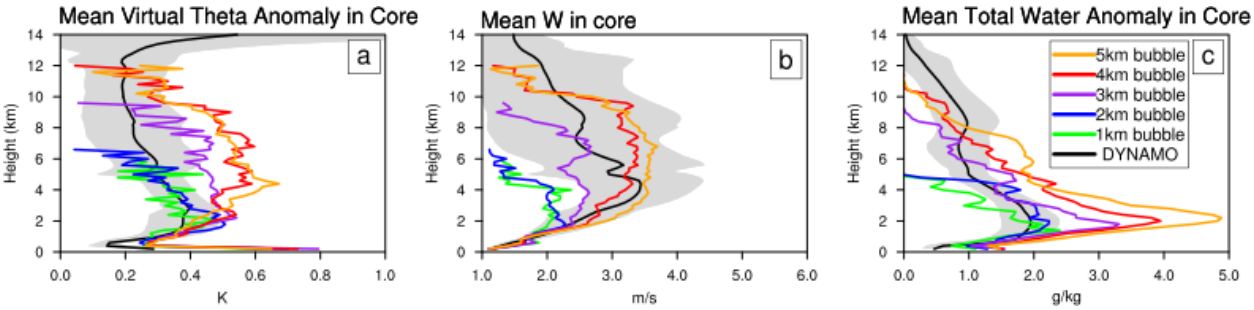

Fig. 4.8 Mean profiles of virtual potential temperature anomaly (a), vertical velocity (b) and total water anomaly (c) averaged over all cloud core points for simulations with realistic forcing from DYNAMO and idealized bubble simulations. Shaded area indicates a spread of two standard deviations from the mean of the DYNAMO simulation data.

4.3.2 Cloud Geometry and Circulation

Figure 4.9 shows the time vs. height evolution of core and cloud radius, calculated with the method of Khairoutdinov and Randall (2006) (See Sec. 4.2). Core radius generally resembles the core area fraction (Fig. 4.5a-e), with the radii values less than half of the initial bubble radius (Fig. 4.9a-e). Cloud radius is larger than the core, as expected, and roughly half of the initial bubble radius. Cloud radius is slightly different than the cloud area fraction (Fig. 4.5f-j), with the cloud anvil somewhat less distinguished in the cloud radius field (Fig. 4.9f-j). This difference is because the radius field was calculated based on areas with a mixing ratio of hydrometoers of at least 0.1 g/kg, which may not be saturated on the periphery of the cloud.

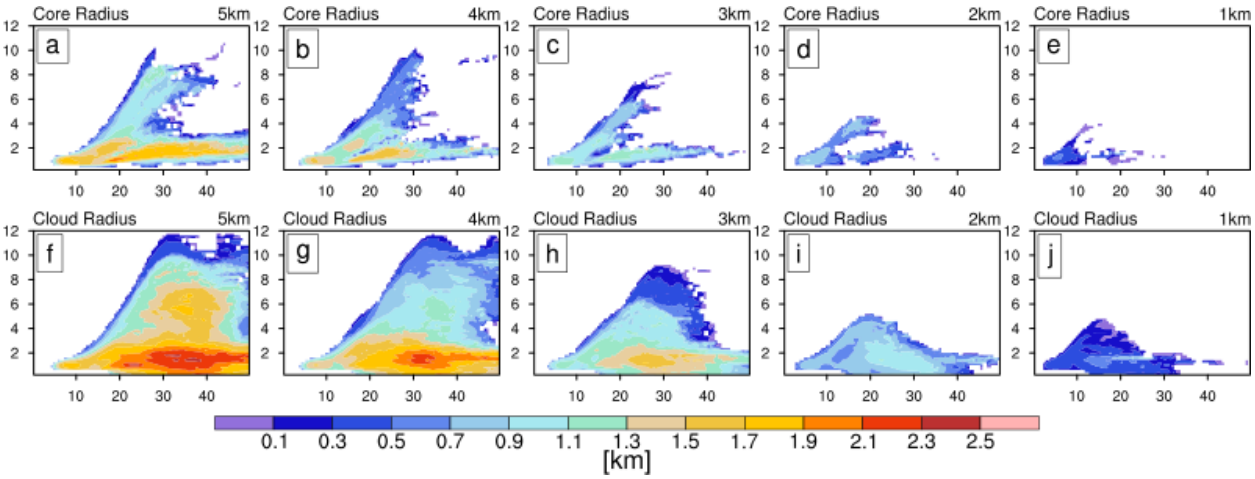

Fig. 4.9 Time vs. height evolution of radius for the cloud core (top) and cloud (bottom) for the control bubble simulations. The abscissa is time in units of minutes.

Radii of the simulated convection is generally consistent with radar and satellite studies of tropical maritime cumulus clouds (LeMone and Zipser 1980; Williams et al. 1992; Rickenbach and Rutledge 1998; Igel and van den Heever 2014), which observe isolated convective clouds to be narrow, with radii around 0.*5-1.0 km*. A key difference between radar and model estimates of cloud width is that most radars can only sense precipitation-size particles, whereas there is no such constraint in the model. This complicates the comparison with radar studies, but in a gross sense the results of Figure 4.9 gives confidence that the idealized cloud simulations are realistic. Furthermore, velocity estimates from Doppler radar measurements are similarly derived from the movement of precipitation-size particles, and so may have errors in estimates of the actual air velocity. Observations show that most maritime tropical clouds have weak updrafts on the order of *3-5 m* s^{-1}. The time vs. height evolution of core and cloud vertical velocity reveals that our idealized bubbles have slightly higher peak vertical velocities on the order of *6-12 m* s^{-1} in the largest clouds (Fig. 4.7).

The radii of core and cloud volumes in the bubble simulations is also generally consistent with the distribution of core and cloud radii from the DYNAMO simulation in

Figure 4.10. These distributions were estimated over 24-32 hours of the DYNAMO simulation at four specific vertical levels (*2.5 km*, *5.0 km*, *7.5 km*, and *10.0 km*) in order to limit the computational expense of the calculation. The distribution changes slightly with height due to the tendency for cores to spread out laterally as they ascend. The distribution of cloud radii is broader than that of cores, indicating a tendency for cloud volumes to be wider, as expected. Both distributions show a peak at radii of *0.4-0.6 km*.

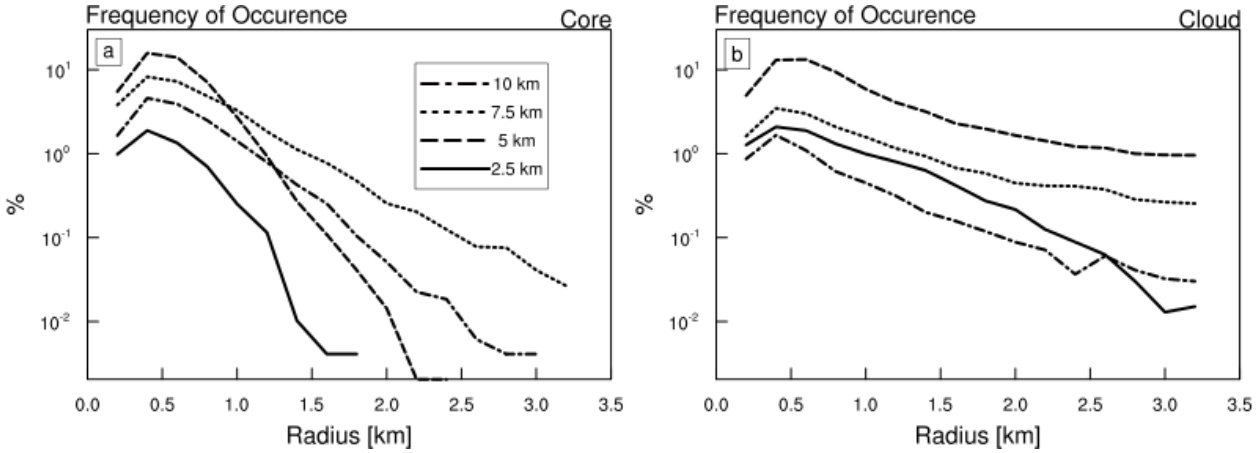

Fig. 4.10 Frequency of occurrence of core (a) and cloud (b) radii estimates in the DYNAMO simulation. Estimates were calculated at 4 heights: 2.5 km (solid), 5 km (dashed), 7.5 km (dotted), and 10 km (dot-dash).

The shell of the cloud that envelopes the core is produced by the detrained core air that makes up the wake of the thermal , and is an important aspect of a convective cloud that can influence the entrainment and dilution (Dawe and Austin 2011a). The shell is not easy to characterize because it can be so variable in space and time. In order to compare the shell in the bubble simulations it is useful to azimuthially averaged the simulation data so that it can be plotted in the height vs. radius plane. Snapshots of the azimuthially averaged core and cloud grid-cell volume fraction in the shading, azimuthially averaged potential temperature perturbation in contour lines, and the azimuthially average circulation in vectors at 00, 05, 11, 18 and 25 minutes of simulation time are shown in

Figures 4.11, 4.12, 4.13, 4.14, and 4.15, respectively. The core and cloud volume fraction in this analysis is used to simply and objectively provide a boundary of each region in the azumithial average. The *1 km* bubble simulation has been omitted here for brevity.

The initial time shows us the spatial character of the starting bubble (Fig. 4.11). After 5 minutes we can see the initial formation of the core volume and also that the initial updrafts are wider for wider initial bubbles (Fig. 4.12). The pattern of the potential temperature anomalies shows the initial gravity wave response eminating from the convection (Bretherton and Smolarkiewicz 1989). After 11 minutes all of the bubbles have risen to *2-3 km* high and exhibit a strong updraft (Fig. 4.13). Also, the gravity wave response has becomes stronger and more complex. Interestingly, the leading edge of the wider bubbles tends to rise more slowly in spite of having stronger updraft strengths. A coherent amount of lateral and upward inflow can be seen all clouds, with corresponding outflow (i.e. detrainment) at the top of the core. At this point in the simulations, almost all of the convective volume is defined as core, with only a small shell region on the periphery. Note that the *2 km* and *3 km* bubbles have a clear signature of a toroidal circulation on the periphery, with descending air in the shell (Fig. 4.13; Zhao and Austin 2005).

After 18 minutes the clouds have grown to an altitude of *~5 km* (Fig. 4.14). The *2 km* bubble is almost completely devoid of a core, indicating that it has reached its terminal height (Fig. 4.14a). The other themals are still rising upwards, and show a thicker cloud shell at the periphery (Fig. 4.14b-d). Air is entering these clouds laterally and from below the level of the main core. Coherent outflow at cloud top can also be observed that is a similar magnitude of the inflow below the core. The circulation in these clouds is reminiscient of the toroidal circulation discussed in previous studies. After 25 minutes the

3 km bubble has reached its level of neutral buoyancy and begun to dissipate (Fig. 4.15b). The *4-5 km* bubbles still have an appreciable amount of core volume and a coherent updraft, and also have formed a secondary core volume at lower levels (Fig. 4.15c-d). These clouds also exhibit a much thicker cloud shell than earlier times. There is still lateral infow from below and outflow at cloud top, but the inflow air must travel an appreciable distance through the cloud shell until it can be ingested into the core. At this time there is still no downward flow at the edge of the cloud to make a coherent closed circulation, but the cloud shell still contains highly turbulent flow.

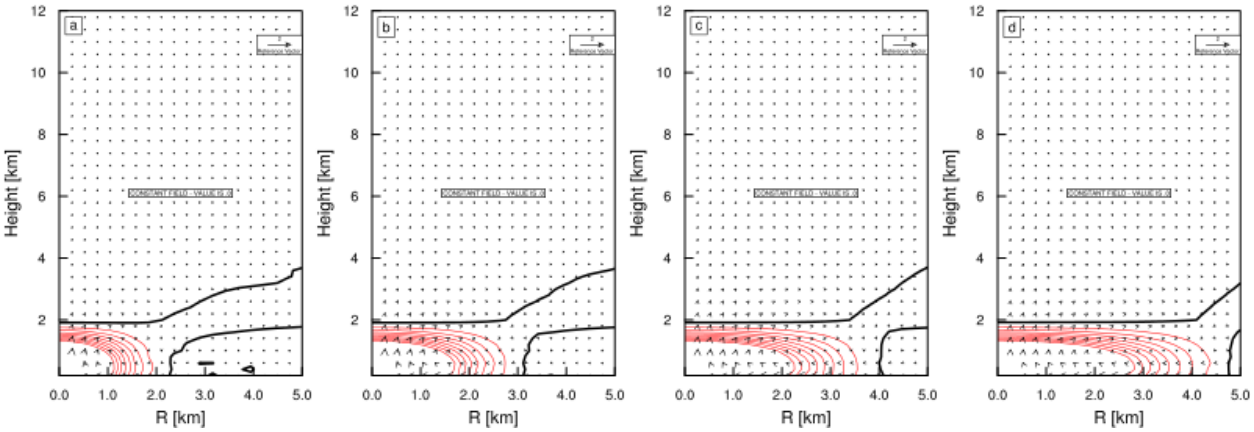

Fig. 4.11 Azimuthially averaged potential temperature anomaly (contours) and circulation (vectors) after 30 seconds of simulation time. Simulations shown are those with intial radii of 2km (a), 3km (b), 4km (c), and 5km (d). Potential temperature contour spacing is *0.05 K* with positive contours in red, negative contours in blue, and the zero contour in the thick black line.

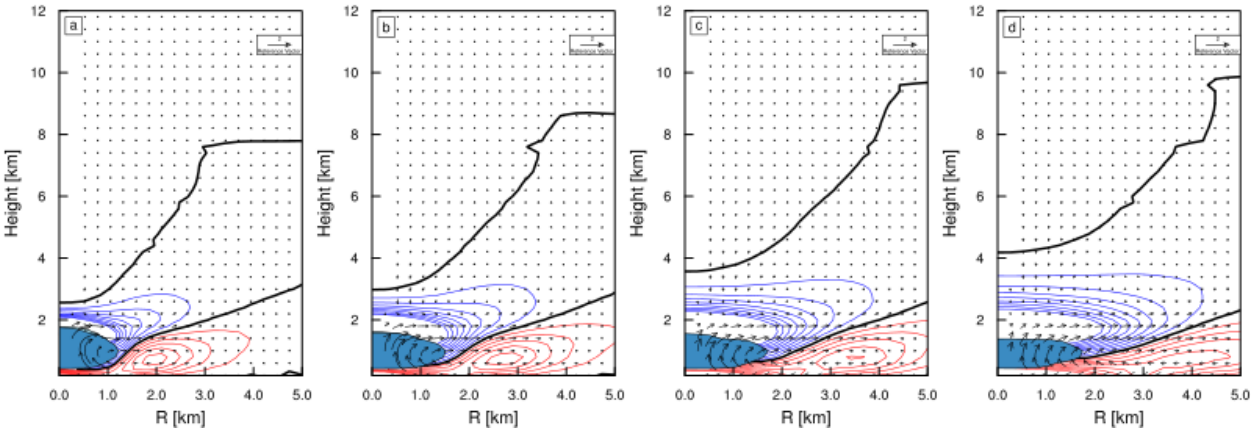

Fig. 4.12 Azimuthially averaged indicator of cloud core (dark blue), cloud shell (light blue), potential temperature anomaly (contours), and circulation (vectors) after 5 minutes of simulation time. Simulations shown are those with intial radii of 2km (a), 3km (b), 4km (c), and 5km (d). Potential temperature contour spacing is *0.05 K* with positive contours in red, negative contours in blue, and the zero contour in the thick black line.

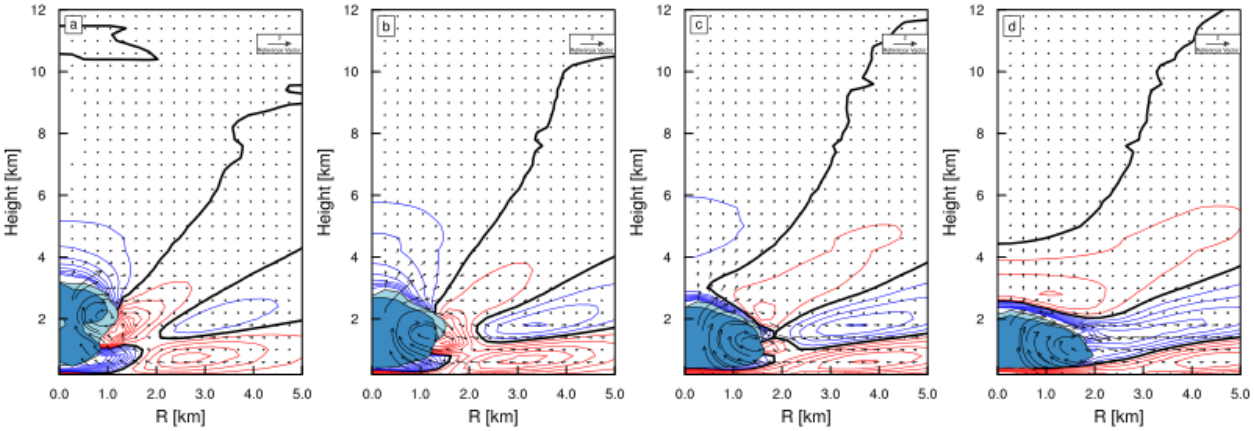

Fig. 4.13 Similar to Fig. 4.12, except at 11 minutes.

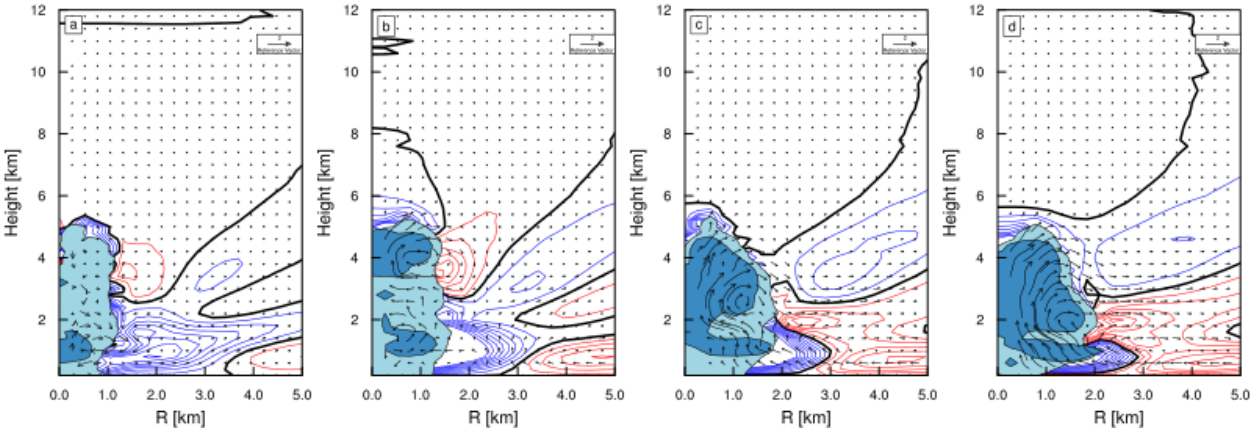

Fig. 4.14 Similar to Fig. 4.12, except at 18 minutes.

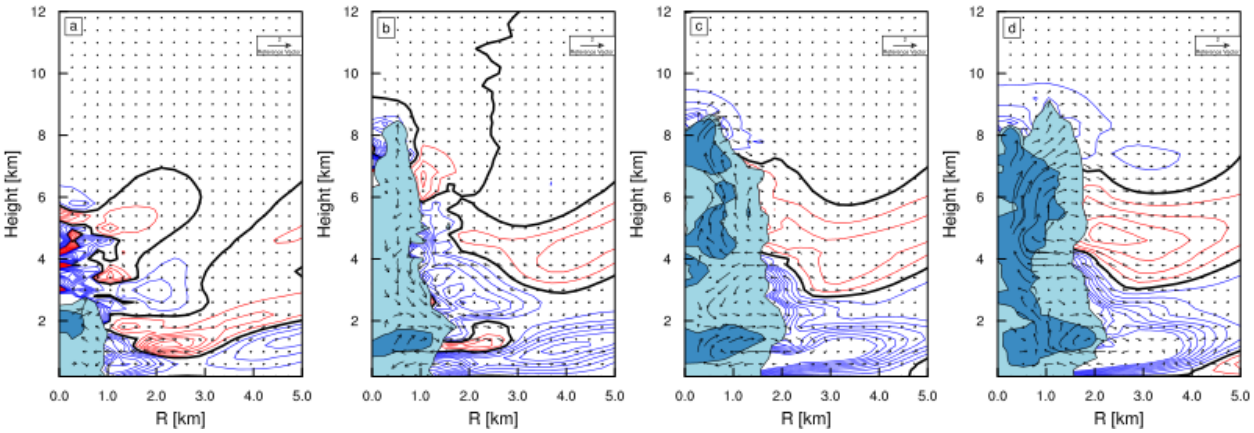

Fig. 4.15 Similar to Fig. 4.12, except at 25 minutes.

From the azimuthal average perspective, entrainment and detrainment appear to be associated with a coherent circulation pattern, with lateral inflow slightly below the rising thermal and lateral outflow at cloud top. Much of the circulation pattern outside the cloud can be associated with the gravity wave response, which may be more clear from the 3D rendering shown in Figure 4.16. The cloud shell appears to play an important role in buffering the core, but not in the sense that the core experiences less entrained mass. The strenth of the circulation actually appears to increase in the larger clouds, suggesting both larger entrainment and larger detrainment. The shell appears to act as a "conditioning" stage for the entrianing air, such that it can mix with the previously detrained air from the core that is still saturated.

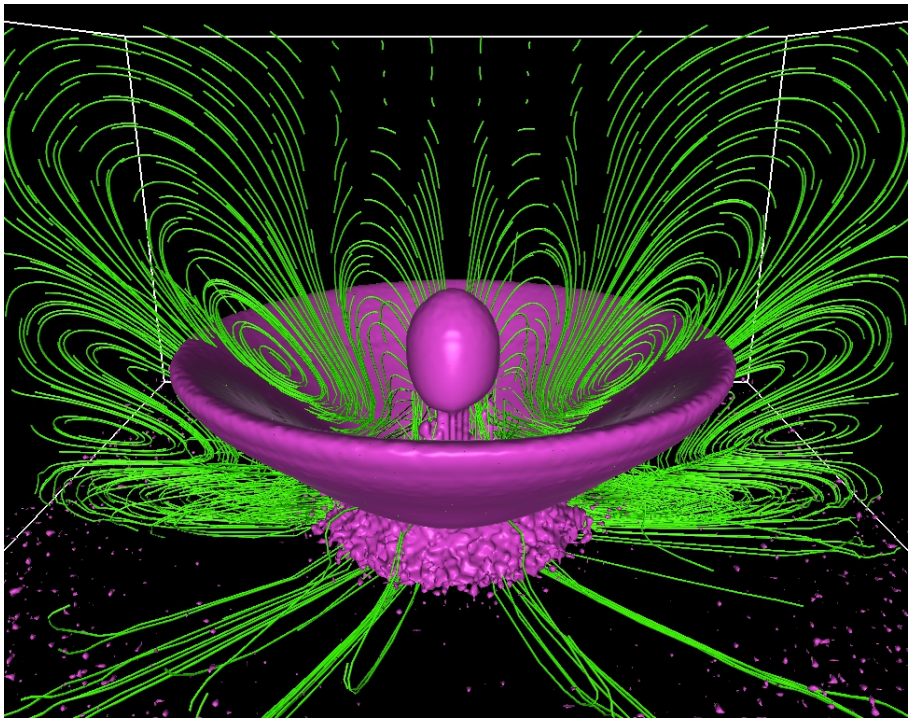

Fig. 4.16 3D rendering of the *0.07 m s^{-1}* iso-surface of vertical velocity and flow streamlines in the x-z plane at the domain center for the *4 km* bubble at 18 minutes of simulation time.

To compare the thicknesses of the cloud shell in a more quantitative way we can use the following expressions,

$$R_{sh} \approx \overline{R_{cld}} - \overline{R_{cor}} \,, \tag{4.4}$$

$$R_{sh}^{*} \approx \frac{\overline{R_{shl}}}{\overline{R_{cld}}} \,. \tag{4.5}$$

The bar in (4.4)-(4.5) represents a vertical average. The formula in (4.4) approximates the shell thickness by taking the difference of the average cloud and core radii at all levels for a given time. (4.5) provides a measure of the "fractional shell thickness" by normalizing with the cloud radius to express the shell thickness as a fraction of the cloud width. Time series of shell thickness and shell thickness fraction are shown in Figure 4.17. The shell thickness steadily increases over the cloud lifetime until the core volume is diminished. The shell thicknesses are comparable among the clouds, but larger bubbles lead to shells that are smaller relative to their size (Fig. 4.17b). I hypothesize that the changing thickness of the

cloud shell over the cloud lifecycle can influence the impact of a given amount of entrainment. The steady increase of the shell in Figure 4.17 appears robust, such that it could be included in the entrainment formulation of a simple cloud model.

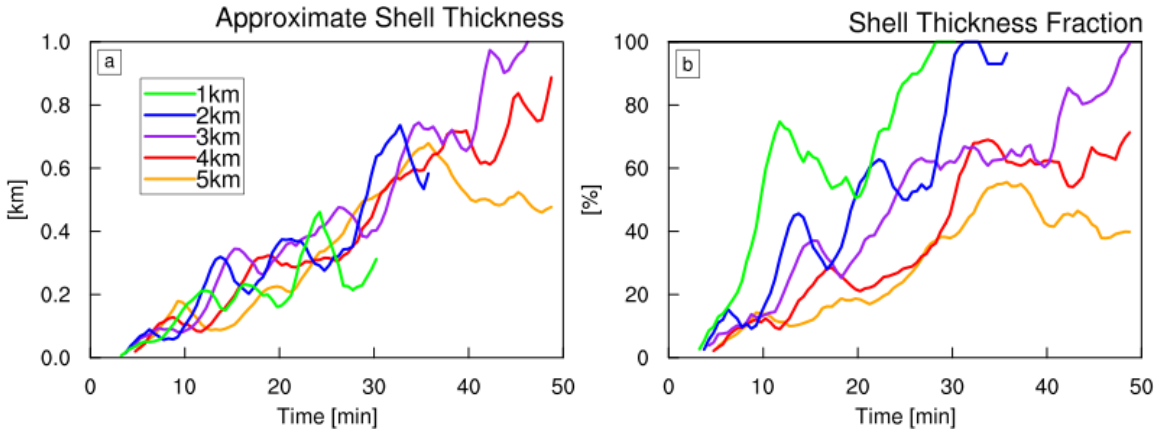

Fig. 4.17 Timeseries of the approximate cloud shell width (a) and shell width fraction (b) as defined in (4.4)-(4.5) for the control bubble simulations.

A comparable diagnostic of shell thickness that could be used on more realistic cloud populations from the DYNAMO simulation is not straightforward. This is due to the slightly more complex geometry of the convection. To illustrate this problem, let us consider some examples. Figure 4.18 shows sample cross sections through selected deep convective clouds in the DYNAMO simulation. Estimating the cloud shell thickness through the clouds in Figures 4.18a-c seems straightforward, since there is a single updraft. The examples in Figures 4.18d-e are complicated by the existence of multiple updrafts and downdrafts in the same cloudy region. The final example in Figure 4.18f appears to be connected to a previously active convective cloud, which would be difficult to objectively account for. These examples show that it would be nearly impossible to objectively analyze the cloud population to get a reliable and accurate metric for the shell thickness. Alternatively, a future study could be conducted on the shell thickness of carefully selected

instances of deep convection from a simulated cloud field to address this and provide further guidance for convective parameterizations.

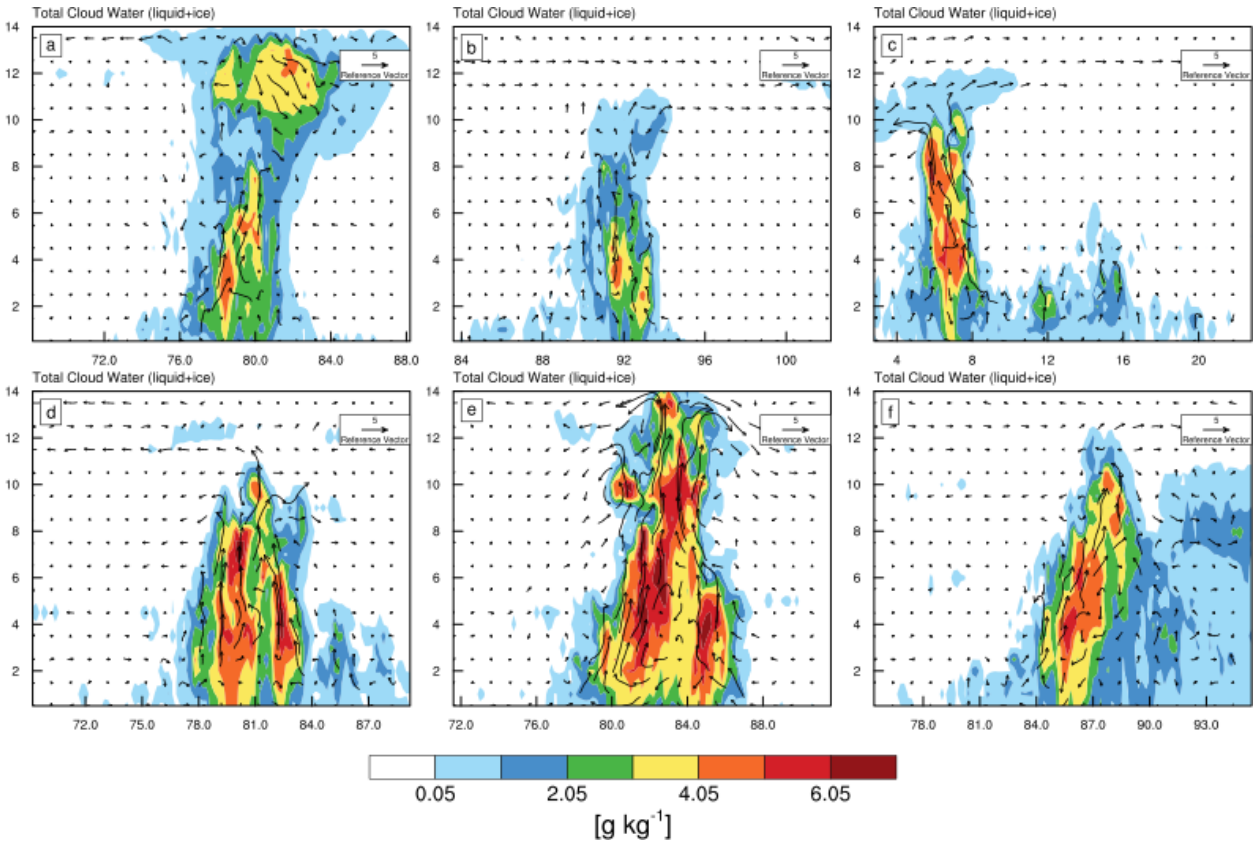

Fig. 4.18 Sample cross sections of total cloud water (vapor+condensate) from selected clouds in the DYNAMO simulation. All panels show a region in the XZ plane that is roughly 20 km across.

4.4 Entrainment and Detrainment

4.4.1 Direct Measurement Results

Now that we are familiar with the nature of the clouds that result from the release of a warm humid bubble in our cloud resolving model, we will proceed to analyze the entrainment and detrainment of these clouds obtained from the direct measurement technique of Dawe and Austin (2011b). As a reminder, entrainment and detrainment are defined here as the transition of air from non-active to active and active to non-active, respectively (Romps 2010). The definition of active air differs depending on whether we

are considering cloud air (i.e. saturated) or core air (i.e. saturated, buoyant, and moving upwards). Also, note that we are not limiting our definition of entrainment to the flux of non-cloudy air across the boundary of an existing cloudy volume, so that the initial formation of a cloud through saturation of an updraft would also be considered as entrainment.

Figure 4.19 shows the time mean profile of entrainment and detrainment rates for the control bubble simulations over the 0-40 minutes of the simulations. Both core and cloud show a similar vertical structure, with large entrainment and detrainment values at cloud base, and smaller values aloft. The peak detrainment occurs just above the peak entrainment, implying that a substantial fraction of the entrainment at cloud base is immediately detrained a short distance above cloud base (e.g. Fig. 4.13). This is similar to the effect of a torroidal circulation at the cloud edge (Zhao and Austin 2005; Sherwood et al. 2013). Entrainment and detrainment rates between core and cloud are generally comparable. Larger bubbles have larger rates of entrainment, which is expected since a larger bubble will lead to a larger saturated volume. Larger bubbles also result in larger detrainment rates at all levels, consistent with a stronger toroidal circulation (see also Fig. 4.13-4.15).

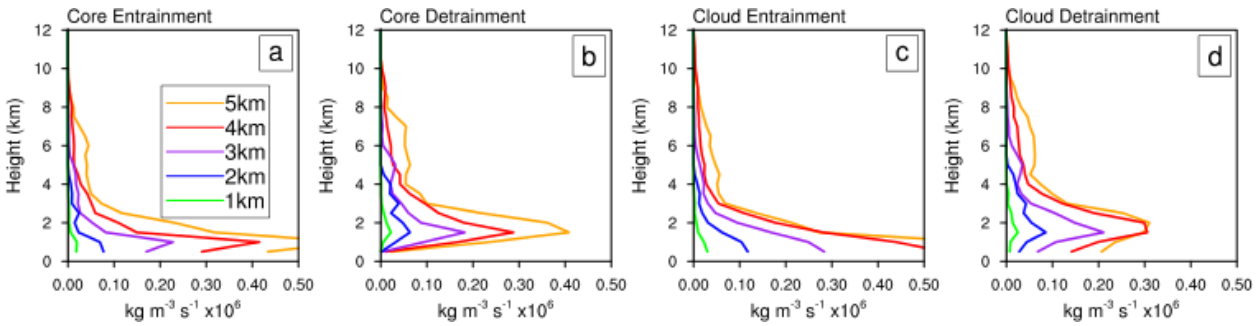

Fig. 4.19 Time mean profiles of core entrainment (a), core detrainment (b), cloud entrainment (c), and cloud detrainment (d) over the initial 40 minutes of the control bubble simulations.

Entrainment and detrainment are often normalized by the vertical mass flux (see Fig. 4.20) to obtain a fractional value, that has units of km^{-1}. The fractional entrainment rate can be interpreted as length scale for mixing processes, associated with the dominant length scale of eddies at a given altitude (Siebesma et al. 2007). A more literal interpretation is that the fractional entrainment represents the additional mass added to updraft by lateral inflow as a fraction of the vertical mass flux, but the utility of this interpretation depends on how well these two quantities are related to each other. If the mass flux was directly tied to entrainment, as in (4.19), then this literal interpretation of the fractional entrainment rate would be more appropriate. However, we know that the change in mass flux with height is largely affected by detrainment as well, so this thinking is somewhat misleading. Romps (2010) pointed out that putting entrainment in a "length per distance" framework is a problematic artifact of early one-dimensional plume theory, since it can lead to negative values of entrainment and detrainment for various reasons (See Fig. 4.22-4.23). Normalizing by the mass flux can also cause issues when its magnitude is close to or equal to zero. To address this problem we omit any data when the vertical mass flux falls under a threshold value of 10^{-6} *kg* m^{-2} s^{-1}, prior to normalization.

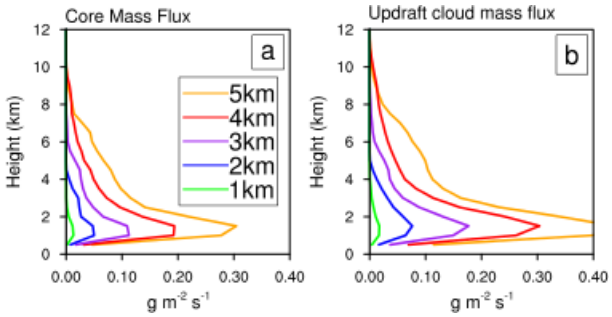

Fig. 4.20 Time mean profiles of core (a) and cloud (b) mass flux over the initial 40 minutes of the control bubble simulations.

Figure 4.21 shows the profiles of fractional core and cloud rates of entrainment and detrainment. Fractional entrainment is large at the lowest levels for both core and cloud (Fig. 4.21a,c), oweing to the small mass flux (Fig. 4.20) and large entrainment. Fractional detrainment is slightly larger than fractional entrainment (Fig. 4.21b,d). When comparing the entrainment and detrainment between the simulations, we can notice a curious tendency for the fractional entrainment to be larger with a larger bubble. We will return to this subject in the next section. The magnitudes of fractional entrainment are surprisingly small in light of the results of Romps (2010), who showed directly measured entrainment in deep convection to be much larger than typical plume calculations. The entrainment rates here are more or less consistent with values used in parameterizations of deep convection (Tiedtke 1989; Chikira and Sugiyama 2010). The explanation of this discrepancy lies in the values of the mass flux profiles used for normalization. As will be shown, typical mass flux values in the DYNAMO simulation are much smaller than those shown in Figure 4.21. This is a consequence of how the bubble simulations are initiated, and the fact that they have slightly larger vertical mass fluxes.. As illustrated by the examples in Figure 4.18, deep convection in a maritime environment is rarely observed as a deep tower with a single coherent updraft that is rooted in the boundary layer. Instead, deep convection often grows out of a population of small cumulus clouds or is associated with an organized mesoscale system.

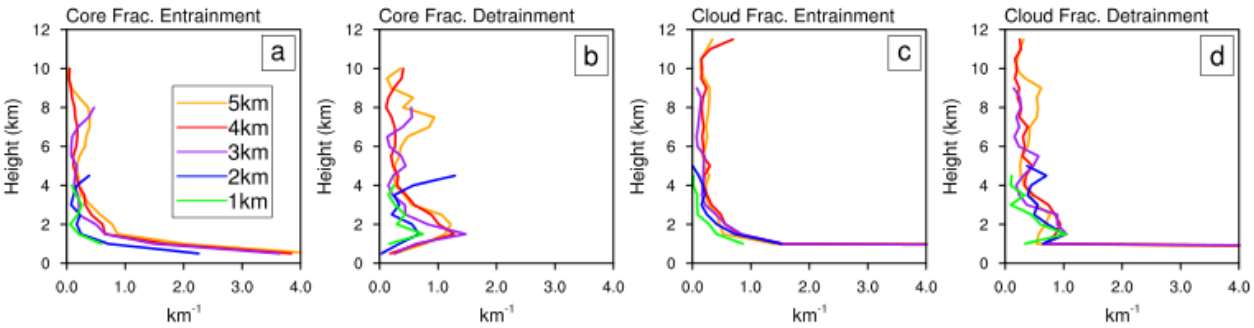

Fig. 4.21 Time mean profiles of core fractional entrainment (a), core fractional detrainment (b), cloud fractional entrainment (c), and cloud fractional detrainment (d) over the initial 40 minutes of the control bubble simulations.

Many previous studies using cloud resolving models estimate entrainment from the budget of some quasi-conservative tracer (Siebesma and Cuijpers 1995; Romps 2010). This method may be more accurately described as estimating an effective entrainment relative to the tracer in question, rather than the actual mass entrainment of the simulated convection. Following Romps (2010), the flux-form budget equations for density and a generic conserved tracer ϕ, horizontally averaged across a cloud can be written as,

$$\partial_t \langle \rho \rangle + \partial_z \langle \rho w \rangle = \langle e \rangle - \langle d \rangle \,, \tag{4.6}$$

$$\partial_t \langle \rho \phi \rangle + \partial_z \langle \rho w \phi \rangle = \phi_e \langle e \rangle - \phi_d \langle d \rangle \,, \tag{4.7}$$

where ρ is density, w is vertical velocity, e is entrainment, d is detrainment, and angle brackets denote a horizontal average over a cloud volume. The quantities ϕ_e and ϕ_d represent the tracer value of the entrained and detrained air, respectively. If we have a way to determine ϕ_e and ϕ_d, then we are left with a system of two equations and two unknowns, which allows us to solve for the mass entrainment and detrainment rates,

$$e = \frac{\phi_d \left(\partial_t \langle \rho \rangle + \partial_z \langle \rho w \rangle \right) - \left(\partial_t \langle \rho \phi \rangle + \partial_z \langle \rho w \phi \rangle \right)}{\phi_d - \phi_e} \,, \tag{4.8}$$

$$d = \frac{\phi_e \left(\partial_t \langle \rho \rangle + \partial_z \langle \rho w \rangle \right) - \left(\partial_t \langle \rho \phi \rangle + \partial_z \langle \rho w \phi \rangle \right)}{\phi_d - \phi_e} \,. \tag{4.9}$$

In order to use (4.8) and (4.9), we need to decide how to specify ϕ_e and ϕ_d. The entrained air tracer values are often assumed to be identical to the mean unsaturated environment, and the detrained air is often assumed to be equal to the mean value across the cloud. Although this assumption ignores the properties of the air residing at the edge of the cloud that makes up the shell (Fig. 4.17), it is often a necessary simplification in formulating a parameterization. Figure 4.22 shows the results of the bulk entrainment and detrainment estimation based on the total water mixing ratio ($q_t = q_v + q_l + q_i$). Here we have plotted the fractional values, normalized by the mass flux, similar to Figure 4.21. The values are generally well constrained and positive except for a few large spikes below *2 km*. Note that negative entrainment in these estimates does not imply positive detrainment, and similarly negative detrainment does not imply positive entrainment. Negative values are a consequence of sources and sinks that are not accounted for in the budget equations of (4.6) and (4.7), such as gravitational sedimentation of hydrometeors. In general, the bulk profiles are somewhat consistent with the mean profiles of directly measured entrainment, but the values are much noisier and less reliable

It is illuminating to compare estimates derived from a different tracers. A good candidate for this is the moist static energy (MSE), defined as,

$$h_f = c_p T + gz + L_v q_v , \tag{4.10}$$

where c_p is the specific heat at constant pressure, T is the absolute air temperature, g is gravity, z is the geopotential height, L_v and is the latent heat of vaporization and fusion, respectively, and q_v represents the mixing ratio of water vapor. MSE is generally conserved in the presence of moist convection and ice. However, both MSE and q_t are not exactly conserved for a parcel when precipitation is falling in or out or the parcel and when

radiative processes affect the parcel temperature. The bulk fractional entrainment and detrainment rates calculated using MSE are shown in Figure 4.23. The fractional entrainment rate is much smaller when based on MSE and has negative values at upper levels associated with radiative and precipitation processes. The fractional detrainment rates are similar for both tracers, except near the surface where detrainment based on MSE has a large negative value. Bulk budget entrainment estimates are known to be systematically biased toward lower values (Romps 2010; Dawe and Austin 2011a), although the bulk rates here seem comparable to the control bubble simulations. Subsequent analysis will show that the fractional entrainment rates in the DYNAMO simulation are much larger, and in better agreement with Romps (2010). Overall, it is clear from Figures 4.21, 4.22, and 4.23 that the direct measurement method is less noisy and more reliable for obtaining entrainment and detrainment rates.

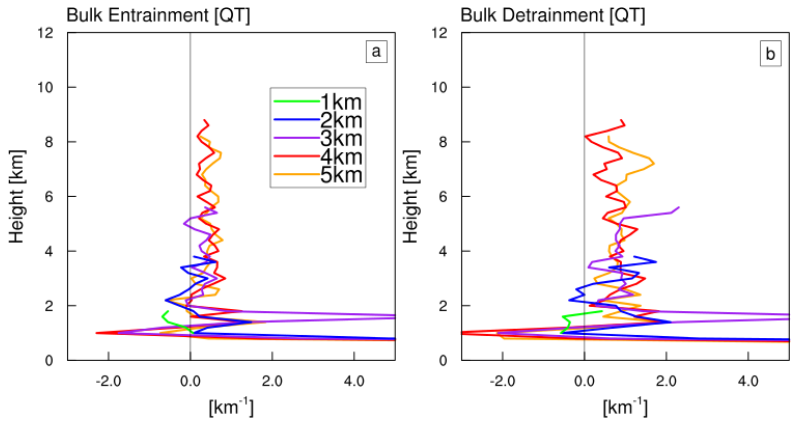

Fig. 4.22 Mean profiles of bulk entrainment (a) and detrainment (b) rates calcualted from the budget of total water mixing ratio (see (4.8) and (4.9))

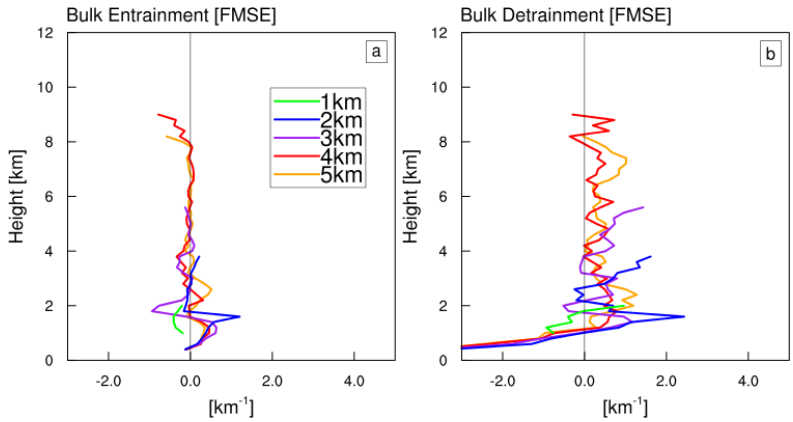

Fig. 4.23 Similar to Fig. 4.22, except frozen moist static energy (MSE) is used, instead of total water.

Comparing the entrainment and detrainment profiles in Figure 4.21 to the profiles from the DYNAMO simulation in Figure 4.24, we can see that the rates are much larger in the DYNAMO simulation. The DYNAMO simulation shows core entrainment and detrainment rates aound *2.0 km*$^{-1}$, whereas the bubble simulations generally have rates under *1.0 km*$^{-1}$. These profiles agree with (Romps 2010) for a simulation of deep convection in radiative-convective equilibrium with identical grid spacing, but a smaller domain (*~25 km*^{3}). As mentioned above, the fractional rates are smaller in the bubble simulations because the vertical mass fluxes are larger than those in Figures 4.25c and 4.26c. An interesting feature of these profiles is the maximum value centered around *4-7 km*. This is due to large entrainment and detrainment value in both core and cloud volumes at the freezing level (Fig. 4.25-4.26), associated with buoyancy generation and acceleration above the freezing level by the latent heat of freezing (see also Fig. 4.32). It is unclear why this feature is not evident in the bubble simulations, but it may be because the larger mass fluxes overwhelm this signal.

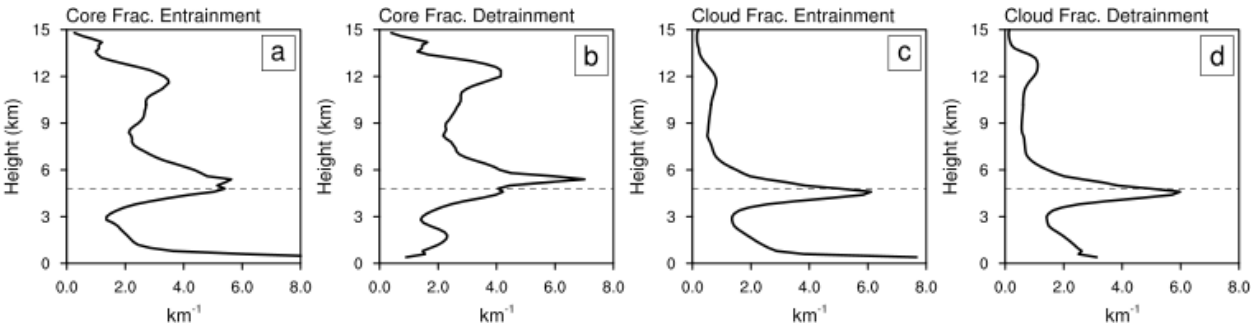

Fig. 4.24 Time mean profiles of core fractional entrainment (a), core fractional detrainment (b), cloud fractional entrainment (c), and cloud fractional detrainment (d) of the DYNAMO simulation. The dashed line indicates the freezing level.

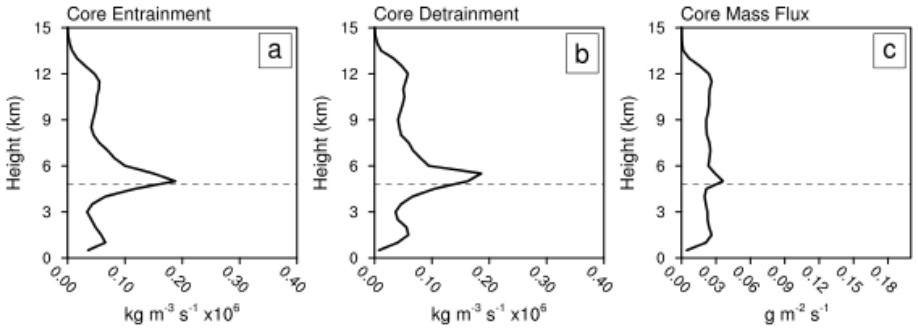

Fig. 4.25 Time mean profiles of core entrainment (a), detrainment (b), and mass flux(c) for the DYNAMO simulations.

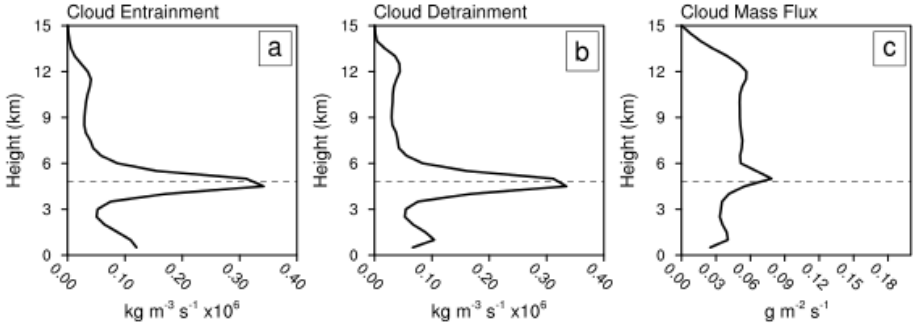

Fig. 4.26 Time mean profiles of cloud entrainment (a), detrainment (b), and mass flux(c) for the DYNAMO simulations.

4.4.2 Entrainment and Cloud Radius

Many simple cloud models and convective parameterizations rely on the hypothesis that entrainment is inversely propotional to cloud radius (Simpson 1971; Arakawa and Schubert 1974; Tokioka et al. 1988; Morton et al. 1956; Wagner and Graf 2010; Stirling and

Stratton 2012). Few attempts have been made to verify this assumption in observations, but they generally support the hypothesis (Sloss 1967b; McCarthy 1974b; Lu et al. 2012a). This relationship can be summarized with the following equation,

$$\mu = \frac{\alpha}{R}\ , \tag{4.11}$$

where μ is the fractional entrainment rate, *R* is radius, and α is a coefficient of proportionality. Entrainment profiles from the bubble simulations suggest that there is not an inverse relationship to cloud or core radius (Fig. 4.21). In fact, the results here suggest that entrainment *increases* slightly with increasing radius. This disparity could possibly be due to the way the clouds were initialized with a non-spherical bubble. Nonetheless, this is a surprising result in light of previous studies, and deserves closer inspection.

Before examining the simulation data, it is useful to review the basic theory behind the idea that entrainment should decreasse with increasing cloud radius. Early lab experiments noticed that a drop of relatively dense fluid release into a tank would expand along a cone as it sank down through a tank (Sànchez et al. 1989; Turner 1986). This expansion of the "thermal" was interpreted to be the result of entraining ambient fluid. This also explained how the drop became more dilute as it sank. Applying this idea to the atmosphere, we can express the thermal radius as a function of altitude,

$$r = \gamma z\ , \tag{4.12}$$

where γ is a constant. From the definition of the fractional entrainment (assuming no detrainment), we can assume spherical geometry and substitute $M = {}^{4}\!/_{3}\pi r^{3}\rho w$ for the mass flux of the buoyant thermal to obtain an equation that relates the fractional entrainment to the radius of the thermal,

$$\mu = \frac{1}{M}\frac{dM}{dz}$$
$$= \frac{1}{\left(\frac{4}{3}\pi r^3 \rho_t w\right)}\frac{d}{dz}\left(\frac{4}{3}\pi r^3 \rho_t w\right), \tag{4.13}$$

where *M* is the vertical cloud mass flux and ρ_t is the thermal density. For an incompressible fluid we can assume that density is invariant with height (i.e. $\frac{d\rho_t}{dz} = 0$). If we also assume the vertical velocity does not vary substantially with height, then we can use (4.12) to express the fractional entrainment as inversely dependent on radius,

$$\begin{aligned}\mu &= \frac{1}{r^3}\frac{d}{dz}\left(r^3\right) \\ &= \frac{\gamma^3}{r^3}\frac{d}{dz}\left(z^3\right) \\ &= \frac{3\gamma^3 z^2}{r^3} \\ &= \frac{3\gamma}{r}\end{aligned}. \tag{4.14}$$

Note that we do not need to be strictly limited to spherical geometry. We could also assume cylindrical geometry and arrive at a similar result, which is more relevant to the shape of the initial bubble perturbation in the simualtions here.

So far we have not considered the expansion of a thermal rising in a stratified atmosphere. A thermal rising in the real atmosphere will expand without any entrainment by virtue of the fact that the ambient pressure decreases with height. This could affect the estimates of entrainment in previous studies, but how big could this effect be? To answer this question, we can describe this expansion from first principles, starting with the enthalpy form of the first law of thermodynamics,

$$c_p \partial T = T \partial s + \frac{1}{\rho}\partial p, \tag{4.15}$$

where T is temperature, c_p is the specific heat at constant pressure, and s is entropy. If we consider the situation of a rising thermal to be psuedoadiabatic, we can assume that the change in entropy is negligible. We can also substitute the equation of state ($p = \rho RT$) to arrive at,

$$c_p \partial T = \frac{1}{\rho} \partial(\rho RT). \tag{4.16}$$

After some rearrangement we have,

$$\left(\frac{c_p}{R} - 1 \right) \frac{\partial T}{T} = \frac{\partial \rho}{\rho}. \tag{4.17}$$

At this point we can take advantage of a logarithmic identity, which makes integration of (4.17) straighforward,

$$\left(\frac{c_p}{R} - 1 \right) \int_{T_o}^{T} \partial \ln(T) = \int_{\rho_o}^{\rho} \ln(\rho), \tag{4.18}$$

$$\ln(T - T_o)^{\frac{c_p}{R} - 1} = \ln(\rho - \rho_o). \tag{4.19}$$

Solving this for density we arrive at,

$$\rho = \rho_o \left(\frac{T}{T_o} \right)^{\frac{c_p}{R_d} - 1}. \tag{4.20}$$

Now that we have an expression for the change in density of a thermal rising through a stratified atmosphere we can derive a relationship of the radius of the rising thermal. Using $\rho = \frac{m}{4/3 \pi r^3}$, where m is mass, and recognizing that mass is conserved in the case with no entrainment, we have,

$$\frac{1}{r^3} = \frac{1}{r_o^3} \left(\frac{T_a}{T_o} \right)^{\frac{c_p}{R_d} - 1}. \tag{4.21}$$

We can replace the atmospheric temperature with a profile based on the lapse rate, $T = T_o - \Gamma z$, and solve for the ratio of final to initial thermal radii as a function of height in the absence of entrainment,

$$\frac{r}{r_o} = \left(\frac{T_o - \Gamma z}{T_o} \right)^{\frac{1 - c_p / R_d}{3}} . \qquad (4.22)$$

Figure 4.27 shows (4.22) for dry and moist adiabatic lapse rates, and suggests the change of thermal radius to be at most *20-40%* of the initial value after rising *10 km*. This value is large enough that it cannot be considered negligible, and suggests that the results of past studies which rely on the assumed relationship between radius and entrainment are likely inaccurate. However, it is uncertain whether this analysis is relevant to an actual thermal with toroidal circulations driving large entrainment and detrainment. The method of Lu et al. (2012b) uses the change in mass with height to estimate entrainment from observations, but assumes detrainment does not affect the cloud mass budget, which we have seen is a very poor assumption (i.e. Fig. 4.13-4.15). The time series of radius in Figure 4.9 does not suggest substantial expansion in the bubble simulations, but given the magnitude of entrainment and detrainment (Fig. 4.21), it seems that mixing processes would overwhelm any signal of this expansion.

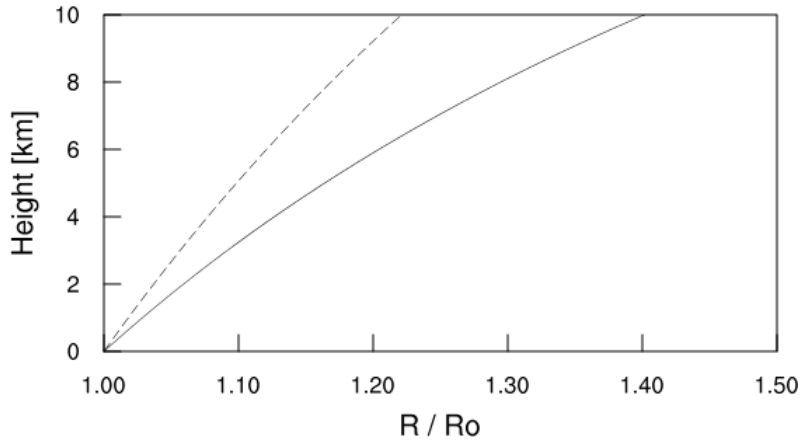

Fig. 4.27 Theoretical ratio of plume radius to initial radius in the absence of entrainment for a dry (solid) and moist (dashed) adiabatic apse rate and assuming a reference temperature of 300K.

We will now investigate whether there is any empirical evidence for a robust relationship between entrainment and cloud radius in the bubble simulations, which were designed to systematically yield a spectrum of cloud and core radii. Figure 4.28 shows scatter plots of core entrainment rate against core radius (see Fig. 4.9). The thin dotted black lines in Figure 4.28 are solutions the inverse relationship in (4.11) with a range of α values from *0.1* to *3.2*. The thick black lines show a binned mean view of the data. The raw data of entrainment and radius, which is dependent on time and height, does not suggest an obvious relationship between entrainment and core radius, but the binned mean values of the data do imply a slight dependence on radius when the radius is less than *1 km* (Fig. 4.28a). Similar results can be found for cloud entrainment and radius (Fig. 4.29a). One might presume that data on 30 second intervals would be too noisy to reveal a coherent relationship. To see the effect of various averaging Figure 4.28b-c shows the temporally averaged and vertically averaged fractional core entrainment rate, respectively. This averaging is done to both core entrainment and core mass flux prior to the normalization for both panels. The temporally averaged core data do not show any coherent relationship, but the amount of data for this is very small (Fig. 4.28b). The temporally averaged cloud data appears to show an increase in entrainment with radius, but again the amount of data in these plots is very small (Fig. 4.29b). Vertically averaging the data actually shows a hint of an inverse relationship for both core and cloud data (Fig. 4.28-4.29c). A caveat of the binned average in these plots is that they are heavily influenced by data outliers that results from small mass flux values, but this analysis suggests that column average bulk

entrainment might be slightly influenced by the radius. Overall, there is not a strong relationship that could support the original hypothesis. Comparison of the bubbles simulations among each other shows weak evidence for increased entrainment with larger radius, but not enough to justify using such a relationship in a simple cloud model.

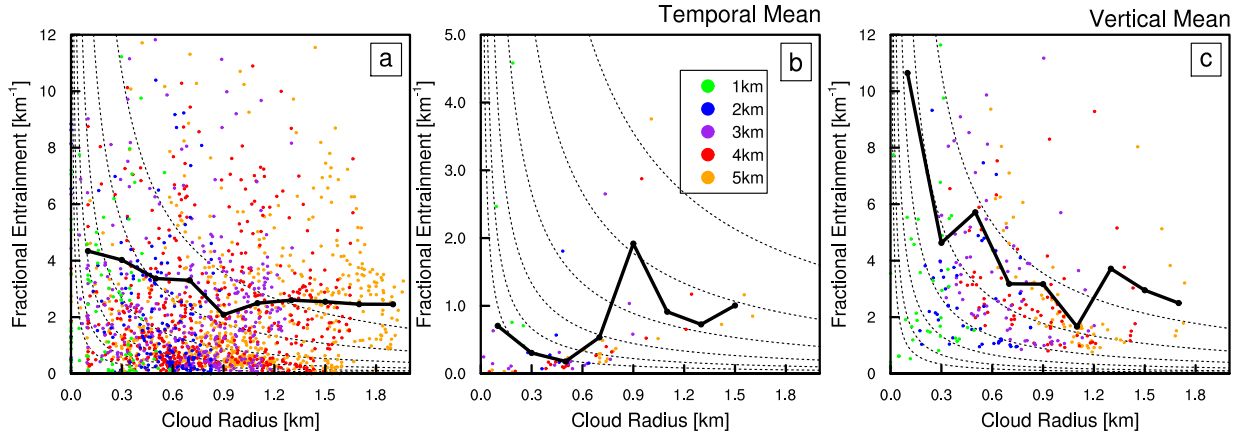

Fig. 4.28 Scatter plots of core entrainment vs. core radius. Thin dashed lines are theoretical estimates of the relationship between entrainment and radius based on (4.11), with constant α values of 0.1, 0.2, 0.4, 0.8, 1.6, and 3.2. The solid black line is a binned average of the data points.

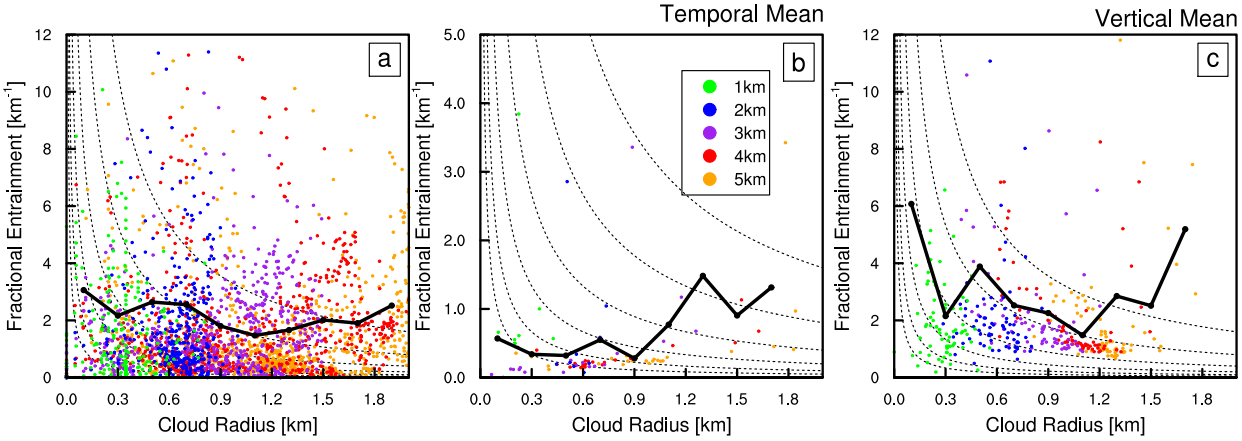

Fig. 4.29 Similar to Fig. 4.28, except for cloud data, instead of core.

Perhaps, a simpler way to view this relationship is to estimate a single entrainment rate for each bubble simulation by averaging in height and time, that is representative of the entire convective evolution, and plot it against the average radius. To do this, the fractional entrainment and radius are calculated and then averaged over all times and altitudes. Figure 4.30 shows the results of this calculation for core and cloud data in a log-

log plot, so that a power law relationship would be indicated by a linear slope of the points. The black line indicates an inverse power law relationship, as in (4.11). The results do not clearly indicate an inverse relationship between fractional entrainment and radius. However, there is a slight hint of an inverse relationship for the core entrainment in the *2-4 km* bubble. These conclusions are consistent with the recent study of shallow convection by Dawe and Austin (2013).

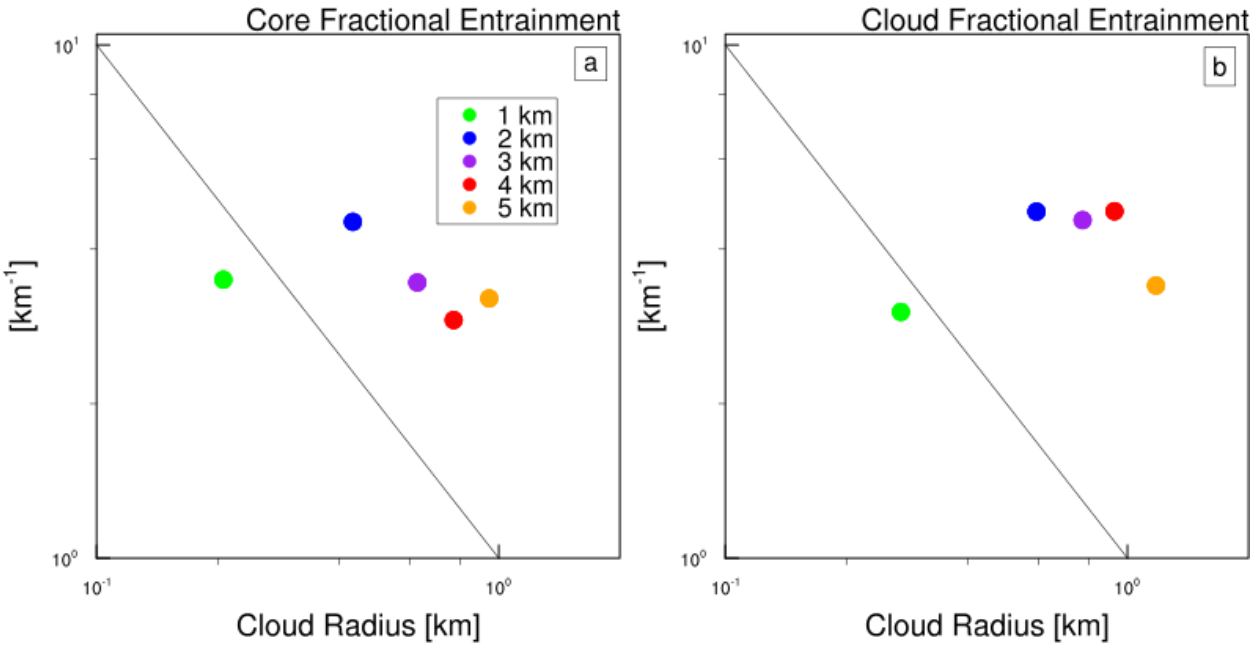

Fig. 4.30 Scatter plot of temporal and vertical average core (a) and cloud(b) fractional entrainment vs. radius. Black line indicates an inverse power law relationship.

A notable caveat of the bubble simulations is that the convection is not triggered in a natural way, which was shown to influence the profiles of entrainment (Fig. 4.21). The DYNAMO simulation offers a opportunity to compare our entrainment result to convection that more closely resembles observed convection. However, isolating convective elements of various radii is a difficult endeveour. In order to objectively analyze the relationship between radius and entrainment in the DYNAMO simulation, and algorithm was developed to randomly select 50 cloud features at every height and time during hours 24-32 of the

simulation. The cutoff of 50 features was a practical decision to limit computation time, as the number of cloud or core features identified at any one time and level could be on the order of 10^3. The values of entrainment, detrainment and mass flux were averaged over an area twice as large as the estimated radius to account for irregularities in cloud geometry, and then progressively binned by radius for core and cloud features. The results of the computation are shown in Figure 4.31.

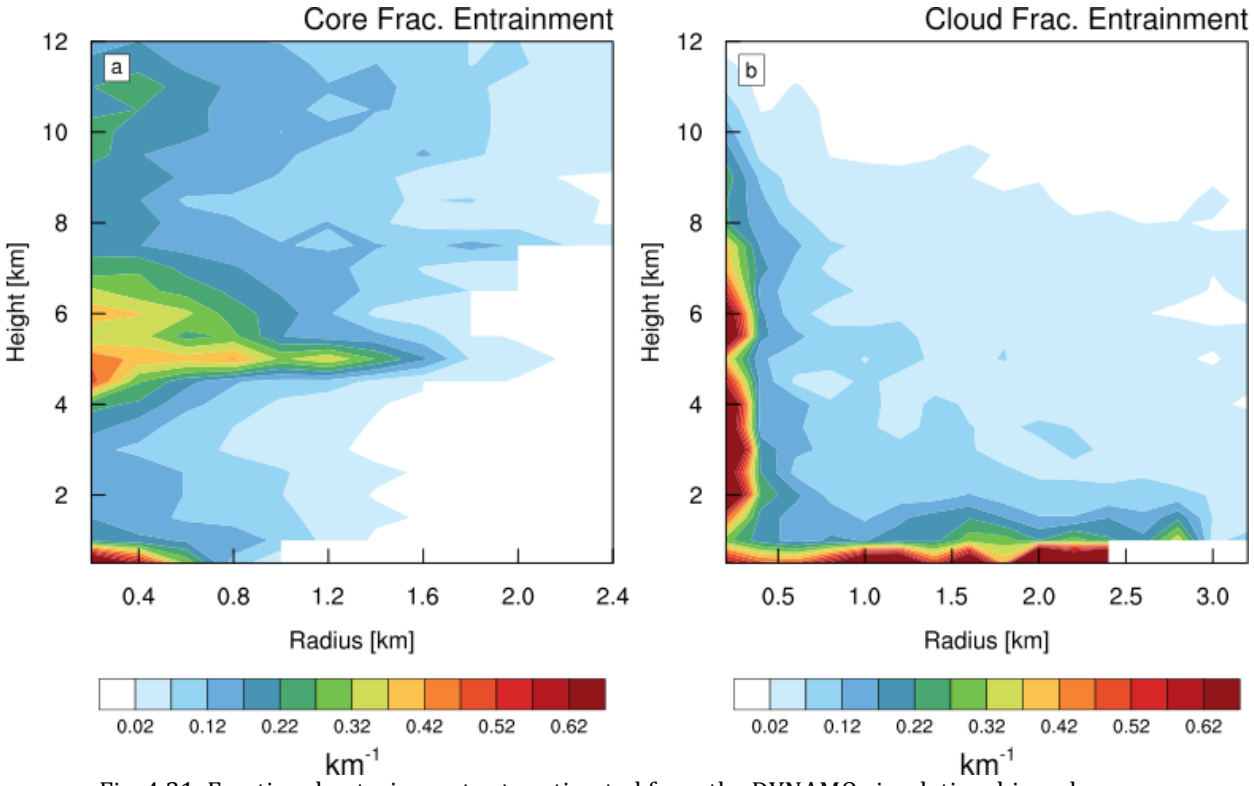

Fig. 4.31 Fractional entrainment rate estimated from the DYNAMO simulation, binned as a function of hight and radius (see text).

The DYNAMO simulation exhibits a clear inverse relationship between entrainment and radius at all altitudes (Fig. 4.31), in stark contradiction with the results of the bubble simulations (Fig. 4.30). However, note that convection in a forced simulation, such as the DYNAMO simulation or that of Dawe and Austin (2013), is not as tightly controlled as in the bubble experiments. Properties of convection in the bubble simulations can be tested

independent of other factors, such as thermal buoyancy or environmental humidity, unlike the convection in the DYNAMO simulation. If we perform a similar bin-average analysis of buoyancy, total water, and vertical velocity in core volumes for the DYNAMO simulation we find that these variables also vary with core radius (Fig. 4.32). All three variables show peaks around *0.5-1.0 km* radii, and then decrease for larger or smaller radii (See also Fig. 4.4, 4.6, 4.7, and 4.8). This shows how different the convection is in the two experimental approaches. The bubble simulations generally exhibited larger buoyancy and total water above cloud base (Fig. 4.8). Similar results can be found for the DYNAMO simulatinos when estimated for cloud volumes, instead of core, but the pattern is not as clear (Fig. 4.33). Cloud buoyancy has a broad peak around *1.0-2.0 km* radii, and vertical velocity peaks around *0.5-1.5 km* radii. Cloud total water increases with cloud radius at mid-levels, but overall does not show a coherent relationship.

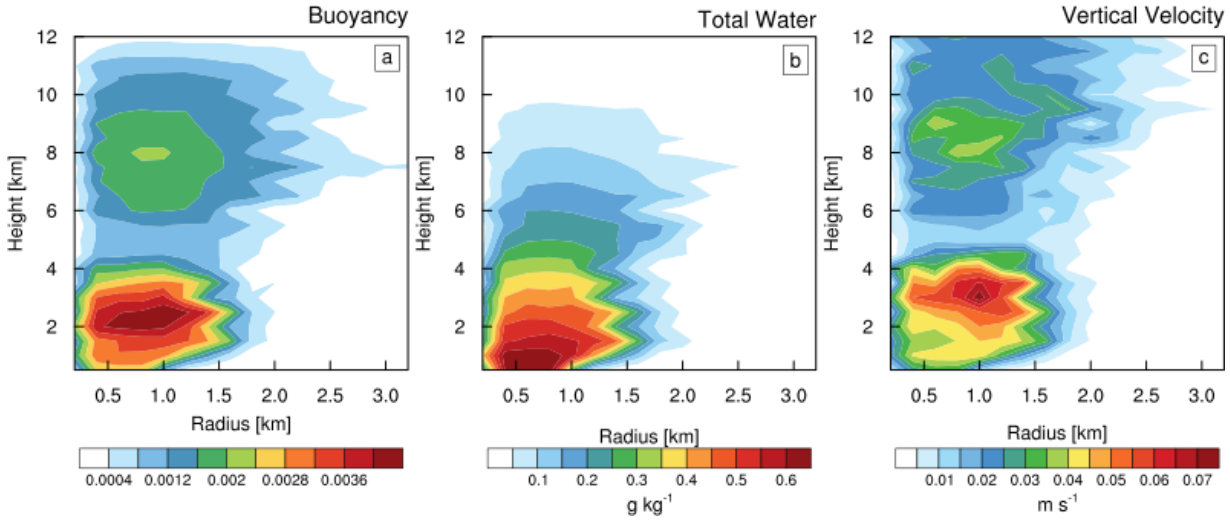

Fig. 4.32 Similar to Fig. 4.31, except for core buoyancy, core total water, and core vertical velocity binned by core radius.

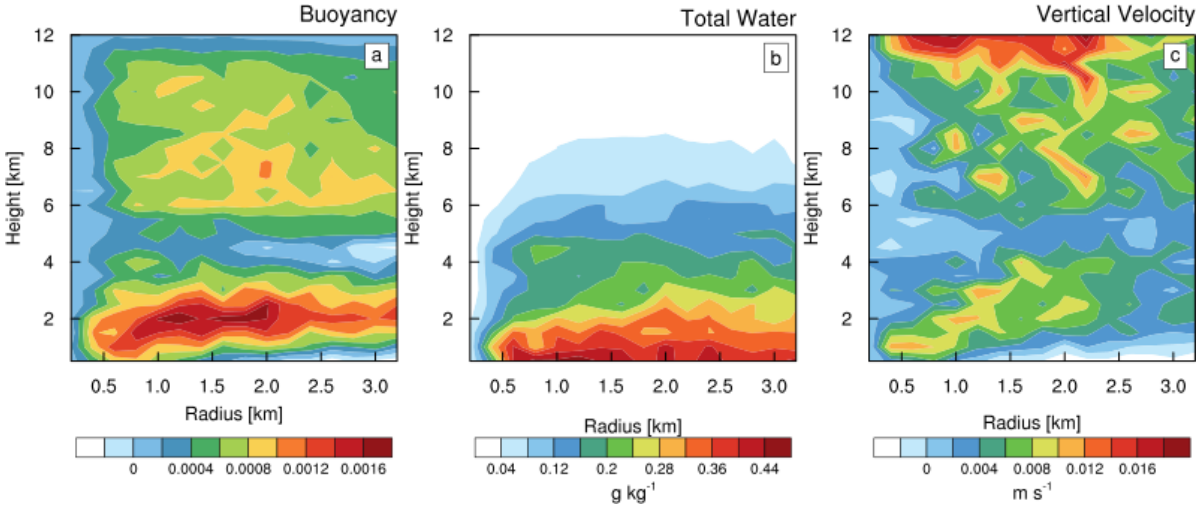

Fig. 4.33 Similar to Fig. 4.32, except data is averaged over cloud volumes and binned by cloud radius.

These results suggest that the inverse relationship between entrainment and radius in a field of deep convection (Fig. 4.31) may be coincidental. If we return to the basic premise of the original hypothesis, that a thermal's fractional entrainment rate is inversely proportional to its radius, then the bubble simulations should exhibit this relationship if the hypothesis were true, despite the fact that the convection is triggered somewhat artificially. If the inverse radius relationship requires other properties of the cloud to also have an inverse relationship (i.e. Fig. 4.33), then the radius relationship should not be used to constrain entrainment in simple models. The fact that the bubble simulations do not show a strong inverse relationship is strong evidence that the factors that constrain entrainment are more complicated than plume theory would suggest.

The recent work of Stirling and Stratton (2012) is a good example of a study that presents a strong argument for an inverse relationship between entrainment and cloud radius. However, it is worth pointing out that this conclusion was reached by estimating entrainment from tracer budgets, which was shown by Dawe and Austin (2011a) to be

problematic and inaccurate due to the effects of the cloud shell. Stirling and Stratton (2012) showed that entrainment and detrainment decreased throughout the transition from shallow to deep convection, but this could possibly be easily explained by the preconditioning and moistening effect of previous convection that would introduce a bias into the tracer budget entrainment estimation, similar to the effect of the shell. One could argue that tracer budget estimates of entrainment are more representative of the entrainment rates used in parameterizations. However, this argument is unsettling, because instead of building parameterizations from a better understanding of entrainment processes, this argument reflects a sense of apathy and tries to bend an interpretation of observations into how we think a priori a parameterization should work. Direct measurement methods reveal the actual entrainment, not just the effective entrainment, and thus future parameterization development would be wise to reflect what we can learn from this new approach.

4.4.3 Entrainment Sources

It would be useful to know the thermodynamic properties of entrained and detrained air when formulating a treatment of entrainment in a cloud model used for a cumulus parameterization. In Section 4.3.2 we saw that the cloud shell is suggested to have a large influence on the air being entrained into the core, since air must pass through the shell to get to the core (ex. Fig. 4.15). The direct entrainment measurement allows us to directly probe the thermodynamic properties of the entrained air and compare to the properties of the core volume. Additionally, we can also look at where entrainment and detrainment are happening in space.

Figure 4.34 shows a 3D rendering of the *4 km* bubble simulation at 12:00, 17:30, 23:30 minutes with iso-surfaces of core entrainment and core detrainment. The initial formation of the cloud experiences strong entrainment at cloud base and equally strong detrainment at cloud top, reminiscient of a torroidal circulation. At later times entrainment and detrainment can be found scattered throughout the cloudy region. Qualitatively, we can see that there is slightly more detrainment (red) occuring than entrainment, consistent with Figure 4.19. The above analysis of azimuthially averaged cloud circualtions suggested entrainment and detrainment were associated with toroidal circulations (Fig. 4.14), but Figure 4.34 shows that there is no consistent pattern of entrainment and detrainment, with the exception of the initial bubble formation. This picture of entrainment at all levels is consistent with the basic idea behind the entraining plume model, in which entrainment is continuously occuring at almost all levels, but this also shows that detrainment is also large, and slightly larger than entrainment (see also Fig. 4.19).

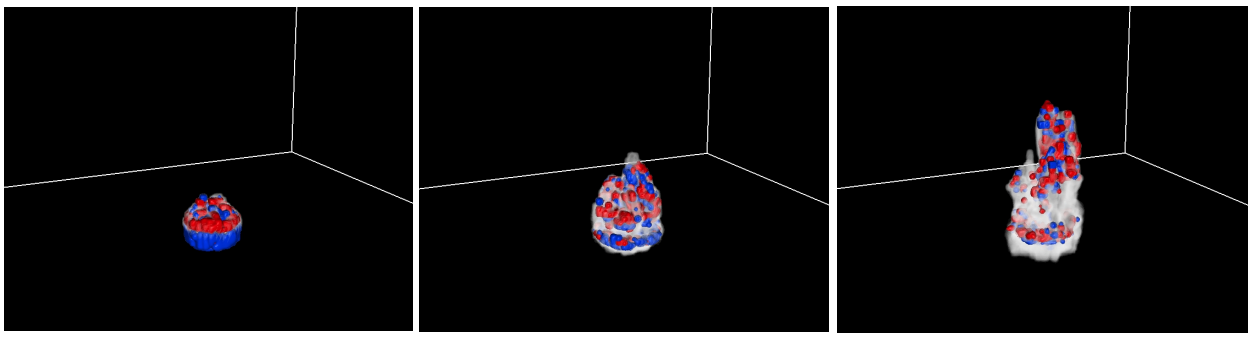

Fig. 4.34 3D rendering of cloud volume (shading) and 0.001 kg m-3 s-1 iso-surfaces of core entrainment (blue) and core detrainmnet (red) at 12:00, 17:30, 23:30 minutes from left to right for the 4km bubble simulation.

A common assumption in entraining plume models is that the thermodynamic properties of entrained air is identical to the average ambient, cloud-free environment. Figure 4.35 shows scatter plots of the total water of the air entraining into the core against

that of the the ambient environment and the cloud shell for each time and level. Points that fall above the line with a slope of one, indicate that the entraining air has more total water than the quantity on the abscissa. Also, note that the total water is strongly dependent on height above the surface, so both axes can be loosely interpreted as the height of the data. The entraining air is notably wetter than the environment, whereas the shell air provides a good predictor of the total water being entrained into the core.

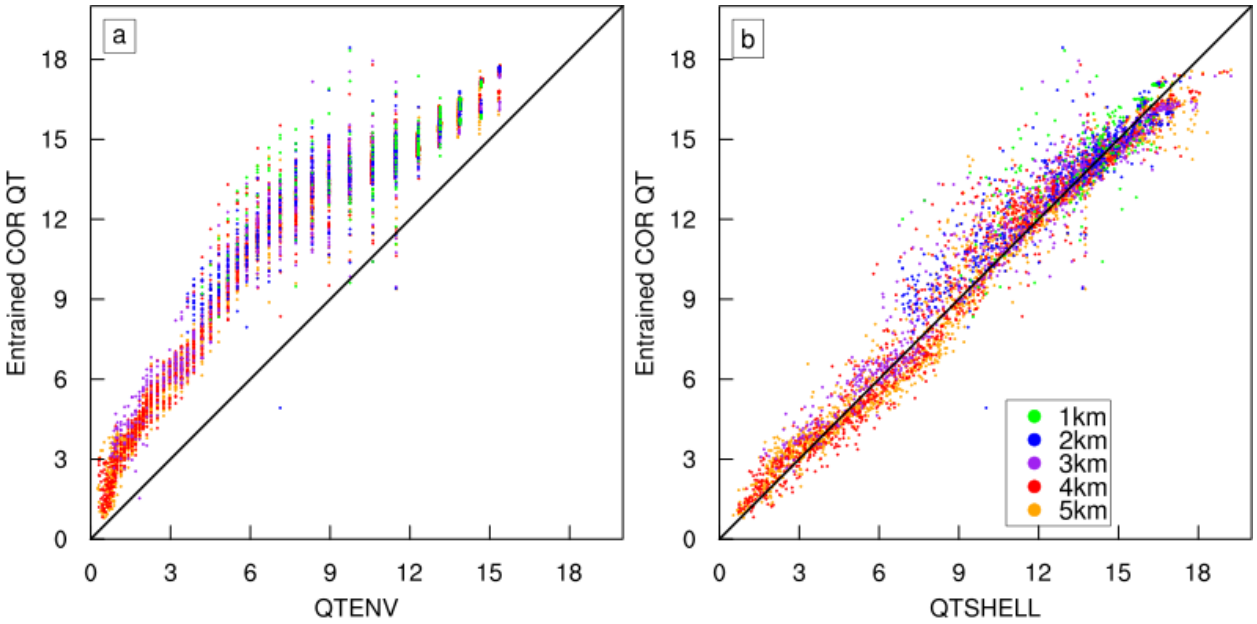

Fig. 4.35 Scatter plot of the total water of air being entrained in the core against that of the cloud shell (a) and the ambient environment (b) for each time and level of the bubble simulations.

There is a discrepancy in the relationship shown in Figure 4.35b at mid-levels, around *8-15 g kg*$^{-1}$, where the entrained air is slightly wetter than the average total water of the shell at those levels. This may indicate a degree of heterogenity in the cloud shell. A slightly different interpretation could be that the entrained air is coming from lower levels that tend to be wetter. In order to see the evolution of the air that is entrained into the core, we can composite the Lagrangian parcel (LP) data around entrainment events. Figure 4.36 shows the lagged composite evolution height and total water of parcels that experience

entrainment into the core between the altitudes of *2-10 km*. Note that the composites are calculated as relative to the value at the time of entrainment. Only the *3-5 km* bubble simulations are shown, due to a lack of parcel entrainment events with smaller bubbles above *2 km*. The composite picture shows that parcels ascend from *100-200 m* before they are entrained, and then descend several hundred meters later on after being detrained (Fig. 4.36a). Interestingly, the *4 km* bubble case suggests that many parcels descend and re-ascend prior to entrainment. This is likely due to parcels that are entrained multiple times (Yeo and Romps 2013). The standard deviation of parcel heights 2-4 minutes prior to entrainment is shown in the gray shading and has a large spread, with some parcels ascending *350 m* prior to entraining into the core. The total water composite shows that parcels become substantially wetter prior to entrainment (Fig. 4.36b), consistent with conditioning of entrained air by the moist shell air. This analysis also shows that parcels entraining into the wider clouds are wetter prior to entrainment, suggesting that the shell has a larger effect on the entrained air in a wider cloud. At first this may seem inconsistent with the Figure 4.17 which showed that the shell thicknesses tended to be similar among the bubble simulations. However, recall the azimuthially averaged picture in Figure 4.15 in which the air entering the core of the larger clouds generally takes a longer path since it is moving inward and upward as it is entrained into the core.

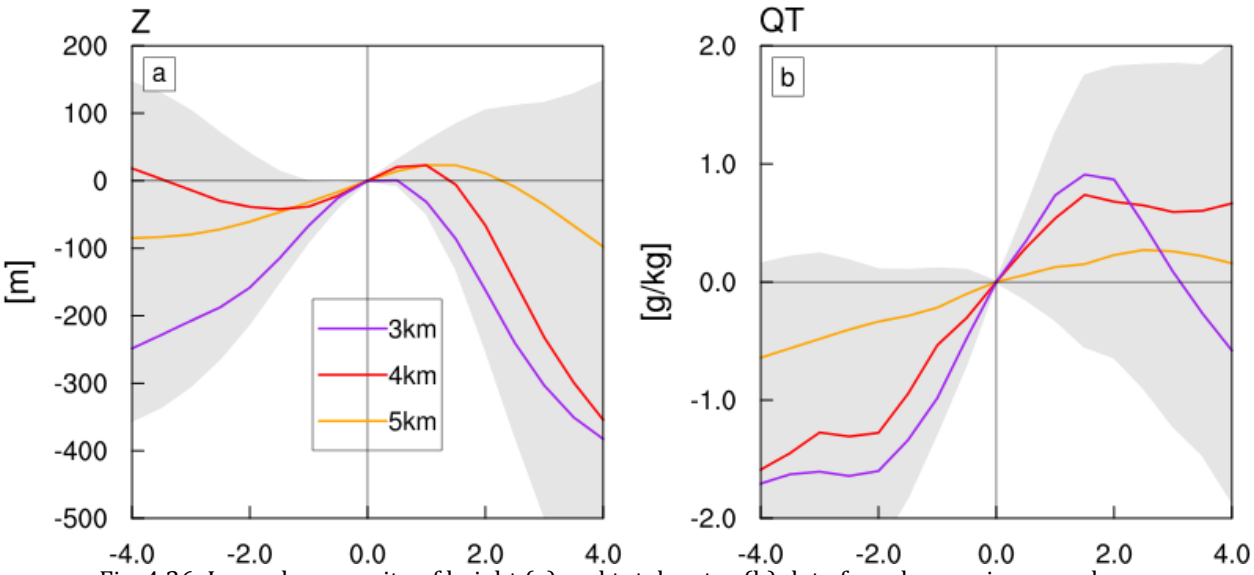

Fig. 4.36 Lagged composite of height (a) and total water (b) data from lagrangian parcels that experience entrainment into the core for the *3-5 km* bubbles. The abscissa indicates the time relative to the time of entrainment. Data is considered in the altitude range of *2-10 km* and is plotted as an anomaly relative to the value at the time of entrainment (i.e. t=0). The shaded region denotes the range of one standard deviation for all data considered.

The composite picture of the LP data in Figure 4.36 provides a smoothed chacterization of entrained parcels, but it masks the interesting complexity of the turbulent circulations within the cloud. Figure 4.37 provides another perspective on the LP data from the *5 km* bubble simulation, by selecting a group of 40 parcels that have the largest variance in height among all parcels, and plotting their height vs. radius from the center of the domain. This parcel selection method is a simple and effective way to identify parcels that are in the core at some point in the simulation, and thus these parcels also generally experience at least one entrainment and detrainment event. The parcel paths are colored such that warmer colors indicate a larger variance in the vertical position. The start and end points are denoted with green and red markers, respectively. Figure 4.37 offers some interesting insight into the cloud circulations. One can notice several "loops" in parcel paths, suggests that several parcels are detrained and subsequently re-entrained (Yeo and

Romps 2013). By focusing on the placement of the start and end markers, we can see a tendency for parcels the be displaced outward from their starting position. Very few parcels are observed to have any large negative height displacement over the evolution of the cloud, consistent with Eulerian metrics that show very little downward mass flux (not shown).

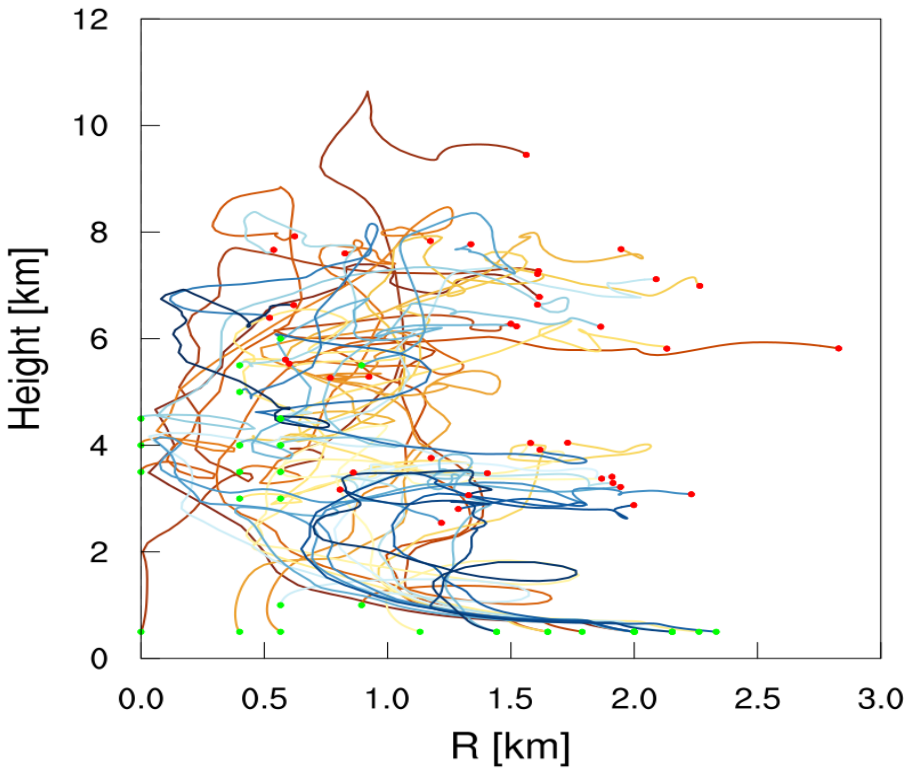

Fig. 4.37 Selected lagragian parcel trajectories from the *5 km* bubble in height vs. radius space (see text). Warmer colors indicate parcels with a larger variance in their vertical position.

Another interesting look at the LP data comes from plotting the parcel trajectories in height vs. MSE (Fig. 4.38) for the same parcels used in Figure 4.37. At low levels we can see that the parcels with larger initial MSE tend to also be colored with a warmer color, indicating that they will end at a higher altitude. At mid levels we can still distinguish the parcels with more vertical displacement as having larger MSE, which indicates that these

parcels have experienced less dilution by entrainment and will continue to rise further in altitude. The final position markers (red) show that many of the parcels end with higher MSE than the domain mean (black line). The dashed black line shows the domain mean saturation static energy, which is often used an neutral buoyancy condition in convective parameterizations (ex. Moorthi and Suarez 1992), and so we can tell when the parcels are buoyant when they lie to the right of this dashed line. It is interesting that we see limited cases where parcels cross this line, indicating negative buoyancy, but then continue to ascend and become positively buoyant again. This could be due to virtual temperature effects, which would lower the saturated static energy, but this could also be due to parcels that are detrained and re-entrained. Generally, once parcels have their MSE fall below the saturation static energy, they forfeit their participation in the core. A parcel that ascends without any dilution would tend to follow a nearly vertical line in this framework, but there does not seem to be any evidence for undilute ascent, which has also been concluded by other studies, such as Romps and Kuang (2010a). This picture suggests a range of dilution rates that might be more accurately treated as a stochastic process, as suggested by (Romps and Kuang 2010b).

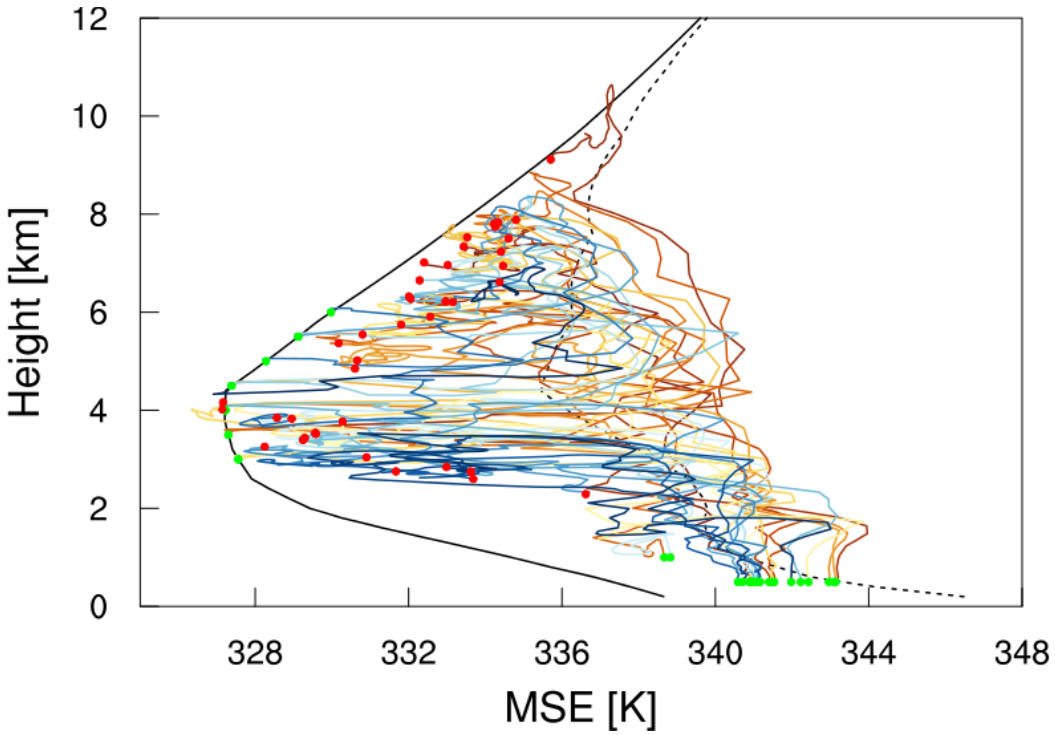

Fig. 4.38 Selected lagragian parcel trajectories from the *5 km* bubble in height vs. MSE space, similar to Fig. 4.37 (see text). Warmer colors indicate parcels with a larger variance in their vertical position. The solid and dashed black lines shows the mean MSE and saturated static energy profiles for the entire domain, respectively.

Yeo and Romps (2013) performed a more comprehensive analysis of Lagrangian parcel tracjectories by using a much higher parcel density. With several parcels existing in each grid cell, they were able to calculate a well constrained estimate of entrainment that agreed with direct measurement results (Romps 2010). They were also able to show that many parcels experience recurring entrainment events and are recycled through the core over the lifetime of a single cloud. Unfortunately, the number of parcels that are entrained in our study is very low, which does not allow us to make a solid conclusion about how much air is recycled through these clouds, and how this varies with cloud size. However, we do in fact observe a small group of parcels that are entrained multiple times.

4.4.4 Cloud Shell Charateristics

The above analysis can provide guidance for formulating entrainment in a convective parameterization. The results suggest that entraining ambient environmental air does not accurately represent the entrainment process. However, we are still left with several challenges. First of all, the results here do not suggest a robust relationship that can be used to determine the magnitude of the entrainment rate, which is outside the scope of this study. Even if we have both the entrainment and detrainment rates accurately predicted we need a way to predict the thermodynamic characteristics of the shell, which then can be used to prescribe the properties of the entrained air. If we plot the total water of the shell against that of the environment, we find that the shell is consistently much wetter than the environment (Fig. 4.39a). When we compare the shell to the core we find an ambiguous result, in that sometimes the shell is wetter, but sometimes it is drier (Fig. 4.39).

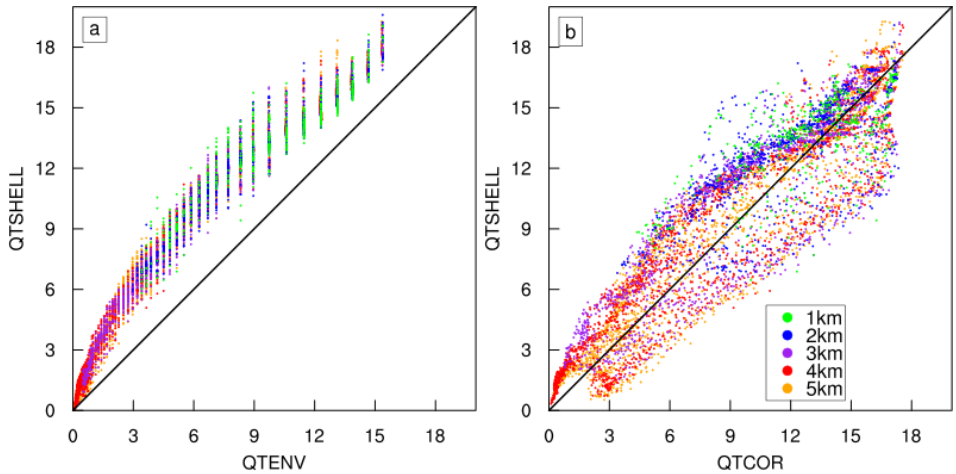

Fig. 4.39 Scatter plot of the total water in the shell against that of the environment (a) and the core (b) for each time and level of the bubble simulations.

We expect the shell to be made up of air that was previously detrained from the core. If we plot the total water of the shell to that of the detrained core air we see that the

detrained air tends to be wetter than the average of the shell air (Fig. 4.40a). Alternatively we might naively assume that the shell is made from a crude mixture of equal parts detrained core air and dry environmental air entrained into the shell. To test this, Figure 4.40b shows the shell air against equal parts mixture of total water from the detrained core air and environmental air at that level. This crude "first guess" approximation of a mixture of detrained core air and environmental air appears to provide a better constraint on the properties of the shell. The shell tends to be slightly wetter than this mixture at all levels, which might be indicating that the environmental air has originated from a lower level where the total water is higher. Alternatively, this could indicate that the detrained core air in the mixture tends to come from higher levels. Employing both of these ideas does in fact reduce the spread of the relationship in Figure 4.40b (not shown), but this does not resolve why the shell tends to be wetter than the mixture. Further tuning of the mixture proportions and height offsets for the detrained and environmental air will likely lead to a more constrained relationship. Overall, we find that even a crude representation of a mixture between detrained core air and environmental air is a reasonable predictor of the properties of the shell air. This result provides a useful guide for developing a cloud model that considers the evolution of the cloud shell in order to buffer the core in the presence of large entrainment rates.

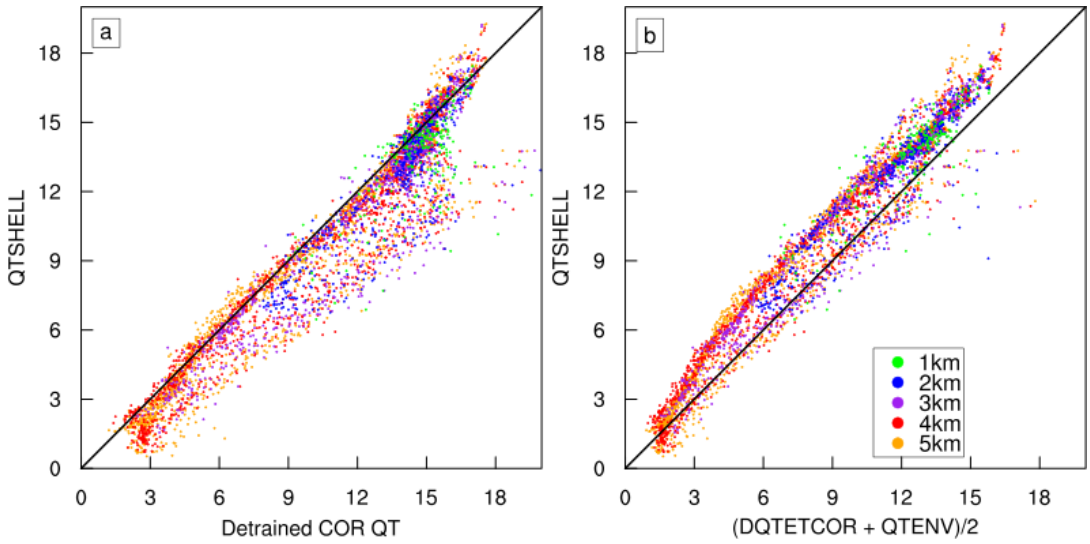

Fig. 4.40 Similar to Fig. 4.39, except for the shell total water against the total water from detrained core air (a) and that of an average of the detrained core air and the ambient dry environment (b).

4.5 Entrainment and Dilution

Entrainment and detrainment exert a strong influence on numerous cloud characteristics, such as cloud top height, cloud lifetime, vertical structure, and updraft speed. Quantifying the effect of entrainment on a specific property is not straightforward. Qualitative descriptions of how entrainment effects convection have been obtained through indirect analysis of the sensitivity to environmental humidity (e.g. Derbyshire et al. 2004). Quantitative analysis of the effects of entrainment can be obtained from a budget analysis, similar to (4.7),

$$\partial_t \langle \rho\phi \rangle = -\partial_z \langle \rho w\phi \rangle + \phi_e \langle e \rangle - \phi_d \langle d \rangle + \rho S_\phi , \qquad (4.23)$$

where S_ϕ represents the sources and sinks of ϕ. This approach gives can estimate the effect of entrainment, but it is not clear how to compare this quantitative estimate between the effect of entrainment on different quantities.

Many studies discuss entrainment as being loosely synonymous with “dilution”. This notion makes sense when thinking of a pre-existing cloud entraining dry air from the

ambient free troposphere, because the mixing of wet and dry air should reduce the condensational heating and rate of buoyancy production, ultimately limiting the updraft intensity and height. This brings the cloud closer to the thermodynamic state of the environment, which defines the state of total dilution. However, the general definition of entrainment used here is not limited to the flux of air across the boundary of an existing cloud (Romps 2010). Thus, the initial formation of a cloudy volume, through condensation at cloud base, is also considered to be entrainment. This leads to large entrainment values at cloud base (see Fig. 4.21), but should not have a diluting effect, and therefore does not provide any valuable information about the sensitivity of cumulus convection to free tropospheric humidity. Alternatively, if we were to estimate the "dilution by entrainment", we should expect no dilution at cloud base, and large dilution at high altitudes where the ambient environment is very dry. We can also consider air being entrained through the cloud shell. If the cloud shell is thicker, then we might expect less dilution by the same amount of entrainment.

Before going further, we need a clear definition of dilution. When discussing the "dilution of a cloud", one should recognize that there are several relevant properties of a cloud, and these may be diluted at different rates for the same amount of entrained mass. Therefore, the word "dilution" in this study is used only in the context of a specific quantity that is relevant to moist convection, such as total water or buoyancy. Hence, we define the dilution of some quantity ψ by some process (i.e. entrainment) as the implied change in the cloud volume mean of anomalous ψ due only to that specific process. The anomaly value of ψ needs to be defined relative to the state of total dilution, which for most cases will be the mean value of the surrounding environment. The specific processes of interest

are entrainment and detrainment, but other processes could be considered, such as the dilution of buoyancy by radiative cooling or precipitation. Notice that this definition allows for *negative dilution*, which can also be referred to as *concentration*. Defining dilution in this way can provide a quantitative measure of the effect of entrainment.

4.5.1 Dilution of Quasi-Conserved Quantities

In order to quantify the dilution by entrainment we make the assumption that the dilution of the anomaly of some anomalous quasi-conserved variable ψ, like moist static energy, can be described by a decay equation,

$$\left[\frac{\partial\bar{\psi}}{\partial t}\right]_{\varepsilon} = -D_{\varepsilon}\bar{\psi}\,, \tag{4.24}$$

where the square brackets on the left-hand side represent an operator that yields the tendency of $\bar{\psi}$ *due only to entrainment*. The overbar represents a horizontal mass weighted mean over a cloud volume defined as:

$$\bar{\psi} = \frac{\Sigma\rho\psi dv}{\Sigma\rho dv}, \tag{4.25}$$

where ρ is the air density and dv is the volume of each grid cell. D_{ε} has units of s^{-1}, and represents the timescale of dilution. If we invert the dilution timescale, we can interpret this as the *e*-folding time of $\bar{\psi}$ due to entrainment. This is the time it would take $\bar{\psi}$ to decrease by the fraction *1/e*, if entrainment were the only process affecting $\bar{\psi}$. Note that it is very important that $\bar{\psi}$ is expressed as an anomaly from the state of total dilution, so that an anomaly value of zero indicates that no more dilution can occur. Otherwise, the dilution timescale would represent the time needed to dilute the absolute value of ψ to absolute zero, which for many variables (i.e. moist static energy) would not make any sense.

We can "discretize" the entrainment tendency operator to get,

$$\frac{\bar{\psi}_2 - \bar{\psi}_1}{\Delta t} = -D_\varepsilon \bar{\psi}_1 . \tag{4.26}$$

The key of this derivation is to make the left-hand side of (4.26) only representative of the change in $\bar{\psi}$ due to entrainment. To do this, $\bar{\psi}_2$ must only include the implied impact of entrainment at the time in question. Since the direct measurement technique gives us accurate entrainment rates at every point, we can formulate this as,

$$\bar{\psi}_2 = \frac{\Sigma(\rho\psi + \varepsilon\psi)dv}{\Sigma(\rho + \varepsilon)dv}, \tag{4.27}$$

where ε represents the mass entrainment over the output period. This is a slightly misleading description, because the raw entrainment rate from the direct measurement scheme is actually expressed as a density flux with units of *kg m^{-3} s^{-1}*. So if we multiply the entrainment by the time-step we get ε, which has units of *kg m^{-3}*. When ε is then multiplied by *dv* we obtain the total mass entrained over the time-step. The timestep for the simulations here is 2 sec.

By solving (4.26) for D_e and using (4.27) we get,

$$\begin{aligned} D_\varepsilon &= -\frac{\bar{\psi}_2 - \bar{\psi}_1}{\bar{\psi}_1 \Delta t} \\ &= -\frac{\left[\dfrac{\Sigma(\rho\psi + \varepsilon\psi)dv}{\Sigma(\rho + \varepsilon)dv}\right] - \bar{\psi}}{\bar{\psi}\Delta t} \end{aligned} \tag{4.28}$$

.

In the second line of (4.28) we have dropped the subscripts for brevity. Some further manipulation allows us to cancel and reorganize terms,

$$
\begin{aligned}
D_e &= -\left[\frac{1}{\Sigma(\rho+e)dv}\right]\frac{\left[\Sigma(\rho\psi+e\psi)dv\right]-\bar{\psi}\Sigma(\rho+e)dv}{\bar{\psi}\Delta t} \\
&= -\left[\frac{1}{\Sigma(\rho+e)dv}\right]\frac{\left(\frac{\Sigma\rho dv}{\Sigma\rho dv}\right)\Sigma\rho\psi dv+\Sigma e\psi dv-\bar{\psi}\Sigma\rho dv-\bar{\psi}\Sigma edv}{\bar{\psi}\Delta t} \\
&= -\left[\frac{1}{\Sigma(\rho+e)dv}\right]\frac{\left(\frac{\Sigma\rho\psi dv}{\Sigma\rho dv}\right)\Sigma\rho dv-\bar{\psi}\Sigma\rho dv+\Sigma e\psi dv-\bar{\psi}\Sigma edv}{\bar{\psi}\Delta t} \cdot \\
&= -\left[\frac{1}{\Sigma(\rho+e)dv}\right]\frac{\cancel{\left(\bar{\psi}\Sigma\rho dv-\bar{\psi}\Sigma\rho dv\right)}+\Sigma e\psi dv-\bar{\psi}\Sigma edv}{\bar{\psi}\Delta t}
\end{aligned}
\tag{4.29}
$$

The third line of (4.29) has substituted the definition of $\bar{\psi}$ from (4.25). Pulling the mass entrainment terms out in front we arrive at a usable expression for estimating the dilution of ψ by entrainment,

$$
D_\varepsilon = \left[\frac{\Sigma\varepsilon dv}{\Sigma(\rho+\varepsilon)dv}\right]\frac{\bar{\psi}-\frac{\Sigma\varepsilon\psi dv}{\Sigma\varepsilon dv}}{\bar{\psi}\Delta t}. \tag{4.30}
$$

We can similarly derive the "dilution by detrainment" as,

$$
D_\delta = \left[\frac{\Sigma\delta dv}{\Sigma(\rho-\delta)dv}\right]\frac{\frac{\Sigma\delta\psi dv}{\Sigma\delta dv}-\bar{\psi}}{\bar{\psi}\Delta t}, \tag{4.31}
$$

Where δ is the mass detrainment rate.

The first term of the product on the right-hand side of (4.30) and (4.31) represents the mass entrainment or detrainment as a fraction of the final mass associated with $\overline{\psi_2}$. This is a necessary correction to the implied reduction in $\bar{\psi}$ indicated by the second term. We must be careful to ignore data points in which entrainment and detrainment are equal to zero, as this will yield a singularity in the numerator of second term of (4.30) and (4.31).

We can immediately see some intrinsic properties of the dilution timescale by considering some special limiting cases. For example, if $\varepsilon \approx 0$ then the first term in the

product of (4.30) will go towards zero so that the cloud dilution is effectively zero. If the entrainment is large and ψ is identical in both the entrained air and cloud air, then D_ε will be zero as we would expect due to the numerator of the second term. If the value of ψ in the entrained air is larger than that of the cloud, then the cloud will experience negative dilution, or concentration, which implies entrainment is enhancing ψ. The scenario we are most interested in that will influence the cloud structure and lifetime, is when the entrained ψ is less than that of the cloud, yielding positive dilution.

4.5.1 Dilution of Non-Conserved Quantities

With some simple modifications to the approach in the previous section, we can also derive a formula for estimating the dilution of a quantity that is strictly not conserved for moist processes. If we return the definition of the dilution by entrainment, but instead of a generic quantity, we use the virtual potential temperature θ_v to get at something analogous to the dilution of buoyancy, then we can write the dilution by entrainment as,

$$D_\varepsilon = -\frac{\overline{\theta_{v2}} - \overline{\theta_{v2}}}{\overline{\theta_{v2}}\Delta t}. \tag{4.32}$$

The challenge for this non-conserved quantity is to formulate $\overline{\theta_{v2}}$. To do this we need to account for the final mixture of cloud air and entrained air, but additionally we need to add a diabatic correction term Q.

$$\overline{\theta_{v2}} = \frac{\Sigma(\rho\theta_v + \varepsilon\theta_v)dv}{\Sigma(\rho + \varepsilon)dv} + Q. \tag{4.33}$$

For the case of virtual potential temperature, the correction term needs to estimate the amount of cooling that occurs when liquid condensate is evaporated into vapor to saturate the entrained air. In other words, we need to calculate the latent heat required to make up

for the saturation deficit of the entrained air, and then average this heat across the final cloud volume. If we ignore the rare case where there is not enough liquid water to saturate the entrained air, as well as the change in the saturation deficit relative to ice, we can write this simply as,

$$Q = -\frac{\frac{L_v}{c_p}\Sigma\varepsilon(q^* - q_\varepsilon)dv}{\Sigma(\rho+\varepsilon)dv}. \tag{4.34}$$

Substituting (4.33) into (4.32) we get,

$$D_\varepsilon = -\frac{\left[\frac{\Sigma(\rho\theta_v + \varepsilon\theta_v)dv}{\Sigma(\rho+\varepsilon)dv} + Q\right] - \overline{\theta_v}}{\overline{\theta_v}\Delta t}. \tag{4.35}$$

This can be simplified, as before, to obtain,

$$D_\varepsilon = \left[\frac{\Sigma\varepsilon dv}{\Sigma(\rho+\varepsilon)dv}\right]\frac{\overline{\theta_v} - \frac{\Sigma\varepsilon\theta_v dv}{\Sigma\varepsilon dv}}{\overline{\theta_v}\Delta t} - \frac{Q}{\overline{\theta_v}\Delta t}. \tag{4.36}$$

Using the diabatic correction term from (4.34) we get,

$$D_\varepsilon = \left[\frac{\Sigma\varepsilon dv}{\Sigma(\rho+\varepsilon)dv}\right]\frac{\overline{\theta_v} - \frac{\Sigma\varepsilon\theta_v dv}{\Sigma\varepsilon dv}}{\overline{\theta_v}\Delta t} + \frac{\frac{L_v}{c_p}\Sigma\varepsilon(q^* - q_\varepsilon)dv}{\overline{\theta_v}\Delta t\Sigma(\rho+\varepsilon)dv}. \tag{4.37}$$

We can see from (4.37) that the cooling by evaporation of cloud water acts to enhance the buoyancy dilution by entrainment, which is what we would logically expect. This also shows that entrainment of drier air will have a larger effect on reducing the buoyancy. For the dilution by detrainment of a non-conserved variable we generally do not need to consider any diabatic correction.

4.5.2 Dilution Analysis

The following analysis will only focus mostly on the core, since the impacts of entrainment on the core are more relevant for convective parameterizations. Notice in (4.30), (4.31), and (4.37) that there are several denominator terms that can potentially be zero, or very close to zero. Each of these potential pitfalls has been carefully considered, and numerical constraints have been rigously tested in the calculation of dilution to avoid unreasonable values. Some of these choices are straightforward, such as when the anomaly value of the tracer is zero and the second term blows up. This represents a situation in which the cloud properties are identical to the surrounding environment and is therefore completely dilute, so omitting data in this scenario makes sense. However, some choices were not so straightforward, such as when the mass of the cloud is small compared to the values of entrainment or detrainment, which can result in extremely large or negative values of the first term in (4.30), (4.31), and (4.37). In order to deal with these cases, we have constrained the first term to be greater than *0.0*, and less than *1.0*. We feel that this is a reasonable simplification that does not significantly influence the results.

Figure 4.41 shows the mean profile of fractional entrainment alongside dilution by entrainment for total water ($q_t = q_v + q_l + q_i$), moist static energy (MSE; $h = c_p T + gz + L_v q_v$), and virtual potential temperature ($\theta_v = \theta(1 + 0.608 q_v)$). Note that MSE is considered as an anomaly from the saturated static energy ($h^* = c_p T + gz + L_v q_v^*$). Unfortunately, the attempts to constrain extreme dilution values were only moderately successful, which is why the dilution estimates for single clouds are very noisy. As will be shown below, averaging over multiple clouds or a field of convection alleviates this problem, and so this approach is still valid and useful for studying entrainment processes. The dilution of q_t and h at cloud base

is small relative to upper levels, as we expect, because although there is large entrainment, the air being entrained is very similar to the air already in the core. At higher altitudes where the environmental air is drier, dilution of q_t and h is larger and positive, except for some erratic spikes. Inverting the dilution, we find that that the dilution timescale of q_t is on the order of ~1 hour at lower levels and approximately ~10 minutes at upper levels (Fig. 4.41b). For h there is generally a shorter timescale of approximately 1-10 minutes, although dilution of h tends to be noisier, for a yet unidentified reason (Fig. 4.41c). The profile of θ_v dilution by entrainment is somewhat different than q_t or h, with large values near the cloud base and generally smaller values at middle levels (Fig. 4.41d). The large values at cloud base are due to the diabatic adjustment term Q_ε particularly in response to the secondary core formation at low levels that can be seen in preceding analysis, such as Figure 4.5. Dilution of θ_v also increases at upper levels, similar to q_t dilution. The dilution timescale of θ_v is roughly ~3-5 minutes at lower levels and ~1 minute or less at upper levels. Similar results can be obtained for cloud volumes instead of core (not shown).

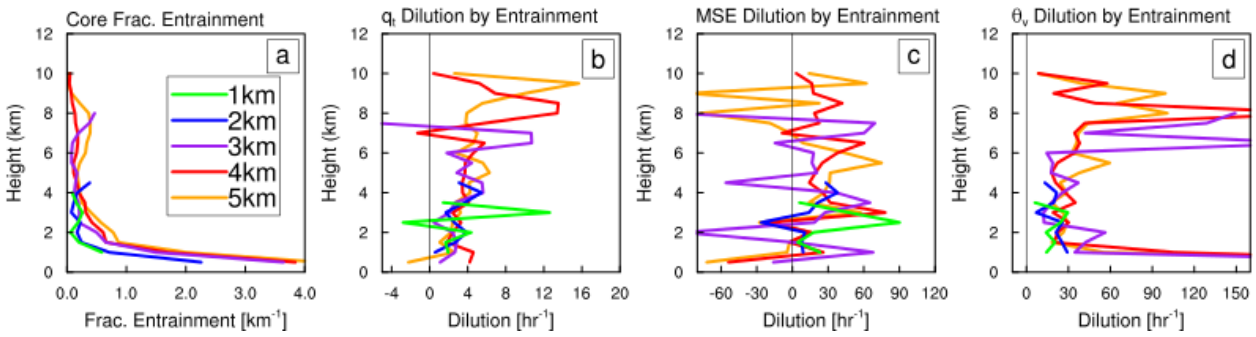

Fig. 4.41 Time mean profiles of fractional entrainment (a), and core dilution by entrainment of q_t (b), h (c), and θ_v (d) over the initial 30 minutes of the bubble simulations.

We can gain a deeper understanding of the dilution profiles by analyzing the individual terms of the entrainment dilution formulas in (4.30) and (4.37). The components of (4.30) can be written as,

$$D_{\varepsilon 1} = \frac{\Sigma \varepsilon dv}{\Sigma(\rho + \varepsilon) dv}, \tag{4.38}$$

$$D_{\varepsilon 2} = \frac{\bar{\psi} - \frac{\Sigma \varepsilon \psi dv}{\Sigma \varepsilon dv}}{\bar{\psi} \Delta t}. \tag{4.39}$$

The term in (4.38) describes the change in mass entrainment, and the term in (4.39) describes the effect of thermodynamic differences of the entraining and cloud air. We can similarly isolate the diabatic correction term from (4.37) as

$$Q_{\varepsilon} = \frac{\frac{L_v}{c_p} \Sigma \varepsilon (q^* - q_{\varepsilon}) dv}{\bar{\theta}_v \Delta t \Sigma (\rho + \varepsilon) dv}. \tag{4.40}$$

Figure 4.42 shows the dilution components for q_t. The first term, $D_{\varepsilon 1}$, is generally small (Fig. 4.42b), whereas the second term, $D_{\varepsilon 2}$, is considerably larger (Fig. 4.42c). These differences balance out in the product (Fig. 4.42a). The second term shows a more robust increase in height and zero values at cloud base, which is expected since the profile of environmental humidity would directly affect this term. Dilution component profiles of h show similar results, but are generally noisier (not shown). Figure 4.43 shows the product of dilution components $D_{\varepsilon 1}$ and $D_{\varepsilon 2}$ for θ_v, and the diabatic adjustment term Q_{ε} that describes the effect of cooling from vaporization of cloud condensate. The product of $D_{\varepsilon 1}$ and $D_{\varepsilon 2}$ yields a similar dilution magnitude to that of q_t, and increases somewhat with height. Q_{ε} is either larger or comparable to the product of $D_{\varepsilon 1}$ and $D_{\varepsilon 2}$, which explains why the final dilution value is larger than that of q_t (Fig. 4.43a). This tells us that the cooling effect of evaporation due to entrainment of sub-saturated air largely influences the dilution of convection by entrainment. Without this diabatic cooling effect the dilution timescale of θ_v would be much longer.

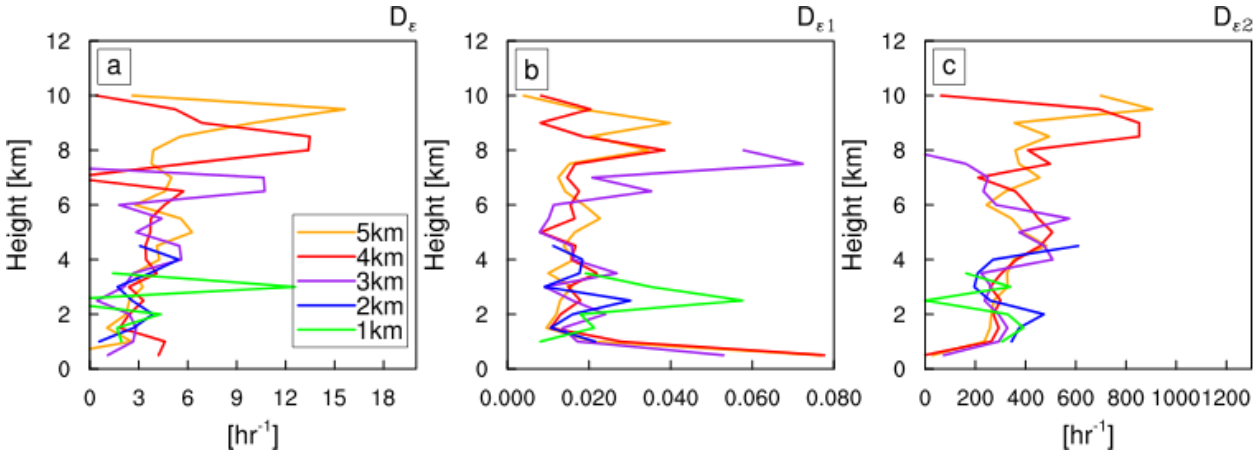

Fig. 4.42 Mean core dilution of q_t by entrainment (a), and core dilution components $D_{\varepsilon 1}$ (b) and $D_{\varepsilon 2}$ (b) for the bubble simulations (see text). Note that the values in (a) are the product of the values in (b) and (c).

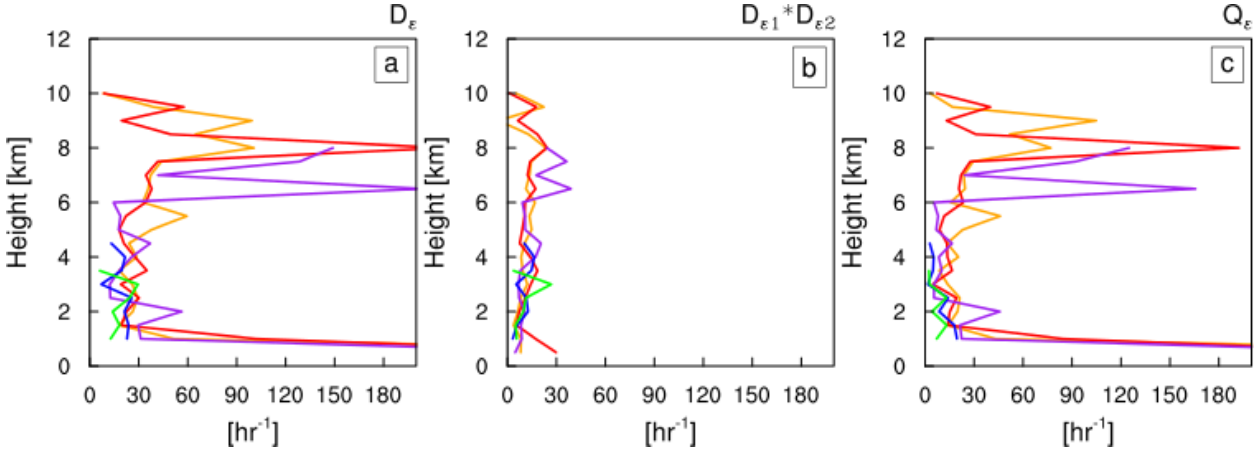

Fig. 4.43 Mean core dilution of θ_v by entrainment (a), the product of core dilution components $D_{\varepsilon 1}$ and $D_{\varepsilon 2}$ (b), and the diabatic adjustment term Q_ε for the bubble simulations (see text). Note that the values in (a) are the sum of the vlaues in (b) and (c).

Figure 4.44 shows similar profiles to that in Figure 4.41, except for dilution by detrainment. Dilution by detrainment is similar to dilution by entrainment for q_t and h, except the sign is reversed and the magnitudes are slightly larger. Note that dilution of θ_v by detrainment is substantially smaller than dilution of θ_v by entrainment (Fig. 4.41d). Negative dilution by detrainment means that the parcels being detrained are effectively keeping the cloud wet and buoyant, and compensating for the detrimental effects of entrainment. This is similar to the shedding thermal concept that some parameterizations

are loosely based on (Raymond and Blyth 1986; Emanuel 1991). A typical entraining plume model only considers entrainment below the level of neutral buoyancy, which would naturally make the net dilution positive. Other theories have modified this idea so that relative amounts of entrainment and detrainment are inversely related to each other and based on some property of the environment, such as the sign of the vertical buoyancy gradient (Bretherton and Smolarkiewicz 1989). The results here suggest that substantial entrainment and detrainment are occurring simultaneously at all levels. The effects of detrainment slightly win out for all three variables.

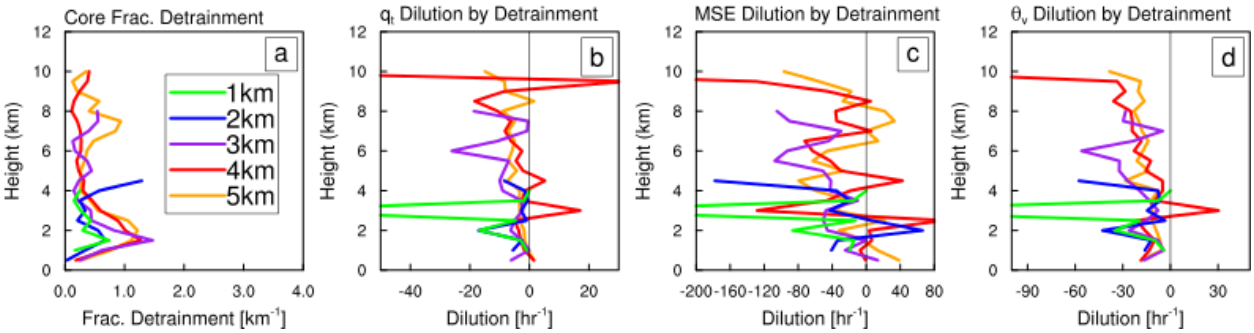

Fig. 4.44 Similar to Fig. 4.41, but for core dilution by detrainment.

An interesting question is what the maximum dilution the core could experience for the given amount of mass entrainment? This is really a question about the thermodynamic properties of the entrained air, so to answer this we can calculate the dilution by entrainment assuming that the entrained air is identical to the environmental air away from the cloud, since this would cause the most dilution. To do this, we modify the numerator of the second term in (4.30) so the "entrained" air has an anomaly of *0.0*, and thus is identical to the mean of the cloud-free environment. This effectively estimates the dilution that would occur if the air entrained into the core did not mix with the cloud shell at all, similar to a typical convective parameterization. Figure 4.45 shows the results of this calculation for core q_t and θ_v. Both variables are notably sensitive to this change, as the

dilution timescale of q_t has increased from ~10-60 minutes in Figure 4.41b, to ~2-3 minute in Figure 4.45a. Dilution of core θ_v by entrainment also increases to the point that the dilution timescale is significantly less than 60 seconds. The profile of the maximum θ_v dilution decreases with height, which simply reflects the environmental θ_v that increases with height. Both of these results give some quantitative insight into how dramatically the shell of previously detrained core air can buffer the core from the effects of dry air entrainment.

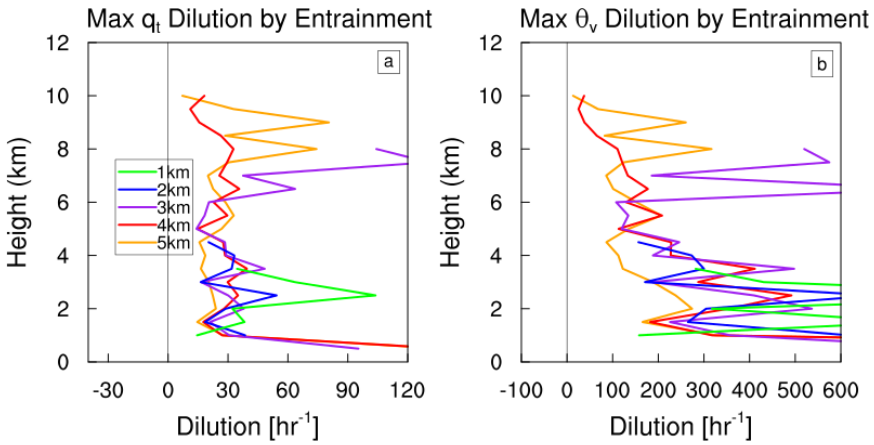

Fig. 4.45 Estimate of the maxium possible dilution by entrainment for q_t and θ_v.

According to the first term in (4.30), more entrainment causes more dilution if all other terms are constant. However, the results above suggest that large entrainment generally does not imply large dilution. This is mainly because the shell can moisten the air before it is entrained into the core, but also because the effects of detrainment can balance out those of entrainment. A more direct way to see that entrainment and dilution are not synonymous is to simply plot the values from each height and time on a scatter plot, such as is done for q_t and θ_v in Figure 4.46. For q_t dilution there is no discernible relationship between dilution and entrainment, which is supported by the binned average relationship in the solid black line (Fig. 4.46a). θ_v dilution exhibits a direct relationship, such that more

entrainment implies more dilution on average. However, from the spread of the scatter points it is evident that this is not a robust relationship (Fig. 4.46b). For both q_t and θ_v there are times when dilution is large and entrainment is small, and vice versa. Similar results can be found for h (not shown).

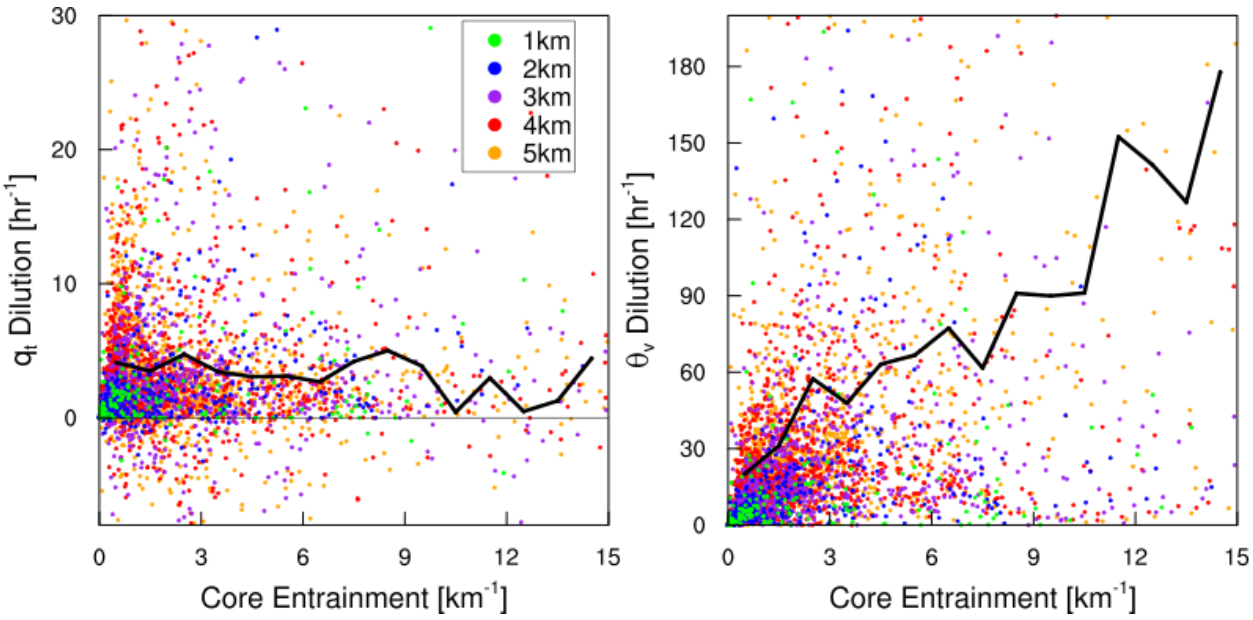

Fig. 4.46 Scatter plot of dilution by entrainment of q_t and θ_v against core entrainment. The solid black line is a binned average of the data points.

We can also plot the core dilution against the core radius to see if wider cores experience less dilution. Figure 4.47 shows the results of this for q_t and θ_v. Interestingly, there does appear to be an inverse relationship between dilution and radius for both q_t and θ_v, although the scatter is still very large. This lends some support to the assumed inverse relationship between entrainment and radius in plume models, because entrainment is effectively synonymous with dilution in those cases. However, these results compel us to conclude that this relationship is not robust enough to justify using it to approximate entrainment to first order in simple cloud models.

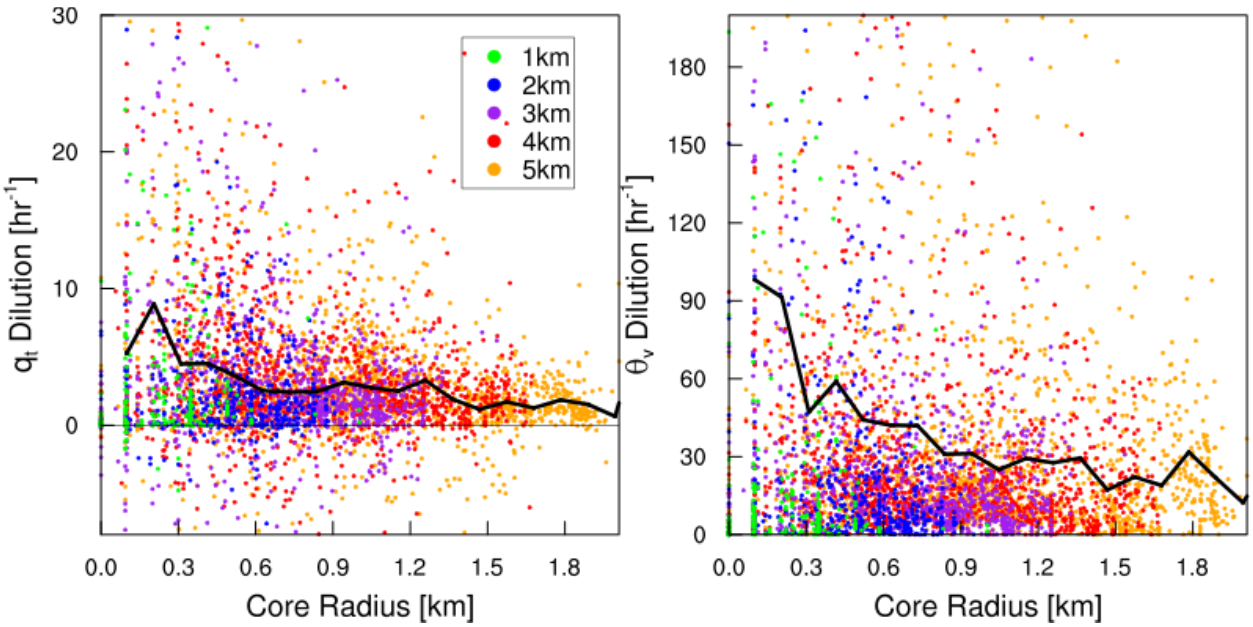

Fig. 4.47 Scatter plot of dilution by entrainment of q_t and θ_v against core radius. The solid black line is a binned average of the data points.

These results are important in the context of the entraining plume model, which are typical designed such that entrainment causes a large net dilution, and entrainment is inversely proportional to radius. Both of these ideas do not hold up to the results from the high-resolution cloud simulations presented here. If these conclusions are robust, then they should be apparent in the DYNAMO simulation, since convection is triggered in a more natural manner. Figure 4.48 shows the mean profiles of entrainment and dilution by entrainment for q_t, h, and θ_v. The DYNAMO simulation has a more humid initial sounding, and therefore we expect weaker dilution by entrainment. Figure 4.48b-c shows that this is the case for q_t and h at upper levels, but lower levels have a similar amount of dilution to the bubble experiments in Figure 4.41. Dilution of θ_v by entrainment also shows a comparable magnitude to the bubble simulations at lower levels, and less dilution at upper levels (Fig. 4.48d). The smaller dilution at upper levels might be related to the smaller core θ_v and q_t anomalies in the DYNAMO simulation at upper levels (Fig. 4.8).

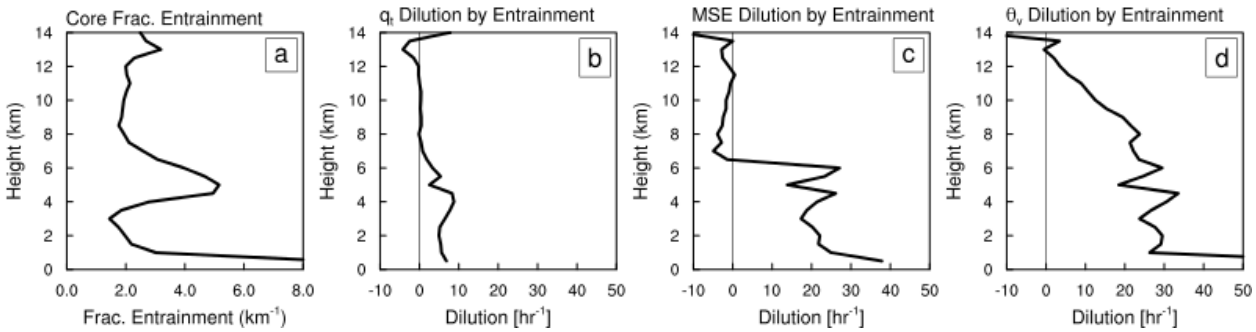

Fig. 4.48 Similar to Fig. 4.41, except for core entrainment and dilution by entrainment from the DYNAMO simulation.

The maximum dilution that would occur from entraining the cloud-free environment, shows a similar increase in dilution by entrainment roughly from ~10 minutes to ~2 minutes for q_t and h (Fig. 4.49b-c). The maximum dilution of θ_v is also larger than the actual dilution, but the increase is more severe, going from ~2-3 minutes to less than a minute at lower levels. Overall, the difference between the actual and maximum dilution highlights the importance of the near-cloud environment that conditions the air that is entrained into the core, and also highlights buoyancy dilution as the prime factor that is affected by the conditioning of the cloud shell.

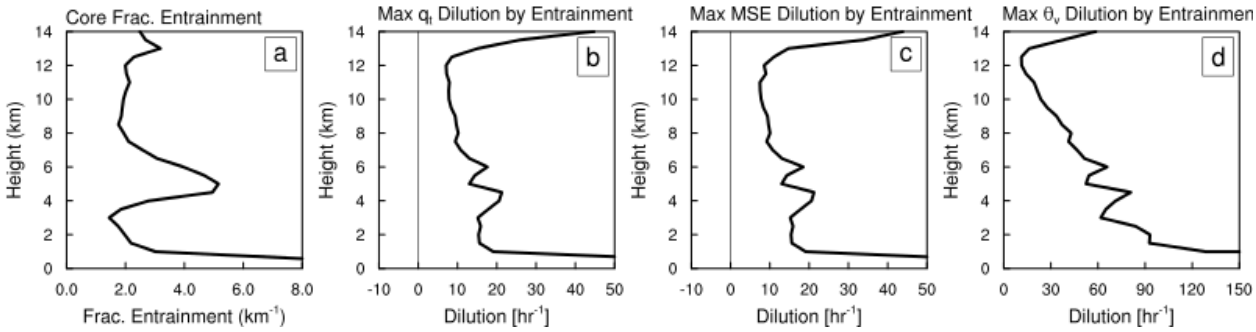

Fig. 4.49 Similar to Fig. 4.45, except for maximum dilution by entrainment from the DYNAMO simulation.

4.6 Sensitivity Experiments

4.6.1 Environmental Humidity

Bechtold et al. (2008) formulated entrainment as proportional to environmental relative humidity in order to improve the sensitivity of convection to environmental moisture in the European Center for Medium Range Forecasting (ECMWF) Integrated Forecasting System (IFS). They proposed that entrainment be specified as,

$$\varepsilon = c_o \left(\frac{q_s}{q_{s,b}} \right)^2 + c_1 \left(\frac{q_s}{q_{s,b}} \right)^3 \left(\frac{q_s - q}{q_s} \right), \tag{4.41}$$

where c_o and c_1 are tunable parameters, q is the specific humidity of the dry environment, and q_s and $q_{s,b}$ are the saturation specific humidity of the parcel level and cloud base, respectively (see their eq. 2). The first term describes the "turbulent" entrainment, which is prescribed to a fixed rate. The second term represents "organized" entrainment, which decreases as environmental humidity increases. This distinction between "turbulent" and "organized" entrainment may be somewhat artificial, but is meant to distinguish between entrainment that happens from relatively small turbulent mixing and convergent circulations on the scale of the cloud circulation.

The idea that entrainment should decrease in a wetter environment was based on many studies that have shown deep convection is highly sensitive to the ambient humidity (Redelsperger et al. 2002; Derbyshire et al. 2004). The recent study of Stirling and Stratton (2012) used tracer budget estimates of entrainment over the course of a diurnal cycle, and found evidence for a direct relationship between entrainment and humidity, instead of an inverse relationship. Using the framework of the bubble experiments and the direct entrainment measurement we can directly test whether entrainment for an individual

cloud changes systematically with a systematic change in the environmental humidity. To do this we conduct additional simulations of the *3*, *4*, and *5 km* bubbles, and increase the tropospheric humidity above *850 hPa*, to avoid affecting the boundary layer where the bubble is initialized. Humidity is increased by adding a value of one standard deviation (σ) at every level. This standard deviation was calculated for the entire Tropics from 2000-2009. The resulting increase in humidity is illustrated in the skew-T diagram in Figure 4.50. These simulations will be referred to by their ambient moisture content as "+1.0σ" and "+0.0σ" (i.e. the control).

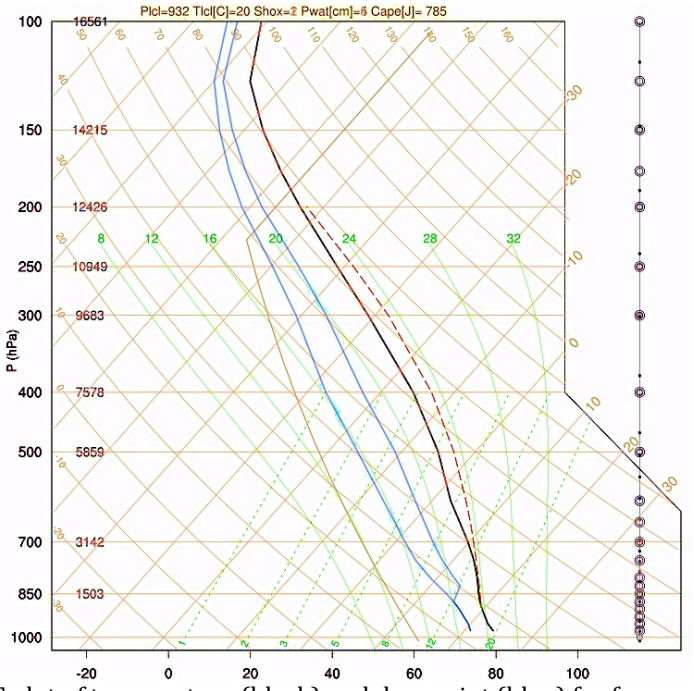

Fig. 4.50 Skew-T plot of temperature (black) and dew point (blue) for four profiles in which the specific humidity has been increased by 0.0 and 1.0 standard deviations, based on ERAi data from the tropical belt (30°S-30°N).

Figure 4.51 shows the time vs. height evolution of core and cloud radius for the *4* km simulations to illustrate the effect of the soundings in Figure 4.50. The terminal height of the core and cloud do not change since the control simulation had already reached the altitude of neutral buoyancy. Other sensitivity simulations with smaller bubbles, that will

not be discussed here, show increased terminal heights in wetter environments (not shown; see also Derbyshire et al. 2004). Radii magnitudes indicate a wider core and cloud volume with higher humidity. The cloud radii also imply that convection last longer with higher humidity, suggesting that the effects of entrainment have somehow been mitigated by the increase in humidity.

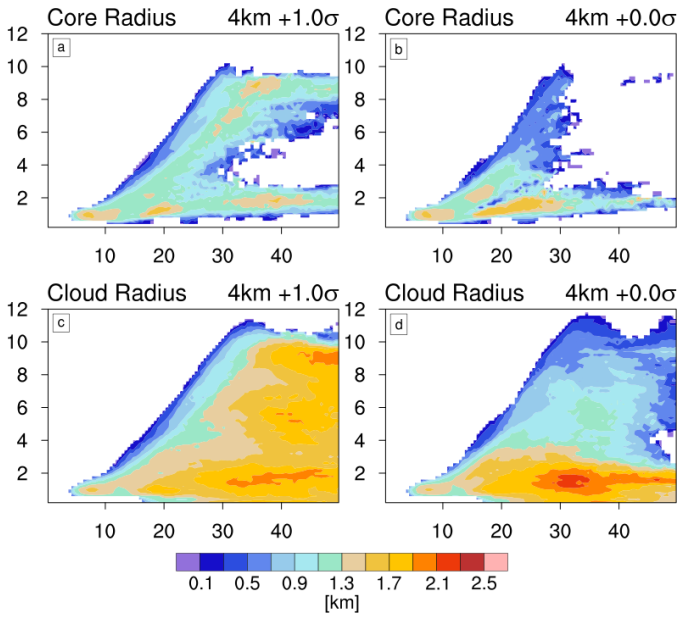

Fig. 4.51 Time vs. height evolution of radius for the cloud core (top) and cloud (bottom) for the *4 km* bubble simulations with varying environmental humidity. The abscissa is time in units of minutes.

The following analysis will compare the control and enhanced humidity cases by averaging across the three simulations for each case to produce average profiles. Figure 4.52 shows the mean fractional core entrainment and detrainment profiles for the simulations with varying tropospheric humidity. We find that the fractional entrainment and detrainment generally increase with increasing humidity, which is contrary to the formulation of Bechtold et al. (2008), but consistent with the findings of (Stirling and Stratton 2012). The un-normalized profiles of core entrainment and mass flux also increase with increasing humidity (Fig. 4.53). Thus, the increase in fractional entrainment rate is

due to an increase in entrainment that is slightly larger in proportion than the increase in mass flux, unlike the assumption of Bechtold et al. (2008).

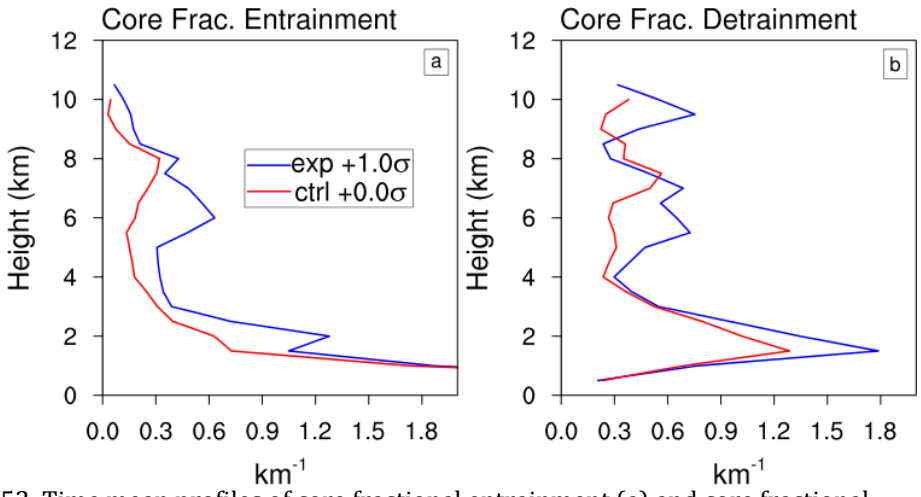

Fig. 4.52 Time mean profiles of core fractional entrainment (a) and core fractional detrainment (b) of the control (red) and increased humidity (red) simulations.

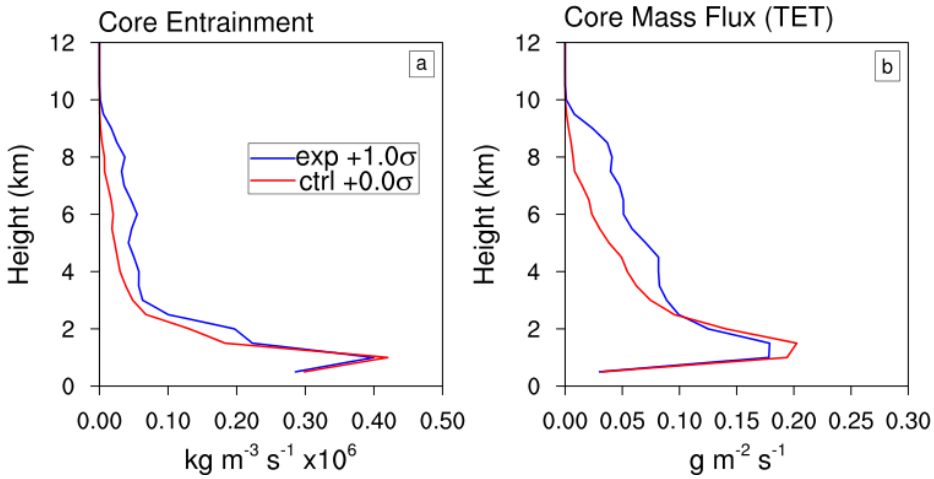

Fig. 4.53 Time mean profiles of core entrainment (a) and core mass flux (b) of the the control (red) and increased humidity (blue) simulations.

Although the entrainment increases with increased humidity, the assumption of Bechtold et al. (2008) could be valid if the effects entrainment are reduced, yielding less dilution by entrainment. Figure 4.54 shows the average profiles of core dilution by entrainment for q_t and θ_v in the control and increased humidity simulations. The results are somewhat similar between the two cases, but there is a hint that the q_t dilution is actually somewhat *larger* with increased humidity, meaning that the core is being diluted faster by

entrainment. Also, there is a hint of the intuitive outcome, that θ_v dilution is reduced at upper levels in the wetter environment.

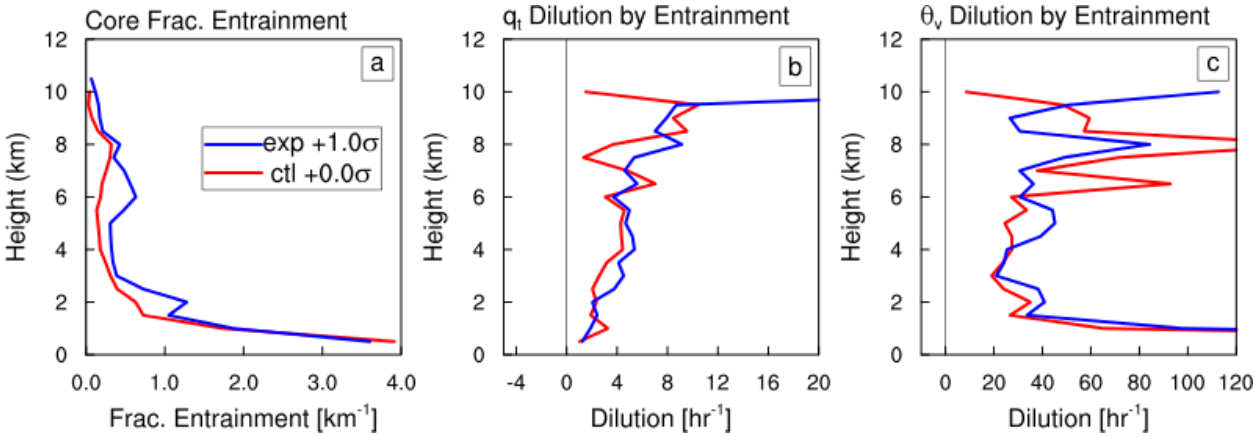

Fig. 4.54 Mean profiles of core entrainment (a), core q_t dilution by entrainment (b), and core θ_v dilution by entrainment (c) of the the control (red) and increased humidity (blue) simulations.

The differences in the simulations with higher entrainment can be seen more clearly if we compare the cloud dilution by entrainment in Figure 4.55. The signals are still somewhat noisy, but the difference in q_t dilution by entrainment clearly shows an increase at mid and upper levels in the wetter environment. On the other hand, dilution of θ_v is reduced at most levels, except for the increase in dilution around an altitude of *3 km*. The overall trend appears to show a decrease of θ_v dilution.

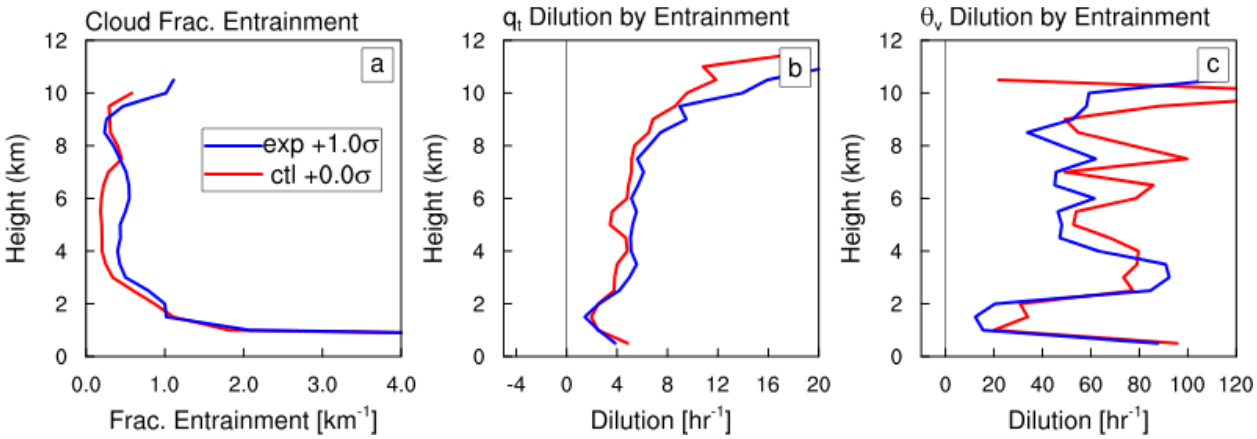

Fig. 4.55 Mean profiles of cloud entrainment (a), cloud q_t dilution by entrainment (b), and cloud θ_v dilution by entrainment (c) of the the control (red) and increased humidity (blue) simulations.

How can we understand the counter-intuitive result that clouds experience more dilution of q_t in a wetter environment? If the ambient air is wetter, we might intuitively think that dilution should decrease, corresponding to a longer dilution timescale. However, a non-intuitive consequence of the wetter environment that we have manufactured is that the saturation specific humidity has not changed. Therefore the total water of the saturated cloud volume has not increased, which means that the cloud is closer to a state of complete dilution (Fig. 4.56). According to the second term of (4.30), if the total water anomaly in the core or cloud is reduced, we can expect a shorter dilution timescale. The other possible explanation for the increased dilution is the increase in mass entrainment, since this would increase the first term of (4.30). However, as will be shown below, the effect of the increased entrainment is not a dominant factor.

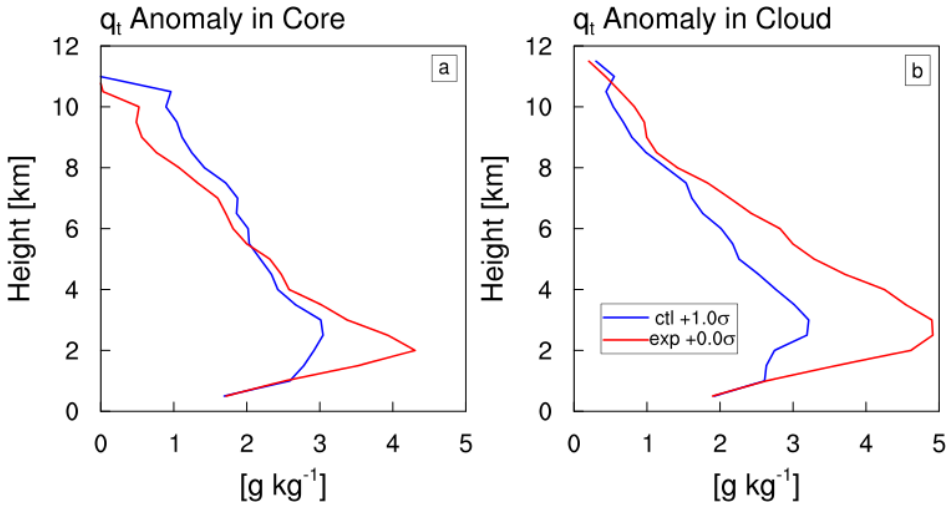

Fig. 4.56 Mean profiles of q_t anomaly for core (a) and cloud (b) of the the control (red) and increased humidity (blue) simulations.

To get a better sense of why the dilution rates have changed in the wetter environment Figure 4.57 shows the cloud q_t dilution by entrainment and the dilution components in (4.38) and (4.39). $D_{\varepsilon 1}$ is similar among the simulations, indicating that the increased mass entrainment is not able to explain the increased cloud dilution in the middle troposphere. The second term ($D_{\varepsilon 2}$) is substantially increased in the wetter environment. The air being entrained into the cloud is naturally wetter in the wetter environment, and so the numerator of $D_{\varepsilon 2}$ is decreased. Hence, the primary reason that explains the increased dilution is that the wetter environment causes the denominator of $D_{\varepsilon 2}$ to decrease. This has the rather simple physical explanation discussed above, that the total water in the cloud has not increased in tandem with the environment. In changing only the humidity we have changed what it means to be completely diluted. Therefore as long as entrainment rate does not change substantially, the cloud will become diluted at a faster rate.

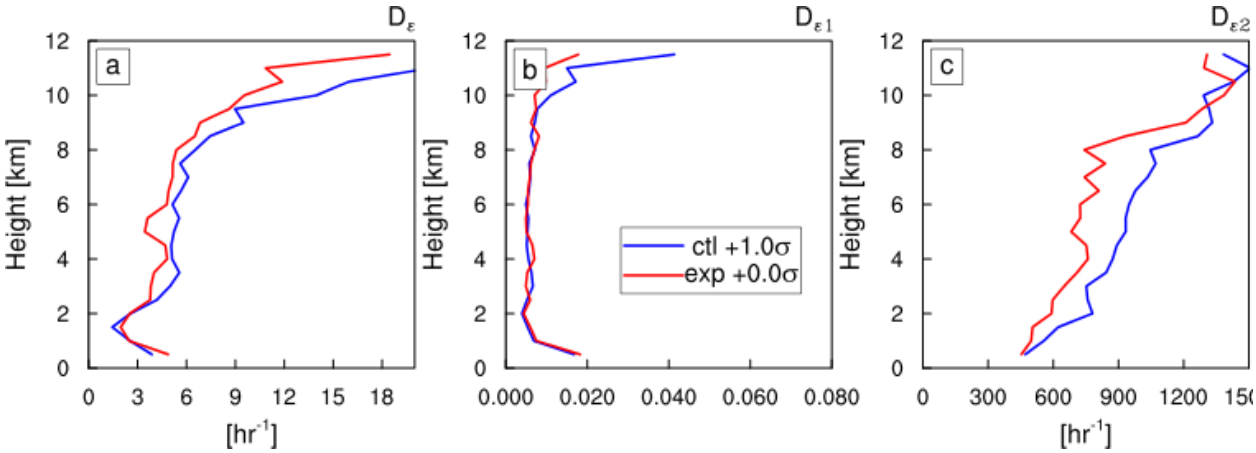

Fig. 4.57 Mean core dilution of q_t by entrainment (a), and core dilution components $D_{\varepsilon 1}$ (b) and $D_{\varepsilon 2}$ (b) for the the control (red) and increased humidity (blue) simulations. Note that the values in (a) represent the product of the vlaues in (b) and (c).

We can understand the decrease of θ_v dilution by examining the product of $D_{\varepsilon 1}$ and $D_{\varepsilon 2}$, and the diabatic term Q_ε (Fig. 4.58). Both components contribute a comparable decrease in dilution of θ_v in the wetter environment (Fig. 4.58b). Therefore the enhancement of convection in a more humid environment can be understood to occur through a reduction in buoyancy dilution by entrainment, both by direct mixing of air with a lower θ_v and diabatic cooling from evaporation of cloud water. It is interesting to note that this reduction in dilution occurs at the same time that entrainment has increased. This indirectly support the assumption of Bechtold et al. (2008), since the entrainment in a convective parameterization is not always the same as entrainment in real clouds(Romps 2010).

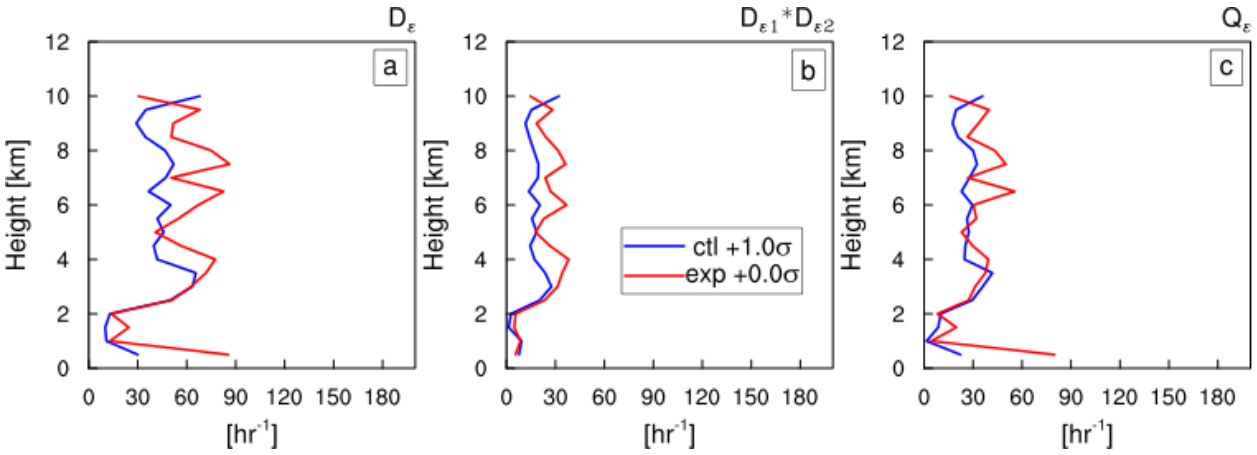

Fig. 4.58 Mean core dilution of θ_v by entrainment (a), the product of core dilution components $D_{\varepsilon 1}$ and $D_{\varepsilon 2}$ (b), and the diabatic adjustment term Q_ε for the the control (red) and increased humidity (blue) simulations. Note that the values in (a) represent the sum of the vlaues in (b) and (c).

So far we have cast some doubt on the assumption of Bechtold et al. (2008). A more comprehensive experiment would be to simulate an entire field of naturally triggered convection and increase the humidity at all levels, similar to the seminal work of Derbyshire et al. (2004). A caveat of this alternative approach is that we might inadvertantly change how the convection initiates, which might influence our interpretation of the relationship between entrainment and tropospheric moisture. Despite this caveat, our results motivate the conclusion that a more humid environment leads to more vigorous circulations within deep convection, which increases the entrainment, but but also reduces the buoyancy dilution by entrainment.

4.6.2 Entrainment in Organized Convection

Vertical shear often promotes more organized convection (Robe and Emanuel 2001), and some have hypothesized that organized convection experiences less entrainment or is less affected by entrainment (Mapes and Neale 2011). The direct entrainment measurement and dilution estimation method allows us to easily test this

hypothesis, and show whether organized convection is less diluted by entrainment. The DYNAMO simulation discussed previously was purposely run with no vertical wind shear, and instead used a height invariant wind profile of $5\ m\ s^{-1}$. As an experiment, we will now discuss results from an additional simulation that is identical to the previous DYNAMO simulation, except that the vertical profile of large-scale horizontal wind is nudged to the observed profile of zonal wind from the October MJO event (see Fig. 4.59). Note that the surface wind has been set to $5\ m\ s^{-1}$ so the mean surface fluxes are consistent with the control simulation. A snapshot of a mock albedo image shows that the simulation with no shear tends to have scattered deep convection, whereas the case with shear produces linear convective features, akin to a squall line (Fig. 4.60). A 3D rendering of these snapshots in Figure 4.61 confirms that the no-shear case produces upright, isolated deep convection. The color on the lower surface of the 3D rendering shows the strength of the surface latent heat flux. The case with realistic shear produces tilted convection that is co-located with enhanced surface fluxes resulting from the formation of a cold pool, and corresponding gust front.

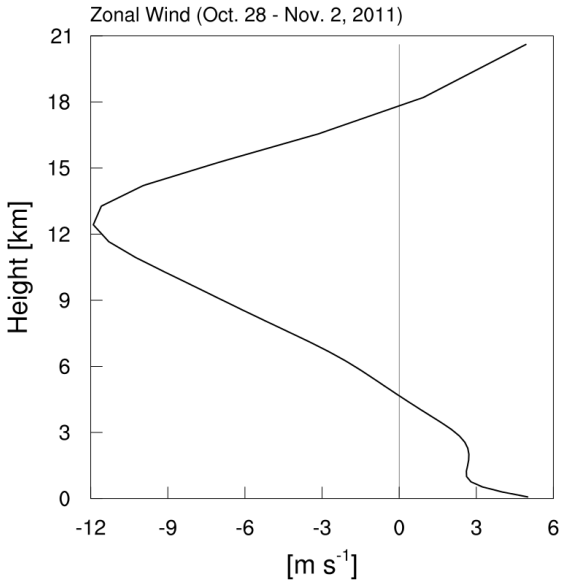

Fig. 4.59 Profile of zonal wind used to force the DYNAMO sensitivyt experiment (see text).

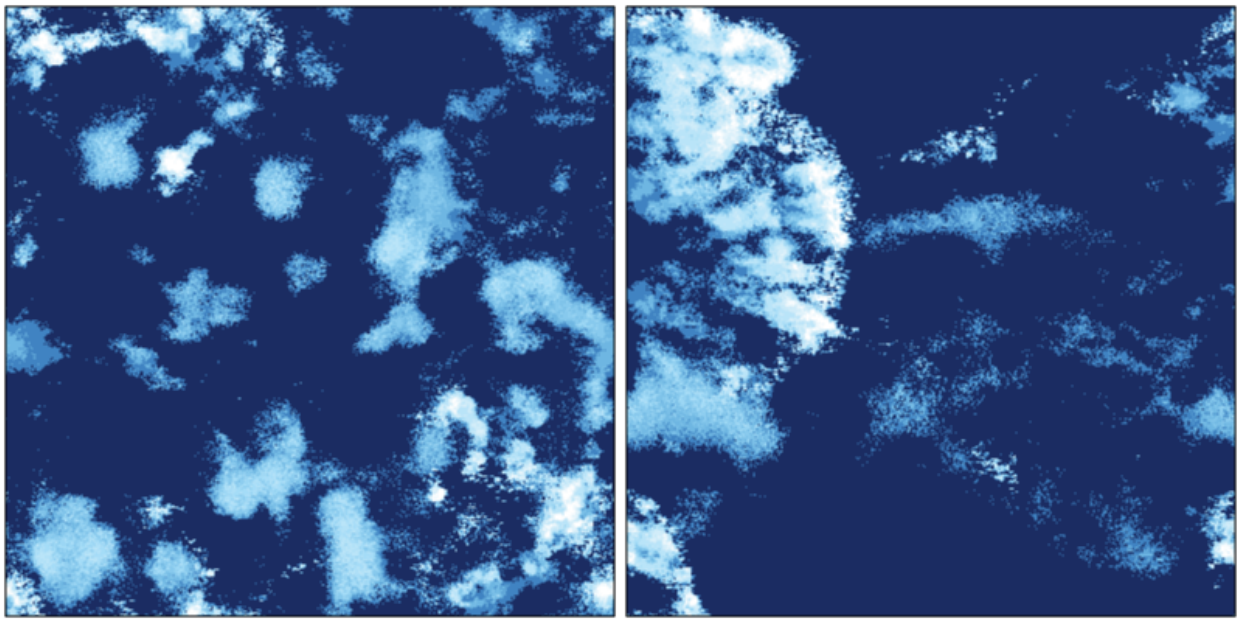

Fig. 4.60 Mock albedo image of two large-scale DYNAMO simulations, one without any vertical wind shear (left) and the other with the observed zonal wind shear (right)

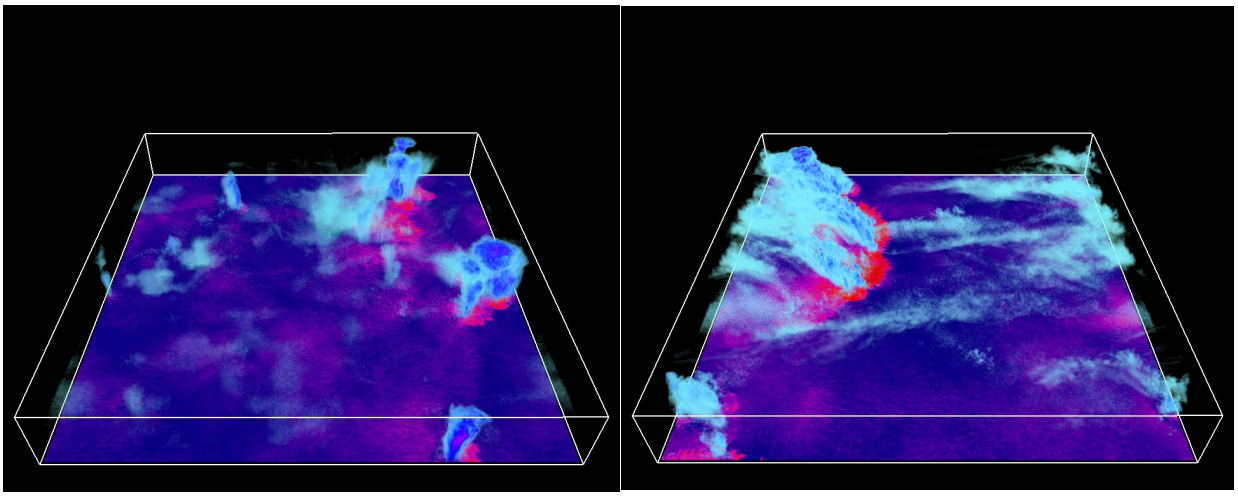

Fig. 4.61 3D rendering of the cloud field in the DYNAMO simulations without shear (left) and with realistic shear (right). Warmer colors on the bottom surface indicate stronger surface latent heat fluxes.

Figure 4.62 shows the mean profiles of fractional entrainment and detrainment, for both core and cloud in the two DYNAMO simulations. The fractional entrainment and detrainment generally show an increase above the freezing level. This result is inconsistent with the assumption of Mapes and Neale (2011), who assumed entrainment was reduced when organized convection developed. Un-normalized profiles of core entrainment, detrainment, and mass flux show that the increase in fractional values is due to increases in the mass entrainment and detrainment, and not due to a decrease in the core mass flux (Fig. 4.63). We see a similar result for the cloud entrainment, detrainment and mass flux (Fig. 4.64).

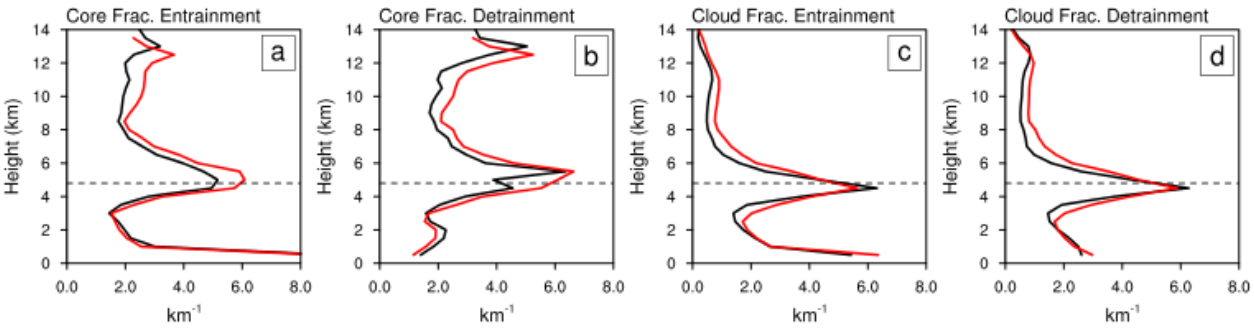

Fig. 4.62 Time mean profiles of core fractional entrainment (a), core fractional detrainment (b), cloud fractional entrainment (c), and cloud fractional detrainment (d) of the DYNAMO simulations without shear (black) and with shear (red). The dashed line indicates the freezing level.

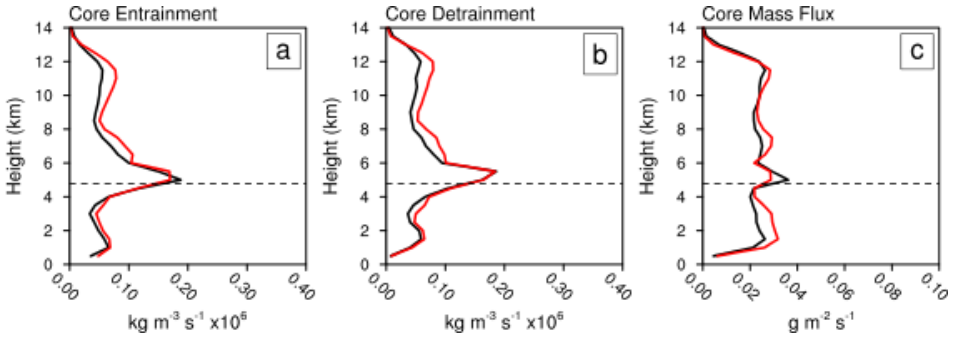

Fig. 4.63 Time mean profiles of core entrainment (a), detrainment (b), and mass flux(c) for the DYNAMO simulations without shear (black) and with shear (red).

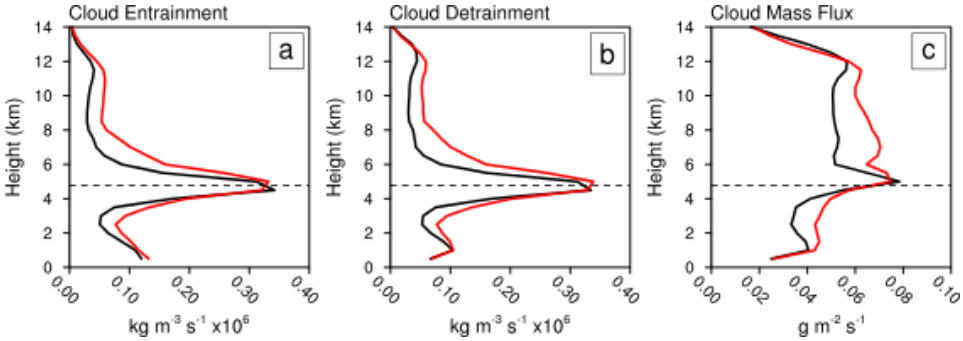

Fig. 4.64 Time mean profiles of cloud entrainment (a), detrainment (b), and mass flux(c) for the DYNAMO simulations without shear (black) and with shear (red)

Figure 4.65 shows the profiles of core fractional entrainment and core dilution by entrainment for q_t and θ_v. Dilution of q_t increases at upper levels for the case with organized convection, whereas lower levels do not show any notable change in q_t dilution. A similar increase can be found in the cloud q_t dilution by entrainment (not shown), but this also increases at lower levels due to the increased cloud entrainment (Fig. 4.64a). These increases are balanced by decreases in dilution by detrainment in the case with organized convection (not shown). Surprisingly, Dilution of θ_v *increases* at upper levels.

This suggests that in spite of organized convection generally known for being more vigorous, organized convection experiences more dilution of buoyancy.

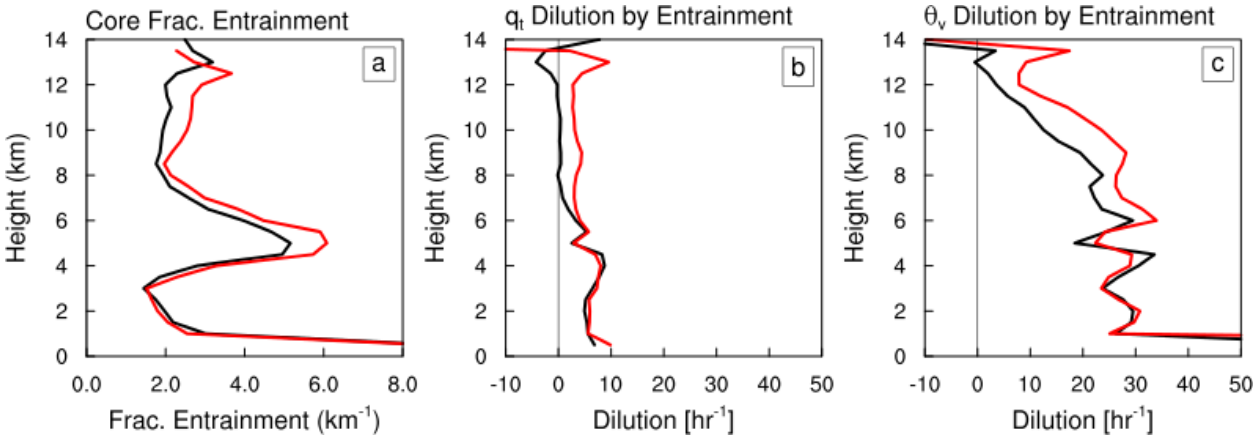

Fig. 4.65 Mean profiles of core fractional entrainment (a), core q_t dilution by entrainment (b), and core θ_v dilution by entrainment (c) for the DYNAMO simulations without shear (black) and with shear (red).

We can understand this counterintuitive result of increased q_t dilution in organized convection by looking at the two individual terms of the q_t dilution formula given in (4.38) and (4.39) shown in Figure 4.66. This analysis shows that the increase in dilution is partially explained by the increase in mass entrainment (Fig. 4.66b), and but mostly explained by changes to q_t differences between the core and the entrained air (Fig. 4.66c). The difference in the domain mean q_t shows that the environment is slightly wetter at upper levels in the case with organized convection (Fig. 4.67a), but the mean core q_t is drier from *8-12 km* (Fig. 4.68a). In other words, the difference between q_t of the core and environment is smaller, and therefore, the increased q_t dilution at upper levels is due to the core air being closer to the state of full dilution at upper levels on average. There is the opposite change at lower levels, with the environment becoming drier and core air becoming wetter. However, this surprisingly does not appear to have any effect the dilution or $D_{\varepsilon 2}$ (Fig. 4.66c), perhaps because the denominator of $D_{\varepsilon 2}$ becomes sufficiently large to compensate.

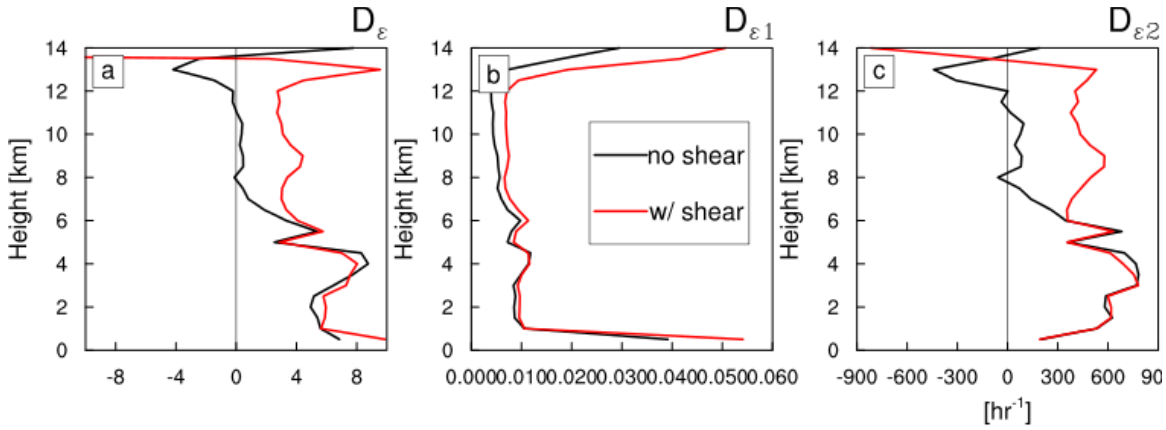

Fig. 4.66 Mean profiles of core q_t dilution by entrainment (D_ε; a) and the two components, $D_{\varepsilon 1}$ (b) and $D_{\varepsilon 2}$ (c) for the DYNAMO simulations without shear (black) and with shear (red).

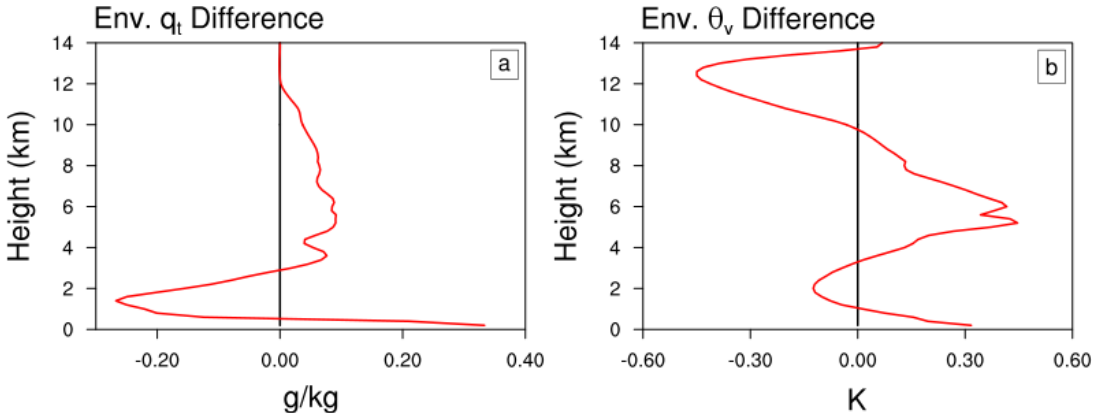

Fig. 4.67 Difference profile of domain mean q_t and θ_v between the simulations with and without vertical wind shear.

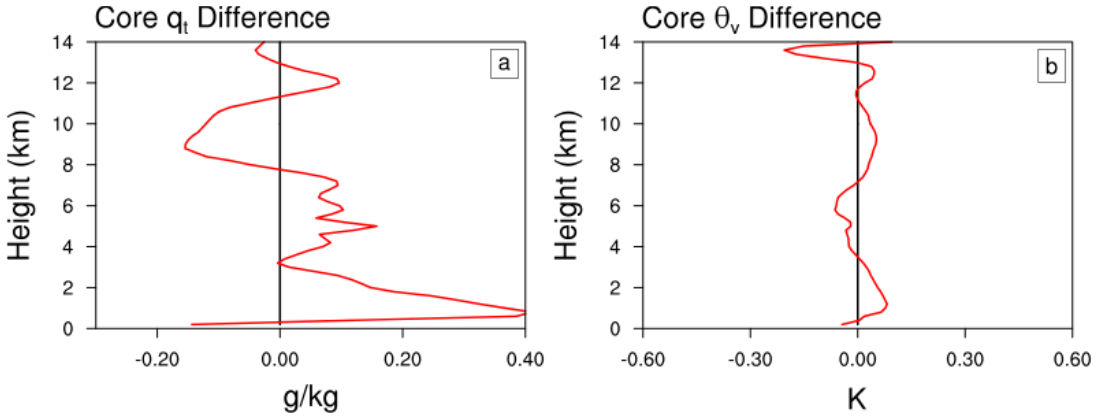

Fig. 4.68 Difference profile of the mean core q_t and θ_v between the simulations with and without vertical wind shear.

To understand the increase in θ_v dilution, Figure 4.69 shows the product of $D_{\varepsilon 1}$ and $D_{\varepsilon 2}$, and the diabatic term Q_ε. The product of $D_{\varepsilon 1}$ and $D_{\varepsilon 2}$ contributes a positive change to the

θ_v dilution above and below the freezing level (Fig. 4.69b), and Q_ε also increases at upper levels (Fig. 4.69b). This result is puzzling and difficult to understand, since we intuitively expect organized convection to experience less buoyancy dilution. The reason for the increased θ_v dilution from the Q_ε term appears to be that the entrained core air tends to be drier on average above *8 km* and around *1-2 km* compared to the organized case (Fig. 4.70a). This also corresponds to drier cloud shell air in the organized case (Fig. 4.70b), and enhanced fallout of precipitation (Fig. 4.70c) at these levels.

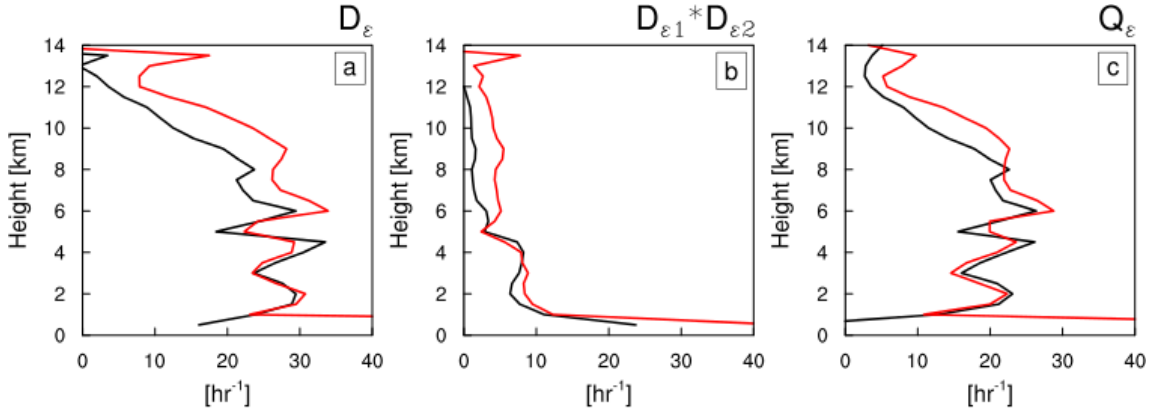

Fig. 4.69 Mean profiles of core θ_v dilution by entrainment (D_ε; a) and the three components, $D_{\varepsilon 1}$ (b), $D_{\varepsilon 2}$ (c), and Q_ε (d) for the DYNAMO simulations without shear (black) and with shear (red).

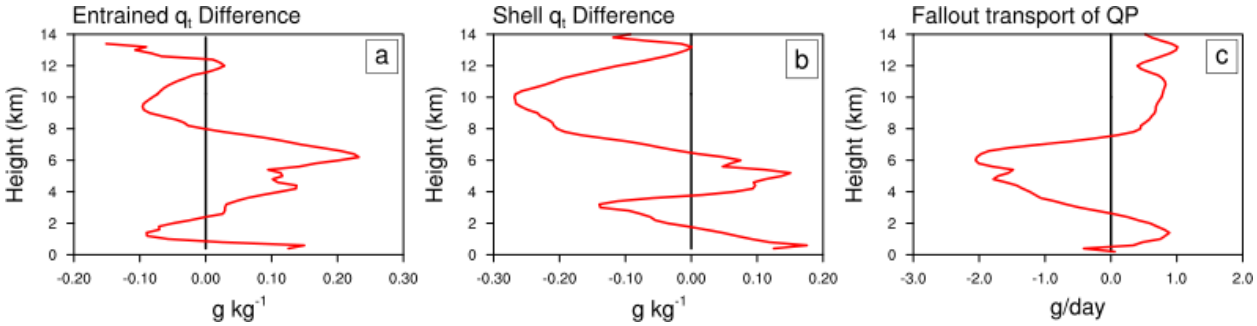

Fig. 4.70 Difference profiles of the mean q_t of the entrained air (a), q_t of the cloud shell (b), and drying rate by fallout or precipitation between the simulations with and without vertical wind shear.

In summary, we have compared two populations of convection, in which one is characterized by isolated deep convection, and the other is characterized by linear organized convective systems. Organized convection generally experiences more

entrainment, inconsistent with the assumption of Mapes and Neale (2011). The dilution of q_t is slightly increased at upper levels because the environment becomes wetter and the convection becomes somewhat drier on average. Analysis of the θ_v dilution suggests that buoyancy dilution is also increased in the case with organized convection, due to both entrainment of lower θ_v air, and diabatic cooling associated with the entrainment of drier air.

A noteworthy caveat of this sensitivity experiment is that the simulations are forced with observations, which tightly constrains the convective response, such that it balances the prescribed forcing. In reality, there is no such disconnect between convection and large-scale processes. One way around this is to employ the weak temperature gradient (WTG) approximation to "parameterize" the large-scale dynamics in a cloud-resolving model. This allows the interaction between the resolved convective scale and larger scales to be more naturally simulated. Diagnosing entrainment and dilution in a WTG model is outside the scope of this study, but would likely prove to be an interesting endeavor. Alternatively, we could compare simulations with varying shear and mesoscale organization in radiative convective equilibrium, so that the domain mean properties of the simulations are not so constrained. A related issue is that the finite domain of these simulations requires no net vertical mass flux. This constrains the convective mass fluxes, and ultimately could influence the entrainment and detrainment. Another key difference in these simulations is the tilting of convection. Parker (2010) argued that upright convection is in an optimal state, and can realize more buoyancy than tilted convection. This could also be leading to influencing the entrainment and dilution results. We also note that we have

not isolated the effect of vertical wind shear on entrainment and dilution. This would be a simple experiment to conduct with bubble simulations, and is left for future work.

4.7 Summary and Discussion

4.7.1 Summary

In this chapter, cloud resolving model experiments were performed to systematically test specific aspects of entrainment in deep tropical cumulus convection in order to guide future convective parameterization development. Bubble release experiments with varying widths of the initial bubble were conducted to obtain a population of cumulus clouds. Additionally, a large *100 km* domain simulation was run with forcing derived from data obtained during the 2011 October MJO event over the DYNAMO northern sounding array. These two very different approaches give us two populations of tropical deep convective clouds that are similar in many respects (Fig. 4.8), but one approach allows specific cloud properties to be systematically tested, whereas the other provides large and diverse field of convection that is produced in a more natural manner. A central result of the analysis is that the shell of saturated air that forms around the core plays a crucial role in buffering the core from the effects of entrainment, which agrees with other studies (Dawe and Austin 2011a).

The bubble experiments tend to produce narrow updraft cores with radii less than *1 km* in radius, despite the radii of the initial guassian bubble being greater than *1 km*. Convection in the bubble simulations develops a shell of saturated air around the core updraft that grows steadily in thickness over the cloud lifecycle (Fig. 4.17). Convection in the DYNAMO simulation also tends to produce narrow updrafts (Fig. 4.10), and also exhibits a shell of saturated air around the updrafts, but an objective analysis of the shell

thickness is difficult to render due to irregular geometry (Fig. 4.18). Analysis of directly measured entrainment and detrainment rates reveals that the largest entrainment occurs at cloud base, oweing to the initial formation of the cloud and core volumes. Detrainment rates are also large at low levels, just above cloud base (Fig. 4.19) due to a toroidal circulation that causes a large portion of the entrained air to be immediately detrained (Fig. 4.13). Detrainment is generally of similar magintude to entrainment, and slightly larger on average (Fig. 4.19), even though a coherent toroid is not always evident (Fig. 4.15).

The bubble simualtions are designed to have a range of widths (Fig. 4.9), which many previous studies have assumed is intimately tied to the entrainment rate through an inverse relationship, as in (4.11). Interestingly, we do not find evidence that a strong inverse relationship exists between radius and entrainment in the bubble simulations (Fig. 4.28-4.30). However, we find clear evidence of an inverse relationship in the DYNAMO simulation (Fig. 4.31). The way to reconcile these opposing results is to recognize that many other factors that influence entrainment, also vary with cloud radius (Fig. 4.32). With this mind, the bubble simulation framework provides a clear test of a robust radius relationship, and therefore we conclude that the assumed inverse relationship used by many studies and parameterizations is not strongly supported. A physical understanding of why there is not a fundamental relationship can be gleened from Figure 4.14, which shows the azimuthially average circulations. The circulations in Figure 4.14 are generally on the scale of the thermal itself. To the extent that this holds for all cumulus clouds, then a wider thermal we would experience a larger circulation, and more lateral entrainment.

The properties of air entrained in the core were shown to be consistent with air residing in the cloud shell, consistent with Dawe and Austin (2011b). We have also shown

that the shell is composed of a mixture of detrained air from the core, and air from the ambient, cloud-free environment. This supports a new conceptual model of a moist convecting thermal, in which the cloud shell properties are influenced by the core detrainment and the environment, and plays a prominent role in determining the thermodynamic properties of the entrained air in to the core (see Fig. 4.71).

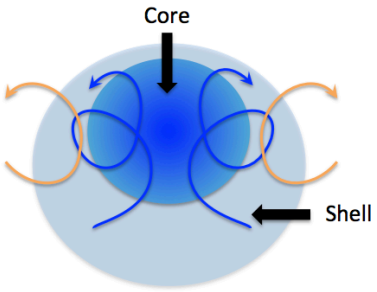

Fig. 4.71 Conceptual model for a thermal core and shell. Arrows indicate the path of air that entrains into the core (blue) and environmental air (orange).

A quantitative method for estimating dilution was introduced and analyzed. Generally, dilution and entrainment are not synonamous, but dilution is strongly influenced by entrainment and detrainment. Dilution by entrainment tends to be very small at cloud base and larger at upper levels, because the air being entrained at low levels is similar to the air in the cloud. Dilution by detrainment is negative, implying that detrainment helps to enhance the cloud, and counteract the effects of entrainment. The dilution analysis also is able to quantify the effects of the cloud shell, by showing that the timescale of dilution by entrainment changs by an order of magnitude when the effect of the cloud shell is artificially neglected (Fig. 4.45). This change is roughly from ~10-60 to ~2-3 minutes for q_t, and from 3-5 minutes to less than 60 seconds for buoyancy. Dilution is found to have a weak dependence on core radius, which somewhat supports the the assumed inverse relationship between entrainment and radius.

Sensitivity experiments were conducted to show the utility of the dilution formulas, but revealed some counter intuitive results. In the case of enhanced free tropospheric humidity we find that the entrainment and dilution of q_t both *increase*, which is the opposite of what some have assumed in convective parameterizations (e.g. Bechtold et al. 2008). The increase in q_t dilution is due to the fact that the anomalies of q_t within the clouds are smaller, and thus the increased humidity inadvertently makes the clouds closer to the state of complete dilution. We also find that buoyancy dilution is reduced, which can explain why convection becomes more vigorous in more humid environments. Another sensitivity simulation tested the idea that organized convection is less affected by entrainment (e.g. Mapes and Neale 2011). Instead, our results show that entrainment, q_t dilution, and buoyancy dilution are all *increased* in the case when vertical shear is added and convection organizes into linear features (e.g. squall line). This is inconsistent with Mapes and Neale (2011), and is ultimately due to entrainment of drier air and a drier cloud shell.

4.7.2 Discussion

The analysis in this chapter was motivated by the results in Chapter 2, which showed that increasing parameterized entrainment can improve the representation of the MJO, but ultimately for the wrong reason. Do the results of this chapter shed light on how to address the problem in Chapter 2? The answer to this question has many facets, and cannot be boiled down into a single suggestion for improving the convective parameterization. First of all, increasing parameterized entrainment generally suppresses the deepest convection. This is due to an emergent property of the parameterization in

which taller clouds tend ot have smaller entrainment rates. In Section 4.4.2 we saw that the entrainment in the tallest and widest clouds was *larger*, and there was no strong evidence for an robust relationship between entrainment rate and cloud radius. The parameterization in Chapter 2 is not be able to qualitatively reproduce this relationship, which may be related to the paradoxical response from increased entrainment in CAM5. Second, parameterized entrainment is often diagnosed to be smaller than directly measured entrainment, which relates to the sensitivity of convection to environmental conditions. The parameterization in Chapter 2 has no representation of the cloud shell, and therefore is forced to diagnose smaller entrainment rates in order to produce deep convection (Dawe and Austin 2011a). With no cloud shell the parameterized entrainment becomes synonymous with dilution, whereas we saw in the simulated convection that the cloud shell allows for large entrainment rates that do not substantially dilute the cloud (See Section 4.5). Finally, entrainment and detrainment are happening throughout the cloud. Many parameterizations assume that entrainment happens through most of the cloud, but detrainment only happens at the top where the cloud is neutrally buoyant. This conceptual picture of deep convection is not consistent with the simulated deep convection in this chapter. A more realistic parameterization would incorporate entrainment and detrainment at all levels and detrainment would help maintain the convection against dilution by entrainment by providing "negative dilution" as was shown in Section 4.5. Overall, the results of the current chapter suggest that several aspects of the convective parameterization in Chapter 2 need to be revised in order to produce a more realistic convective response. Hopefully, these ideas will also lead to an improvement in the representation of the MJO for the right reasons.

The results of this study particularly highlight the role of the cloud shell in the evolution of deep tropical convection in a way that is not consistent with a typical entraining plume model used for convective parameterization. The conceptual model proposed here in Figure 4.71 is similar in several ways to the "slippery thermal" model presented by Sherwood et al. (2013). Both of these ideas put strong emphasis on the recirculating nature of the flow associated with a convecting thermal. Sherwood et al. (2013) incorporated this concept into a simple plume model and showed that it produced superior results when compared to a traditional plume model, and was able to use larger entrainment rates that we know to be more realistic (Romps 2010). Their model did not explcitly include a shell, but did include a way to indirectly include the effects of cloud inhomogeneity.

Consider the following example equations, as a template for how one could incorporate the cloud shell into a simple, steady state plume model,

$$\frac{\partial \phi_{cor}}{\partial z} = \varepsilon\left(\phi_{\varepsilon\_cor} - \phi_{cor}\right) - \delta\left(\phi_{\delta\_cor} - \phi_{cor}\right), \tag{4.42}$$

$$\begin{aligned}\frac{\partial \phi_{shl}}{\partial z} = {} & \varepsilon\left(\phi_{\varepsilon\_shl} - \phi_{shl}\right) - \delta\left(\phi_{\delta\_shl} - \phi_{shl}\right) \\ & -\left[\varepsilon\left(\phi_{\varepsilon\_cor} - \phi_{cor}\right) - \delta\left(\phi_{\delta\_cor} - \phi_{cor}\right)\right]\end{aligned}. \tag{4.43}$$

These two equations are meant to describe the vertical profile of some tracer ϕ that has an average value in the core (ϕ_{cor}) and another in the shell (ϕ_{shl}), and is influenced by the fractional rates of entrainment (ε) and detrainment (δ). The core entrains air from and detrains air into the shell. Similarly, the shell entrains from and detrains into both the core and ambient environment, as depicted in Figure 4.72. The results of section 4.4.3 provide some insight into how to prescribe the tracer values being entrained and detrained

from the core and shell, specifically ϕ_{ε_cor}, ϕ_{δ_cor}, ϕ_{ε_shl}, and ϕ_{δ_shl}. Generally, the entrained and detrained values can be taken from the corresponding source of the air being fluxed out of the reservoir, although this may require more concise analysis to determine the appropriate values to use for an accurate prediction of the core and shell properties.

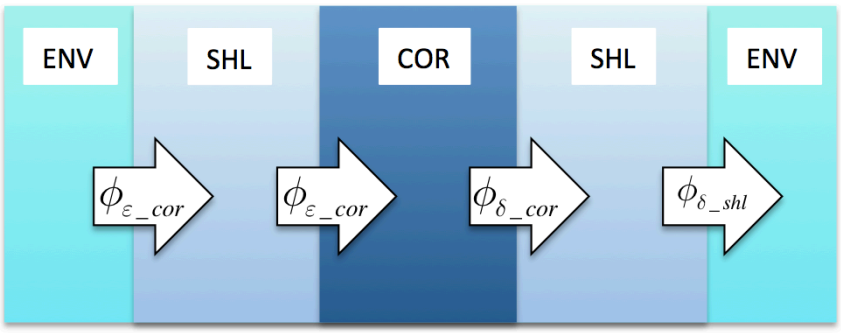

Fig. 4.72 Schematic drawing of buffered thermal "box" model that incorporates a shell that is dependent on the detrainment from the core.

The development and implementation of this concept into a convective parameterization is planned for future work, and will incorporate ideas surrounding momentum transfer and friction of a slippery thermal, as discussed by Sherwood et al. (2013). This is no silver bullet for addressing the inadequacies of convective parameterization, but it may help to improve some aspects of the behavior of deep convection, such as the issues highlighted in Chapter 2, in which a parameterized models was modified to obtain a robust MJO, but ultimately got the right answer for the wrong reason.

This novel treatment will not only be more physically realistic, but also may lead to new ways of probing convective processes. One example would be to examine what controls the timing of transitions from shallow to deep convection. Deep convection can often be observed as forming in the vicinity of a population of shallow convection. This overlap of convective thermals could be treated by using information about previous cloud

detrainment to modify the shell of convection in the proceeding timesteps. A potential extension of these ideas could be to investigate whether mesoscale organization could be parameterized by considering a “mesoscale cloud shell”. In other words, the nature of certain organized convective systems could be thought about as existing within a sub-grid volume that is more favorable for convection than the grid-scale mean environment. These research efforts will also require more detailed analysis using observations or high-resolution simulations, but the buffered thermal framework provide a potential way for understanding the relationships in a simple manner.

CHAPTER 5 CONCLUSIONS

This dissertation has described aspects of hindcast experiments for Madden-Julian Oscillation (MJO) events during the Dynamics of the MJO (DYNAMO) field campaign. The model sensitivities found in the hindcast experiments motivated further explorations of entrainment processes in high-resolution simulations of tropical deep convection. The main findings of this work are outlined in section 5.1. Outstanding questions are discussed in section 5.2, followed by suggestions for future work in section 5.3, and concluding remarks in section 5.4.

5.1 Main Findings

There have been numerous studies of MJO dynamics using multi-year simulations with global models (Slingo et al. 1996; Kim et al. 2009; Benedict and Randall 2009), but much less work has been done with short term MJO simulations, in which models are initiated from observations so the results can be directly compared with an observed MJO event. Chapter 2 examined this approach to simulating the MJO with the National Center for Atmospheric Research (NCAR) Community Atmosphere Model version 5 (CAM5), which employs parameterized convection. The entrainment rate of the dilute CAPE calculation was varied, and found to have a large impact on the simulated MJO (see also Neale et al. 2008). Larger entrainment appears to effectively suppress convection and improve the MJO, consistent with previous studies (Hannah and Maloney 2011). However, analysis of the column integrated moist static energy (MSE) budget shows that this method produces the right answer for the wrong reasons, when compared to the European Center for

Medium Range Weather Forecasting (ECMWF) interim reanalysis product (ERAi). The main findings of Chapter 2 that support this conclusion can be summarized by four points:

1. Cloud-radiative feedbacks in the model are weaker than ERAi. These feedbacks play an important role in maintaining column MSE anomalies associated with the MJO (Andersen and Kuang 2012; Pritchard and Bretherton 2014), and therefore are likely related to the poor MJO representation in the control simulation.
2. Increasing the entrainment rate enhances the column MSE import by vertical advection for conditions with weak MSE anomalies. This appears to compensate for the weak cloud-radiative feedbacks in the model and improve the MJO. This may also explain the mean-state degradation that accompanies an improved MJO simulation noted by previous studies (Kim et al. 2009).
3. The vertical component of gross moist stability (VGMS) is positive in observations, but significantly negative in the model with higher entrainment. This indicates that the model with higher entrainment can more easily destabilize a moisture mode when compared to the model with lower entrainment.
4. Effective VGMS is similar between observations and the model with larger entrainment. This means that moisture modes can be destabilized in both cases, but the partitioning of processes that dictate moisture mode dynamics are not accurate in the model.

The last decade has seen the emergence of a novel way of explicitly treating unresolved convection in global models with embedded 2D cloud resolving models, often referred to as super-parameterization. Early versions of the super-parameterized CAM (SP-CAM) produced one of the most robust representations of the MJO of any global model at that time. A natural hypothesis is that SP-CAM can produce more realistic simulations of the DYNAMO MJO events, so the hindcast experiments from Chapter 2 were repeated in Chapter 3 to test this. As expected, SP-CAM produces a better representation of the DYNAMO MJO events when compared to CAM5, although a systematic drift in the model projects strongly onto the Real-time Multivariate MJO (RMM) index spatial patterns, and negatively impacts RMM skill metrics. Analysis of the column MSE budget shows that SP-CAM has a bias in the vertical MSE advection, similar to, but not as large as CAM5, with stronger MSE import for conditions with weak MSE anomalies. SP-CAM hindcasts also exhibits negative VGMS, which is inconsistent with ERAi. The conclusions of Chapter 3 can be summarized by these points:

1. Model drift in SP-CAM has a large impact on RMM skill metrics, which is mainly due to a systematic drift away from the initial conditions in low-level wind and convective intensity.
2. SP-CAM hindcasts exhibit much more realistic cloud-radiative feedbacks compared to CAM5.
3. MSE export by meridional advection increases with hindcast lead-time in SP-CAM due partly to an enhancement of off-equatorial synoptic eddies.
4. Vertical MSE advection in SP-CAM exhibits an import of column MSE that is inconsistent with ERAi, similar to the bias of CAM5 identified in Chapter 2.

5. VGMS in SP-CAM is negative, similar to CAM5, and inconsistent with ERAi. This is associated with a bottom-heavy bias in large-scale vertical velocity and diabatic heating, relative to ERAi.

In Chapter 2, from the apparent compensation of weak cloud-radiative feedbacks by the enhanced vertical MSE advection with increased entrainment rate in CAM5, it was concluded that the improved MJO in CAM5 was due to the model producing the right answer for the wrong reason. Making a similar conclusion about SP-CAM is not as straightforward, because there does not appear to be the same type of compensating errors that were found in CAM5. It is true that the vertical advection in SP-CAM has a bias towards more import of column MSE whereas ERAi suggests weak export. This bias may be unrealistic, but to make a solid conclusion that this is inaccurate we would need to overcome the data scarcity of the Indian Ocean. More generally, we need to obtain better estimates of large-scale vertical velocity. Vertical velocities from reanalysis products, such as ERAi, are model-derived. This means that the estimates rely heavily on the model's parameterizations of moist processes. Data from field campaigns, like DYNAMO, can be used to generate better estimates of vertical velocity, but their spatial and temporal coverage is limiting.

The issues with the parameterized model in Chapter 2 motivated a more in depth look at entrainment processes. This was done in Chapter 4 using high resolution simulations of tropical deep convection with a cloud resolving model. Two approaches were used to simulate deep convection; the first used the release of a warm and humid bubble so that clouds could be individual simulated, and the other produced a field of naturally triggered convection using large-scale forcing derived from DYNAMO northern

sounding array data during the active phase of the October MJO event (Johnson and Ciesielski 2013). The main findings of this research were:

1. Deep convection forms a shell of moist air around the core that plays a crucial role in conditioning the air being entrained into the core.
2. Deep convection has large rates of fractional entrainment and detrainment due to toroidal circulation features that cycle air through the cloud.
3. Fractional entrainment does not appear to be fundamentally related to cloud or core radius due to the scale of toroidal circulations being similar to the scale of the convecting thermal.
4. Entrainment and dilution are generally not synonymous. Large entrainment can occur with little dilution, and vice versa.
5. Fractional entrainment increases in a more humid environment, but convection becomes more vigorous due to reduced dilution of buoyancy by entrainment.
6. Fractional entrainment and dilution of total water and buoyancy increase when convection becomes organized by vertical wind shear, because the entrained air from the cloud shell tends to be drier, associated with more fallout of precipitation.

These conclusions specifically point to two fundamental problems with the parameterization scheme used in Chapter 2, namely the assumption that wider clouds have smaller entrainment and that the effects of the cloud shell are not considered. It seems reasonable to expect that a similar convective scheme that explicitly considers the cloud shell and is not bound to the inverse radius assumption would be more realistic, and hence

perform better in hindcast simulations of the DYNAMO MJO events. However, a scheme with these properties will likely diverge significantly in the details of its implementation, and will not be directly comparable to the scheme used in Chapter 2. Instead of comparing two very different schemes, we could get around this problem by designing a scheme that can be modified to test the importance of physical processes, such as the thickness of the cloud shell. Performing hindcast experiments with such a scheme would broaden our understanding of the interaction between convection and large-scale dynamics.

5.2 Outstanding Questions

An outstanding issue relevant to the hindcast analysis is that reanalysis vertical velocity fields are not well constrained by observations. This has serious implications for the estimation of gross moist stability, but more importantly, this could be influencing our understanding of the fundamental nature of the MJO. Unfortunately, there is really no way around this problem. Localized in-situ estimates of vertical velocity can be obtained from certain radars and wind profilers, but these datasets are sparse, and so analysis over a wide area, like the Indian Ocean, is not possible. These techniques rely on certain tracers, such as hydrometeors of a certain size, and thus are not always able to measure clear air velocity in the vicinity of convection, which would be a valuable measurement (Glenn and Krueger 2014). Therefore, even if the measurements were available over a large area, it is unclear whether they would be able to offer a good estimate of the large-scale vertical velocity that would be needed to better constrain the gross moist stability. Space-borne Doppler radar could possibly provide large-scale coverage of vertical velocities associated with convection, but this presents significant technical hurdles. Efforts are currently underway

to obtain such measurements, but it is unclear what caveats will come with this new data (Augustynek and Battaglia 2012). Vertical velocity can also be estimated from a sounding array, such as the one used in DYNAMO (Johnson and Ciesielski 2013), by estimating the divergence profiles and obtaining the vertical velocity from the continuity equation. This type of estimate is good to first order, but can be affected by deficiencies in the temporal or spatial sampling (Ciesielski et al. 1999; Katsumata et al. 2011)

If accurate and reliable observations of vertical velocity over large areas are unobtainable, how can we answer fundamental questions about large-scale dynamics that depend on the vertical velocity? One might be tempted to invoke the use of high-resolution models with large-domains in order to circumvent the observational difficulties (Khairoutdinov et al. 2009). However, this approach has it's own problems. Even at very fine grid spacing we must make simplifications in regards to sub-grid turbulence, radiation and microphysical processes. Even if these were not a problem, we would still be confronted with the enormous computational expense of simulating fine-scale processes over a large area.

This brings us to question the validity of limited domain cloud resolving simulations, such as the ones presented here. In order to perform these simulations we have relied on an artificial distinction between "large" and convective scales (Mapes 1997). This thinking has long been used to develop practical modeling techniques and understand the role of convection (e.g. Arakawa and Schubert 1974), but may be obstructing a deeper understanding of scale interaction (Mapes 1997). Overall, this issue has negligible consequences for the conclusions discussed here about the fundamental nature of cumulus entrainment. Other aspects of limited domain cloud-resolving simulations, such as grid

spacing, domain size, and microphysical processes, have more potential to influence entrainment processes. These details could also influence cloud-radiative feedbacks, which were shown to be a problem for the parameterized model hindcasts in Chapter 2. Detailed investigation of these sensitivities is a worthwhile pursuit, and is left for future research.

5.3 Future Work

This work has highlighted many areas to focus on for future work. Some of these are rather obvious, such as comparing our hindcast conclusions to other models and convection scheme assumptions or modifications. Other issues, such as the overly weak cloud-radiative feedbacks identified in CAM5, are not as easy to understand and address. The weak cloud-radiative feedbacks are likely a consequence of the fact that radiation does not directly interact with deep convection. The reduction of out-going longwave radiation by enhanced convection occurs indirectly in CAM5. Detrainment of cloud water from deep convection is added to the grid cell mean properties, and then influences the microphysical and radiative calculations on the model's resolved scale to produce a radiative feedback. SP-CAM provides a way to investigate this interaction, because the radiative calculations are done on the CRM grid, instead of the host GCM (Khairoutdinov et al. 2005). Analyzing how radiation directly interacts with deep convective towers in the CRM might provide some insight into how this could be better treated in conventional models (Cole et al. 2005).

It was shown in Chapter 3 that SP-CAM exhibits net MSE import on average by vertical advection and negative gross moist stability, which is inconsistent with ERAi. These differences are interesting, and deserve further study. It would be useful to know how

aspects of the embedded CRM affect the large-scale MSE budget. The grid columns of the CRM are typically *4 km* wide, in order to allow for a domain that can support mesoscale convection, and also to limit the computational cost. The CRM also typically has very coarse vertical grid spacing. Generally, the representation of large-scale phenomena is not very sensitive to the horizontal grid spacing of the embedded CRM, because the convective response is largely determine by the large-scale destabilization. So, to the extent that an "equilibrium control" paradigm of convective forcing is relevant (Mapes 1997), the convective mass flux is constrained by the destabilization from large-scale processes. Unfortunately, computational expense limits how much we can test SP-CAM's sensitivity to CRM grid structure. It would be interesting to see if a dramatic increase in horizontal resolution could lead to narrower and taller clouds. This may alter the bottom-heavy nature of the large scale vertical velocity and consequently affect the vertical advection of MSE. A tendency for taller convection may reduce the bottom-heavy bias of the large-scale vertical velocity, which was shown to have an influence on the gross moist stability (see Sec. 3.5).

The method of direct entrainment measurement to investigate deep tropical convection has only been explored by a handful of studies, and much more work can be done in this area. A major outstanding issue is that we do not have a good way to diagnose the entrainment rate in deep convection. The analysis here has shown that the common method of relating the entrainment to the cloud radius is likely flawed. Many other ideas have been proposed to formulate the entrainment rate based on certain properties of the convection or the environment, such as environmental stratification or cloud vertical velocity (Salzen and McFarlane 2002; Gregory 2001; Neggers et al. 2002). Some studies

have tested the validity these ideas and found mixed results (Del Genio and Wu 2010; Romps 2010), while others have shown improved results by implementing these ideas into cumulus parameterizations (Chikira and Sugiyama 2010; Chikira 2014). Dawe and Austin (2013) embarked on an in depth characterization of entrainment and detrainment in simulations of shallow convection and found that entrainment was strongly related to cloud buoyancy and the environmental stratification, while detrainment relied strongly on vertical velocity and a critical mixing fraction (de Rooy and Siebesma 2008). This type of empirical estimation should be extended to transitional cases (i.e. shallow to deep) and cases with deep convection, and combined with theoretical work to produce a deeper understanding of what constrains these rates. This can then be used in the framework of the "buffered thermal model" discussed in Section 4.7.2, such that the effects of the cloud shell can be included in a calculation of sub-grid cloud processes.

A full understanding of entrainment and dilution processes will likely benefit from further sensitivity experiments, like the ones discussed in Section 4.6. The case of varying humidity is especially interesting. An alternate approach to exploring this would be to run several simulations of convective populations initialized with a range of humidity profiles (e.g. Derbyshire et al. 2004), or forced by a range of advective humidity tendencies. This might provided a clearer analysis of the impact of wetter environments on entrainment and dilution. There are other factors that could be tested in this manner as well, such as cloud buoyancy or vertical wind shear. Simulations with a range of surface temperatures would likely lead to higher initial cloud buoyancy. This will also affect the boundary layer turbulence, which might affect the initial entrainment and dilution of convection (Romps and Kuang 2010b). Profiles of horizontal wind with a range of vertical shear could be easily

imposed in a simulation. One issue with this is that the effects of organization might be difficult to separate from the effects of shear, but shear profiles could be specified in such a way to test this by minimizing the organizing effects of cold pools (Rotunno et al. 1988). Both shear and cloud buoyancy could also be explored with bubble simulations, similar to the ones discussed here.

Another interesting avenue of research could be to test the sensitivity to microphysical assumptions or aerosol concentrations. The simulations here took advantage of the computational efficiency of a single moment microphysical scheme, in which the condensate number concentrations are constant. A two-moment scheme might reveal some interesting changes in the sensitivity of entrainment and dilution to certain conditions like environmental moisture (Meyers et al. 1997). Microphysical assumptions and aerosols have been shown to affect aspects of organized convection (Seigel et al. 2013; Igel et al. 2014), and so a fruitful area of future research will be a more in depth investigation of entrainment processes in organized convection. Maritime convection is important to understand for tropical meteorology, but more interesting organization often occurs over land where instability is generally larger and surface latent heat fluxes are weaker, which leads to longer cold pool recovery times and stronger organized systems (Tompkins 2001). Organized systems over land have strong and complex internal circulations (Seigel and van den Heever 2013), and so the differences in entrainment characteristics between organized and non-organized systems over land might be much larger than for that over the ocean.

5.4 Concluding Remarks

This dissertation is the culmination of 4+ years of work, concentrated into a single document. I have not discussed the numerous dead-ends and unfruitful avenues that were pursued, because these are not uncommon experiences for doctoral candidates, and frankly, discussing failure is boring and somewhat depressing. I have tried my best to provide new insight into some long standing questions surrounding the MJO and cumulus entrainment by standing on the shoulders of those who have explored these problems before me. I hope that this work has at least partially achieved this goal, and motivated others to pursue these issues further.

REFERENCES

Alaka, G. J., and E. D. Maloney, 2012: The Influence of the MJO on Upstream Precursors to African Easterly Waves. *J. Clim.*, **25**, 3219–3236.

Albrecht, B. A., 1989: Aerosols, Cloud Microphysics, and Fractional Cloudiness. *Science (80-.).*, **245**, 1227–1230.

Andersen, J. A. J., and Z. Kuang, 2012: Moist Static Energy Budget of MJO-like Disturbances in the Atmosphere of a Zonally Symmetric Aquaplanet. *J. Clim.*, **25**, 2782–2804.

Arakawa, A., 1969: Parameterization fo cumulus clouds. *Proc. Symp. on Numerical Weather Prediction*, Tokyo, Japan, WMO/International Union of Geodesy and Geophysics, 1–6.

Arakawa, A., 2004: The cumulus parameterization problem: Past, present, and future. *J. Clim.*, **17**, 2493–2525.

Arakawa, A., and W. H. Schubert, 1974: Interaction of a cumulus cloud ensemble with the large-scale environment, Part I. *J. Atmos. Sci.*, **31**, 674–701.

Arakawa, A., and C.-M. Wu, 2013: A Unified Representation of Deep Moist Convection in Numerical Modeling of the Atmosphere. Part I. *J. Atmos. Sci.*, **70**, 1977–1992.

Arakawa, A., J.-H. Jung, and C.-M. Wu, 2011: Toward unification of the multiscale modeling of the atmosphere. *Atmos. Chem. Phys.*, **11**, 3731–3742.

Augustynek, T., and A. Battaglia, 2012: Retrieving hydrometeor motions using space-borne EarthCARE Doppler radar Simulator based study. *19th International Radar Symposium*, Warsaw, Poland, 509–512.

Back, L., and C. Bretherton, 2006: Geographic variability in the export of moist static energy and vertical motion profiles in the tropical Pacific. *Geophys. Res. Lett.*, **33**, L17810.

Bechtold, P., M. Köhler, T. Jung, F. Boblas-Reyes, M. Leutbecher, M. J. Rodwell, F. Vitart, and G. Balsamo, 2008: Advances in simulating atmospheric variability with the ECMWF model: From synoptic to decadal time-scales. *Q. J. R. Meteorol. Soc.*, **1351**, 1337–1351.

Benedict, J. J., and D. Randall, 2007: Observed characteristics of the MJO relative to maximum rainfall. *J. Atmos. Sci.*, **64**, 2332–2354.

Benedict, J. J., and D. Randall, 2009: Structure of the Madden-Julian oscillation in the superparameterized CAM. *J. Atmos. …*, **66**, 3277–3296.

Benedict, J. J., A. H. Sobel, E. D. Maloney, and D. M. W. Frierson, 2014: Gross Moist Stability and MJO Simulation Skill in Three Full-Physics GCMs. *J. Atmos. Sci.*, **in Review**.

Betts, A., 1982: Saturation point analysis of moist convective overturning. *J. Atmos. Sci.*, **39**, 1484–1505.

Betts, A. K., and M. J. Miller, 1986: A new convective adjustment scheme. Part 11: Single column tests using GATE wave, BOMEX, ATEX and arctic air-mass data sets. *Quart. J. Roy. Meteor. Soc*, **2**, 693–709.

Bjerknes, J., 1937: Theorie der aussertropischen Zyklonenbildung. *Meteorol. Zeitschrift*, **54**, 463–466.

Bladé, I., and D. Hartmann, 1993: Tropical intraseasonal oscillations in a simple nonlinear model. *J. Atmos. Sci.*,.

Blyth, A. M., W. a. Cooper, and J. B. Jensen, 1988: A study of the source of entrained air in montana cumuli. *J. Atmos. …*, **45**, 3944–3964.

Bony, S., 2005: Marine boundary layer clouds at the heart of tropical cloud feedback uncertainties in climate models. *Geophys. Res. Lett.*, **32**, L20806.

Bony, S., and K. A. Emanuel, 2005: On the role of moist processes in tropical intraseasonal variability: Cloud-radiation and moisture-convection feedbacks. *J. Atmos. Sci.*, 2770–2789.

Bretherton, C., and S. Park, 2009: A new moist turbulence parameterization in the Community Atmosphere Model. *J. Clim.*, **22**, 3422–3448.

Bretherton, C. S., 1987: A theory for nonprecipitating moist convection between two parallel plates. Part I: thermodynamics and "linear" solutions. *J. Atmos. Sci.*, **44**, 1809–1827.

Bretherton, C. S., 2002: Wave-CISK. *Encyclopedia of Atmospheric Sciences*, J.R. Holton, J.A. Curry, and J.A. Pyle, Eds., Academic Press.

Bretherton, C. S., and P. K. Smolarkiewicz, 1989: Gravity waves, compensating subsidence and detrainment around cumulus clouds. *J. Atmos. …*, **46**, 740–759.

Bryan, G., 2003: Resolution requirements for the simulation of deep moist convection. *Mon. Weather …*, **131**, 2394–2416.

Camargo, S., M. C. Wheeler, and A. H. Sobel, 2009: Diagnosis of the MJO modulation of tropical cyclogenesis using an empirical index. *J. Atmos. Sci.*, **66**, 3061–3074.

Cassou, C., 2008: Intraseasonal interaction between the Madden-Julian Oscillation and the North Atlantic Oscillation. *Nature*, **455**, 523–527.

Chang, C.-P., 1970: A statistical study of easterly waves in the western Pacific: July-December 1964. *J. Atmos. …*, **27**, 195–201.

Charney, J., 1947: The dynamics of long waves in a baroclinic westerly current. *J. Meteorol.*, **4**, 135–162.

Charney, J., 1948: On the scale of atmospheric motions. *Geof. publ,.*

Charney, J., 1963: A note of large-scale motions in the tropics. *J. Atmos. Sci.*, **20**, 607–609.

Charney, J., and A. Eliassen, 1964: On the growth of the hurricane depression. *J. Atmos. Sci.*, **21**, 68–75.

Chepfer, H., S. Bony, D. Winker, M. Chiriaco, J.-L. Dufresne, and G. Sèze, 2008: Use of CALIPSO lidar observations to evaluate the cloudiness simulated by a climate model. *Geophys. Res. Lett.*, **35**, L15704.

Chikira, M., 2010: A cumulus parameterization with state-dependent entrainment rate. Part II: Impact on climatology in a general circulation model. *J. Atmos. Sci.*, **67**, 2194–2211.

Chikira, M., 2014: Eastward-Propagating Intraseasonal Oscillation Represented by Chikira–Sugiyama Cumulus Parameterization. Part II: Understanding Moisture Variation under Weak Temperature Gradient Balance. *J. Atmos. Sci.*, **71**, 615–639.

Chikira, M., and M. Sugiyama, 2010: A cumulus parameterization with state-dependent entrainment rate. Part I: Description and sensitivity to temperature and humidity profiles. *J. Atmos. Sci.*, **67**, 2171–2193.

Ciesielski, P. E., W. H. Schubert, and R. H. Johnson, 1999: Large-scale heat and moisture budgets over the ASTEX region. *J. …*, **56**, 3241–3261.

Cohen, C., 2000: A quantitative investigation of entrainment and detrainment in numerically simulated cumulonimbus clouds. *J. Atmos. Sci.*, 1657–1674.

Cole, J. N. S., H. W. Barker, D. a. Randall, M. F. Khairoutdinov, and E. E. Clothiaux, 2005: Global consequences of interactions between clouds and radiation at scales unresolved by global climate models. *Geophys. Res. Lett.*, **32**, L06703.

Damiani, R., G. Vali, and S. Haimov, 2006: The structure of thermals in cumulus from airborne dual-Doppler radar observations. *J. Atmos. …*, **63**, 1432–1450.

Dawe, J. T., and P. H. Austin, 2011a: The Influence of the Cloud Shell on Tracer Budget Measurements of LES Cloud Entrainment. *J. Atmos. Sci.*, **68**, 2909–2920.

Dawe, J. T., and P. H. Austin, 2011b: Interpolation of LES cloud surfaces for use in direct calculations of entrainment and detrainment. *Mon. Weather Rev.*, **139**, 444–456.

Dawe, J. T., and P. H. Austin, 2013: Direct entrainment and detrainment rate distributions of individual shallow cumulus clouds in an LES. *Atmos. Chem. Phys.*, **13**, 7795–7811.

Deardorff, J., 1980: cloud top entrainment instability. *J. Atmos. Sci.*, **37**, 131–147.

Dee, D. and Coauthors, 2011: The ERA-Interim reanalysis: Configuration and performance of the data assimilation system. *Quart. J. Roy. Meteor. Soc*, **137**, 553–597.

DeMott, C. a., D. a. Randall, and M. Khairoutdinov, 2007: Convective Precipitation Variability as a Tool for General Circulation Model Analysis. *J. Clim.*, **20**, 91–112.

DeMott, C. a., C. Stan, D. a. Randall, J. L. Kinter, and M. Khairoutdinov, 2011: The Asian Monsoon in the Superparameterized CCSM and Its Relationship to Tropical Wave Activity. *J. Clim.*, **24**, 5134–5156.

Derbyshire, S. H., I. Beau, P. Bechtold, J.-Y. Grandpeix, J.-M. Pirou, R. J.-L., and P. M. M. Soares, 2004: Sensitivity of moist convection to environmental humidity. *Q. J. …*, **130**, 3055–3079.

Ding, R., J. Li, and K.-H. Seo, 2010: Predictability of the Madden–Julian Oscillation Estimated Using Observational Data. *Mon. Weather Rev.*, **138**, 1004–1013.

Donald, A., H. Meinke, B. Power, A. D. H. N. Maia, M. C. Wheeler, N. White, R. C. Stone, and J. Ribbe, 2006: Near-global impact of the Madden-Julian Oscillation on rainfall. *Geophys. Res. Lett.*, **33**, L09704.

Donner, L., and V. Phillips, 2003: Boundary layer control on convective available potential energy: Implications for cumulus parameterization. *J. Geophys. Res.*, **108**, 4701.

Emanuel, K. A., 1987: An air-sea interaction model of the intraseasonal oscillations in the tropics. *J. Atmos. Sci.*, **44**, 2324–2340.

Emanuel, K. A., 1991: A scheme for representing cumulus convection in large-scale models. *J. Atmos. Sci.*, **48**, 2313–2335.

Emanuel, K. A., 1994: *Atmospheric Convection*. oxford university press, New York, NY,.

Emanuel, K. A., 2003: Tropical Cyclones. *Annu. Rev. Earth Planet. Sci.*, **31**, 75–104.

Emanuel, K. A., J. D. Neelin, and C. S. Bretherton, 1994: On large-scale circulations in convectiv. *Q. J. …*, **120**, 1111–1143.

Espy, J. P., 1841: *The Philosophy of storms*. Little and Brown, Eds. Boston,.

Feddersen, H., A. Navarra, and M. N. Ward, 1999: Reduction of Model Systematic Error by Statistical Correction for Dynamical Seasonal Predictions. *J. Clim.*, **12**, 1974–1989.

Fierro, A. O., J. Simpson, M. a. LeMone, J. M. Straka, and B. F. Smull, 2009: On How Hot Towers Fuel the Hadley Cell: An Observational and Modeling Study of Line-Organized Convection in the Equatorial Trough from TOGA COARE. *J. Atmos. Sci.*, **66**, 2730–2746.

Flatau, M., and Y.-J. Kim, 2013: Interaction between the MJO and Polar Circulations. *J. Clim.*, **26**, 3562–3574.

Frierson, D., and D. Kim, 2011: Structure of AGCM-simulated convectively coupled Kelvin waves and sensitivity to convective parameterization. *J. …*, **68**, 26–45.

Fritsch, J. M., and C. F. Chappell, 1980: Numerical prediction of convectively driven mesoscale pressure systems. Part I: convective parameterization. *J. Atmos. Sci.*, **37**, 1722–1733.

Fu, X., and B. Wang, 2004: The Boreal-Summer Intraseasonal Oscillations Simulated in a Hybrid Coupled Atmosphere-Ocean Model*. *Mon. Weather Rev.*, **132**, 2628–2649.

Fuchs, Ž., S. Gjorgjievska, and D. J. Raymond, 2012: Effects of Varying the Shape of the Convective Heating Profile on Convectively Coupled Gravity Waves and Moisture Modes. *J. Atmos. Sci.*, **69**, 2505–2519.

Del Genio, A. D., 2012: Representing the Sensitivity of Convective Cloud Systems to Tropospheric Humidity in General Circulation Models. *Surv. Geophys.*, **33**, 637–656.

Del Genio, A. D., and J. Wu, 2010: The role of entrainment in the diurnal cycle of continental convection. *J. Clim.*, **23**, 2722–2738.

Glenn, I. B., and S. K. Krueger, 2014: Downdrafts in the near cloud environment of deep convective updrafts. *J. Adv. Model. Earth Syst.*, **6**, 1–7.

Golding, B., 1984: of the structure of mid-latitude depressions in a numerical model using trajectory techniques. I: Development of ideal baroclinic waves in dry and moist atmospheres. *Q. J. R. Meteorol. …*, **110**, 847–879.

Gottschalck, J. and Coauthors, 2010: A Framework for Assessing Operational Madden–Julian Oscillation Forecasts: A CLIVAR MJO Working Group Project. *Bull. Am. Meteorol. Soc.*, **91**, 1247–1258.

Gottschalck, J., P. E. Roundy, C. J. Schreck, A. Vintzileos, and C. Zhang, 2013: Large-Scale Atmospheric and Oceanic Conditions During the 2011-2012 DYNAMO Field Campaign.

Grabowski, W. W., 2001: Coupling Cloud Processes with the Large-Scale Dynamics Using the Cloud-Resolving Convection Parameterization (CRCP). *J. Atmos. Sci.*, **58**, 978–997.

Grabowski, W. W., and T. L. Clark, 1993: Cloud-environment interface instability. Part II: Extension to three spatial dimensions. *J. Atmos. …*, **50**, 555–573.

Grabowski, W. W., and M. W. Moncrieff, 2004: Moisture–convection feedback in the tropics. *Q. J. R. Meteorol. Soc.*, **130**, 3081–3104.

Grabowski, W. W., X. Wu, M. W. Moncrieff, and W. D. Hall, 1998: Cloud-resolving modeling of cloud systems during Phase III of GATE. Part II: Effects of resolution and the third spatial dimension. *J. …*, **55**, 3264–3282.

Gregory, D., 2001: Estimation of entrainment rate in simple models of convective clouds. *Q. J. R. Meteorol. …*, 53–72.

Grell, G., 1993: Prognostic evaluation of assumptions used by cumulus parameterizations. *Mon. Weather Rev.*, **121**, 764–787.

Hannah, W. M., and E. D. Maloney, 2011: The role of moisture-convection feedbacks in simulating the Madden-Julian oscillation. *J. Clim.*, **24**, 2754–2770.

Hayashi, Y., 1970: A theory of large-scale equatorial waves generated by condensation heat and accelerating the zonal wind. *J. Meteorol. Soc. Japan*, **48**, 140–160.

Held, I., and B. Soden, 2000: Water vapor feedback and global warming. *Annu. Rev. Energy Environ.*, **25**, 441–475.

Hill, M. J. M., 1894: On a spherical vortex. *Philos. Trans. Roy. Met. Soc.*, **185**, 213–245.

Hirons, L. C., P. M. Inness, F. Vitart, and P. Bechtold, 2013: Understanding advances in the simulation of intraseasonal variability in the ECMWF model. Part I: The representation of the MJO. *Q. J. R. Meteorol. Soc.*, **139**, 1417–1426.

Hogan, R. J., and A. J. Illingworth, 2003: Parameterizing Ice Cloud Inhomogeneity and the Overlap of Inhomogeneities Using Cloud Radar Data. *J. Atmos. Sci.*, **60**, 756–767.

Hohenegger, C., and B. Stevens, 2013: Preconditioning Deep Convection with Cumulus Congestus. *J. Atmos. Sci.*, **70**, 448–464.

Horel, J., and J. Wallace, 1981: Planetary-scale atmospheric phenomena associated with the Southern Oscillation. *Mon. Weather Rev.*, **109**, 813–829.

Hu, Q., and D. Randall, 1995: Low-frequency oscillations in radiative-convective systems. Part II: An idealized model. *J. Atmos. Sci.*, **52**, 478–490.

Huang, B., Z.-Z. Hu, and B. Jha, 2007: Evolution of model systematic errors in the tropical Atlantic basin from coupled climate hindcasts. *Clim. Dyn.*, **28**, 661–682.

Huffman, G. and Coauthors, 2007: The TRMM Multisatellite Precipitation Analysis (TMPA): Quasi-global, multiyear, combined-sensor precipitation estimates at fine scales. *J. …*, 38–55.

Igel, A. L., M. R. Igel, and S. C. van den Heever, 2014: Make it a double: Sobering results from simulations using single-moment microphysics schemes. *J. Atmos. Sci.*, **In Review**.

Igel, M. R., and S. C. van den Heever, 2014: Deep Convective Cloud Morphology as Observed by CloudSat. *J. Atmos. Sci.*, **Accepted**.

Inness, P. M., J. M. Slingo, S. J. Woolnough, R. B. Neale, and V. D. Pope, 2001: Organization of tropical convection in a GCM with varying vertical resolution; implications for the simulation of the Madden-Julian Oscillation. *Clim. Dyn.*, **17**, 777–793.

Jeong, J.-H., C.-H. Ho, and B.-M. Kim, 2005: Influence of the Madden-Julian Oscillation on wintertime surface air temperature and cold surges in east Asia. *J. Geophys. Res.*, **110**, D11104.

Jiang, X., D. E. Waliser, M. C. Wheeler, C. Jones, M.-I. Lee, and S. D. Schubert, 2008: Assessing the Skill of an All-Season Statistical Forecast Model for the Madden–Julian Oscillation. *Mon. Weather Rev.*, **136**, 1940–1956.

Johari, H., 1992: Mixing in thermals with and without buoyancy reversal. *J. Atmos. Sci.*, **49**, 1412–1426.

Johnson, R., 1976: The role of convective-scale precipitation downdrafts in cumulus and synoptic-scale interactions. *J. Atmos. Sci.*, **33**, 1890–1910.

Johnson, R., T. Rickenbach, S. A. Rutledge, P. E. Ciesielski, and W. H. Schubert, 1999: Trimodal characteristics of tropical convection. *J. Clim.*, **12**, 2397–2418.

Johnson, R. H., and P. E. Ciesielski, 2013: Structure and Properties of Madden–Julian Oscillations Deduced from DYNAMO Sounding Arrays. *J. Atmos. Sci.*, **70**, 3157–3179.

Jonas, P., 1990: Observations of cumulus cloud entrainment. *Atmos. Res.*, **25**, 105–127.

Jones, C., D. E. Waliser, K. M. Lau, and W. Stern, 2004: The Madden-Julian Oscillation and its impact on Northern Hemisphere weather predictability. *Mon. Weather …*, **132**, 1462–1471.

Jones, T. R., and D. a. Randall, 2011: Quantifying the limits of convective parameterizations. *J. Geophys. Res.*, **116**.

Jung, J., and A. Arakawa, 2005: Preliminary Tests of Multiscale Modeling with a Two-Dimensional Framework: Sensitivity to coupling methods. *Mon. Weather Rev.*, **133**, 649–662.

Jung, T., 2005: Systematic errors of the atmospheric circulation in the ECMWF forecasting system. *Q. J. R. Meteorol. Soc.*, **131**, 1045–1073.

Kanamitsu, M., W. Ebisuzaki, J. Woollen, S.-K. Yang, J. J. Hnilo, M. Fiorino, and G. L. Potter, 2002: NCEP–DOE AMIP-II Reanalysis (R-2). *Bull. Am. Meteorol. Soc.*, **83**, 1631–1643.

Kang, I.-S., J.-Y. Lee, and C.-K. Park, 2004: Potential predictability of summer mean precipitation in a dynamical seasonal prediction system with systematic error correction. *J. …*, **17**, 834–845.

Katsumata, M., P. E. Ciesielski, and R. H. Johnson, 2011: Evaluation of Budget Analyses during MISMO. *J. Appl. Meteorol. Climatol.*, **50**, 241–254.

Kemball-Cook, S. R., and B. C. Weare, 2001: The onset of convection in the Madden-Julian oscillation. *J. Clim.*, **14**, 780–793.

Khairoutdinov, M., and D. Randall, 2001: A cloud resolving model as a cloud parameterization in the NCAR community climate system model: preliminary results. *Geophys. Res. Lett.*, **28**, 36173620.

Khairoutdinov, M., and D. Randall, 2003: Cloud resolving modeling of the ARM summer 1997 IOP: Model formulation, results, uncertainties, and sensitivities. *J. Atmos. …*, **60**, 607–625.

Khairoutdinov, M., and D. A. Randall, 2006: High-resolution simulation of shallow-to-deep convection transition over land. *J. Atmos. …*, 3421–3436.

Khairoutdinov, M. F., D. A. Randall, and C. A. DeMott, 2005: Simulations of the atmospheric general circulation using a cloud-resolving model as a superparameterization of physical processes. *… Atmos. …*, **62**, 2136–2154.

Khairoutdinov, M. F., S. K. Krueger, C.-H. Moeng, P. a. Bogenschutz, and D. a. Randall, 2009: Large-eddy simulation of maritime deep tropical convection. *J. Adv. Model. Earth Syst.*, **2**, 15.

Khouider, B., and A. Majda, 2006: A simple multicloud parameterization for convectively coupled tropical waves. Part I: Linear analysis. *J. Atmos. Sci.*, **63**, 1308–1323.

Kiladis, G. N., M. C. Wheeler, P. T. Haertel, K. H. Straub, and P. E. Roundy, 2009: CONVECTIVELY COUPLED EQUATORIAL WAVES. 1–42.

Kiladis, G. N., J. Dias, K. H. Straub, M. C. Wheeler, S. N. Tulich, K. Kikuchi, K. M. Weickmann, and M. J. Ventrice, 2014: A comparison of OLR and circulation based indices for tracking the MJO. *Mon. Weather Rev.*, In Press.

Kim, D. and Coauthors, 2009: Application of MJO Simulation Diagnostics to Climate Models. *J. Clim.*, **22**, 6413–6436.

Kim, D., A. H. Sobel, E. D. Maloney, D. M. W. Frierson, and I.-S. Kang, 2011: A Systematic Relationship between Intraseasonal Variability and Mean State Bias in AGCM Simulations. *J. Clim.*, **24**, 5506–5520.

Kim, D., A. H. Sobel, A. D. Del Genio, Y. Chen, S. J. Camargo, M.-S. Yao, M. Kelley, and L. Nazarenko, 2012: The Tropical Subseasonal Variability Simulated in the NASA GISS General Circulation Model. *J. Clim.*, **25**, 4641–4659.

Kim, D., J.-S. Kug, and A. H. Sobel, 2013: Propagating vs. Non-propagating Madden-Julian Oscillation Events. *J. Clim.*, 130719115456001.

Klaassen, G. P., and T. L. Clark, 1985: Dynamics of the cloud-environment interface and entrainment in small cumuli: two-dimensional simulations in the absence of ambient shear. *J. Atmos. Sci.*, **42**, 2621–2642.

Klein, S. A., J. S. Boyle, J. Tannahill, D. Lucas, R. B. Neale, S. Xie, and K. R. Sperber, 2012: Perturbed-parameter hindcasts of the MJO with CAM5. *2012 AGU Fall Meet. San Fr. CA, 3-7 Dec.*,.

Klingaman, N. P., and S. J. Woolnough, 2014: Using a case-study approach to improve the madden-julian oscillation in the Hadley centre model. *Q. J. R. Meteorol. Soc.*, **in press**.

Klingaman, N. P., H. Weller, J. M. Slingo, and P. M. Inness, 2008: The Intraseasonal Variability of the Indian Summer Monsoon Using TMI Sea Surface Temperatures and ECMWF Reanalysis. *J. Clim.*, **21**, 2519–2539.

Klingaman, N. P., S. J. Woolnough, H. Weller, and J. M. Slingo, 2011: The Impact of Finer-Resolution Air–Sea Coupling on the Intraseasonal Oscillation of the Indian Monsoon. *J. Clim.*, **24**, 2451–2468.

Kuo, H. L., 1965: On formation and intensification of tropical cyclones through latent heat release by cumulus convection. *J. Atmos. Sci.*, **22**, 40–63.

Kuo, H. L., 1974: Further studies of the parameterization of the influence of cmulus convection on large-scale flow. *J. Atmos. Sci.*, **31**, 1232–1240.

Landu, K., and E. D. Maloney, 2011: Intraseasonal moist static energy budget in reanalysis data. *J. Geophys. Res.*, **116**, D21117.

Lane, T. P., and M. W. Moncrieff, 2010: Characterization of Momentum Transport Associated with Organized Moist Convection and Gravity Waves. *J. Atmos. Sci.*, **67**, 3208–3225.

Lawrence, D. M., and P. Webster, 2002: The boreal summer intraseasonal oscillation: Relationship between northward and eastward movement of convection. *J. Atmos. …*, **59**, 1593–1606.

LeMone, M., and E. Zipser, 1980: Cumulonimbus vertical velocity events in GATE. Part I: Diameter, Intensity and mass flux. *J. Atmos. Sci.*, **37**, 2444–2457.

Leonard, B. P., 1991: The ULTIMATE conservative difference scheme applied to unsteady one-dimensional advection. *Comput. Methods Appl. Mech. Eng.*, **88**, 17–74.

Leroy, A., and M. C. Wheeler, 2008: Statistical Prediction of Weekly Tropical Cyclone Activity in the Southern Hemisphere. *Mon. Weather Rev.*, **136**, 3637–3654.

Li, F., D. Rosa, W. D. Collins, and M. F. Wehner, 2012: "Super-parameterization": A better way to simulate regional extreme precipitation? *J. Adv. Model. Earth Syst.*, **4**, M04002.

Liebmann, B., and C. A. Smith, 1996: Description of a complete (interpolated) outgoing longwave radiation datasets. *Bull. Amer. Meteor. Soc.*, **77**, 1275–1277.

Lin, C., 1999: Some bulk properties of cumulus ensembles simulated by a cloud-resolving model. Part II: Entrainment profiles. *J. Atmos. Sci.*, 3736–3748.

Lin, C., and A. Arakawa, 1997a: The macroscopic entrainment processes of simulated cumulus ensemble. Part II: Testing the entraining-plume model. *J. Atmos. Sci.*, 1044–1053.

Lin, C., and A. Arakawa, 1997b: The macroscopic entrainment processes of simulated cumulus ensemble. Part I: Entrainment sources. *J. Atmos. Sci.*, 1027–1043.

Lin, H., G. Brunet, and J. Derome, 2008a: Forecast Skill of the Madden–Julian Oscillation in Two Canadian Atmospheric Models. *Mon. Weather Rev.*, **136**, 4130–4149.

Lin, H., G. Brunet, and J. Derome, 2009: An observed connection between the North Atlantic Oscillation and the Madden-Julian oscillation. *J. Clim.*, **22**, 364–380.

Lin, J. and Coauthors, 2006: Tropical intraseasonal variability in 14 IPCC AR4 climate models. Part I: Convective signals. *J. Clim.*, **19**, 2665–2690.

Lin, J.-L., M.-I. Lee, D. Kim, I.-S. Kang, and D. M. W. Frierson, 2008b: The Impacts of Convective Parameterization and Moisture Triggering on AGCM-Simulated Convectively Coupled Equatorial Waves. *J. Clim.*, **21**, 883–909.

Lin, J.-L., T. Shinoda, T. Qian, W. Han, P. Roundy, and Y. Zheng, 2010: Intraseasonal Variation of Winter Precipitation over the Western United States Simulated by 14 IPCC AR4 Coupled GCMs. *J. Clim.*, **23**, 3094–3119.

Lin, X., and R. Johnson, 1996: Heating, moistening, and rainfall over the western Pacific warm pool during TOGA COARE. *J. Atmos. Sci.*, **53**, 3367–3383.

Lindzen, R., 1967: Planetary waves on beta-planes. *Mon. Weather Rev.*, **95**, 441–451.

Lindzen, R., 1974: Wave-CISK in the tropics. *J. Atmos. Sci.*, **31**, 156–179.

Ling, J., C. Zhang, and P. Bechtold, 2013: Large-Scale Distinctions between MJO and Non-MJO Convective Initiation over the Tropical Indian Ocean. *J. Atmos. Sci.*, **70**, 2696–2712.

Liu, F., and B. Wang, 2012: A Frictional Skeleton Model for the Madden–Julian Oscillation*. *J. Atmos. Sci.*, **69**, 2749–2758.

Liu, P. and Coauthors, 2009: An MJO Simulated by the NICAM at 14- and 7-km Resolutions. *Mon. Weather Rev.*, **137**, 3254–3268.

Lord, S. J., 1982: Interaction of a cumulus cloud ensemble with the large-scale environment. Part III: Semi-prognostic test of the Arakawa-Schubert cumulus parameterization. *J. Atmos. Sci.*, **39**, 88–103.

Lu, C., Y. Liu, S. Niu, and A. M. Vogelmann, 2012a: Lateral entrainment rate in shallow cumuli: Dependence on dry air sources and probability density functions. *Geophys. Res. Lett.*, **39**, n/a–n/a.

Lu, C., Y. Liu, S. S. Yum, S. Niu, and S. Endo, 2012b: A new approach for estimating entrainment rate in cumulus clouds. *Geophys. Res. Lett.*, **39**, n/a–n/a.

Lu, C., Y. Liu, S. S. Yum, S. Niu, and S. Endo, 2012c: A new approach for estimating entrainment rate in cumulus clouds. *Geophys. Res. Lett.*, **39**, n/a–n/a.

Luo, Z., and G. L. Stephens, 2006: An enhanced convection-wind-evaporation feedback in a superparameterization GCM (SP-GCM) depiction of the Asian summer monsoon. *Geophys. Res. Lett.*, **33**, L06707.

Ma, H.-Y., S. Xie, J. S. Boyle, S. a. Klein, and Y. Zhang, 2013: Metrics and Diagnostics for Precipitation-Related Processes in Climate Model Short-Range Hindcasts. *J. Clim.*, **26**, 1516–1534.

Madden, R., and P. Julian, 1971: Detection of a 40-50 day oscillation in the zonal wind in the tropical pacific. *J. Atmos. Sci.*, **28**, 702–708.

Madden, R. A., and P. R. Julian, 1972: Description of global-scale circulation cells in the tropics with a 40-50 day period. *J. Atmos. Sci.*, **29**, 1109–1123.

Madden, R. A., and P. R. Julian, 1994: Observations of the 40-50-day tropical oscillation - a review. *Mon. Weather Rev.*, **122**, 814–837.

Madden, R. A., and P. R. Julian, 2005: Historical perspective. *Intraseasonal Variability in the …*, W.K. Lau and D.E. Waliser, Eds., Springer, 1–18.

Maloney, E. D., 2009: The Moist Static Energy Budget of a Composite Tropical Intraseasonal Oscillation in a Climate Model. *J. Clim.*, **22**, 711–729.

Maloney, E. D., and D. L. Hartmann, 2000: Modulation of Hurricane Activity in the Gulf of Mexico by the Madden-Julian Oscillation. *Science (80-.).*, **287**, 2002–2004.

Maloney, E. D., and D. Hartmann, 2001: The sensitivity of intraseasonal variability in the NCAR CCM3 to changes in convective parameterization. *J. Clim.*, **14**, 2015–2034.

Maloney, E. D., A. H. Sobel, and W. M. Hannah, 2010: Intraseasonal variability in an aquaplanet general circulation model. *J. Adv. Model. Earth Syst.*, **2**, 5.

Manabe, S., and R. F. Strickler, 1964: Thermal equilibrium of the atmosphere with a convective adjustment. *J. Atmos. Sci.*, **21**, 361–385.

Manabe, S., J. Smagorinsky, and R. F. Strickler, 1965: Simulated climatology of a general circulation model with a hydrologic cycle. *Mon. Weather Rev.*, **93**, 769–798.

Mapes, B., 1993: Gregarious tropical convection. *J. Atmos. Sci.*, **50**, 2026–2037.

Mapes, B., 1997: Equilibrium vs. activation control of large-scale variations of tropical deep convection. *The Physics and Parameterization of Moist Atmospheric Convection*, Kluwer Academic Publishers, Dordrecht, 321–358.

Mapes, B., 2000: Convective inhibition, subgrid-scale triggering energy, and stratiform instability in a toy tropical wave model. *J. Atmos. Sci.*, **57**, 1515–1535.

Mapes, B., and R. Neale, 2011: Parameterizing Convective Organization to Escape the Entrainment Dilemma. *J. Adv. Model. Earth Syst.*, **3**, M06004.

Mapes, B. E., and J. T. Bacmeister, 2012: Diagnosis of Tropical Biases and the MJO from Patterns in the MERRA Analysis Tendency Fields. *J. Clim.*, **25**, 6202–6214.

Matsuno, T., 1966: Quasi-Geostrophic Motions Equatorial Area. *J. Meteor. Soc. Japan*, **44**, 25–43.

McCarthy, J., 1974a: Field verification of the relatinoship between entrainment rate and cumulus cloud diameter. *J. Atmos. Sci.*, **31**, 1028–1039.

McCarthy, J., 1974b: Field verification of the relatinoship between entrainment rate and cumulus cloud diameter. *J. Atmos. Sci.*, **31**, 1028–1039.

Meyers, M. P., R. L. Walko, J. Y. Harrington, and W. R. Cotton, 1997: New RAMS cloud microphysics parameterization. Part II: The two-moment scheme. *Atmos. Res.*, **45**, 3–39.

Miura, H., 2005: A climate sensitivity test using a global cloud resolving model under an aqua planet condition. *Geophys. Res. Lett.*, **32**, L19717.

Mo, K., 2000: The association between intraseasonal oscillations and tropical storms in the Atlantic basin. *Mon. Weather Rev.*, **128**, 4097–4107.

Mo, K., and R. Higgins, 1998: Tropical influences on California precipitation. *J. Clim.*, **11**, 412–430.

Moncrieff, M., and C. Liu, 2006: Representing convective organization in prediction models by a hybrid strategy. *J. Atmos. Sci.*, **63**, 3404–3420.

Moncrieff, M. W., 1992: Organized Convective Systems: Archetypal Dynamical Models, Mass and Momentum Flux Theory, and Parametrization. *Q. J. R. Meteorol. Soc.*, **118**, 819–850.

Moncrieff, M. W., 2010: The Multiscale Organization of Moist Convection and the Intersection of Weather and Climate.

Moncrieff, M. W., D. E. Waliser, M. J. Miller, M. a. Shapiro, G. R. Asrar, and J. Caughey, 2012: Multiscale Convective Organization and the YOTC Virtual Global Field Campaign. *Bull. Am. Meteorol. Soc.*, **93**, 1171–1187.

Mooley, D. a., and B. Parthasarathy, 1982: Fluctuations in the deficiency of the summer monsoon over India, and their effect on economy. *Arch. Meteorol. Geophys. Bioclimatol. Ser. B*, **30**, 383–398.

Moon, J.-Y., and K.-J. Ha, 2003: Association between tropical convection and boreal wintertime extratropical circulation in 1982/83 and 1988/89. *Adv. Atmos. Sci.*, **20**, 593–603.

Moorthi, S., and M. Suarez, 1992: relaxed arakawa-schubert: a parameterization of moist convection for general circulation models. *Mon. Weather Rev.*, **120**, 978–1002.

Morrison, H., and A. Gettelman, 2008: A New Two-Moment Bulk Stratiform Cloud Microphysics Scheme in the Community Atmosphere Model, Version 3 (CAM3). Part I: Description and Numerical Tests. *J. Clim.*, **21**, 3642–3659.

Morton, B., G. Taylor, and J. Turner, 1956a: Turbulent Gravitational convection from maintained and instantaneous sources. *Proc. R. Soc. london. Ser. A, Math. Phys. Sci.*, **234**, 1–23.

Morton, B. R., G. Taylor, J. S. Turner, L. Series, and P. Sciences, 1956b: Turbulent gravitational convection from maintained and instantaneous sources. **234**, 1–23.

Narasimha, R., S. S. Diwan, S. Duvvuri, K. R. Sreenivas, and G. S. Bhat, 2011: Laboratory simulations show diabatic heating drives cumulus-cloud evolution and entrainment. *Proc. Natl. Acad. Sci. U. S. A.*, **108**, 16164–16169.

Neale, R. B., J. H. Richter, and M. Jochum, 2008: The Impact of Convection on ENSO: From a Delayed Oscillator to a Series of Events. *J. Clim.*, **21**, 5904–5924.

Neale, R. B. and Coauthors, 2010: Description of the NCAR Community Atmosphere Model (CAM 5 . 0).

Neelin, J., I. Held, and K. Cook, 1987a: Evaporation-wind feedback and low-frequency variability in the tropical atmosphere. *J. Atmos. …*, **44**, 2341–2348.

Neelin, J., I. Held, and K. Cook, 1987b: Evaporation-wind feedback and low-frequency variability in the tropical atmosphere. *J. Atmos. …*, **44**, 2341–2348.

Neelin, J. D., and I. M. Held, 1987: Modeling tropical convergencebased on the moist static energy budget. *Mon. Weather Rev.*, **115**, 3–12.

Neelin, J. D., O. Peters, J. W.-B. Lin, K. Hales, and C. E. Holloway, 2008: Rethinking convective quasi-equilibrium: observational constraints for stochastic convective schemes in climate models. *Philos. Trans. A. Math. Phys. Eng. Sci.*, **366**, 2581–2604.

Neggers, R., A. P. Siebesma, and H. J. J. Jonker, 2002: A multiparcel model for shallow cumulus convection. *J. …*, **59**, 1655–1668.

Numaguti, A., and Y. Hayashi, 1991: Behavior of cumulus activity and the structures of circulations in an “Aqua planet” model Part I: The Structure of super clusters. *J. Meteor. Soc. Japan*, **69**, 541–561.

Ooyama, K., 1964: a dynamical model for the study of tropical cyclone development. *Geofis. Intern.*, **4**, 187–198.

Ooyama, K., 1969: Numerical simulation of the life cycle of tropical cyclones. *J. Atmos. Sci.*, **26**, 3–40.

Oreopoulos, L., and R. Cahalan, 2005: Cloud inhomogeneity from MODIS. *J. Clim.*, **18**, 5110–5124.

Paluch, I., 1979: the Entrainment mechanism in colorado cumuli. *J. Atmos. Sci.*, **36**, 2467–2478.

Pan, D., and D. A. Randall, 1998: A cumulus parametrization with a prognostic closure. *Q. J. R. …*, 949–981.

Park, S., and C. S. Bretherton, 2009: The University of Washington Shallow Convection and Moist Turbulence Schemes and Their Impact on Climate Simulations with the Community Atmosphere Model. *J. Clim.*, **22**, 3449–3469.

Parker, M. D., 2010: Relationship between System Slope and Updraft Intensity in Squall Lines. *Mon. Weather Rev.*, **138**, 3572–3578.

Pavan, V., and F. J. Doblas-Reyes, 2000: Multi-model seasonal hindcasts over the Euro-Atlantic: skill scores and dynamic features. *Clim. Dyn.*, **16**, 611–625.

Peters, M. E., and C. S. Bretherton, 2006: Structure of tropical variability from a vertical mode perspective. *Theor. Comput. Fluid Dyn.*, **20**, 501–524.

Pielke, R. A., J. Gratz, C. Landsea, D. Collins, M. A. Saunders, and R. Musulin, 2008: Normalized hurricane damage in the United States: 1900–2005. *Nat. Hazards Rev.*, **9**, 29–42.

Powell, S. W., and R. a. Houze, 2013: The cloud population and onset of the Madden-Julian Oscillation over the Indian Ocean during DYNAMO-AMIE. *J. Geophys. Res. Atmos.*, **118**, 11,979–11,995.

Pritchard, M. S., and R. C. J. Somerville, 2009: Assessing the diurnal cycle of precipitation in a multi-scale climate model. *J. Adv. Model. Earth Syst.*, **2**, 12.

Pritchard, M. S., and C. S. Bretherton, 2014: Causal evidence that rotational moisture advection is critical to the superparameterized Madden-Julian Oscillation. *J. Atmos. Sci.*, **In Press**.

Randall, D. a., 2013: Beyond deadlock. *Geophys. Res. Lett.*, **40**, 5970–5976.

Randall, D. a., M. Khairoutdinov, A. Arakawa, and W. Grabowski, 2003: Breaking the Cloud Parameterization Deadlock. *Bull. Am. Meteorol. Soc.*, **84**, 1547–1564.

Rashid, H. a., H. H. Hendon, M. C. Wheeler, and O. Alves, 2010: Prediction of the Madden–Julian oscillation with the POAMA dynamical prediction system. *Clim. Dyn.*, **36**, 649–661.

Raymond, D., and A. Blyth, 1986: A stochastic mixing model for nonprecipitating cumulus clouds. *J. Atmos. Sci.*, **43**, 2708–2718.

Raymond, D. J., 2001: A New Model of the Madden–Julian Oscillation. *J. Atmos. Sci.*, **58**, 2807–2819.

Raymond, D. J., and D. J. Torres, 1998: Fundamental Moist Modes of the Equatorial Troposphere. *J. Atmos. Sci.*, **55**, 1771–1790.

Raymond, D. J., and Ž. Fuchs, 2009: Moisture Modes and the Madden–Julian Oscillation. *J. Clim.*, **22**, 3031–3046.

Raymond, D. J., S. L. Sessions, and A. H. Sobel, 2009: The Mechanics of Gross Moist Stability ˇ.

Redelsperger, J.-L., D. B. Parsons, and F. Guichard, 2002: Recovery processes and factors limiting cloud-top height following the arrival of a dry intrusion observed during TOGA COARE. *J. …*, **59**, 2438–2457.

Richards, J. M., 1963: Comparisons between calculated thermal motions and experiments. *J. Atmos. Sci.*, **20**, 241–242.

Richter, J. H., and P. J. Rasch, 2008: Effects of Convective Momentum Transport on the Atmospheric Circulation in the Community Atmosphere Model, Version 3. *J. Clim.*, **21**, 1487–1499.

Rickenbach, T., and S. Rutledge, 1998: Convection in TOGA COARE: Horizontal scale, morphology, and rainfall production. *J. Atmos. …*, 2715–2729.

Riehl, H., and J. S. Malkus, 1958: On the heat balance in the equatorial trough zone." Geophysica 6.3-4 (1958): 503-538. *Geophysica*, **6**, 503–538.

Robe, F. R., and K. a. Emanuel, 2001: The Effect of Vertical Wind Shear on Radiative–Convective Equilibrium States. *J. Atmos. Sci.*, **58**, 1427–1445.

Romps, D. M., 2010: A Direct Measure of Entrainment. *J. Atmos. Sci.*, **67**, 1908–1927.

Romps, D. M., 2012a: Weak Pressure Gradient Approximation and Its Analytical Solutions. *J. Atmos. Sci.*, **69**, 2835–2845.

Romps, D. M., 2012b: On the Equivalence of Two Schemes for Convective Momentum Transport. *J. Atmos. Sci.*, **69**, 3491–3500.

Romps, D. M., and Z. Kuang, 2010a: Do Undiluted Convective Plumes Exist in the Upper Tropical Troposphere? *J. Atmos. Sci.*, **67**, 468–484.

Romps, D. M., and Z. Kuang, 2010b: Nature versus Nurture in Shallow Convection. *J. Atmos. Sci.*, **67**, 1655–1666.

De Rooy, W. C., and a. P. Siebesma, 2008: A Simple Parameterization for Detrainment in Shallow Cumulus. *Mon. Weather Rev.*, **136**, 560–576.

De Rooy, W. C. and Coauthors, 2013: Entrainment and detrainment in cumulus convection: an overview. *Q. J. R. Meteorol. Soc.*, **139**, 1–19.

Rossby, C.-G., 1939: Relation between variations in the intensity of the zonal circulation of the atmosphere and the displacements of the semi-permanent centers of action. *J. Mar. Res.*, **2**, 38–55.

Rotunno, R., J. B. Klemp, and M. L. Weisman, 1988: A theory for strong, long-lived squall lines. *J. Atmos. …*, **45**, 463–485.

Rougier, J., D. M. H. Sexton, J. M. Murphy, and D. Stainforth, 2009: Analyzing the Climate Sensitivity of the HadSM3 Climate Model Using Ensembles from Different but Related Experiments. *J. Clim.*, **22**, 3540–3557.

Roundy, P., 2012: Tropical–extratropical interactions. *Intraseasonal Variability in the …*, W. Lau and D. Waliser, Eds., 497–512.

Roundy, P. E., and L. M. Gribble-Verhagen, 2010: Variations in the Flow of the Global Atmosphere Associated with a Composite Convectively Coupled Oceanic Kelvin Wave. *J. Clim.*, **23**, 4192–4201.

Roundy, P. E., K. MacRitchie, J. Asuma, and T. Melino, 2010: Modulation of the Global Atmospheric Circulation by Combined Activity in the Madden–Julian Oscillation and the El Niño–Southern Oscillation during Boreal Winter. *J. Clim.*, **23**, 4045–4059.

Sahany, S., J. D. Neelin, K. Hales, and R. B. Neale, 2012: Temperature–Moisture Dependence of the Deep Convective Transition as a Constraint on Entrainment in Climate Models. *J. Atmos. Sci.*, **69**, 1340–1358.

Salby, M. L., R. Garcia, and H. H. Hendon, 1994: Planetary-scale circulations in the presence of climatological and wave-induced heating. *J. Atmos. …*, **51**, 2344–2367.

Salzen, K. von, and N. McFarlane, 2002: Parameterization of the bulk effects of lateral and cloud-top entrainment in transient shallow cumulus clouds. *J. Atmos. …*, **59**, 1405–1430.

Sànchez, O., D. J. Raymond, L. Libersky, and A. G. Petschek, 1989: The Developement of thermals from rest. *J. Atmos. Sci.*, **46**, 2280–2292.

Sardeshmukh, P. D., and B. J. Hoskins, 1988: The generation of global rotational flow by steady idealized tropical divergence. *J. Atmos. Sci.*, **45**, 1228–1251.

Sato, T., H. Miura, M. Satoh, Y. N. Takayabu, and Y. Wang, 2009: Diurnal Cycle of Precipitation in the Tropics Simulated in a Global Cloud-Resolving Model. *J. Clim.*, **22**, 4809–4826.

Satoh, M., T. Matsuno, H. Tomita, H. Miura, T. Nasuno, and S. Iga, 2008: Nonhydrostatic icosahedral atmospheric model (NICAM) for global cloud resolving simulations. *J. Comput. Phys.*, **227**, 3486–3514.

Scorer, R. S., 1957: Experiments on convection of isolated masses of buoyant fluid. *J. Fluid Mech.*, **2**, 583–594.

Scorer, R. S., and C. Ronne, 1956: Experiments with convection bubbles. *Weather*, **11**, 151–155.

Seigel, R. B., and S. C. van den Heever, 2013: Squall-Line Intensification via Hydrometeor Recirculation. *J. Atmos. Sci.*, **70**, 2012–2031.

Seigel, R. B., S. C. van den Heever, and S. M. Saleeby, 2013: Mineral dust indirect effects and cloud radiative feedbacks of a simulated idealized nocturnal squall line. *Atmos. Chem. Phys.*, **13**, 4467–4485.

Seo, K.-H., W. Wang, J. Gottschalck, Q. Zhang, J.-K. E. Schemm, W. R. Higgins, and A. Kumar, 2009: Evaluation of MJO Forecast Skill from Several Statistical and Dynamical Forecast Models. *J. Clim.*, **22**, 2372–2388.

Sherwood, S. C., D. Hernández-Deckers, M. Colin, and F. Robinson, 2013: Slippery Thermals and the Cumulus Entrainment Paradox*. *J. Atmos. Sci.*, **70**, 2426–2442.

Siebesma, a. P., P. M. M. Soares, and J. Teixeira, 2007: A Combined Eddy-Diffusivity Mass-Flux Approach for the Convective Boundary Layer. *J. Atmos. Sci.*, **64**, 1230–1248.

Siebesma, A., and J. Cuijpers, 1995: Evaluation of parametric assumptions for shallow cumulus convection. *J. Atmos. …*,.

Simpson, J., 1971: On Cumulus Entrainment and One-Dimensional Models. *J. Atmos. Sci.*, **28**.

Simpson, J., 1972: Reply. *J. Atmos. Sci.*, **29**, 220–225.

Simpson, J., R. H. Simpson, U. S. W. Bureau, U. S. Army, W. Point, N. York, and U. S. Navy, 1965: Experimental Cumulus Dynamics. *Rev. Geophys.*, **3**, 387–431.

Slingo, J. M. and Coauthors, 1996: Intraseasonal oscillations in 15 atmospheric general circulation models : results from an AMIP diagnostic subproject. *Clim. Dyn.*, **12**, 325–357.

Sloss, P., 1967a: An Empirical examination of cumulus entrainment. *J. Appl. Meteorol.*, **6**, 878–881.

Sloss, P., 1967b: An Empirical examination of cumulus entrainment. *J. Appl. Meteorol.*, **6**, 878–881.

Sobel, A., and E. D. Maloney, 2012: An Idealized Semi-Empirical Framework for Modeling the Madden–Julian Oscillation. *J. Atmos. Sci.*, **69**, 1691–1705.

Sobel, A., and E. D. Maloney, 2013: Moisture Modes and the Eastward Propagation of the MJO. *J. Atmos. Sci.*, **70**, 187–192.

Sobel, A. H., J. Nilsson, and L. M. Polvani, 2001: The Weak Temperature Gradient Approximation and Balanced Tropical Moisture Waves*. *J. Atmos. Sci.*, **58**, 3650–3665.

Sobel, A. H., E. D. Maloney, G. Bellon, and D. M. Frierson, 2010: Surface fluxes and tropical intraseasonal variability: A reassessment. *J. Adv. Model. Earth Syst.*, **2**, 2.

Squires, P., 1958: The spatial variation of liquid water and droplet concentration in cumuli. *Tellus*, **10**, 372–380.

Stephens, G. L., 2005: Cloud feedbacks in the climate system: A critical review. *J. Clim.*, **18**, 237–273.

Stirling, a. J., and R. a. Stratton, 2012: Entrainment processes in the diurnal cycle of deep convection over land. *Q. J. R. Meteorol. Soc.*, **138**, 1135–1149.

Stith, J. L., 1992: Observations of cloud-top entrainment in cumuli. *J. Atmos. Sci.*, **49**, 1334–1347.

Stommel, H., 1947: Entrainment of air into a cumulus cloud. *J. Meteorol.*, **4**, 91–94.

Straub, K., and G. Kiladis, 2003: The observed structure of convectively coupled Kelvin waves: Comparison with simple models of coupled wave instability. *J. Atmos. Sci.*, **60**, 1655–1668.

Straub, K. H., 2013: MJO Initiation in the Real-Time Multivariate MJO Index. *J. Clim.*, **26**, 1130–1151.

Subramanian, A. C., M. Jochum, A. J. Miller, R. Murtugudde, R. B. Neale, and D. E. Waliser, 2011: The Madden–Julian Oscillation in CCSM4. *J. Clim.*, **24**, 6261–6282.

Sugiyama, M., 2009: The Moisture Mode in the Quasi-Equilibrium Tropical Circulation Model. Part I: Analysis Based on the Weak Temperature Gradient Approximation. *J. Atmos. Sci.*, **66**, 1507–1523.

Tao, W.-K. and Coauthors, 2009: A Multiscale Modeling System: Developments, Applications, and Critical Issues. *Bull. Am. Meteorol. Soc.*, **90**, 515–534.

Taylor, G., and M. Baker, 1991: Entrainment and Detrainment in Cumulus Clouds. *J. Atmos. Sci.*,.

Telford, J. W., 1975: Turbulence, entrainment, and mixing in cloud dynamics. *Pure Appl. Geophys. PAGEOPH*, **113**, 1067–1084.

Thayer-Calder, K., 2012: Downdraft impacts on tropical convection. Colorado State University, .

Thayer-Calder, K., and D. a. Randall, 2009: The Role of Convective Moistening in the Madden–Julian Oscillation. *J. Atmos. Sci.*, **66**, 3297–3312.

Tiedtke, M., 1989: A comprehensive mass flux scheme for cumulus parameterization. *Mon. Weather Rev.*, **117**, 1779–1800.

Tokioka, T., K. Yamazaki, A. Kitoh, and T. Ose, 1988: The Equatorial 30-60 day Oscillation and the Arakawa-Schubert Parameterization. *J. Meteorol. Soc. Japan*, **66**, 883–901.

Tompkins, a. M., 2000: The Impact of Dimensionality on Long-Term Cloud-Resolving Model Simulations. *Mon. Weather Rev.*, **128**, 1521–1535.

Tompkins, A. M., 2001: Organization of Tropical Convection in Low Vertical Wind Shears: The Role of Cold Pools. *J. Atmos. Sci.*, **58**, 1650–1672.

Tung, W., J. Gao, J. Hu, and L. Yang, 2011: Detecting chaos in heavy-noise environments. *Phys. Rev. E*, **83**, 046210.

Turner, J., 1986: Turbulent entrainment: the development of the entrainment assumption, and its application to geophysical flows. *J. Fluid Mech*, **173**, 431–471.

Turner, J. S., 1962: The "starting plume" in neutral surroundings. *J. Fluid Mech.*, **13**, 356–368.

Turner, J. S., 1969: Buoyant Plumes and Thermals. *Annu. Rev. Fluid Mech.*, **1**, 29–44.

Twomey, S., 1977: The influence of pollution of the shortwave albedo of clouds. *J. Atmos. Sci.*, **34**, 1149–1152.

Vecchi, G. a., and N. A. Bond, 2004: The Madden-Julian Oscillation (MJO) and northern high latitude wintertime surface air temperatures. *Geophys. Res. Lett.*, **31**, L04104.

Vitart, F., S. Woolnough, M. a. Balmaseda, and a. M. Tompkins, 2007: Monthly Forecast of the Madden–Julian Oscillation Using a Coupled GCM. *Mon. Weather Rev.*, **135**, 2700–2715.

Wagner, T. M., and H.-F. Graf, 2010: An Ensemble Cumulus Convection Parameterization with Explicit Cloud Treatment. *J. Atmos. Sci.*, **67**, 3854–3869.

Waliser, D. E., 2005: Predictability and forecasting. *Intraseasonal Variability in the Atmosphere-Ocean Climate System*, Springer Praxis Books, 389–423.

Waliser, D. E., K. M. Lau, W. Stern, and C. Jones, 2003: Potential Predictability of the Madden–Julian Oscillation. *Bull. Am. Meteorol. Soc.*, **84**, 33–50.

Wang, B., 1988: Dynamics of tropical low-frequency waves: an analysis of the moist kelvin wave. *J. Atmos. Sci.*, **45**, 2051–2065.

Wang, W., and M. E. Schlesinger, 1999: The Dependence on Convection Parameterization of the Tropical Intraseasonal Oscillation Simulated by the UIUC 11-Layer Atmospheric GCM. *J. Clim.*, **12**, 1423–1457.

Warner, J., 1955: The Water content of cumuliform cloud. *Tellus*, **4**, 449–457.

Warner, J., 1970: On steady-state One-dimensional models of cumulus convection. *J. Atmos. Sci.*, **27**, 1035–1040.

Warner, J., 1972: Comments "On cumulus entrainment and one-dimensional models." *J. Atmos. Sci.*, **29**, 218–219.

Weller, R., and S. Anderson, 1996: Surface meteorology and air-sea fluxes in the western equatorial Pacific warm pool during the TOGA Coupled Ocean-Atmosphere Response Experiment. *J. Clim.*, **9**, 1959–1990.

Wetherald, R. T., and S. Manabe, 1980: Cloud cover and climate sensitivity. *J. Atmos. …*, **37**, 1485–1510.

Wheeler, M., and G. N. Kiladis, 1999: Convectively Coupled Equatorial Waves: Analysis of Clouds and Temperature in the Wavenumber–Frequency Domain. *J. Atmos. Sci.*, **56**, 374–399.

Wheeler, M., G. N. Kiladis, and P. Webster, 2000: Large-scale dynamical fields associated with convectively coupled equatorial waves. *J. Atmos. …*, **57**, 613–640.

Wheeler, M. C., and H. H. Hendon, 2004: An All-Season Real-Time Multivariate MJO Index: Development of an Index for Monitoring and Prediction. *Mon. Weather Rev.*, **132**, 1917–1932.

Williams, E. R., S. A. Rutledge, S. G. Geotis, N. Renno, E. Rasmussen, and T. Rikenbach, 1992: A radar and electrical stidy of tropical "hot towers." *J. Atmos. Sci.*, **49**, 1386–1395.

Woodward, B., 1959: The motion in and around isolated thermals. *Quart. J. Roy. Meteor. Soc*, **85**, 144–151.

Woolnough, S. J., F. Vitart, and M. A. Balmaseda, 2007: The role of the ocean in the Madden – Julian Oscillation : Implications for MJO prediction. *Quart. J. Roy. Meteor. Soc*, **128**, 117–128.

Xie, S., H.-Y. Ma, J. S. Boyle, S. a. Klein, and Y. Zhang, 2012: On the Correspondence between Short- and Long-Time-Scale Systematic Errors in CAM4/CAM5 for the Year of Tropical Convection. *J. Clim.*, **25**, 7937–7955.

Yamaguchi, T., and D. a. Randall, 2012: Cooling of Entrained Parcels in a Large-Eddy Simulation. *J. Atmos. Sci.*, **69**, 1118–1136.

Yamasaki, M., 1969: Large-scale disturbances in the conditionally unstable atmosphere in low latitudes. *Pap. Meteorol. Geophys.*, **20**, 289–336.

Yanai, M., S. Esbensen, and J. Chu, 1973: Determination of bulk properties of tropical cloud clusters from large-scale heat and moisture budgets. *J. Atmos. …*, **30**, 611–627.

Yano, J., and K. A. Emanuel, 1991: an improved model of the equatorial troposphere and its coupling with the stratosphere. *J. Atmos. Sci.*, **48**, 377–389.

Yeo, K., and D. M. Romps, 2013: Measurement of Convective Entrainment Using Lagrangian Particles. *J. Atmos. Sci.*, **70**, 266–277.

Yoneyama, K., C. Zhang, and C. N. Long, 2013: Tracking Pulses of the Madden–Julian Oscillation. *Bull. Am. Meteorol. Soc.*, **94**, 1871–1891.

Yu, J., C. Chou, and J. Neelin, 1998: Estimating the Gross Moist Stability of the Tropical Atmosphere*. *J. Atmos. …*, **55**, 1354–1372.

Zhang, C., 2005: MADDEN-JULIAN OSCILLATION. 1–36.

Zhang, C., 2013: Madden-Julian Oscillation: Bridging weather and climate. *Bull. Am. Meteorol. Soc.*,.

Zhang, C., and S. Anderson, 2003: Sensitivity of intraseasonal perturbations in SST to the structure of the MJO. *J. Atmos. Sci.*, **60**, 2196–2207.

Zhang, G. J., 2003: Convective quasi-equilibrium in the tropical western Pacific: Comparison with midlatitude continental environment. *J. Geophys. Res.*, **108**, 4592.

Zhang, G. J., and N. A. Mcfarlane, 1995: Sensitivity of Climate Simulations to the Parameterization of Cumulus Convection in the Canadian Climate Centre General Circulation Model. **33**, 407–446.

Zhang, Y., S. a. Klein, J. Boyle, and G. G. Mace, 2010: Evaluation of tropical cloud and precipitation statistics of Community Atmosphere Model version 3 using CloudSat and CALIPSO data. *J. Geophys. Res.*, **115**, D12205.

Zhao, M., and P. H. Austin, 1998: Episodic Mixing and Buoyancy-sorting Representations of Shallow Convection : A Diagnostic Study.

Zhao, M., and P. Austin, 2005: Life cycle of numerically simulated shallow cumulus clouds. Part II: Mixing dynamics. *J. Atmos. Sci.*, **62**, 1291–1310.

Zheng, Y., D. Waliser, W. Stern, and C. Jones, 2004: The role of coupled sea surface temperatures in the simulation of the tropical intraseasonal oscillation. *J. Clim.*, **17**, 4109–4134.

Zhou, L., R. B. Neale, M. Jochum, and R. Murtugudde, 2012: Improved Madden–Julian Oscillations with Improved Physics: The Impact of Modified Convection Parameterizations. *J. Clim.*, **25**, 1116–1136.

Zhu, H., H. H. Hendon, and C. Jakob, 2009: Convection in a Parameterized and Superparameterized Model and Its Role in the Representation of the MJO. *J. Atmos. Sci.*, **66**, 2796–2811.

Zipser, E., 2003: Some views on “hot towers” after 50 years of tropical field programs and two years of TRMM data. *Meteorol. Monogr.*, **29**, 49–58.